ACCESS

A SPACE CORONAGRAPH CONCEPT
FOR DIRECT IMAGING AND SPECTROSCOPY OF EXOPLANETARY SYSTEMS

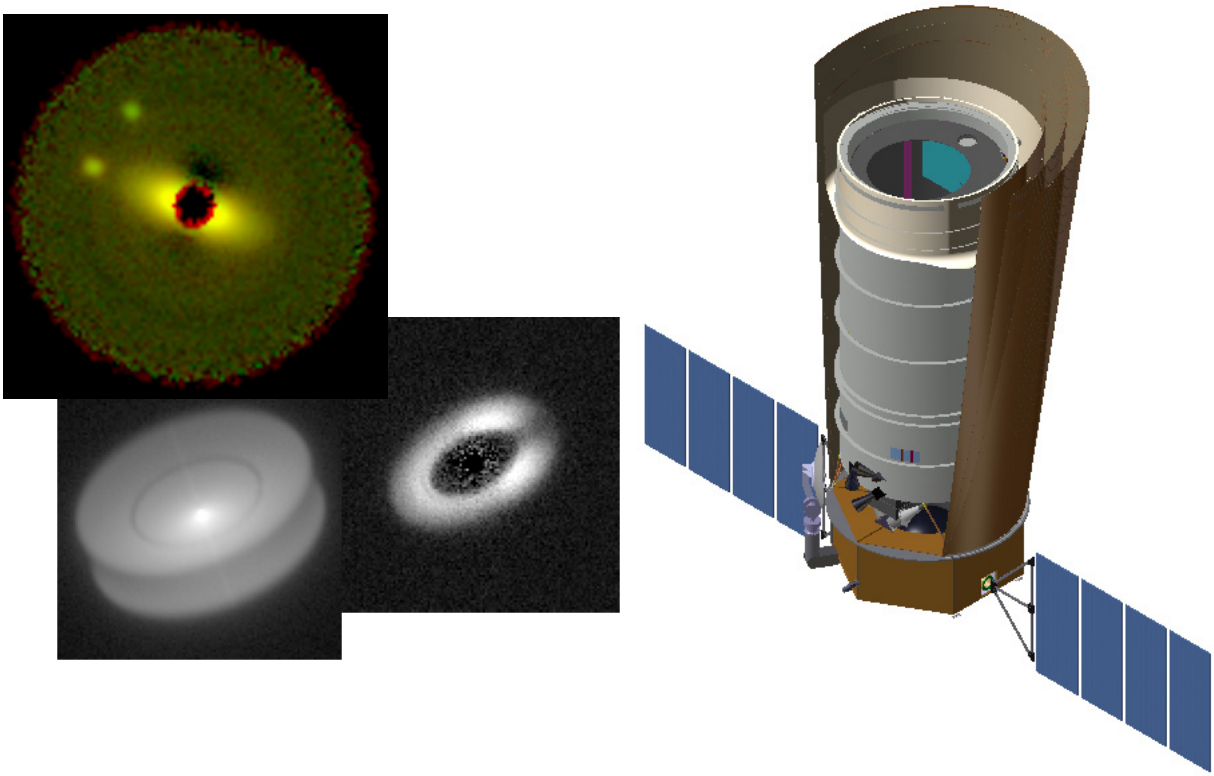

***ACCESS* SCIENCE AND ENGINEERING TEAM**

John Trauger (Principal Investigator), James Alexander, Paul Brugarolas, Olivia Dawson, Robert Gappinger, Curt Henry, John Krist, Dimitri Mawet, Virgil Mireles, Dwight Moody, Peggy Park, Laurent Pueyo, Eugene Serabyn, Stuart Shaklan, Karl Stapelfeldt, John Trauger, Wesley Traub (Jet Propulsion Laboratory, California Institute of Technology); Olivier Guyon (U. Arizona and Subaru Telescope); Ruslan Belikov (NASA/Ames); Jeremy Kasdin, David Spergel, Robert Vanderbei (Princeton University); Geoffrey Marcy (UC Berkeley); Robert A. Brown (STScI); Jean Schneider (Paris Observatory); Bruce Woodgate (NASA/Goddard); Gary Matthews, Robert Egerman, Phillip Vallone, Jason Elias, Perry Voyer, Yves Conturie (ITT Space Systems LLC); Ronald Polidan, Charles Lillie, Connie Spittler, David Lee, Reem Hejal, Allen Bronowick, Nick Saldivar, David O'Connor, Richard Patrick, Pawel Orzechowski, Vanessa Camelo (Northrop Grumman Aerospace Systems); Thomas Price, Mark Ealey (Northrop Grumman/Xinetics)

This page is intentionally left blank.

ACCESS

A SPACE CORONAGRAPH CONCEPT
FOR DIRECT IMAGING AND SPECTROSCOPY OF EXOPLANETARY SYSTEMS

1. INTRODUCTION AND OVERVIEW

We describe the science potential and engineering readiness of a space mission for the direct coronagraphic imaging and spectroscopy of exoplanetary systems at visible wavelengths. The ACCESS study has compared the four major coronagraph architectures (Lyot, vector vortex, pupil mapping, and shaped pupil) in the context of a conceptual space observatory platform of high technology maturity. The study has also compared recent physical demonstrations with JPL's High Contrast Imaging Testbed (HCIT) and other laboratories as a measure of technology readiness. We have selected one of these coronagraph types to represent the highest readiness level among the coronagraph architectures, for a reliable estimate of science performance available with today's technology and for a reliable determination of mission cost, risk, and schedule. We describe the exciting new science enabled by a NASA medium-class coronagraph mission that could be initiated in the coming year with proven high-maturity technologies.

The ACCESS telescope, spacecraft, and pointing systems are representative of the "best" available for exoplanet coronagraphy within the scope (cost, risk, schedule) of a NASA medium-class mission. ACCESS operates at visible wavelengths (500–900 nm) for high contrast imaging at small inner working angles, owing to the need to suppress diffracted light at small angular separations from the star. We note that all coronagraph types require an observatory system with exceptional pointing control, exceptional wavefront stability, and active wavefront control. ACCESS defines a baseline observatory architecture that fully supports any of the major coronagraph types, hence it is a platform that provides a meaningful performance comparisons among coronagraph types.

We believe that ACCESS is a capable and ready coronagraph mission for the study of exoplanetary systems, based on demonstrated technologies that are already at high levels of technology readiness. We outline further advancements in the area of coronagraph performance that could be achieved in the coming year, based on ongoing laboratory programs that are actively developing well-understood technologies.

ACCESS could make a nearly complete census of giant planets orbiting 3–20 AU from their parent stars and zodi dust structures at the level of our solar system, for over 100 nearby stars. A measure of the prevalence of exoplanetary systems, the first pioneering images and spectra of their exoplanets, observations of tell-tale asymmetries in the dust disks, all promise a wealth of new information, seeding further investigations of the nearby planetary systems, while laying the science and technology groundwork for still more ambitious programs of exoplanet exploration.

2. OBJECTIVES AND REQUIREMENTS

Planetary systems consist of gas giant planets, rocky terrestrial planets, and belts of small bodies which generate debris particles. Amazing progress has been made in their study over the past 14 years—more than 300 giant exoplanets have been detected indirectly by the radial velocity technique; more than 50 hot planets have been identified from transit observations, and thermal emission differentially measured from a small subset of them [1]; infrared excesses indicative of debris disks as faint as 50× our Kuiper Belt have been detected in 15% of FGK stars [2]; and direct imaging has just revealed a few widely separated, very young planets orbiting their host stars [3, 4]. These exciting discoveries, made with previously existing facilities (sometimes with modest

instrument upgrades), offer a taste of the science returns that could be realized by a major new facility designed from the outset to meet the specific needs of exoplanet science.

Here we outline the science capabilities of ACCESS, a 1.5 meter space telescope and high-contrast coronagraph. We then review the current trajectory of exoplanet science with existing and developing astronomical facilities. Well beyond the advances anticipated on this trajectory, ACCESS offers the prospect of resolved images and spectra of planetary systems like our own, noting that to directly detect mature giant planets, exozodiacal dust structures at the levels found in our solar system, and terrestrial planets, nearby stars must to be probed at imaging contrasts of 10^{-9} or better. ACCESS is ready to carry out pioneering exoplanet science and general astrophysics as a medium-class NASA mission, while proving the technology and laying the scientific groundwork for still more ambitious future missions.

2.1 Science Mission Objectives

Spectra of Known RV Planets Beyond 2 AU

Radial velocity (RV) surveys have singled out the nearby stars that host Jovian planets. Ten nearby stars are currently known to host RV planets whose apastron distances project to angular separations greater than the ACCESS inner working angle of 3 λ/D (0.23 arcseconds at λ= 550 nm). These are cold objects with a contrast of 10^{-9} in the optical and near-IR, and thus are only accessible to a space mission. Existing ephemerides allow observations to be timed to coincide with their maximum elongations, as indicated by the diagram at right. Thirteen additional stars within 20 pc show long-term accelerations indicating the presence of outer planets with orbits still not yet defined. ACCESS will directly detect these 23 giant planets, measure their colors, take spectra at R ~20, and provide astrometry that will resolve the *sin i* ambiguity in their masses. The spectra will allow the strength of CH_4 features to be measured and the depth of the uppermost cloud deck to be inferred. The planet's albedo and presence of bright ring systems can be inferred using the observed photometry and planet sizes estimated from their measured masses. Multi-epoch imaging showing the planetary orbital motions will make a powerful impression of the reality of exoplanetary systems in the public mind.

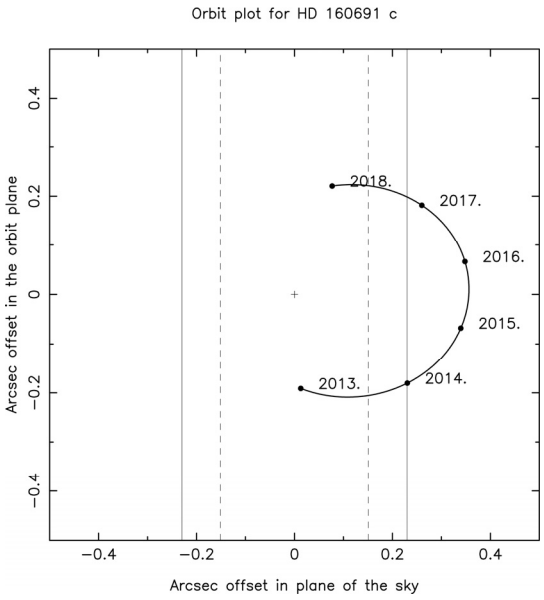

Planet Searches beyond RV Survey Limits

RV searches to date have yielded detections of giant planets within 6 AU of (primarily) FGK stars with low chromospheric activity. Planets with longer periods or face-on orbits, and those orbiting active stars or A stars that lack a rich absorption spectrum, will escape RV detection. Two epochs of ACCESS imaging can detect objects to within 3 AU for stars within 15 pc, and in to 1 AU for perhaps a dozen targets. The stability of the ACCESS telescope will allow exoplanet detections down to contrasts of 10^{-10}, corresponding to the brightness of a giant planet at 15 AU separation. Among the eighteen young stars (age <1 Gyr) within 20 pc, ACCESS can detect any companions >5 Jupiter masses in their thermal emission at z band. For searches of the 3–15 AU region, 3 epochs of observations spaced at the beginning, middle, and end of a five-year mission will provide a sufficient exploration of orbital phase space to achieve a detection completeness exceeding 70%.

For the dozen stars where searches as close as 1 AU are possible, 6–10 epochs of imaging may be needed to compile good completeness results. The newly discovered planets will then be characterized spectroscopically. For a handful of the brightest and nearest stars, ACCESS performance may be good enough to detect terrestrial planets in the habitable zone (HZ), for low levels of exozodiacal dust.

We have computed a metric to provide an indication of the search sensitivities with various coronagraph options, as described in Appendix 8.9. Using simulated coronagraph images, computed according to the optical models described in Appendix 8.7 and subjected to a Monte Carlo set of pointing errors predicted for the ACCESS observatory, we compute the number of fiducial Jupiters that could be observed at 45 degrees and 15 degrees from elongation at six epochs, with S/N=10 detections in V-band for each epoch, over a 2.5 year period with 70% observing efficiency. The first example, highlighted in green, corresponds to a TRL 6 Lyot coronagraph with an IWA = 3 λ/D, representing the performance floor for ACCESS coronagraphs. Highlighted in blue are tabulation for coronagraph configurations that may reach TRL 6 in laboratory demonstrations in the coming 12 months. Note that planets appear at or beyond the 45-degree separations from their stars at least half the time, therefore a sequence of six observing epochs spread across several years provides an observational completeness approaching 100%.

Table 2.1-1. Number of nearby stars that can be surveyed for 5.2 AU Jupiters, IWA 3.0 λ/D

Coronagraph Type	Planet 45° from max elong	Planet 15° from max elong
Lyot	117	175
PIAA	166	278
Vortex	135	204

Table 2.1-2. Number of nearby stars that can be surveyed for 5.2 AU Jupiters, IWA 2.5 λ/D

Coronagraph Type	Planet 45° from max elong	Planet 15° from max elong
Lyot	153	218
PIAA	178	278
Vortex	154	228

Table 2.1-3. Number of nearby stars that can be surveyed for 5.2 AU Jupiters, IWA 2.0 λ//D

Coronagraph Type	Planet 45° from max elong	Planet 15° from max elong
Lyot	170	230
Vortex	164	241

Note: *Accurate PIAA wavefront control solution not available for this IWA*

We show another metric for ACCESS sensitivities in the figure at right. Computed in the same manner as the tables above, the diagram indicates how many detections of fiducial planets with the size and albedos of Jupiter, Saturn, Uranus, and super-earths (with twice the diameter of earth) at S/N=10 in integration times of 1 day or less, as a function of distance from the star. Exozodiacal dust at 1 zodi equivalent level is assumed. For this simulation, we used the Lyot coronagraph, operating with an IWA of 2.5 λ/D, which is scheduled for demonstrations on the HCIT later this year.

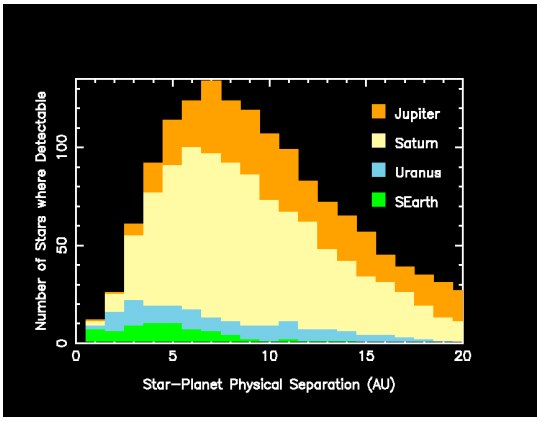

ACCESS Exoplanet Discovery Space

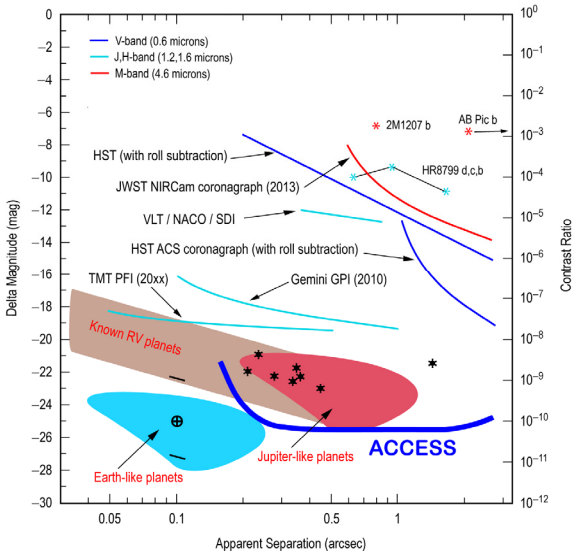

ACCESS imaging sensitivity compared to other methods available now and in the coming decade. Shaded areas indicate the regions of high probability (from Monte-Carlo simulations) of detecting planets orbiting the nearest 100 AFGK stars. Jupiters in 5 AU orbits fall in the red-shaded area, where specific RV-identified planets are shown by asterisks. Earth-like planets fall in the blue-shaded area. The location of an Earth-twin at elongation at 10 pc is indicated by the ⊕ symbol, with a dash above for the background from a dust disk similar to the solar system, and a dash below to indicate the level of background noise after one day of integration. The detection range for ACCESS is the area above the blue curve at bottom right.

Zodi Structure as an Indicator of Unseen Planets

ACCESS will make the most sensitive imaging survey to date of tenuous debris disks, the signposts of planetary systems. These are clouds of small dust grains created by the mutual collisions of asteroids and comets, as well as by comet sublimation. Without continual replenishment by such events the dust would be cleared away within a small fraction of a star's lifetime by stellar radiation, stellar wind pressure, or self-radiation. The interplanetary dust cloud in our own solar system, which can be seen as the zodiacal light, is a debris disk created primarily by the collisions of asteroids. Spitzer observations have identified more than 80 stars within 25 pc that possess debris disk analogs to our Kuiper Belt, at the levels of a few hundred zodis. Some of these dust clouds have been spatially resolved and show warps, asymmetries, or narrow rings that are strongly suggestive of planetary perturbations. The structure of the eccentric, sharp-edged Fomalhaut debris ring demanded a nearby planetary perturber which was spectacularly confirmed by recent HST [3]. Another example is dust in our own solar system resonantly trapped with the Earth [5]. Computations of our Hundreds of nearby stars are likely to have debris disks that can be imaged with ACCESS contrast capabilities at 1 AU resolution. As a canvas on which planets can impress dynamical signatures, dust disk structures will enable indirect detections of numerous planets too faint or too distant to be discovered any other way.

Probe of Zodi Dust as a Potential Problem for Terrestrial Planet Detection

High levels of exozodiacal dust will be a major impediment to direct imaging of extrasolar terrestrial planets, no matter what telescope architecture is eventually employed [6]. These dust clouds reflect starlight and emit in the thermal infrared, adding photon noise and scene confusion to exoplanet signals. It is therefore crucial to assess the dust levels around nearby stars. The Keck and LBT interferometers use 10 μm nulling observations to probe HZ dust. However, atmospheric and instrumental phase instability has limited the achievable null depth thus far to sensitivities of roughly a hundred zodis. Additional ways to attack the problem are needed. Detailed coronagraphic imaging simulations show that ACCESS can provide sensitivity down to the sub-zodi level, extending inward to 3 AU across the full target sample envisaged for a Terrestrial Planet Finder (TPF) mission, and in to 1 AU for about a dozen stars. Transport models can be used to relate dust levels at 3 AU to those at 1 AU; for our solar system, these models are well-calibrated by dust counts from interplanetary

probes. Reflected light observations with ACCESS will thus be an outstanding tool for assessing the dust content in the HZs of nearby stars.

General Astrophysics with ACCESS

Extending a thousand times beyond the performance of HST, the contrast capabilities of ACCESS will enable groundbreaking studies of circumstellar matter and quasar/AGN host galaxies.

For protostellar amd protoplanetary disks, thousands of targets are known within 500 pc from IRAS and Spitzer surveys but very few have been detected against the glare of their central star. Imaging detections to date have taken place largely in special circumstances of external illumination [7], edge-on orientation [8], or large central clearings [9]. At the contrast levels accessible to HST, JWST, and ground-based AO, numerous disks are unseen, perhaps because of dust grain evolution or settling which can produce self-shadowing in these optically thick systems [10]. These dimmer, more evolved disks will be revealed around young stars by ACCESS. The disk structures seen will trace the disk dispersal process (possibly showing radial zones cleared by protoplanets), and measure the dust content as a function of age as the systems evolve toward main sequence debris disks.

For post-main sequence stars, ACCESS will image the shell structures which trace the mass-loss that takes place in the Red Giant and Asymptotic Giant Branch regions of the HR diagram. The effect of low-mass companions and pre-existing debris disks on these outflows is thought to be very important for defining the variety of structures seen in the subsequent planetary nebula phase. These outflows seed the ISM with processed gas and dust leading to the next generation of stars and planetary systems. Furthermore, the large luminosity increases of a Red Giant star (~30–100 Lsun) should lead to evaporation and disintegration of any Kuiper belt that was present during the prior main sequence phase, producing a "reborn" debris disk around first ascent red giants and possibly enabling direct imaging of extrasolar comets [11].

2.2 Expected Significance for Exoplanet Science

Over the next decade, how will the current and building astronomy facilities add to our knowledge, and what kind of major new facility can have the greatest impact?

RV surveys are beginning to find "super-Earth" planets in short-period orbits. Around Sun-like stars, they will probe for Neptune-mass planets orbiting within 1 AU and Jupiter-mass planets orbiting as distant as 7 AU. For the very low mass stars, RV should achieve detections of objects as small as a few Earth masses at orbital distances of a few tenths of an AU [12]. The orbital element distribution for the major inner planets of nearby stars should be well in hand by the end of the next decade.

Upcoming transit observations will reveal the frequency and radii of inner rocky exoplanets by photometrically monitoring large ensembles of solar-type stars. COROT is apparently finding examples of large terrestrial planets in short orbital periods, while Kepler will probe for Earth-mass planets in 1 AU orbits. Spectroscopic measurements made during transit and secondary eclipse by warm Spitzer, the upgraded HST, and JWST will constrain their albedos and detect high opacity atmospheric species such as Na I, CH_4, and Ly a [13]. By the middle of this coming decade, transit work should have yielded a statistical understanding of the inner parts of extrasolar planetary systems.

High contrast imaging detections of self-luminous exoplanet and brown dwarf companions are expected from large ground-based telescopes deploying the next generation of adaptive optics systems, and from space using JWST. Contrasts of 10^{-7} are projected at 0.2 arcsec separation in the near-infrared [14], extending well beyond today's performance of 10^{-5} contrast at 1 arcsec. This would enable detection of warm (young/massive) gas giant planets with today's 8-m class telescopes, while an optimized 30-m telescope would extend this to a 0.07 arcsec inner working angle. At 4.5 μm, JWST's NIRCam coronagraph will be capable of detections at contrasts of 10^{-6} at

separations beyond 1.5 arcsec, capturing objects like our own Jupiter in thermal emission as companions to the nearest M stars [15]. The uncertain luminosity evolution of young giant planets clouds the picture somewhat [16], but it appears that the outer, massive planets orbiting nearby (d<20 pc), young (age <1 Gyr), low-mass (M <0.5 Msun) stars could be in view midway through the coming decade.

Imaging of protoplanetary disks will be revolutionized by ALMA, which will be able to resolve dynamical structures driven by protoplanets at angular resolutions approaching 0.01 arcsec. For the more nearby debris disks, ALMA will be able to map systems brighter than 1000 zodis at 0.1 arcsec resolution. A 5σ detection of the Fomalhaut debris ring surface brightness can be achieved at 450 μm in 6 hours at this resolution, according to the online ALMA sensitivity calculator. At 20 μm JWST will resolve warm debris around nearby A stars with 0.3 arcsec resolution. Large ground telescopes with adaptive optics operating in the near-IR will push toward the 1000 zodi sensitivity benchmark established by HST. Herschel will detect exoKuiper belts down to the ~10 zodi level. A wealth of new data detailing the internal structure of bright circumstellar disks will be emerging in 2015, seeding a new theoretical understanding of disk structure, dynamics, and evolution.

The ACCESS Mission

While the advances described above will be remarkable scientific milestones, these existing and developing facilities fall well short of the objective of obtaining resolved images and spectra of dynamically full exoplanetary systems like our own, systems that may harbor terrestrial planets in habitable zones. Are such systems commonplace? Given that ACCESS could provide the first spectral measurements from a dozen or more RV planets, and a census of yet unknown exoplanets orbiting between 3 and 20 AU from their stars, and quite possibly a number of super-earths, the impact on exoplanet science could be huge. We know essentially nothing about exozodiacal dust disks at the level of our solar system, yet these disks are signposts of planetary systems and unseen planetesimals, and their eccentricities and asymmetries are sensitive indicators of unseen planets. An ACCESS survey of many such systems would provide compelling evidence for the nature and prevalence of exoplanetary systems. ACCESS offers a pathway to the nearby exoplanet systems, by way of giant planets and debris structures, for more than 100 stars within ~20 pc. ACCESS is a compelling and logical next step for NASA's Exoplanet Exploration Program.

3. TECHNICAL APPROACH AND METHODOLOGY

3.1 Mission Description

A summary of key requirements appears on the next page. The mission begins with a launch from the Cape Canaveral Air Force Station aboard a Delta IV or Atlas V-class vehicle. The launch puts the observatory on a direct trajectory to the Sun-Earth Lagrange point 2 (L2), where the system enters into a halo orbit for a prime mission of 5 years. This orbit provides a stable thermal environment and the ability to observe a large fraction of the sky, while requiring a delta-V of only 20 m/s to maintain the orbit for the 5 years.

The total mass of the observatory (telescope, coronagraph, wet spacecraft) is 2074 kilograms, including an overall 20% contingency based on the maturity of the individual components. The smallest variant of the launch vehicle class, the Atlas V-401, provides a lift capacity to L2 of 3793 kg, hence a lift mass margin of 45%. The observatory fits within the Atlas standard, 4-meter diameter, Extended Payload Fairing. The maximum power load of the observatory is 1916 watts, including a 30% contingency for growth. The solar array capability is 2568 watts at end-of-life, providing an additional 25% margin beyond the contingency. The arrays are sized for the 30° off-pointing required during rolls.

Table 3.1-1. Summary of Key Requirements

Objectives	Measurement	Mission & Observatory	Coronagraph	Telescope	Spacecraft	Ground System & Mission Operations
Search for planets	Observe > 50 star systems; inner working angle of £ 3λ/D	Field of regard available at L2, 5-year mission life	SNR > 10 mask designs, occulter designs, 3 e- read noise	Primary mirror diameter of at least 1.3 m	Gimbaled solar arrays, gimbaled HGA	Two telecom contacts per week, 8 Gbits/day data volume
	Contrast of £ 1 x 10^{-9}	Thermal stability enabled by L2 orbit and a three-layer sunshield providing 6000× isolation	48 x 48 element DM, 10 mK / 1000 s thermal stability of DMs, 10 mK stability of optics table, 1 K stability of CCDs, λ/200 rms optics, 0.1 mas pointing accuracy, 0.45 mas pointing stability / 1000 s	Thermoelastic perturbation of PM figure <0.2 nm rms, Surface finish of primary <8 nm rms over 5 to 50 cm / cycle, 1 mas pointing accuracy, 1 mas pointing stability / 1000 s	30 as pointing accuracy, 100 mas stability / 1000 s, isolation of jitter from RWAs	
Characterize planets	Coverage from 500 to 870 nm in three spectral bands		20% bandwidth for each band achromatic optics, sensitivity range of detectors, photon counting integral field spectrograph with <1 e- read noise	Reflective optics, protected silver coatings		
Accommodate coronagraph and telescope					Provide >2000 W to observatory, support >1065 kg instrument, provide >8 Gbytes of storage	
Affordable		Fit smallest possible EELV and fairing, technical margins consistent with JPL Design Principles	Avoid UV lithograph state-of-the-art small optics	1.5 m diameter primary	TRL 9 technology, production line system, S-band	Commercial ground station for optional telecommunications contacts
Reliable	Selective block redundancy, risk management practices per Class B mission					

The observatory is designed to access stars outside a solar avoidance angle of 80 degrees. To minimize thermal settling time following a slew from one target star to another, ACCESS will normally restrict the angle between the Sun and target star to a range between 80 and 120 degrees. The yearly rotation of the observatory around the Sun then provides natural observing windows for two or more visits of any target star per year.

The Deep Space Network is used for essential telecommunications. The radio frequency is S-band. Data volumes of about 3 GB are downlinked twice per week. Observing sequences are uplinked during downlink passes. Estimates are that two passes of 8 hours each per week support nominal operations. Engineering data is routed to a JPL operations center for pipeline analysis, distributed to investigators for further analysis, and finally archived. Science data is archived at the Infrared Processing and Analysis Center or an equivalent repository.

3.2 Observatory

As referred to herein the instrument is a combination of the coronagraph and the telescope. The observatory is the combination of the instrument and the spacecraft. Pictured here is a view of the system stowed for launch, two views of it deployed, and a raytrace diagram of the optical system.

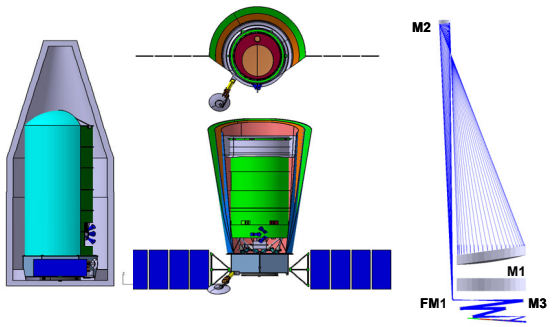

The total mass of the observatory is 2074 kilograms if 19.4% contingency is included based on the maturity of the individual components. The Atlas 401's lift capability provides a 45% margin. The maximum power load of the observatory is 1728 Watts with 30% contingency for growth included. The solar arrays' 2768 W capability at end-of-life provides an additional 27.2% margin beyond the contingency. The arrays are sized for the 30° off-pointing required during rolls.

	Mass (kg)
Coronagraph	143
Sunshield	163
Spacecraft	533
Telescope	1002
Total Dry	**1841**
Propellant	234
Total Wet	**2075**
Capability	3793
Margin	**45%**

	Power (W)
Coronagraph	190
Battery Recharge	26
Spacecraft	433
Telescope	700
Distribution Losses	125
30% Contingency	442
Total	**1916**
Capability	2568
Margin	**25%**

3.3 Telescope

The telescope optical design is an unobstructed off-axis Gregorian design that delivers a diffraction-limited visible image to the science instrument coronagraph. At the heart of the optical telescope assembly (OTA), is the system's 1.5 m lightweight (areal density of 40–50 kg/m^2) primary mirror. Due to the stringent stability requirements for the system, the glass for the PM and secondary mirror is specified to be the highest quality ULE® glass. The PM is constructed in a manner similar to that for the fabrication of the Advanced Mirror System Demonstrator (AMSD) optic, which was built under funding of a consortium of government agencies including NASA. The PM has front and back facesheets and a light-weighted core formed by abrasive water jet. The three components are fused together, resulting in a mirror that is pure ULE®, enabling the most thermally stable optic possible.

The prescription for the optical figure of the PM was chosen to be identical to the 1.8 m Technology Demonstration Mirror (TDM) funded by the TPF program. This decision was made to mitigate risk on the ACCESS mission because the metrology null that was to be used to test the TDM has been manufactured and calibrated. Calibration results showed that the uncertainty in the null was ~2 nm-rms, fitting within the wavefront and contrast error budget for ACCESS. ITT has already achieved these wavefront requirements on optics in a similar size class to ACCESS.

Although ACCESS is an off-axis system, modern metrology techniques and tools allow this type of system to be aligned nearly as easily as on-axis systems. ITT has significant experience in aligning on-and off axis telescopes of various sizes.

The precision structures of the optical telescope assembly design benefit from commonality with TRL 9 components of the 1.1 m high-resolution NextView Electro-Optical payload developed by ITT, which was launched in September 2008. This maximizes the use of high TRL hardware, materials, and proven design and manufacturing processes.

The composites selected for the OTA metering structures use an ITT co-patented resin system that are insensitive to changes in the system's thermal or hygroscopic environments. The stability of the metering structures is on the same order of magnitude of the stability achieved for the Corning ULE® optics that they support. ULE® glass has a coefficient of thermal expansion that is less than 30 ppb/K.

1.1 m Aperture NextView OTA

To achieve the thermal stability ACCESS requires, prevent contamination during ground operations and launch, and provide a structure onto which the system's sunshade can mount, the OTA is surrounded by a non-precision but lightweight composite Outer Barrel Assembly (OBA) which employs an ejectable cover. Thermal analyses have been performed on the ACCESS system. The resulting thermo-elastic motions of the structure demonstrate that thermal stability over an observation is maintained to the required levels to maintain the required contrast in the coronagraph.

3.4 Spacecraft

The spacecraft is comprised entirely of TRL 9 elements. It provides all housekeeping functions for the observatory, including power, propulsion for orbit insertion and maintenance, attitude control, command and data handling, communications, and thermal control of the bus itself. The spacecraft bus also serves as the primary structural interface to the launch vehicle, the sunshade, the Optical Telescope Assembly (OTA) and the Outer Barrel Assembly (OBA). A V-groove sunshade, derived from the JWST design, ensures that changes in observatory orientation will not adversely affect the telescope thermal environment. The spacecraft structure draws from NG's modular Advanced Bus family of products. The bus has an aluminum hexagonal structure with a central cylinder and six shear panels to support the telescope and instrument. The central cylinder is sized for direct attachment to the Atlas V and carries the primary structural loads.

The propulsion subsystem provides a reaction control capability for the observatory. It is used for trajectory correction maneuvers after launch and during cruise to a Sun-Earth L2 halo orbit, for halo orbit insertion, and for station keeping and momentum dumping. It can also be used for attitude control during contingency operations. The propulsion subsystem is sized for 10 years of operation, with total delta-V budget of 150 m/s. The propulsion subsystem uses a simple, flight-proven hydrazine mono-propellant system, which has a capacity of 225 m/s, providing 33% margin. One 4.45 N thruster is used for delta-V maneuvers and three 4.45 N thrusters are used for attitude control.

The ACS consists of the following components (and redundancy): Coarse Sun Sensor Assembly (CSSA) (2:1), Inertial Reference Unit (IRU) (internally redundant), Star Tracker Assembly (STA) (3:2), Reaction Wheel Assembly (RWA) (4:3), HGA Biaxial Gimbal, two gimbals with a single actuator and dual windings for each gimbal (2 for 1 redundancy), Solar Array Drive Assembly (SADA), each with one gimbal axis with a single drive and dual windings (2 for 1 redundancy)

The HGA biaxial gimbal allows the HGA to move 210° in azimuth and ±90° in elevation. The single axis SADA gimbal allows rotation of the solar array wings. They are not operated while the spacecraft is inertially pointed to minimize overall Observatory jitter during data collection.

The Thermal Control System (TCS) maintains spacecraft bus components within required temperature limits. The TCS subsystem uses high-heritage parts to ensure reliability. The TCS subsystem design is simplified by the aluminum bus structure which conducts heat more efficiently than a composite structure, Aluminum doublers and heat pipes are also used on the bus panels to increase heat transfer. Aluminized Kapton multi-layer insulation (MLI) is used for the spacecraft bus compartment, STAs, IRU and HGA reflector backside. Silverized Teflon tape is used on the HGA gimbal drive to reject heat. Room temperature vulcanization (RTV) or compressed aluminum foil (CAF) is used when mounting high power avionics to the panels to ensure proper heat rejection. Mechanical thermostats, heaters and MLI are used to maintain propulsion equipment at proper operating temperatures. Heaters controlled by mechanical thermostats maintain bus-mounted equipment and appendages on the anti-sun side of the spacecraft above their minimum operating temperatures.

The purpose of the sunshade is to ensure that changes in Observatory orientation will not adversely affect the telescope thermal environment. It is designed to improve the thermal stability to maintain the primary mirror surface figure to within tolerable or correctable limits. The sunshade attenuates solar input by a factor of approximately 6000. The sunshade is composed of three Kapton layers, each layer separated by 2.5°. The outer layer is a 2 mil Kapton-E membrane with a Si coating on the outer surface and Vacuum-Deposited Aluminum (VDA) coating on the inner surface. The two inner layers have VDA coatings on both surfaces. The layers are supported by fiberglass frames using wishbone structures to provide shape control.

The Communications subsystem provides RF links for commanding the Observatory, for transmitting telemetry and science data to Earth, and for orbit determination. The Communications subsystem is fully CCSDS compatible. S-band was selected for both science data and command and telemetry links. The Communications subsystem is capable of providing a maximum data rate of 2 Mbps for transmitting science data. The science data downlink has low rate mode and high rate modes. The low rate mode is and is used to transmit compressed images of the coronagraph images.

The C&DH Subsystem provides the command processing and distribution, telemetry data collection and formatting, mass data storage, instrument support, and time service functions for the spacecraft. The C&DH subsystem a spacecraft processor (SCP) uses a RAD750 processor and interfaces to all subsystems via a MIL-STD-1553 bus. The SCP is designed with sufficient on-board memory to meet the 24 GB data storage requirement.

The observatory's flight software is modular and table-driven to permit easy incorporation of mission-specific upgrades without impacting the core. It is primarily written in C and C++ and is compact, leaving large margins in the on-board RAD750 processor. The S/W is developed on an engineering model flight processor and validated using tested engineering model hardware containing all the components of the data management subsystem, a flight-like harness, and elements of the attitude control subsystem. The S/W includes fault detection and correction capabilities. The primary "safe haven" mode implemented in the S/W is sun capture using the inertial attitude determination system and the coarse sun sensors. The fault detection logic is tailored to meet the mission requirements.

3.5 Pointing Control System

Pointing errors degrade optical contrast in two main ways: (i) telescope pointing errors walk the beam across the primary and secondary mirrors; and (ii) coronagraph occulting mask centering (on the star) errors spill light outside the mask. The philosophy behind the PCS design is to propose the best pointing system for a mid-class observatory with nearly available technology (TRL 6 or above). This led to a three-stage pointing control system; a fine guidance camera design within the coronagraph, and an extensive disturbance rejection strategy to minimize environmental jitter.

Modeling of the instrument and science has simulated the effects of pointing errors and guided the specification of requirements. We performed a detailed simulation of the disturbances using models of the optics, fine steering mirror (FSM) and fine guidance camera located within the coronagraph, the spacecraft ACS system, a hexapod pointing system, and structural dynamics. The pointing stability requirement of 1 milliarcsec (3σ, over 1000 seconds) for the tip/tilt of the telescope line-of-sight drives the need to augment the spacecraft pointing capability with an active hexapod jitter control stage. The fine pointing requirements were derived for the most demanding science case, corresponding to a coronagraph inner working angle of $2\,\lambda/D$.

The pointing system starts with a standard 3-axis stabilized spacecraft bus and is augmented by a hexapod system and FSM. The hexapod enables pointing the telescope with body-pointing stability better than Hubble for central guide stars brighter than 7^{th} magnitude. The FSM allows for additional pointing capability within the coronagraph. The first stage is the spacecraft ACS reaction wheel system that stabilizes the spacecraft to 100 mas in pitch and yaw and 5000 mas in roll. This capability is comparable to that of the Kepler mission. The second stage is the active hexapod telescope pointing system that stabilizes the telescope line-of-sight to 1 mas in tip and tilt (corresponding to pitch and yaw axes of the SC). The hexapod also provides a vibration suppression capability. The third stage is the FSM within the coronagraph that centers the star in the occulting mask to 0.1 mas in tip and tilt.

Pointing knowledge starts with a fine guidance camera in the coronagraph, measuring the tip and tilt errors using the target star. The information from the fine guidance camera is used by an advanced control architecture to command the FSM and the hexapod. This architecture allows smooth and effective offloading of the FSM by the hexapod. The FSM loop has a high bandwidth loop that responds quickly to pointing errors, the hexapod has a mid-bandwidth which responds slower and offloads the FSM. In turn, the hexapod is offloaded by the spacecraft ACS by generating a high accuracy offset angle derived from the hexapod pointing angles. Since the hexapod is tracking the guide star with a precision of 1 mas, measurement of the hexapod pointing angles yields a SC pointing error of the same accuracy.

The strategy towards disturbances is to minimize the jitter at the source. We have selected a quiet orbital environment (L2), designed a thermally-controlled telescope and instrument, planned operational constraints during science observations (limitations on reaction wheel speeds, keeping solar array drives and HGA gimbals motionless), and added reaction wheel isolators, solar array dampers and a vibration suppression capability within the hexapod.

There are options for mitigation should the pointing requirements prove to be too stringent. Higher quality optics before the FSM can compensate for beamwalk caused by pointing errors. If the telescope stability requirement is relaxed to 10 mas through a choice of higher quality optics, we can consider descoping the hexapod stage. Other descope options are elimination of the fine alignment mechanism to center the PSF at the crosshairs of the fine guidance camera and elimination of the FSM. Additional details about the PCS are available in Appendix 8.5.

3.6 Coronagraph Configurations

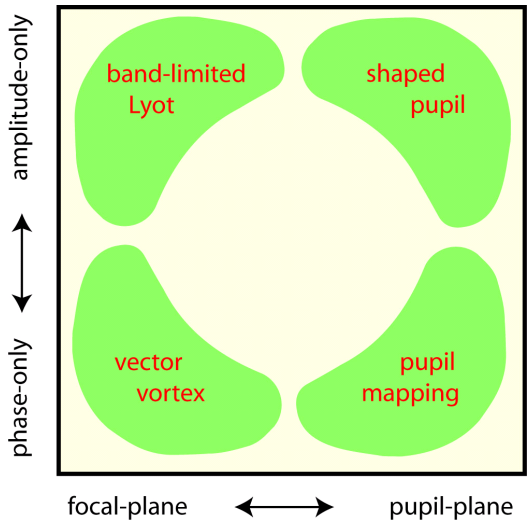

ACCESS has compared four coronagraphs representative of the major coronagraph types, indicated schematically in the figure to the right. Here, we describe the elements of the ACCESS coronagraph instrument that are common to all four types. Then we describe the unique coronagraph elements that distinguish each of the architectures and define the physical models for our comparisons.

The coronagraph optical assembly is structurally attached to the bulkhead of the optical telescope assembly, which includes the telescope primary and secondary mirrors, a fold mirror, and a collimating mirror. The instrument receives the collimated beam and relays an image of the primary mirror (the pupil of the system) to a 48 mm (2300 actuator) deformable mirror mounted in a gimbaled tip/tilt fine steering mechanism. The optics to this point define the telescope line of sight (LOS), which is stabilized on the sky to 1 milliarcsecond (3σ) with the AIMS attitude control system. The beam passes to a second 48 mm deformable mirror in a fixed mount, then to a paraboloidal mirror that brings the beam to a focus. The image of the target star is stabilized at this focal point to 0.45 milliarcseconds (3σ) using the pointing knowledge from the fine guidance camera. Therefore, all coronagraph instruments share an observatory platform that provides (1) a stabilized telescope LOS, (2) an internal fine guiding sensor and tip/tilt mechanism that stabilizes the star image at the first instrument focus, and (3) a pair of high-TRL precision deformable mirrors for wavefront control. Optical elements specific to each coronagraph type follow this common "front end," and are described below.

Following the unique coronagraph optics, there are the "back end" elements common to all four coronagraphs. These elements use dichroic mirrors to split the light into three 20% spectral bands (500–600 nm, 600–720 nm, and 720–870 nm), then project these spectrally filtered high-contrast images simultaneously onto a single low-noise CCD focal plane. An integral field spectrograph, with resolving power of 20 [17], receives light from a selected area in the coronagraph dark field by means of a steerable mirror. Finally, a realistic physical description of these optical elements, derived from measured characteristics of commercially available components, are embedded in an optical diffraction propagation model written in IDL using the PROPER library of coronagraph elements [15]. The elements unique to each coronagraph type are described in the following sections.

Lyot Coronagraph

The band-limited Lyot coronagraph was introduced by Kuchner and Traub [18] and extended to higher-order apodizations by Kuchner et al. [19]. These band-limited masks have been manufactured most recently as vacuum-deposited metal films on glass. The highest contrast results to date have been obtained with a Lyot coronagraph in JPL's High Contrast Imaging Testbed (HCIT; [20]). Recent work has shown that hybrid metal-dielectric masks, band-limited in both real and imaginary parts, can achieve high contrast over bandwidths of 20% with useful throughputs of order 65% [21]. Analysis has shown that a trade can be made between useful throughput and inner working angle, and that IWAs as small as 2 λ/D are feasible. The testbed has also demonstrated open-loop contrast stability of 10^{-11} over periods of five hours or more [22], enabling post-observation image subtraction techniques that demonstrate contrasts better than 10^{-10}.

Vector Vortex Coronagraph

The phase mask coronagraph has been developed in a number of forms, including most recently the vector vortex mask [23]. Our main interest lies in the performance and readiness of phase vortex masks designed for topological charge of 4 or greater. The new mask is implemented with a liquid crystal polymer technology developed by JDSU. The technology provides a natural pathway to achromatized phase masks capable of a 20% bandwidth at a contrast of 10^{-9}.

Shaped Pupil Coronagraph

The shaped pupil coronagraph was introduced by Spergel [24] and developed at Princeton [25]. Physical masks have been manufactured from silicon wafers at JPL's Micro Devices Laboratory and validated in tests in JPL's HCIT. The "Ripple3" design has achieved 2×10^{-9} contrast with a spectral bandwidth of 10% over a field of view spanning 4–10 λ/D. The shaped pupil masks to date have been limited to an inner working angle of 4 λ/D, where a hard-edged focal plane mask blocks the direct light from the star. Inner working angles smaller than 4 λ/D can be achieved only by adding an element of pupil mapping to the coronagraph,as described by Pueyo et al. [26], who showed that, in principle, the use of a pair of deeply-figured mirrors in conjunction with the shaped pupil could improve coronagraph IWA to 2.5 λ/D. We note that in this approach, the shaped pupil concept takes on some characteristics of the pupil mapping coronagraph.

Pupil Mapping Coronagraph

The pupil-mapping system [27], also known as phase induced amplitude apodization (PIAA), uses a pair of steeply aspheric mirrors to concentrate and apodize the light towards the center of the coronagraph pupil. PIAA can in principle achieve high contrast and high throughput at inner working angles of 2 λ/D. Guyon, et al. [28] and Belikov, et al. [29] have shown that additional grey-scale or binary apodizations are needed to suppress wavelength-dependent diffraction effects, leading to hybrid designs that achieve in principle bandwidths of 20% and throughputs of order 85%. Studies have been made of the pupil-mapping coronagraph with one or two deformable mirrors [30]. The best reported laboratory performance with the first generation of PIAA mirrors is a contrast level of 2.2×10^{-7} averaged between 1.6 and 4.4 λ/D in monochromatic light [31]. Manufacturing of the PIAA mirrors is challenging. A second generation of PIAA mirrors has been fabricated by Tinsley and will begin laboratory testing in the HCIT in Spring 2009.

3.7 Coronagraph Implementation

Optical schematics for Lyot and pupil-mapping versions of the coronagraph appear below. The vector vortex and shaped pupil options are similar, using different coronagraph masks inserted into the same layout of mirrors and mechanisms. The pupil-mapping option is taller, requiring six additional mirrors in the optical path and two additional mechanisms. All options feature redundant assemblies of these critical elements for single-point fault tolerance: fine guidance cameras, deformable mirrors, and science cameras. These bands are focused simultaneously onto adjacent areas of a single CCD detector or to the spectrograph.

The mechanical concept uses low CTE materials for dimensional stability. Stack height is a critical dimension so as not to outgrow the launch vehicle fairing. The Lyot, vector vortex, and shaped pupil options fit with 0.4 m of stack height to spare. The pupil-mapping option fits but with little margin. Cameras are placed out of plane for easy access during integration and test and to simplify temperature control of the detectors. Access panels exist so that other elements are readily accessed for troubleshooting and alignment without forcing major disassembly of the instrument. All options feature several, single-fault tolerant mechanisms. Where possible, the same mechanism design (e.g., a linear positioner) is repeated. Temperature stability is achieved by using blankets, electrical heaters, and heat pipes.

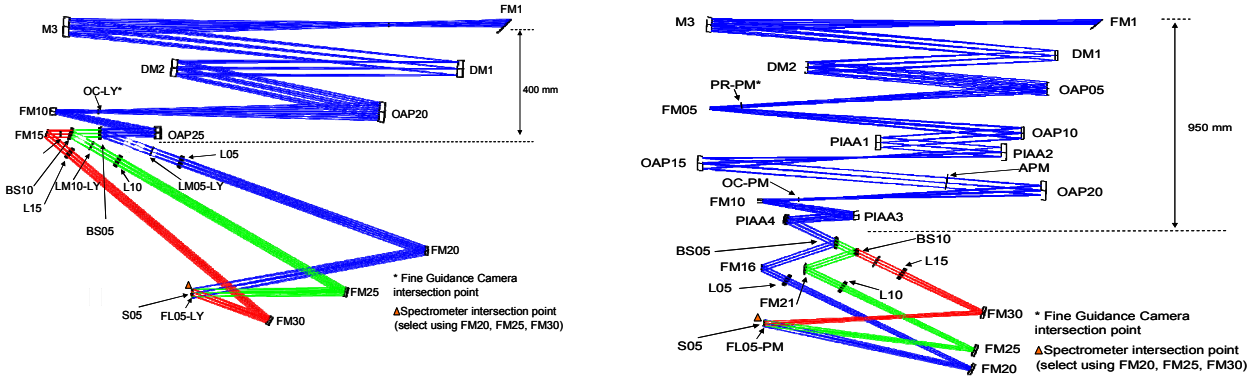

4. TECHNOLOGY READINESS AND DEVELOPMENT

4.1 Coronagraph Performance Comparison Matrix

The four coronagraph types are evaluated with respect to each other using two sets of criteria, as shown in Appendix 8.7.5. The first of the criteria define a performance floor that corresponds to TRL 6 coronagraph performance that has been demonstrated in JPL's High Contrast Imaging Testbed (HCIT), a space-like environment for technology validation. This sets the minimum performance requirements for the ACCESS mission and helps define the minimum science mission.

The second set of criteria provides discriminators among the coronagaph types. Here we rank the four types according to performance metrics that may be achieved and demonstrated in the HCIT test environment in the coming 12 months. Each criterion receives a relative weight and a score. Weights were formulated by averaging votes from science team advocates for each of the options with a vote for the engineering team. Each advocate got one vote in an attempt to minimize bias in the outcome. Scores are multiplied by weights to arrive at weighted scores, which are then summed to arrive at a total. Totals are then compared. A greater total indicates a more favorable option. The scores were debated by the group and occasionally adjusted to more accurately capture what the group valued most.

The outcome is that a Lyot design would be optimum for this mission *given what is known and demonstrated today*. The vector vortex, owing to its simplicity, may advance significantly this year with process refinements. The shaped pupil did not match the inner working angles of the other three, however it has demonstrated high contrast in the HCIT should not be ruled out as a viable candidate. The promise of greater performance of the pupil mapping option has not yet been proven in the laboratory, and due to its additional cost, complexity, and current uncertainty it would not be recommended if project start were imminent. The Lyot option continues to be attractive because it is the most mature in terms of its demonstrated capability and in the validation of the analytical model of its performance. It has demonstrated performance that defines the minimum science mission for ACCESS. The vector vortex is attractive because it is easy to combine with the Lyot and offers the promise of somewhat greater performance. Significant coronagraph developments can be expected in the coming year, based on ongoing funded research with known technologies. Additional progress may possibly be made over the next 2–4 years. Such advances should be evaluated and compared with reference to the demonstrated state of the art. We conclude that at least one, and possibly more, coronagraph technologies will be fully ready in the coming year.

4.2 Feasibility and Mission Critical Technologies

In addition to coronagraph performance, the ACCESS mission is critically dependent on the performance of the observatory systems. Detailed descriptions of the observatory and its critical systems appear in the following appendices, including the ITT telescope optical design and heritage

(8.2), the NG spacecraft design and heritage (8.3), the observatory structural and thermal models (8.4), and the pointing control systems (8.5). These analyses describe an observatory that fully supports the ACCESS mission with high-maturity components, while demonstrating a high level of teamwork among JPL, ITT, and NG engineers.

4.3 Current Technology Readiness Levels

All spacecraft components are at TRL 9 today. The requirements for the ACCESS spacecraft system do not demand invention and are consistent with existing commercial products by design choice. The technologies required to fabricate and qualify the telescope have also yielded successful flight articles of equivalent quality and size and are therefore TRL 9 today. The Active Isolation Mounting System (AIMS) used to isolate spacecraft disturbances from the instrument is at TRL 6+. A full scale testbed for a 2 m class flight system exists.

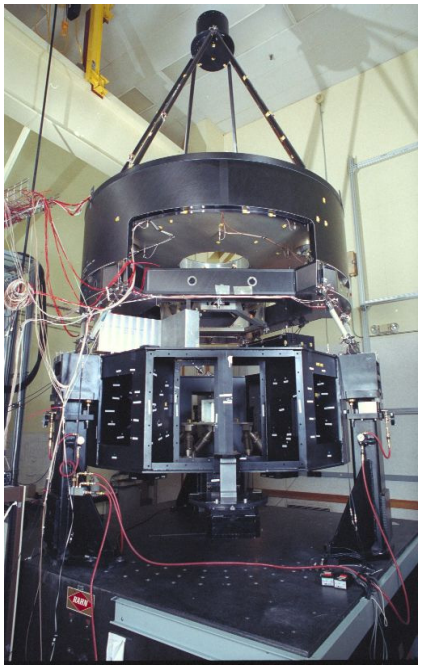

Flight traceable testbed for AIMS

Much of the coronagraph can be constructed of TRL 9 elements. This includes most of the optical elements including the fold mirrors, off-axis paraboloidal mirrors, dichroic beamsplitters, for which commercially available $\lambda/100$ to $\lambda/500$ rms quality elements are available. There are a few elements not yet at TRL 9. The deformable mirrors are at TRL 6. The DMs have been tested in vacuum and vibrated to representative levels. Radiation testing is a logical next step though there are no parts of the DM suspected to be vulnerable. While the coronagraph cameras will use TRL 6+ CCDs with 3–5 electron / pixel read noise and high quantum efficiencies, the spectrograph requires a sensor having ultra-low read noise (<1 e-/pix). Candidates are a photon counting CCD that is at TRL 3–4 and a skipper CCD at TRL 2–3. We have defined a coronagraph performance floor derived from the demonstrated laboratory performance of a TRL 6 coronagraph configuration. Advances in coronagraph techniques expected in the coming 12 months, due to active development and laboratory validations of well-understood technologies, may provide an enhancement above this level, but are now rated at TRL 3–5 as described in Appendix 8.7.

4.4 Technology Development and Cost Plan

An estimate of the technology development investment necessary to achieve the performance floor is $9–$13M (FY09). One part of this investment would be used to mature a photon counting CCD for the integral field spectrograph from TRL 4 to 6. This estimate was provided by the detector expert of Team X. The second part of ~$2M would be used to develop the design of the integral field spectrograph.

Further technology development investments would be valuable as either ways to build performance margin into the system or to retire engineering risk beyond that equivalent to a level of maturity of TRL 6. Candidate applications of funding would be

1. Improve the inner working angle from 3 to 2 λ/D with 10^{-9} contrast and 20% bandwidth for the Lyot option (linear and circular masks $1M)
2. Improve the vector vortex bandwidth from 2% to 20% with 10^{-9} contrast ($1M)
3. Mature the pupil mapping option (next generation mirrors and apodizers, improved propagation models, refer to the PECO concept study for a cost estimate)

5. MANAGEMENT APPROACH

The objective of the ACCESS management strategy is an on-cost, on-schedule mission that meets the scientific goals and objectives by drawing upon the experience of a proven JPL/NG/ITT/NG-Xinetics team, rigorously identifying and mitigating risk at the earliest stage of development, maintaining robust cost reserves and schedule margins, and planning sound descopes as necessary.

The PI is the central person in charge of the investigation, with full responsibility for its scientific integrity and for the integrity of all other aspects of the mission, including the E/PO program. The PI's commitment is full time for Phases A through E. He delegates authority for project implementation to the JPL Project Manager. JPL provides expertise in project management, mission design, systems engineering, pointing control, mission operations and I&T for the ground data system, telecommunication design and development, and E/PO.

The project is supported by a Project Advisory Board consisting of the PI, the JPL Director for Astronomy and Physics, the NG Chief Architect, and the Director of ITT Space Systems Division. Advisory Board members ensure that their organizations provide the project with adequate and timely support as needed for ACCESS success.

5.1 Organization

The ACCESS team is implemented by JPL with coronagraph instrument, science management, system engineering, and mission management. NG provides the spacecraft bus configured for L2 operations, ITT with 1.5 meter off-axis Gregorian telescope, NG-Xinetics with high density deformable mirrors. These organizations form a cohesive team to which each member brings unique strengths. Upon NASA's selection for medium-class exoplanet mission, JPL prepares and executes contracts with NG, ITT, and NG-Xinetics. Incentives focus the commitment of all team members to the return of science data at or above the performance floor, at or below the total mission cost proposed, and on the schedule proposed. This also allows the maximum freedom to use successfully demonstrated processes to achieve the mission goals.

5.2 Science Management

The PI leads the JPL science support team, serves as the science technical manager for individual science contracts, negotiates the statement of work and monitors and maintains the science contracts. The PI and science team will maximize the mission's science return within the available resources, enables the greatest flexibility for the scientists, and helps to foster the wonder and excitement of the project. The PI and science team will establish end-of-mission and post mission activities such as data analysis and archiving, contract closeout, disposition of equipment and facilities.

ACCESS will initiate a Guest Observer (GO) program in the second year of its mission. It is essential that observatory checkout, science calibrations, and overall operations be well underway before scheduling GO requests. We fully expect that science operations and requisite calibration procedures will have been rendered routine during the first year of the mission. The science team will work with NASA to help initiate a competitive selection process, with the intention of integrating the GO targets into the scheduling pool for observations after the first year of operations.

5.3 Risk Management

Our approach to providing the appropriate services to ensure investigation success is to use JPL's integrated review process, as identified in the JPL life cycle and defined in the JPL Guidelines for Reviews (D-10401). This process is compliant with 7120.5B and with NASA Integrated Action Team (NIAT) Recommendation 10.

In order to deliver the project on-cost and on-schedule, the ACCESS team implements risk management per JPL Rules DocID 35507. The ACCESS team risk management methodology is

based on the project risk position, which is the consideration of both the "knowable" and inherent "unknown-unknown" risk possibilities in any project, and is acknowledged when judging adequacy of the reserves. The risk consequences are assessed in two categories, (1) the threat to achieving launch and operational capability within cost and schedule constraints, and (2) the threat to achieving mission success, that is loss of some of the expected achievement of scientific data return. The ACCESS project team minimizes risks by utilizing guidelines for managing, implementing, designing, verifying/validation, and operating flight systems. We have experienced team members with a successful record in Spitzer and Kepler efforts. Robust technical, cost and schedule reserves, multiple metrics to identify and assess risks early and often with close monitoring and tracking system, avoidance of new technology developments, and no international contributions all minimize risk. This minimization of risk, combined with the identified risk mitigation processes, allows for smart and rapid risk mitigation decisions.

We manage the remaining project risks with the JPL risk management process, which is consistent with 7120.5B and with NIAT Recommendation 7. The process steps of risk management are planning, risk identification and assessment, risk mitigation where appropriate, documentation of risk information in a significant risk list, and risk tracking. We emphasize open communications from all project elements and review teams.

ACCESS comprises a single science instrument. While there are no major components that are readily identified as candidates for elimination, there are avenues for graceful performance degradation that preserve the major science objectives. ACCESS risk mitigation operates on four fronts: (1) simplifying the design to the maximum extent possible, (2) assembling a strong team having the expertise to accomplish its portion of the work, (3) assuring that technology risk is adequately retired during the formulation phase, and (4) making use of ample resource margins (technical, cost, and schedule) to keep the implementation on schedule and on cost.

The technical, cost, and schedule reserves are adequate to cover design and development uncertainties. The PM will control the expenditure of reserves except for the cases where the quality and quantity of science data is affected. In those cases the PI has final authority.

5.4 Risk Matrix

The top 5 technical risks for this mission have been identified and mapped onto the standard JPL risk matrix. Risk #1 is that the pupil mapping mirrors cannot be fabricated to the tolerances required for this mission in a reasonable timeframe. This is judged to have a significant likelihood and have a significant reduction in mission return. It is unknown whether additional technology development investment can mitigate this risk in a reasonable time to consider this option for this mission concept. Risk #2 is that the shaped pupil option cannot achieve an inner working angle less than 4 λ/D. The current assessment is this is almost certain and has a moderate reduction in mission return. While the shaped pupil option has merits for other observatory designs it is not a good fit for this mission concept. Because of these risks the Lyot and Vector Vortex options are the most promising. Risk #3 is that the spectrometer detector read noise requirement cannot be met. Risk #4 is that pointing requirements cannot be met. These are judged to have a significant likelihood and have a moderate reduction in mission

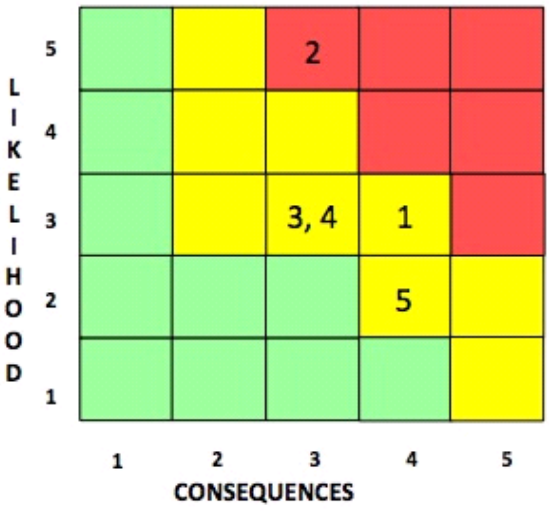

return. It is considered likely that these risks can be mitigated by additional technology development investment before commitment to phase C development. Risk #5 is that we are unable to achieve a 20% spectral bandwidth at a contrast level of 10^{-9}. This is judged to be unlikely given laboratory demonstrations and continued technology investment but would have a significant impact on mission return were it not mitigated.

Project Schedule

The project schedule shows all mission phases, major project reviews, major milestones, and the top-level operation. This schedule assumes an ideal federal funding profile beginning in FY 2011. The duration of Phase B and C/D is estimated at 51 months with a 30-day launch period. The 51 month estimate is a composite of our team's estimate and JPL's Team-X. There are 84 work days (WD) of fully funded schedule reserve on the critical path to launch. Independent of the critical path, we have allocated 22 WD of margin at the end of Phase B.

Schedule management will be integrated with cost management through the Earned Value Management (EVM) system that JPL uses on all flight projects. JPL will integrate the cost/schedule management systems of NG and ITT with the JPL EVM system beginning Phase B.

The PM manages and controls the project schedule. JPL supports the PM in this effort through an assigned project schedule analyst. The JPL schedule management process requires the development of a baseline master schedule that integrates all intermediate and detail planning, identifies key performance milestones, and assists in the measurement of work progress and completion. JPL supports this effort using three major processes: an integrated master schedule (IMS), an integrated Rec/Del system, and the institutional reserve management system (RMS).

The IMS provides an inclusive summary as well as detailed schedule plans at the work breakdown structure (WBS) level. It provides the framework for identifying and analyzing schedule problems, and managing schedule reserve and the budget. JPL plans and distributes schedule reserve in a manner consistent with project-established margin guidelines.

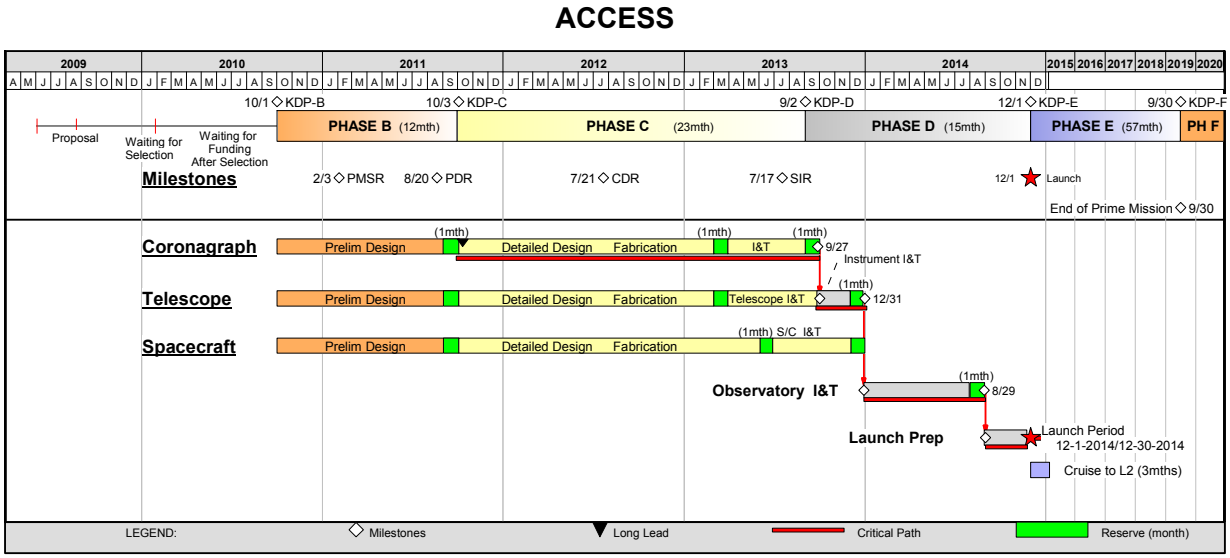

6. FUNDING REQUIREMENTS

Necessary technologies are to be matured to at least TRL 6 by the end of Phase B. ACCESS benefits from the substantial technology development investments already made for the Terrestrial Planet Finder mission. Technologies requiring additional maturation are limited primarily to component technologies within the instrument; therefore, the risk to cost and schedule associated with technology development is considered to be modest.

The ACCESS concept was submitted for detailed review by JPL's Team X concurrent engineering team for mission formulation studies, so that an independent cost estimate could be produced consistent with other current astrophysics mission concepts.

Team X guidelines for the ACCESS study were to provide independent design and costing analysis for the mission concept. Project-provided designs were used, but not project-provided cost estimates. The cost estimates summarized in this document were generated as part of a Pre-Phase-A preliminary concept study, are model-based, were prepared without consideration of potential industry participation, and do not constitute an implementation-cost commitment on the part of JPL or Caltech. The accuracy of the cost estimate is commensurate with the level of understanding of the mission concept, typically Pre-Phase A, and should be viewed as indicative rather than predictive. Following Team-X guidelines, the cost estimate includes 30% reserves for development (Phases A–D) and 15% for operations (Phase E). This cost estimate, summarized in the table, was provided by Team-X in March 2009.

Mission cost is roughly $830M FY09 with appropriate contingencies, including 5 years of science operations. Details are shown in the table that follows. We note that this Team-X cost estimate is consistent with an overall cost estimate developed independently by the ACCESS engineering team, including JPL and industry partners, based on a detailed bottom-up cost estimate for components, subsystem and system integrations and tests, and mission operations. As estimated by Team X, the Shaped Pupil option for the coronagraph adds another $13M to the development cost. This option is more complex as it requires additional optics which add to complexity, volume, and mass.

While fundamentally a different instrument and capability, the Kepler mission provides a reality check for ACCESS costs. Kepler carries a single instrument and a space telescope with a 1.4 m diameter primary mirror in a drift-away orbit. ACCESS is a 1.5 meter space telescope with a single instrument in an L2 orbit. The duration of Kepler's prime mission is 3.5 years, while ACCESS's is 5 years. Both observatories are solar powered. Both missions seek to observe exoplanets. Both missions are partnerships between JPL and experienced aerospace systems companies. A major difference is that Kepler's attitude stability requirements are not as strict as those for ACCESS. Kepler's requirement is 9 mas (3σ) over 15 minutes whereas ACCESS's is 0.5 mas (3σ), a difference that can be quantified in terms of an attitude control system based on high TRL 6+ components. NASA's February 2009 Press Kit for the Kepler launch includes the statement: "The project's life-cycle cost is approximately $600 million. This includes funding for 3.5 years of operations." While the quoted cost is in real year dollars rather than FY09 dollars, this suggests that the ACCESS estimate is of the right magnitude and reasonable.

Table 6-1. Team-X and ACCESS grassroots cost estimates

Item	Team X Cost ($M 2009)*	Project Grass Roots ($M 2009)
Management, Systems Engr., Mission Assurance	46	
Payload System	220	
-- Coronagraph (Lyot, Vector Vortex, Shaped Pupil or Pupil Mapping)	70 (LY, VV, SP) or 83 (PM)	
-- Telescope	150	148**
Flight System	165	170**
Mission Ops/Ground Data System	60	
Launch vehicle (Atlas V-401)	140	
Assembly, Test, Launch Operations	16	
Science	21	
Education and Public Outreach	5	
Mission Design	7	
Reserves	150	
Total Project Cost	830 or 843	

* Individual WBS elements have been rounded to 2 significant digits.

** Estimates include JPL management of system contracts

Phase A	6
Phase B	56
Phase C/D	710
Phase E/F	58
Total	830

7. REFERENCES

[1] Pont, F., et al. Eds. 2009. "Transiting Planets: Proceedings of IAU Symposium 253," Cambridge Univ. Press.

[2] Trilling, D., et al. 2008. "Debris Disks around Sun-like Stars," *Ap.J.* 674: 1086.

[3] Kalas, P., et al. 2008. "Optical Images of an Exosolar Planet 25 Light-Years from Earth," *Science* 322: 1345.

[4] Marois, C., et al. 2008. "Direct Imaging of Multiple Planets Orbiting the Star HR 8799," *Science* 322: 1348.

[5] Dermott, S., et al. 1994. "A Circumsolar Ring of Asteroidal Dust in Resonant Lock with the Earth," *Nature* 369: 719.

[6] Beichman, C., et al. 2006. "New Debris Disks around Nearby Main-Sequence Stars: Impact on the Direct Detection of Planets," *Ap.J.* 652: 1674.

[7] Bally, J., C.R. O'Dell, M.J. McCaughrean 2000. "Disks, Microjets, Windblown Bubbles, and Outflows in the Orion Nebula," *A. J.* 119: 2919.

[8] Burrows, C., et al. 1996. "Hubble Space Telescope Observations of the Disk and Jet of HH 30," *Ap.J.* 473: 437.

[9] Krist, J., et al. 2000. "WFPC2 images of a face-on disk surrounding TW hydrae," *Ap.J.* 538: 793.

[10] Dullemond, C., C. Dominik 2004. "Flaring vs. self-shadowed disks: The SEDs of Herbig Ae/Be stars," *Astronomy and Astrophysics*, 417, 159.

[11] Jura, M. 2005. "Direct Detection of Extrasolar Comets is Possible," *A.J.* 130: 1261.

[12] Udry, S., et al. 2007. "A Decade of Radial Velocity Discoveries in the Exoplanet Domain," in *Protostars and Planets V*, Univ. of Arizona Press, 685–700.

[13] Charbonneau, D., et al. 2007. "When Exoplanets Transit their Host Stars," in *Protostars and Planets V*, Univ. of Arizona Press, 701–716.

[14] Beuzit, J.-L., et al. 2007. "Direct Detection of Exoplanets," in *Protostars and Planets V*, Univ. of Arizona Press, 717–732.

[15] Krist, J., et al. 2007. "Hunting Planets and Observing Disks with the JWST NIRCam Coronagraph," *SPIE* 6693: 66930H.

[16] Marley, M., et al. 2007. "On the Luminosity of Young Jupiters," *Ap.J.* 655: 541

[17] Woodgate, B., E. Mentzell, G. Hilton, and D. Lindler. 2006. "An integral field spectrograph design concept for the terrestrial planey finder coronograph." *New Astronomy Reviews* 50: 297.

[18] Kuchner, M.J., and W.A. Traub. 2002. "A Coronagraph with a Band-limited Mask for Finding Terrestrial Planets," *Ap.J.* 570: 900.

[19] Kuchner, M. J., J. Crepp, J. Ge 2005. "Eighth-order image masks for terrestrial planet finding," *Ap.J.* 628 466.

[20] Trauger, J., et al. 2007. "Laboratory demonstrations of high-contrast imaging for space coronagraphy," *Proc. SPIE* 6693: 66930X.

[21] Moody, D., B. Gordon, and J. Trauger. 2008. "Design and demonstration of hybrid Lyot coronagraph masks for improved spectral bandwidth and throughput," *Proc. SPIE* 7010: 70103P.

[22] Trauger, J.T., and W.A. Traub 2007. "A laboratory demonstration of the capability to image an Earth-like extrasolar planet," *Nature* 446: 771.

[23] Mawet, D., P. Riaud, O. Absil, J. Surdej. 2005. "Annular Groove Phase Mask Coronagraph," *Ap.J.* 633: 1191.

[24] Spergel, D.N. 2000. "A new pupil for detecting extra-solar planets," astro-ph/0101142.

[25] Kasdin, N.J., R.J. Vanderbei, M.G. Littman, D.N. Spergel. 2005. "Optimal one-dimensional apodizations and shaped pupils for planet finding coronagraphy," *Applied Optics* 44: 1117.

[26] Pueyo, L., R. Belikov, J. Kasdin, R. Vanderbei. 2007. "Performance study of integrated coronagraph-adaptive optics designs," *Proc. SPIE* 6693: 669307.

[27] Guyon, O., et al. 2006. "Theoretical limits on extrasolar terrestrial planet detection with coronagraphs," *Ap.J.Suppl.* 167: 81.

[28] Guyon, O., et al. 2005. "Exoplanet imaging with a Phase-Induced Amplitude Apodization coronagraph. I. Principle," *Ap. J.* 622: 744.

[29] Belikov, R., et al. 2006. "Toward 10^{-10} contrast for terrestrial exoplanet detection: demonstration of wavefront correction in a shaped pupil coronagraph," *Proc. SPIE* 6265: 626518.

[30] Shaklan, et al. 2007, "Broadband wavefront control in a pupil mapping coronagraph," Techniques and Instrumentation for Detection of Exoplanets III. Edited by Coulter, Daniel R. *Proceedings of the SPIE* 6693: 66930R–66930R-11.

[31] Guyon, O. 2009. "Imaging and Characterizing the Habitable Zones of nearby Planetary Systems with the Pupil mapping Exoplanet Coronagraphic Observer (PECO)," American Astronomical Society, AAS Meeting #213, #234.08; *Bulletin of the American Astronomical Society* 41: 507.

ACKNOWLEDGEMENTS

This research was carried out at the Jet Propulsion Laboratory, California Institute of Technology, under a contract with the National Aeronautics and Space Administration.

Astrophysics Strategic Mission Concept Studies

ACCESS -- A SCIENCE AND ENGINEERING ASSESSMENT OF SPACE CORONAGRAPH CONCEPTS FOR THE DIRECT IMAGING AND SPECTROSCOPY OF EXOPLANETARY SYSTEMS

John Trauger, Karl Stapelfeldt, Wesley Traub, John Krist, Dimitri Mawet, Dwight Moody, Laurent Pueyo
Gene Serabyn, Stuart Shaklan, Peggy Park, Curt Henry, Paul Brugarolas, Rob Gappinger, Olivia Dawson (JPL/Caltech)
Olivier Guyon (U Arizona & Subaru); Jeremy Kasdin, Robert Vanderbei, David Spergel (Princeton); Ruslan Belikov (NASA/Ames)
Geoff Marcy (UC Berkeley); Robert Brown (STScI); Jean Schneider (Paris Obs); Bruce Woodgate (NASA/GSFC)
Rob Egerman, Gary Matthews (ITT); Ron Polidan, Chuck Lillie, Connie Spittler, David Lee (NGST); Mark Ealey, Tom Price (NGC/Xinetics)

ACCESS = Actively-corrected Coronagraph Concepts for Exoplanetary System Studies

- ACCESS is one of four medium-class exoplanet concepts selected by NASA for ASMCS studies ($660M + launch vehicle)
- Coronagraphic imaging and spectroscopy of exoplanetary systems in reflected starlight at visible wavelengths (450-900 nm)
- Study compares performance and readiness of four major coronagraph architectures
- Defines a conceptual space observatory platform as the "level playing field" for comparisons among coronagraph types
- Also uses laboratory validation on JPL's HCIT as another "level playing field" for coronagraph hardware readiness
- Evaluates science reach of a probe-class coronagraph mission
- Goal is to identify one or more capable mission concepts at TRL6+

1

ACCESS science objectives

Emphasis is on exoplanetary systems, possibly dynamically full, that harbor exoplanets, planetesimals, zodi dust, as in our Solar System

- Direct coronagraphic imaging and low-resolution (R=20) spectroscopy of exoplanet systems in reflected starlight, to include:
- Census of nearby known RV planets in orbits beyond ~1AU
- Search for mature exoplanet systems beyond the RV survey limits, including giant planets, super-earths, and possibly a dozen earth-mass planets
- Observe Zodi structure as an indicator of unseen planets and planetesimals
- Survey Zodi dust as a critical architecture issue for future large life-finding exoplanet missions
- Dust structure in the circumstellar environment as a probe of the life cycle of planetary systems: from young stellar objects to proto-planetary nebulae

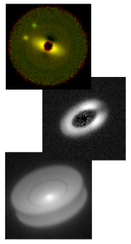

2

Laboratory coronagraph contrast and stability demonstrates capability to detect exoplanets

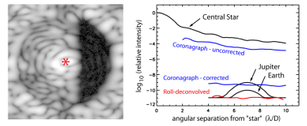

Comparison of azimuthally averaged PSFs of (a) the star, with focal plane mask offset and lyot stop in place; (b) the coronagraph field with all DM actuators set to equal voltages; (c) the coronagraph with DM set for a dark half-field; and (d) the result of simulated roll deconvolution with the set of 480 consecutive coronagraph images. PSFs of a nominal Earth and Jupiter are also indicated. (Trauger & Traub, Nature, 12 April 2007, p771)

3

ACCESS Discovery Space is critically dependent on observatory pointing control and wavefront stability

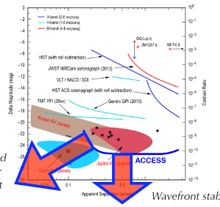

Pointing control and low-order wavefront stability

Wavefront stability

4

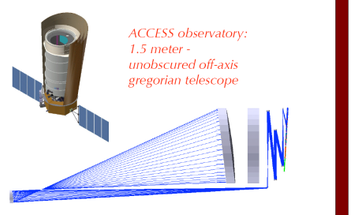

ACCESS observatory: 1.5 meter - unobscured off-axis gregorian telescope

5

ACCESS observatory

- Observatory architecture is representative of the "best" available for exoplanet coronagraphy within the scope (cost, risk, schedule) of a NASA medium-class mission
  - visible wavelengths (500-900 nm) for smaller λ/D and better IWA
  - single spacecraft (external occulter + telescope exceeds medium cost)
- In particular, all coronagraphs require an observatory system with
  - exceptional pointing control
  - exceptional wavefront stability and
  - active (deformable mirrors) wavefront control
- ACCESS requires systems with high technology readiness (TRL6+) for
  - reliable estimates of science capabilities and
  - reliable determinations of cost and schedule
- Baseline observatory architecture defines a capable platform for meaningful comparisons among coronagraph types.

6

ACCESS gamut of coronagraph types

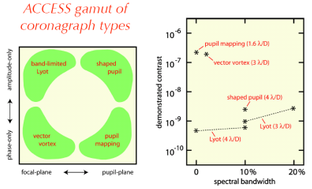

The four major coronagraph types perform starlight rejection with combinations of phase and amplitude elements placed in focal and pupil planes. Best demonstrated laboratory contrast to date (March 2009) are indicated at right, while noting that significant improvements are expected this year as an outcome of active laboratory developments with well-understood technologies.

7

ACCESS compares four major coronagraph types

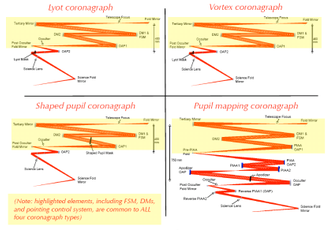

(Note: highlighted elements, including FSM, DMs, and pointing control system, are common to ALL four coronagraph types)

8

Precision deformable mirrors provide wavefront control

Evolution of monolithic PMN deformable mirrors: left to right: 32x32 array, used for all HCIT milestones to date; 64x64 array to be installed on HCIT spring 2009; 48x48 array (also shown on JPL shake table) will be used to demonstrate TRL6 flight-readiness this year.

Mirror facesheets are fused silica, with surfaces polished nominally to λ/100 rms. Surface figure (open loop) is settable and stable to 0.01 nm rms over periods of 6 hours or more in a vacuum testbed environment. All DMs were delivered to JPL by Xinetics.

9

Observatory pointing and thermal control systems

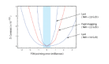

Fine steering mirror stabilizes the star image on the coronagraph occulting mask (all four coronagraphs have an occulting mask) to 0.45 milliarcsec (3-sigma), as required for high contrast at inner working angles as small as 2 λ/D. Contrast deltas at the IWA for representative coronagraphs designed for 2.0, 2.5, and 3.0 λ/D are shown for illustration.

Telescope body pointing (i.e., line of sight) is stabilized to 1 milliarcsec (3 sigma) with an active jitter control system. Shown here are the contrast deltas (vs. rms surface figure of the optical elements following the primary mirror) due to beamwalk on the optics upstream of the fine steering mirror.

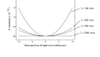

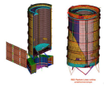

Structural and thermal models guide the observatory design and inform the optical performance models with estimates of structure dynamics, vibration isolation, pointing control, thermal gradients across the primary mirror and forward metering structures, alignment drift in response to telescope slews and roll.

10

Exoplanet completeness space

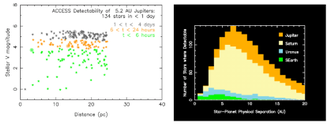

Examples of exoplanet search space. At left, a plot of integration times needed to detect Jupiter twins within 45 degrees of elongation from their parent stars, to S/N = 10, using the ACCESS lyot coronagraph with an IWA = 2 lambda/D. At right, the number of planets detectable to S/N = 10, in integration times of one day or less, using the ACCESS lyot coronagraph with an IWA = 2.5 lambda/D.

11

Science completeness metric: 2.0, 2.5, and 3.0 λ/D

Table 1: Number of nearby stars that can be surveyed for 5.2 AU Jupiters, IWA 3 I/D

Coronagraph Type	Planet 45° from max elong	Planet 15° from max elong
Lyot	117	173
PIAA	166	272
Vortex	135	204

Table 2: Number of nearby stars that can be surveyed for 5.2 AU Jupiters, IWA 2.5 I/D

Coronagraph Type	Planet 45° from max elong	Planet 15° from max elong
Lyot	133	218
PIAA	178	262
Vortex	134	228

Table 3: Number of nearby stars that can be surveyed for 5.2 AU Jupiters, IWA 2.0 I/D

Coronagraph Type	Planet 45° from max elong	Planet 15° from max elong
Lyot	170	230
Vortex	164	241

Note: Accurate PIAA wavefront control solution not available for this IWA

Tabulation of the number of nearby stars that could be searched with various ACCESS coronagraphs to the depth of 10-sigma detections of Jupiter twins in each of six visits to the star over a period of 2.5 years. The green-highlighted row is the demonstrated coronagraph state of the art, 3.0 lambda/D with the lyot coronagraph. The blue-highlighted rows represent coronagraph demonstrations that can realistically be achieved this year. Columns for 45 degrees from maximum elongation corresponds to an observational completeness of 50% or more in each visit, approaching 100% after six epochs spread over several years, and for systems with more than one major planet.

12

All four coronagraph types are to be tested in JPL's High Contrast Imaging Testbed

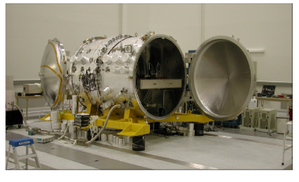

13

lyot coronagraph demonstrations on the HCIT

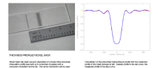

Recent contrast demonstrations in the HCIT:
IWA = 3 λ/D, 10% bandwidth, C = 1.2 e-9
IWA = 3 λ/D, 20% BW, C = 2.7 e-9
IWA = 4 λ/D, 10% BW, C = 6 e-10,
with 4th-order metallic or metal+dielectric 4th-order Lyot masks. All masks manufactured at JPL. Narrower (2.5 λ/D) lyot masks, and circular masks will be manufactured this year.

Vector vortex coronagraph mask for HCIT experiments

Recent contrast demonstrations in the HCIT:
IWA = 3 λ/D, 2% bandwidth, C = 2.0 e-7
with the first-ever charge-4 liquid crystal polymer vortex mask from JDSU (seen at left through crossed polarizers). Close agreement between HCIT performance and models predict that reduction of internal reflections and multilayer achromatization will lead to contrast ~1e-9 with a 20% bandwidth, to be attempted by the end of this year.

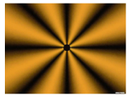

14

HCIT laboratory setup for pupil mapping demonstrations

To date, the best contrast result for a pupil mapping (PIAA) coronagraph: IWA = 1.6 λ/D, monochromatic, C = 2.2e-7 was achieved by Guyon (2009) at the Subaru Observatory laboratories. A new PIAA system, commissioned by NASA/Ames and manufactured by Tinsley, is now mounted in the HCIT in preparation for its first experiments in a vacuum environment.

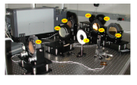

Shaped pupil coronagraph experiments with HCIT

At left, the transmittance profile of a representative shaped pupil apodization (black indicates opaques). This "Ripple 3" design achieved: IWA = 4 λ/D, 10% bandwidth, C = 2.4 e-9 on the HCIT (Belikov et al. 2007). Smaller inner working angles are possible with the use of a pair of DMs

15

Summary

- The ACCESS study considers the relative merits and readiness of four major coronagraph types, and hybrid combinations.
- Using demonstrated high-TRL technologies, the ACCESS minimum science program surveys the nearest 120+ AFGK stars for exoplanet systems, and survey the majority of those for exozodiacal dust to the level of 1 zodi at 3 AU.
- Follow-up with R=20 spectrophotometry.
- Technology demonstrations in the coming year are expected to further enhance the science reach of an ACCESS mission, in advance of a NASA AO for a medium class mission.
- The study also identifies areas of technology development that would advance the readiness of the major coronagraph types in the coming 5 years.

16

8. APPENDICES

8.1 Team-X Reports

Information Provided by:

John Trauger (PI), Peggy Park, Curt Henry, Robert Gappinger, and Paul Brugarolas
(Jet Propulsion Laboratory)

Robert Egerman, Phillip Vallone, Perry Voyer, and Yves Conturie
(ITT Space Systems LLC)

Chuck Lillie, Connie Spittler, David Lee, and Reem Hejal
(Northrop Grumman Aerospace Systems)

Prepared by:

Team-X Full Mission Report
Keith Warfield, Charles Baker, Joan Ervin, Stephen Ringler, Dwight Geer, Celeste Satter, Christopher Landry, Jeff Parker, Ronald Hall, Barbara Lam, Barry Nakazono, Daniel Turner, William Smythe, Michael Pugh, Partha Shakkottai, Bogdan Oaida, Jairus Hihn, Joseph Smith, Ashton Vaughs
(Jet Propulsion Laboratory)

Team-X ACCESS Instrument Report
Keith Warfield, Casey Heeg, Curt Henry, Joan Ervin, Olivia Dawson, Phillip Walkemeyer, Lawrence Scherr, Blake Jacquot, Larry Hovland, Konstantine Penanen, David Hodges, Jason Dawson
(Jet Propulsion Laboratory)

8.1.1 Team-X Full Mission Report

This study was carried out at the Jet Propulsion Laboratory, California Institute of Technology, under a contract with the National Aeronautics and Space Administration. The primary objectives of the ACCESS study were: a comparison of four possible coronagraph designs including instrument masses and costs; and designing, sizing and costing a mission utilizing one of the instrument designs. The customer's goal was to gather information to determine the cost/benefit trade among four different coronagraph architectures for use in a space-based telescope mission for the direct imaging and spectral characterization of exoplanetary systems including giant planets, super Earths and possibly a few Earth-size planets.

Four ACCESS studies were conducted. The first was an instrument study looking to assess four similar coronagraph architectures (Lyot, Phase Mask, Pupil Mapping, and PIAA). The four designs were set by the customer, and the Team was provided with an optical design for each. The designs shared as much design information as possible; most of the optical layouts and parts were common across all four, and three of the four were nearly identical with only some minor differences. The second study took the Lyot design from the instrument session and placed it behind a 1.5 m off-axis Gregorian telescope on a mission at L2. This study designed, scoped and costed the baseline mission. The other three coronagraphs were not studied at the mission level individually; it was agreed that their results could be assumed as delta shifts from the baseline based on the differences in the masses and costs of their respective instrument designs. The third study was another instrument study. The customer had some corrections to the optics layouts and master equipment lists that needed to be included in the earlier designs. The fourth and final study looked at repeating

the earlier mission study with the corrected payload, and resolving some questions the customer identified after reviewing the earlier mission study results.

The ACCESS mission proposes to do direct imaging and spectroscopy of exoplanet systems using an actively pointed 1.5 m off-axis telescope/coronagraph payload. The system has tight pointing and payload thermal stability requirements which will be addressed by a two-stage pointing control system, a two-stage vibration isolation system, and a "sugar-scoop" thermal shield. The spacecraft will operate at an L2 orbit for 5 years. It is a class B mission. The baseline spacecraft and mission parameters are summarized in the Table 8.1.1-1. Key design features are:

Table 8.1.1-1. Baseline spacecraft and mission parameters

Subsystem	Parameter		Value
System	Launch Mass (kg)		2528
	Spacecraft Power (W)		1862
	Total Mission Cost ($M FY09)		830
	Radiation TID (krad)		26
Science	Science Goals		Direct coronagraphic imaging and low resolution spectroscopy of exo-planet systems in reflected starlight. This includes nearby RV planets, mature exo-planet systems beyond the RV survey limits, zodi structure and dust.
	Key Measurements		Planet discovery, proper motion verification, deep characterization
	No. of Scientists		7
	Total Data Volume (Gbits)		9830
Mission Design	Launch Date		June 1st, 2015
	Launch Vehicle		Atlas V 401
	Launch Mass Allocation (kg)		3480
	Target Body		N/A
	Trajectory/Orbit Type		L2 Trajectory
	Mission Duration (months)		60
	Key Mission Phases		Launch, Cruise, L2 Insertion, Science
Instruments	Telescope	Type	Off-axis Gregorian
		Size	1.5m
		Frequency Range	500-900 nm
	No. of Instruments		2
	Instrument Types		Telescope and Lyot Coronagraph
	Payload Mass (kg) - CBE		923
	Payload Power (W)		742
	Payload Data Rate (Mbps)		64 kbps
	Operating Temperature (K)		183 - science cameras; 243 - fine guidance camera; (Coronagraph)
ACS	Pointing Control (arcsec)		30
	Pointing Knowledge (arcsec)		as long as control requirement is met
	Pointing Stability (arcsec)		0.1 (pitch and yaw); 3 (roll) -- over 1000 sec
	Stabilization Type (3-axis, spin, gravity grad.)		3-axis
	Pointing Technologies		start trackers, sun sensors, SIRU, reaction wheels, gyros, fast steering mirror
CDH	Processor Type		RAD750
	Redundancy (hot, cold, single string)		Dual (cold)
	Data Storage (Gbytes)		96
Telecom	Bands		S
	Antenna Types		Two LGAs, one 1m HGA
	Uplink Rate (kbps)		2
	Downlink Rate (kbps)		2048 (DSN); 40 (USN)
	Gimbaled? (Y/N)		Y
Power	Solar Array Area (m^2)		7.4
	Solar Array Type		GaAs Triple Junction (30%) Rigid
	Articulated SA? (Y/N)		Y
	EOL Power (W)		1862
	Battery Storage Size(s) (A-hrs)		16
	Battery Type(s)		Li-Ion
Propulsion	No. of Prop Systems		1
	Type(s) of System(s)		Blowdown Monoprop
	Propellant Mass(es) (kg)		276
Structures	Primary Structural Mass (kg) - CBE		163
	No. of Mechanisms		12
Thermal	Active/Passive		Primarily Passive
	Key Operating Temperature(s) (K)		283
	Thermal Stability (mK/hr)		-
	Thermal Control Technologies		MLI, coatings, heat pipes, heaters, thermistors
Ground System	Ground Antenna(s)		DSN: 34m; USN: TBD
	Average Pass Duration (hrs)		DSN: 8; USN: TBD (quick look)
	Links/week		DSN: 1; USN: 2

- **Telescope**—1.5 m unobstructed off-axis Gregorian design, operating from 450 nm to 900 nm.
- **Instrument**—The sole instrument on this mission is a three channel Lyot coronagraph with two deformable mirrors for wave front correction and a fast steering mirror (FSM) mechanism for image pointing stability (0.1 arcsec/1000 sec). The FSM is controlled by an internal, redundant fine guidance sensor. The instrument has redundant science detectors. The instrument also includes a simple Offner spectrometer.
- **ACS**—Pointing requirements are within the capabilities of current commercial spacecraft so the design is a more conventional approach—reaction wheels, precision star trackers, and SIRU gyros. The system is redundant. ACS will provide the first stage of a two stage pointing system. The second stage is done by a fast steering mirror within the instrument. The ACS system also includes a vendor provided active vibration isolation system.
- **Structure**— The spacecraft bus is an aluminum box with the first stage (reaction wheel mounts) of a two-stage passive/active vibration isolation system. Solar arrays and the HGA are articulated. A deployable telescope cover is also included. The vendor's deployable sun shield is a shape memory structure that is curled up within the fairing for launch, then releases into place once the fairing is opened.
- **Telecom**—Per customer direction, the telecom system is a fully redundant system with S-band downlink and uplink.
- **Power**—The power system consists of: two 16 A-hr Li Ion batteries; 7.4 m^2 solar array area on two deployable, articulated wings; and dual string power electronics.
- **CDH**—Cold spare redundant system based on JPL standard avionics architecture. The system includes a RAD750 processor and a 96 GByte NVM card.

A number of commercial bus manufacturers would be able to construct the needed spacecraft, but for uniformity in assumptions across all ASMCS studies, Team X assumed a JPL built bus as the baseline.

8.1.1.1 Key Trades

Several key trades were examined as part of the Team X studies. The most significant trades were:

- **Instrument Architectures**—Four coronagraph architectures were compared as part of the instrument studies. A Lyot, Phase Mask, Pupil Mapping, and Phase Induced Amplitude Apodization (PIAA) architectures were developed, scoped and costed for this comparison. The four designs were deliberately configured to have as much commonality as possible. Team X did not assess the relative performances of the four architectures; the customer assumed responsibility for this part of the assessment. Team X only provided input on the cost, mass and risks of each option. Essentially, the first three designs were indistinguishable from one another with respect to size and cost. Only the PIAA stood out as larger, more expensive ($85M vs. $70M) and requiring significantly more technology development.
- **4 m vs. 5 m Fairing Design**—The spacecraft did not fit within the 4 m fairing so the 5 m was assumed for the first mission study. The design was adjusted before the second mission study allowing the use of the 4m fairing and the less expensive Atlas V 401.
- **Ground Link Operations Scenarios vs. Cost**—The GSE chair ran some downlink scenarios to look for the most cost effective approach. A single weekly 8-hour pass at 2 Mbps (using Turbocode) was the best DSN option. The customer requested that the Team add the use of commercial tracking network (USN or equivalent) to return quick-look science data twice a week in addition to the DSN pass. This was done for science operations consideration only, and required the Telecom system to shift to S-band.

- **Mission Class A/B vs. Class B**—The customer requested that the Team look at the difference in cost between a reliability class A/B mission and a class B mission. Some single string architectures are permitted (though no single point failures are allowed) under class B, and the testing and sparing are less demanding. Class B is also in keeping with a mission of ACCESS's expected cost. Most of the subsystems remained fully redundant and the class B option only ended up costing about $30M less than the class A/B.

8.1.1.2 Cost Estimate Interpretation Policy, Reserves, and Accuracy

Team X guidelines for this study were to provide independent design and costing analysis for each mission concept. Project-provided designs were used, but not project-provided cost estimates. The cost estimates summarized in this document were generated as part of a Pre-Phase-A preliminary concept study, are model-based, were prepared without consideration of potential industry participation, and do not constitute an implementation-cost commitment on the part of JPL or Caltech. The accuracy of the cost estimate is commensurate with the level of understanding of the mission concept, typically Pre-Phase A, and should be viewed as indicative rather than predictive. Team X typically adds 30% reserves for development (Phases A–D) and 15% for operations (Phase E).

8.1.1.3 Cost Estimate

Project cost is roughly $830M '09 with appropriate contingencies, including 5 years of science operations (Table 8.1.1-2).

Table 8.1.1-2. Team-X full mission cost with reserves

Item	Cost ($M 2009)*	Notes
Management, Systems Engr., Mission Assurance	45	
Payload System	220	1
-- Lyot coronagraph	70	
-- Telescope	150	
Flight System	165	
Mission Ops/Ground Data System	60	
Launch vehicle	140	Atlas V 401
Assembly, Test, Launch Operations	16	
Science	20	
Education and Public Outreach	5	
Mission Design	7	
Reserves	150	
Total Project Cost	**830**	

Notes

* Individual WBS elements have been rounded to 2 significant digits.

1. Payload system includes instrument.

Table 8.1.1-3. Phase cost table—costs are in $M FY2009

Phase A	Phase B	Phase C/D	Phase E/F	Total
6	55	710	58	830

8.1.1.4 Technology Costing

Team X does not provide technology development costing. Models are based on assuming TRL 6 by the end of Phase B. The L3CCD assumed for this study is not yet at TRL 6. The Team X Instrument detector expert estimated the technology development cost at around $5M.

8.1.2 Team-X ACCESS Instrument Report

8.1.2.1 Study Description

The ACCESS Instrument Follow-on Study (1062) was a two day study to look at the impact of several specific design assumption clarifications on an earlier instrument study for the ASMCS road mapping exercise. The ACCESS Instrument study differed from the other ASMCS instrument studies in that it was looking at the four primary coronagraph design types to understand the cost benefit trades among those four options. Team X looked at scoping the designs and estimating their cost of each, but did not look at their performance. The layout designs and master equipment lists for the options were settled ahead of the study sessions and were deliberately as similar as possible so that the customer could gauge the relative advantages of the different approaches rather than the advantages of any unique design feature.

This study was a follow-on study to an earlier study which set out with similar intent but fell short due to insufficient detail in its initial assumptions. In the first study the optics layouts were incomplete, and the need to characterize technology development costs was omitted. This second study aimed to close these and generate more meaningful estimates of cost and scope for the four options.

The primary products of this study from Team X were: (1) new mass estimates for all four options; (2) new cost estimates, including technology development costs, for all options; (3) MELs and block diagrams for all options; (4) updated CAD mechanical designs for 3 of the 4 options; and (5) a final report capturing the design assumptions, issues, and design result for all options.

8.1.2.2 Option Descriptions

All designs share a common high-level architecture with light collected by the telescope moving first through an instrument front-end (for stabilization and correction of the optical wavefront), then into the middle coronagraph stage (for suppression of scattered starlight), then into a sensing back-end (with imaging and spectroscoptic focal planes). All design differences exist in the middle stage. The first three options (Lyot, Vector Vortex, and Shaped Pupil) are nearly identical while the fourth option (Pupil Mapping) has a significantly more complex coronagraph stage. The front end consists of a fold mirror to direct light from the telescope into the instrument, two deformable mirrors (DMs) to correct figure issues with upstream optics, and a 2-axis fast steering stage for one DM to handle fine pointing/jitter issues.

The Lyot, Vector Vortex, and Shaped Pupil occulting stages share a common optical path and only differ in the type of masks being used and their location in the path. Wavefront-corrected light leaving the second DM passes through a pupil plane and is focused by an off-axis parabolic (OAP) mirror. Past the focal point, the now diverging beam is collimated by a second OAP mirror. The exiting beam is then divided into three spectral bands with dichroic beam splitters. Each beam passes through its own focusing lens to reduce the beam size for the detectors. All three beams can be independently directed into either the spectrograph or into one of two redundant science detectors via actuated fold mirrors. The overall size of the system is controlled by several additional fold mirrors throughout the system. For the Lyot approach, a precision linear actuator moves one of several occulting masks into the beam in the focal plane between the two OAPs. Corresponding Lyot masks are inserted into the three spectral beams following the beam splitters and prior to the focusing lenses. The Vector Vortex design is nearly identical to the Lyot; the difference is in the

types of occulting masks being used. In the case of the Shaped Pupil approach, the mask is in the pupil plane between the second DM and the first OAP. Like the other masks, it too is a series of different masks on a precision linear actuator. The occulter is located in the focal plane.

The Pupil Mapping occulting method is a bit different than the other three. As before, the wavefront is first corrected with a pair of DMs, then focused and recollimated with a pair of OAPs. Following the second OAP the beam enters into the first pair of Phase Induced Amplitude Apodization (PIAA) mirrors which produce a non-uniform (apodized) intensity profile with most of the incoming light concentrated in the middle of the pupil. This exiting beam is focused with a third OAP and occulting is done at the focal plane. A two DOF positioner is required for occulter placement. The occulted beam is recollimated and returned to a uniform distribution with a second (reverse) pair of PIAA mirrors. This beam then enters the same beam splitter/lens/detector arrangement as the other three designs.

All four designs control the two-stage FSM with feedback from a fine guidance CCD that uses light reflected from the occulter.

8.1.2.3 Findings

Masses for the first three options were essentially the same. The fourth option came in at close to 50% heavier due to the larger optical bench and added structure needed to house the PIAA system. All option masses were down somewhat from the earlier study due to a resizing of the supporting structure and bipods based on a more accurate assessment of the optical element masses.

Team X Instrument study cost estimates are produced with an adjusted NASA Instrument Cost Model (NICM) estimation method. The Team first produces an objective NICM estimate based on the individual option design parameters. The estimates are adjusted chair by chair based on the subjective assessments of each area expert in the study. Issues of relative complexity and heritage are assessed this way. Technology development costs are added to NICM since it does not include these numbers in its database. The resulting estimates are summarized below Table 8.1.2-1; again there is little difference in the first three options, but the fourth is significantly more expensive. This is due in part to the complexity and technology development costs of the PIAA mirrors and the increased size of the instrument. Additional costs were added to all options for detector technology development and DM complexity. Overall, while at the high end of the NICM estimate range, these estimates still remain consistent with historical experience.

Table 8.1.2-1. Coronagraph Instrument Costs

	Option 1	Option 2	Option 3	Option 4
Coronagraph Design	Lyot	Vector Vortex	Shaped Pupil	Pupil Mapping
Mass (CBE)	123 kg	123 kg	119 kg	161 kg
Cost ($FY09)	$70 M	$70 M	$69 M	$83 M
Technology Development	Detectors			PIAA Mirrors; Detectors
Issues/Risks	Spectrograph design is not mature; thermal stability not analyzed.			Spectrograph design is not mature; thermal stability not analyzed; PIAA layout is not mature

8.1.2.4 Key Trade Results

The focus of this study was on scoping and estimating the costs of various options in question. Given the study time limitation few trades could be considered. However, a comparison between the baselined e2V detector and the proposed "skipper" CCD detector was examined for the spectrograph focal plane. Skipper presents the possibility of reducing read noise to less than 1e-/pixel) through multiple sampling capabilities that are integrated into the detector. The skipper architecture is currently under development and would require a significant investment to make it flight ready. A detailed discussion of the trade is included in the Detector section of this report.

8.1.2.5 Issues/Concerns/Comments

Several areas of the design are in a low state of maturity and could significantly impact cost and mass estimates once better understood. The Pupil Mapping layout is an assumed adaptation of the design common to the other three options; it has not been optimized for performance, design considerations specific to the option, or to minimize size. Some significant departure from the design scoped in this study is expected. The thermal stability aspects of the options were not analyzed as part of the study. Given the tight positional requirements on many of the optical elements, this is likely to be a significant design issue. Finally, the spectrograph design has not been fleshed out. A general assumption of an Offner design like the Moon Mineralogical Mapper (M3) was made but no performance requirements have been discussed so no real performance analysis has been made.

This page is intentionally left blank.

8.2 ITT Telescope Design and Heritage

Prepared by:

Robert Egerman
(ITT Space Systems LLC)

The ACCESS telescope optical design is an unobstructed off-axis Gregorian design which delivers a diffraction limited visible image in collimated space to the science instrument coronagraph. This is accomplished through the use of 3 concave off-axis parabolas and a fold flat, all constructed from Corning ULE® glass.

At the heart of the optical telescope assembly (OTA), is the systems 1.5 m lightweight (areal density of 40–50kg/m^2) Primary Mirror. Due to the stringent stability requirements for the ACCESS system, the glass for the PM and secondary mirror will be specified to be the highest quality ULE® available. The PM will be constructed in a manner similar to that which was used for the fabrication of the Advanced Mirror System Demonstrator (AMSD) optic which was built under funding of a consortium of government agencies including NASA. The PM will have a front and back face sheet and a light-weight abrasive water jet core. The three components will be fused together resulting in a mirror that is pure ULE®, enabling the most thermally stable optic possible.

The ACCESS PM prescription was chosen to be identical to the Terrestrial Planet Finder (TPF) Program funded 1.8 m Technology Demonstration Mirror (TDM). This decision was made to mitigate risk on the future flight ACCESS mission because the metrology null that was to be used to test the TDM has been manufactured and calibrated. This calibration activity was performed in collaboration with Dr. James Burge, of the University of Arizona, and the results of the activity showed that the uncertainty in the null was ~2 nm-rms, fitting well within the wavefront and contrast error budget for ACCESS. ITT has already come very close to achieving the wavefront requirements on optics in a similar size class to ACESS and TDM as shown in Figure 8.2-1.

The precision structures of the ACCESS optical telescope assembly (OTA) design is highly leveraged from the recently launched 1.1 m high resolution NextView Electro-Optical payload developed by ITT and shown Figure 8.2-2. This approach maximizes the use of high TRL hardware and proven design and manufacturing processes. The NextView GeoEye-1 satellite was launched in September of 2008. A press release along with the first light image can be found at http://geoeye.mediaroom.com/index.php?s=43&item=308.

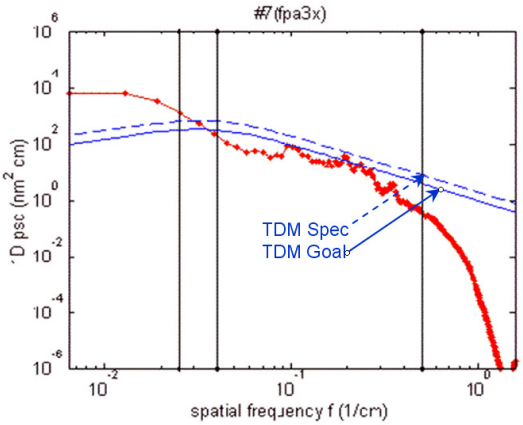

Figure 8.2-1. ITT has polished optics in the appropriate size class that will satisfy the requirements of ACCESS. The low frequency errors shown on this PSD are easily corrected through figuring and can also be corrected by the instrument DMs.

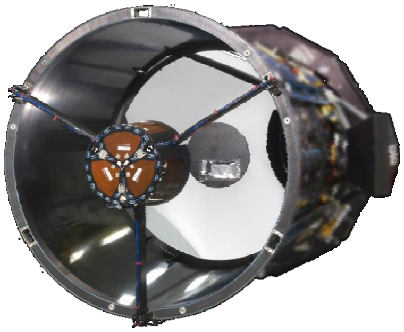

Figure 8.2-2. 1.1 m Aperture Nextview OTA

The composites selected for ACCESS OTA metering structures utilize an ITT co-patented resin system, that when coupled with ITT's design experience yield structures that are insensitive to changes in the systems thermal or hygroscopic environments. The stability of the metering structures is on the same order of magnitude of the stability achieved for the Corning ULE® optics that they support. ULE® glass has a coefficient of thermal expansion that is by definition less than 30 ppb/K.

Although ACCESS is an off-axis system (see Figure 8.2-3) modern metrology techniques and tools allow this type of system to be aligned nearly as easily as on-axis systems. ITT has significant experience in aligning on-and off axis telescopes of various sizes.

In order to achieve the on-orbit optical and pointing stability required, the OTA has an optimized thermal control system which holds the metering structures and optics to close to room temperature as well as an Active Isolation Mount System (AIMS) which uses closed loop active dynamic control to isolate the optical payload from reaction wheel disturbances on the spacecraft bus.

In order to maintain the thermal stability, to prevent contamination during ground operations and launch, and to provide a structure onto which the systems sugarscoop sunshade can mount, the OTA is surrounded by a non-precision structure, but lightweight composite Outer Barrel Assembly (OBA), which employs an ejectable cover for contamination purposes.

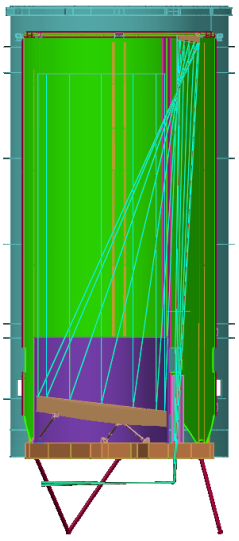

Figure 8.2-3. The ACCESS OTA and OBA (OBA Struts and Star-trackers not shown)

Thermal analyses have been performed on the ACCESS system using Thermal Desktop. The resulting thermo-elastic motions of the structure demonstrate that thermal stability over an observation is maintained to the required levels to maintain the required contrast in the coronagraph.

Dynamic simulations of the ACCESS system mounted on AIMS using FEM and Matlab, when coupled with previous work done on the full scale 2-m class dynamic test (shown in Figure 8.2-4) indicate that the pointing of ACCESS can be held to the required 5 nano-radians 3σ.

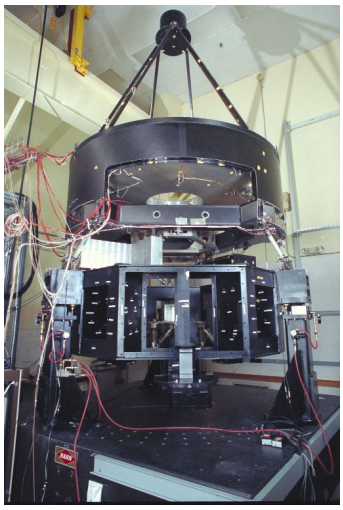

Figure 8.2-4. ITT has demonstrated its AIMS active dynamics capabilities on this flight traceable testbed

This page is intentionally left blank.

8.3 Spacecraft Design and Heritage

Prepared by:

Connie Spittler, Chuck Lillie, David Lee, and Nick Saldivar
(Northrop Grumman Aerospace Systems)

The spacecraft bus provides all housekeeping functions for the Observatory, including power, propulsion for orbit insertion and maintenance, attitude control, command and data handling, communications, and thermal control of the bus itself.

The spacecraft bus also serves as the primary structural interface to the launch vehicle, the sunshade, the OTA and OBA.

The spacecraft bus is composed of several subsystems, including:

- Electrical Power Subsystem (EPS)
- Attitude Control Subsystem (ACS)
- Thermal Control Subsystem (TCS)
- Communications Subsystem (COMM)
- Command & Data Handling Subsystem (C&DH)
- Propulsion Subsystem (SPS)
- Structures Subsystem (SMS)
- Flight Software Subsystem (FSW)

The ACCESS mass and power budgets are shown in Table 8.3-1 and Table 8.3-2, respectively. The total mass of the observatory is 2074 kilograms with 19.4% contingency, based on the maturity of the individual components. The launch vehicle's lift capability provides a 45% mass margin. The maximum power load of the observatory is 1728 Watts with 30% margin. The electrical power system's 2768 W capability at end-of-life provides an additional 27.2% margin.

The spacecraft bus has an aluminum hexagonal structure with a central cylinder and six shear panels to support the launch loads of the telescope and instrument.

Table 8.3-1. ACCESS mass budget

ACCESS Observatory	
Element/Component Description	Total Mass (kg)
PAYLOAD	1144.8
Telescope	1002.34
Instrument (non-PIAA)	142.47
Thermal Enclosure	162.5
SPACECRAFT BUS	533.1
OBSERVATORY DRY MASS (KG)	1840
PROPELLANT MASS (KG)	234
PRESSURANT MASS (KG)	
TOTAL WET MASS (KG)	2074
LAUNCH VEHICLE BASELINE (KG)	3793
% MARGIN	45%

Table 8.3-2. ACCESS power budget

ACCESS Observatory	POWER BY MISSION PHASE				
ELEMENT/SUBSYSTEM	Launch (W)	On Orbit in sun (W)	On Orbit w/eclipse (W)	Safe (W)	Survival (W)
Payload	0.0	890.0	890.0	890.0	890.0
Telescope	0.0	700.0	700.0	700.0	700.0
Instrument	0.0	190.0	190.0	190.0	190.0
Spacecraft Bus	184.3	432.7	432.7	432.7	277.3
Unit load subtotal (no margin)	184	1323	1323	1323	1167
Unit load subtotal (30% margin)	240	1720	1720	1720	1517
Power System & Harness losses	7.2	125.0	51.6	51.6	45.5
Battery recharge	0.0	26.0	0.0	14.0	14.0
Total Observatory Power with Margin	247	1871	1771	1785	1577
EOL Power		2568			
% Margin		27.2%			

8.3.1 Spacecraft Configuration

8.3.1.1 Electrical Power Subsystem

The Electrical Power Subsystem supplies continuous electrical power to the ACCESS spacecraft bus, instrument and telescope for all mission modes. The EPS subsystem consists of the following elements:

- Solar Array
- Battery
- Power Distribution Module
- Solar Array Drive Assembly

The EPS is capable of providing sufficient power to the Observatory to accommodate the loads of the spacecraft bus, instrument and telescope and is sized to include losses due to the 30° off-pointing required during rolls.

8.3.1.2 Attitude Control Subsystem

The Attitude Control Subsystem (ACS) provides the following functions:

- Observatory attitude determination and control
- High gain antenna (HGA) pointing control
- Thruster control for mid-course corrections, station keeping and momentum unloading
- Observatory momentum management control
- System level fault management.

During normal operations, the ACS provides attitude knowledge and control as required. At all times the ACS points the solar arrays at the sun, receives and processes commands, makes measurements to determine observatory attitude, uses reaction wheels to control the observatory's attitude and provides state-of-health data via telemetry. The ACS is designed to meet the pointing requirements of the ACCESS Observatory, with a high degree of redundancy, to ensure accurate Observatory pointing.

The ACS consists of the following components (and redundancy):

- Coarse Sun Sensor Assembly (CSSA) (2:1)
- Inertial Reference Unit (IRU) (internally redundant)
- Star Tracker Assembly (STA) (3:2)
- Reaction Wheel Assembly (RWA) (4:3)

- HGA Biaxial Gimbal, two gimbals with a single actuator and dual windings for each gimbal (2 for 1 redundancy)
- Solar Array Drive Assembly (SADA) , each with one gimbal axis with a single drive and dual windings (2 for 1 redundancy)

The HGA biaxial gimbal allows the HGA to move 210° in azimuth and ±90° in elevation. The single axis SADA gimbal allows rotation of the solar array wings. They are not operated while the spacecraft is inertially pointed to minimize overall Observatory jitter during data collection.

8.3.1.3 Thermal Control Subsystem

The Thermal Control System (TCS) maintains spacecraft bus components within required temperature limits. The TCS subsystem uses high-heritage parts to ensure reliability. The TCS subsystem design is simplified by the aluminum bus structure which conducts heat more efficiently than a composite structure, Aluminum doublers and heat pipes are also used on the bus panels to increase heat transfer. Aluminized Kapton multi-layer insulation (MLI) is used for the spacecraft bus compartment, STAs, IRU and HGA reflector backside. Silverized Teflon tape is used on the HGA gimbal drive to reject heat. Room temperature vulcanization (RTV) or compressed aluminum foil (CAF) is used when mounting high power avionics to the panels to ensure proper heat rejection. Mechanical thermostats, heaters and MLI are used to maintain propulsion equipment at proper operating temperatures. Heaters controlled by mechanical thermostats maintain bus-mounted equipment and appendages on the anti-sun side of the spacecraft above their minimum operating temperatures.

8.3.1.4 Sunshade

The purpose of the sunshade is to ensure that changes in Observatory orientation will not adversely affect the telescope thermal environment. It is designed to improve the thermal stability to maintain the primary mirror surface figure to within tolerable or correctable limits. The sunshade attenuates solar input by a factor of approximately 6000. The sunshade is composed of three Kapton layers, each layer separated by 2.5°. The outer layer is a 2 mil Kapton-E membrane with a Si coating on the outer surface and Vacuum-Deposited Aluminum (VDA) coating on the inner surface. The two inner layers have VDA coatings on both surfaces. The layers are supported by fiberglass frames using wishbone structures to provide shape control.

8.3.1.5 Communications Subsystem

The Communications subsystem provides RF links for commanding the Observatory, for transmitting telemetry and science data to Earth, and for orbit determination. The Communications subsystem is fully CCSDS compatible. S-band was selected for both science data and command and telemetry links. The main components of the Communications subsystem are:

- S-Band Transponder
- Omni Antenna
- High Gain Antenna (Gimbaled)

The Communications subsystem is capable of providing a maximum data rate of 2 Mbps for transmitting science data. The science data downlink has low rate mode and high rate modes. The low rate mode is used to transmit compressed images of the coronagraph images. This data (60 Mbits) is transmitted daily with a 25 minute pass at 40 kbps using the Universal Space Network (USN) 13 m dish. The high rate mode is used to transmit all science and engineering data. This is done once weekly to download 6.7 GB of data with a 7.4 hour pass at 2 Mbps using a Deep Space Network (DSN) 34 m dish.

8.3.1.6 Command and Data Handling (C&DH) Subsystem

The C&DH Subsystem provides the command processing and distribution, telemetry data collection and formatting, mass data storage, instrument support, and time service functions for the spacecraft. The C&DH subsystem a spacecraft processor (SCP) uses a RAD750 processor and interfaces to all subsystems via a MIL-STD-1553 bus. The SCP is designed with sufficient on-board memory to meet the 24 GB data storage requirement.

8.3.1.7 Propulsion Subsystem (SPS)

The propulsion subsystem provides a reaction control capability for the ACCESS Observatory. It is used for trajectory correction maneuvers after launch and during cruise to a Sun-Earth L2 halo orbit, for halo orbit insertion, and for station keeping, and momentum dumping. It can also be used for attitude control during contingency operations. The propulsion subsystem is sized for 10-years of operation, with total delta V budget of 150 m/s. The Propulsion subsystem uses a simple, flight-proven hydrazine mono-propellant system, which has a capacity of 224.9 m/s, providing 33.3% margin. The Propulsion subsystem is completely redundant and single fault tolerant, and uses a modular design with an existing all-welded propellant tank integrated into the propulsion module. One 4.45 N (1 lbf) thruster is used for delta-V maneuvers and three 4.45 N (1 lbf) thrusters are used for attitude control. All thrusters, isolation valves, fill/drain valves, filters and pressure transducers are standard propulsion system components that have flown on many previous missions.

8.3.1.8 Flight Software (FSW)

The ACCESS observatory's on-board flight software is highly modular and table-driven to permit easy incorporation of mission-specific upgrades without impacting the core software. It is primarily written in C and C++ and is quite compact, leaving large margins in the on-board RAD750 processor. The flight software for ACCESS will be developed on an engineering model flight processor, and validated using tested engineering model hardware which contains all the components of the data management subsystem, a flight-like harness, and elements of the attitude control subsystem. The flight software includes fault detection and correction capabilities. The primary "safe haven" mode implemented in the flight software is sun capture using the inertial attitude determination system and the coarse sun sensors. The fault detection logic will be tailored to meet the ACCESS mission requirements.

8.3.1.9 Structures and Mechanisms Subsystem (SMS)

The ACCESS spacecraft structure draws from NG's modular Advanced Bus family of products. The SMS has a central cylinder which encloses the propellant tank and carries the primary structural loads. Six radial shear webs support equipment panels and provide rigid, load-bearing paths. The modular bus design enables parallel manufacturing, and integration and test that significantly reduces program schedule. The central cylinder is sized for direct attachment to the Atlas V launch vehicle, and to support launch loads of the telescope and instrument.

8.3.1.10 AI&T Flows and I&T Philosophy

Assembly, Integration and Test (AI&T) activities for ACCESS include spacecraft and payload mechanical build-up and integration, electrical integration, software integration, comprehensive performance tests, observatory mechanical and electrical integration, observatory environmental tests, and final observatory launch preparation.

The following AI&T activities are performed in parallel: Instrument I&T: Fabrication of components for the instrument at JPL, Telescope I&T: The telescope at ITT and Spacecraft Bus I&T: The spacecraft bus at Northrop Grumman Aerospace Systems and its subcontractors. These components are then electrically and mechanically integrated and unit performance tests are conducted.

After calibration at JPL, the instrument will be shipped to ITT's Rochester, NY facility for mechanical and electrical integration with the telescope and performance testing of the assembled payload in a simulated space environment. At the same time, the spacecraft bus will be mechanically and electrically integrated at NG's Redondo Beach, CA facility and will undergo comprehensive performance testing to demonstrate satisfactory operation of the spacecraft hardware and software. Following a successful Payload Integration Readiness Review, the payload will be shipped to NGAS. The ACCESS Observatory AI&T flow is shown in Figure 8.3.1-1.

With support from the payload suppliers, NG will then integrate the spacecraft bus and the payload; test the performance of the observatory; subject it to a series of environmental tests; verify proper post-test performance; configure the observatory for shipment; and transport it to the launch site (Kennedy Space Center) for integration with an Atlas V 401 and launch to L2.

Several end-to-end systems tests will be performed during I&T and launch site operations. This includes RF compatibility tests of the RF links to verify all telemetry and command control functions, and simulated mission operations of the observatory by the mission operations team and ground system during comprehensive performance and thermal vacuum tests.

The comprehensive performance tests will include end-to-end test of the attitude control subsystem and science camera with a payload stimulus (a sub-aperture collimated light source) to check the payload error signal control loop and overall instrument performance.

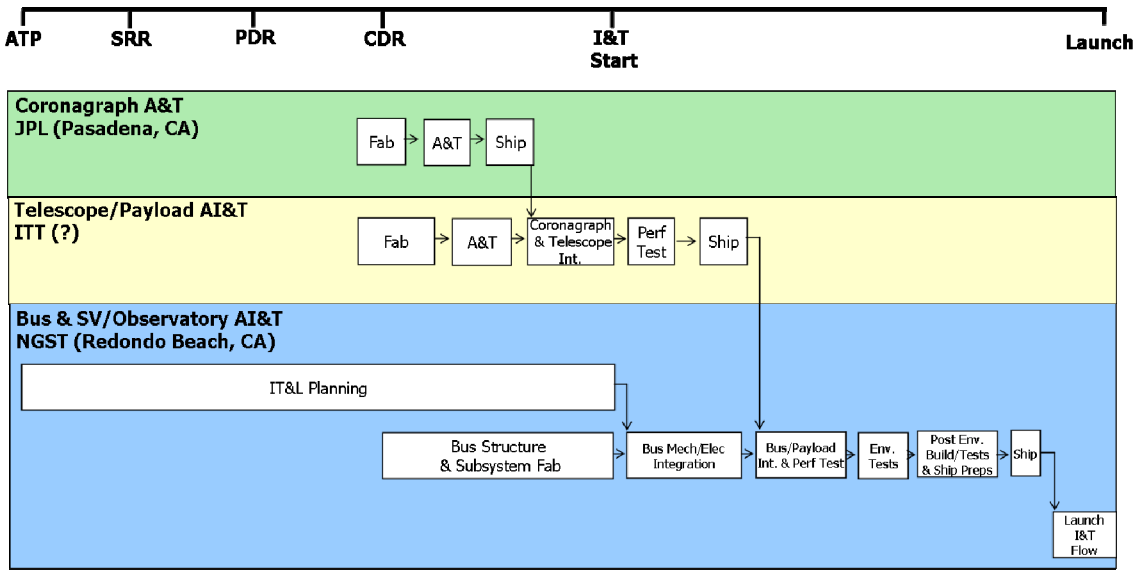

Figure 8.3.1-1. Observatory AI&T flow

This page is intentionally left blank.

8.4 Analytical Models

Prepared by:

Curt Henry
(Jet Propulsion Laboratory)

Robert Egerman, Phillip Vallone, Perry Voyer, Yves Conturie, and Jason Elias
(ITT Space Systems LLC)

Connie Spittler
(Northrop Grumman Aerospace Systems)

The following appendices describe design and analytical models developed to assess the ACCESS concept. Summaries of the results from exercising these models are provided in the respective sections. The descriptions appear in the following order:

- 8.4.1 Telescope Thermal Model
- 8.4.2 Telescope Structural Model
- 8.5 Pointing Control System
- 8.8 End-to-End Optical Propagation Models

The models described in detail were critical to assessing key performance parameters. Other models were developed that seeded these analyses. A thermal model of the entire observatory (spacecraft, instrument, and telescope) was developed that has over 2000 nodes and elements. The observatory thermal model was used to derive the boundary conditions that seeded the analysis of the telescope response to thermal disturbances described in Section 8.4.1. Similarly, structural models of the spacecraft and coronagraph were developed to seed the analyses described in Appendix 8.5.

8.4.1 Telescope Structural Model

ITT generated two Finite Element Models (FEM) of the ACCESS OTA during the study. The first was based upon existing models of similar systems and was customized to reflect the design concept of the ACCESS telescope, science instrument and the interface to the initially base-lined NG small square-shaped spacecraft. The model incorporated line-of-site (LOS) multi-point constraint equations based on ACCESS specific optical LOS sensitivities so that pointing performance could be assessed. This is the model that was transformed into a state-space model and was used for the majority of analyses used to simulate the closed loop pointing control performance of the observatory discussed in Section 8.5. The base-line observatory design concept had several shortcomings which were revealed in system trades and ultimately resulted in a change to the spacecraft design and the interfaces to the OTA, OBA and deployable sunshade. The redesigned spacecraft significantly increased the efficiency of the stiffness and load to the OTA and OBA and preliminary analyses (also discussed in Section 8.5) indicate that these changes also allow for better pointing closed loop control and dynamic isolation of the telescope from the jitter disturbance sources on the spacecraft. ITT refined the OTA and OBA designs as a first step towards optimizing the observatory design. These changes were incorporated into the mechanical CAD drawings as well as into an updated FEM. The notable changes include:

- A change in shape of the Aft Metering Structure (AMS) of the OTA, the optical metering structure for the PM. This change enables the PM to be radiatively heated in a more uniform fashion, increasing thermal stability of the PM.

- A change to the struts which provide a kinematic interface between the OBA and the spacecraft. In the initial baseline observatory concept, this interface could not be designed efficiently, keeping system mass low and the first modes of the OBA high enough for most launch vehicle requirements. This was one of the primary issues identified in the system trades which drove the change to the hexagonal spacecraft.
- A minor change to the kinematic struts which connect the AMS of the OTA to the spacecraft through a second set of kinematic struts. These struts incorporate ITT's Active Isolation Mount System (AIMS) to control pointing and actively minimize the pointing errors of the observatory.

Although the updated FEM was not used for all of the pointing trades and simulations due to programmatic schedule constraints, sufficient work was done do demonstrate that the work done with the initial model was conservative (discussed in more detail in Section 8.5). Images of the telescope FEM are shown in Figure 8.4.1-1. An image of the observatory FEM and the first flexible mode of the OTA are shown in Figure 8.4.1-2.

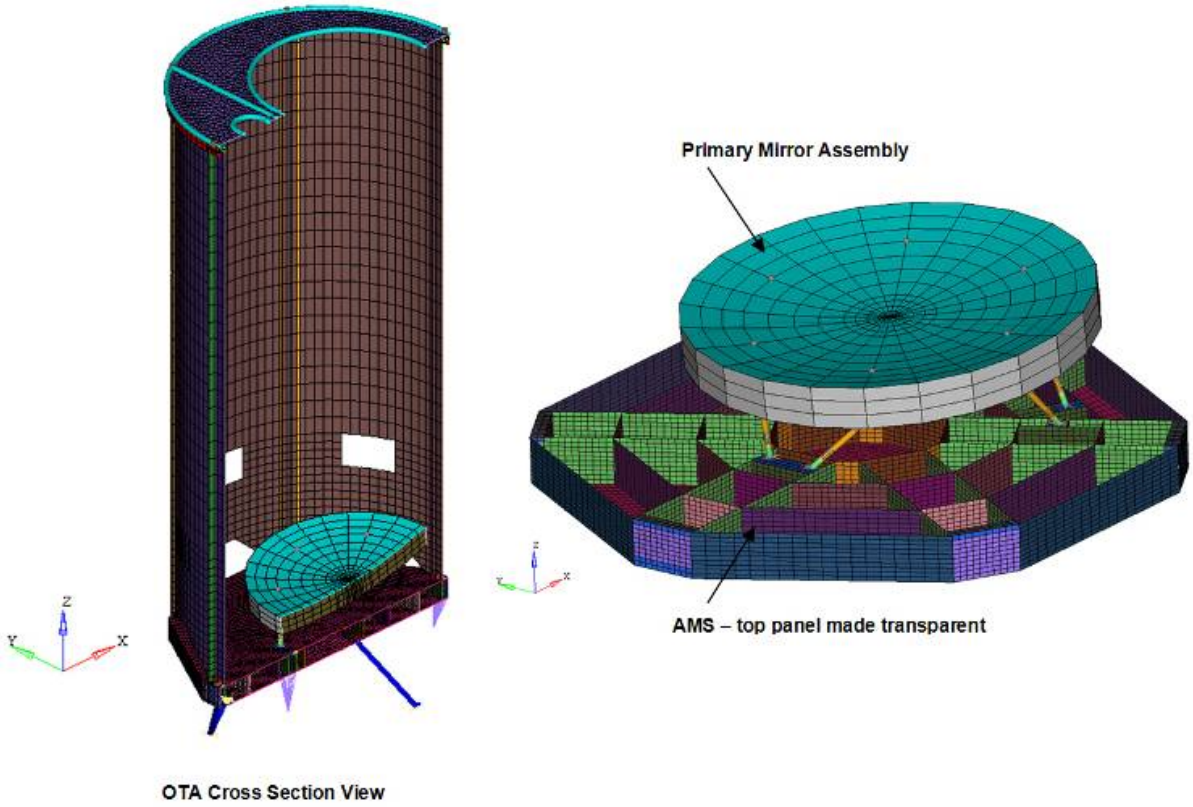

Figure 8.4.1-1. FEM reflecting optimized OTA design

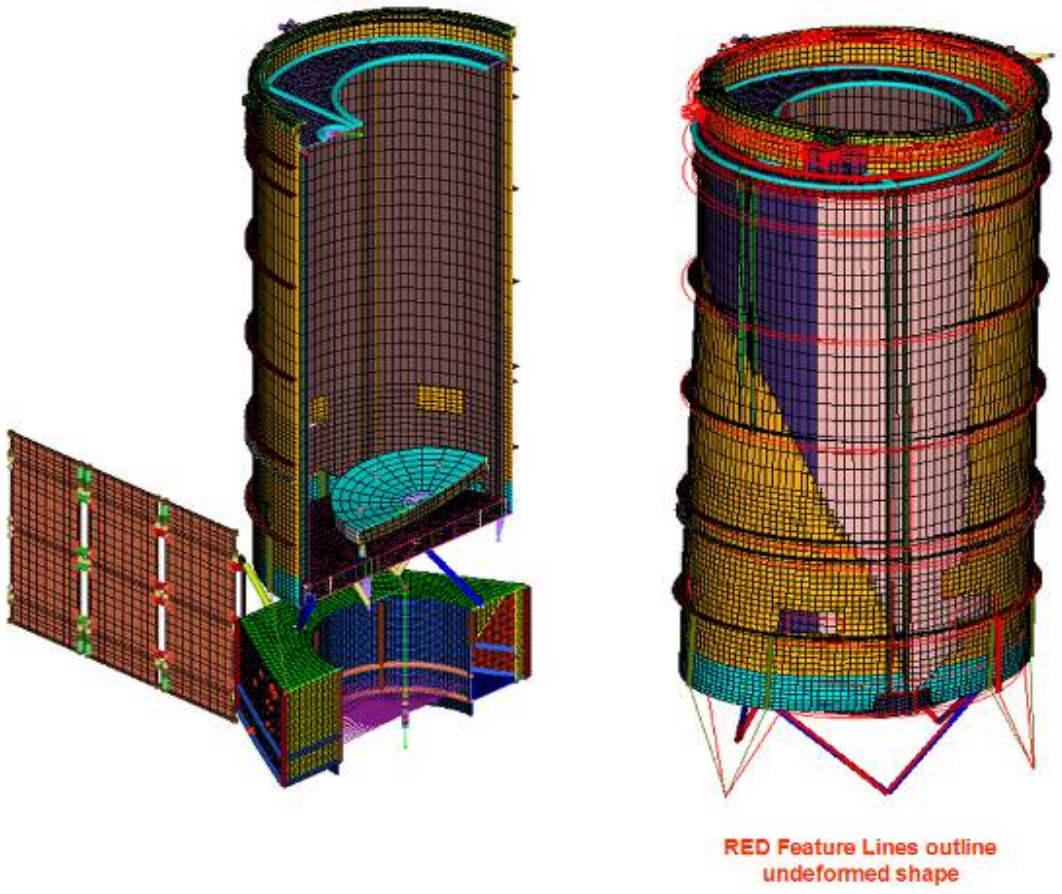

Figure 8.4.1-2. Cross section of integrated observatory FEM (*left*), 1st flexible mode of payload is 13.9 Hz (*right*, spacecraft not shown)

8.4.2 Telescope Thermal Model

The ACCESS Optical Telescope Assembly (OTA) Thermal Control System (TCS) is designed to minimize thermal distortion of the telescope structure and optics to maintain optimal optical stability over the course of an observation. The OTA TCS is a simple standard design based on having a cold biased telescope where positive control can be maintained over the thermal environment. It is designed to maintain the telescope as close to an isothermal 293 K as possible given the Observatory thermal environment in L2 Orbit. In order to maximize the thermal stability of the OTA, it is enclosed in an Outer Barrel Assembly which in turn is shielded from the heat loads of the sun, earth, and moon through a three-layer v-groove sugar-scoop sunshade that encompasses approximately 120° of the sun-side of the OBA. This sunshade reduces incident heat flux by approximately a factor of 6000×, functioning in a similar manner to the Sunshade NG is fabricating for JWST. Given the benign thermal environment provided by the sunshade and the L2 orbit, the analyses performed to date indicate that a very basic TCS system is required. If future more detailed analyses indicate finer stability is required necessary, a more sophisticated TCS system which has flight heritage can be implemented at a slightly higher cost to minimize thermal excursions.

Thermal analyses were performed to predict the temperatures, time constant, and heater power under various conditions (steady state and transient) that represent a worst case observational thermal environment. In addition, several trade studies were performed to optimize the thermal

control system architecture to minimize the OTA TCS power requirement. The result of these trade studies dictate what is being carried as the ACCESS baseline OTA TCS including:

1. Simple heater controllers
2. The incorporation of a heated thermal shroud nested inside the FMS that surrounds the PM.
3. The configuration of thermal blankets
4. The OTA has a short time constant of ~5.5 hrs (1σ) which allows the entire telescope to return to thermal stability after a space vehicle attitude maneuver. The time constant of the primary mirror is considerably shorter at ~0.5 hours and for certain types of maneuvers may enable science data to be acquired without having to wait for any thermal settling.
5. The current baseline TCS design requires ~670 Watts to heat the OTA, a reduction of over 30% from the initial design.

The thermal model of the OTA was developed in Thermal Desktop using both CAD and finite element models to facilitate the model generation. An image of the model, without the PM thermal shroud, is shown in Figure 8.4.2-1.

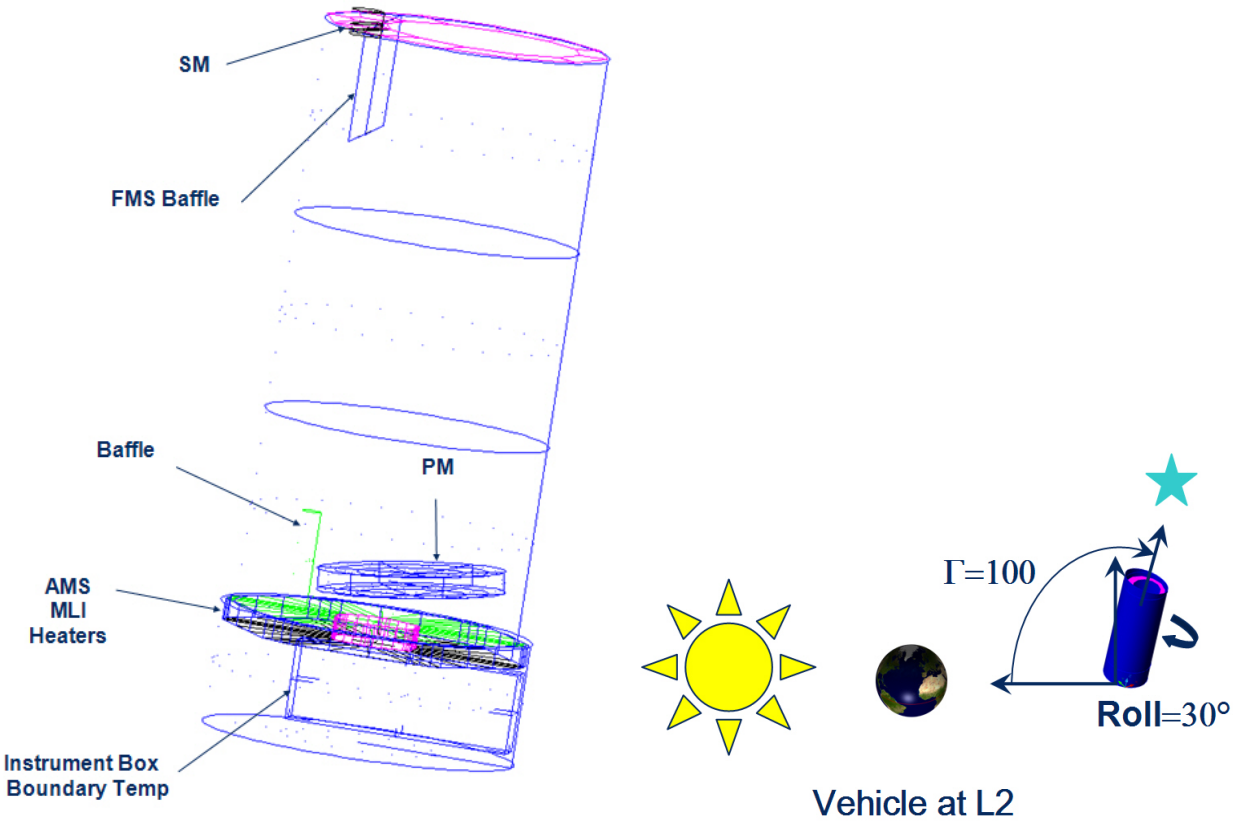

Figure 8.4.2-1. OTA Thermal Model Detail and Coordinate System (OBA and PM thermal shroud not shown)

The boundary conditions used in the thermal model of the OTA were generated from a JPL observatory thermal model which is discussed in Section 8.4.1. ITT took these thermal boundary conditions and nominally considered four cases:

1. A steady state hot operational case (model results showed that this environment was not acceptable because positive thermal control over the OTA TCS was lost because the system was not cold biased)
2. A steady state cold operational case
3. A very conservative transient operational case involving an 80° slew and a 30° roll.
4. Refined transient operational case to allow OTA approach thermal stability after it was determined that the operational case 3 was too conservative. A less conservative case was considered where it was assumed that the telescope reached equilibrium after 12-hour pointing at a sun Γ angle of 100° followed by a 30 degree roll in 10 minutes followed by a 12-hour hold. The angle is shown also depicted in Figure 8.4.2-1.

In addition to predicting temperatures and power need using the OTA thermal model, ITT also integrated thermoelastic sensitivities (based on the structural FEM) into the model which enabled the assessment of the PM wavefront and PM-SM relative motion changes due to changes in the thermal environment. These 7 metrics (1 WFE change + 6 relative rigid body motions) have the highest sensitivity in terms of assessing how the contrast in the coronagraph changes during an image collect. The PM wavefront change was calculated using a Monte Carlo analysis that combined, through linear superposition, WFE sensitivities based on changes in the nominal temperature of the PM (Isothermal) as well as radial, axial and diametrical gradients. The complete surface maps are incorporated into an optical contrast model so that the impact of the thermoelastic stability can be assessed. For simplicity in reporting results, surface WFE is summarized in terms of the RMS in this appendix. The WFE sensitivities are raw surface sensitivities (i.e., no Zernike's such as power subtracted). The sensitivities used, in terms of RMS, for the different thermal changes on the PM are summarized in Table 8.4.2-1.

After the initial assessment of the results from the three cases analyzed, ITT went through several trades, as discussed above, In order to optimize the system and to reduce the conservatism in the operational scenario. The baseline nominal factory-to-orbit shifts and on-orbit stability are denoted by cases 11 through 13 and updated cases 11 through 13a in Tables 8.4.2-2 through 8.4.2-6 (which summarize all of the thermal modeling results). These cases reflect predictions of the baseline TCS design. It is important to note that the transient case 6 is overly conservative based on the orientation degree of slew that was simulated. Results of interest are:

- Table 8.4.2-2: 666 Watts for case 11
- Table 8.4.2-3: PM average temperature of 17.4°C with minimal gradients for case 11 (nominal ground-to-orbit shift)
- Table 8.4.2-3: Tight thermal stability (cases 12 and 13)
- Table 8.4.2-4: PM Factory-orbit WFE shift of 15.8 nm-rms prior to 6 dof SMA focus and alignment (case 11) and WFE stability of 1.3 nm-rms (case 13)

Thermal study sensitivity trend analyses indicate the OBA temperature variations have a minimal effect on OTA thermal impact (due to the solar shade) and OTA TCS architecture will be the limiting factor in determining the OTA thermal stability. Additional optimization of the TCS can be performed if required and an assessment of a less conservative transient thermal environment will also show improved performance.

Table 8.4.2-1. Thermoelastic PM surface WFE sensitivities

Sensitivity	Change in surface (nm-rms)
1K Average Axial Gradient Change (through the thickness)	12.13219
1K Diametrical Gradient Change Across Aperture	0.57401
1K Average Radial Gradient Change (center to edge)	0.33388
1K Average Isothermal Change	0.81842

Table 8.4.2-2. Telescope Power Predictions

Heater Power Raw Predict Summary, Watts (No Margin Included)

	Case	PM Shell	FMS	AMS Top	AMS Bot	SMA	Total
1	SS Hot Operational	N/A	0	0	0	0	0
2	SS Cold Operational	N/A	989	60	11	2	1062
3	Transient Cold Operational Slew	N/A	988	43	10	2	1042
4	SS Cold Operational with MLI on ID of FMS	N/A	330	308	12	7	657
5	SS Cold Operational with Full of FMS Length Heated with MLI on ID of FMS and PM Heated Shell	125	319	215	11	6	676
6	Transient Slew Cold Operational with Full of FMS Length Heated with MLI on ID of FMS and PM Heated Shell	132	323	150	45	6	656
7	SS Cold Operational with 2/3 of FMS Length Heated and with MLI on ID of FMS and PM Heated Shell	130	189	230	11	7	568
8	Transient Slew Cold Operational with 2/3 of FMS Length Heated and with MLI on ID of FMS and PM Heated Shell	143	193	150	52	7	545
9	SS Cold Operational with 1/3 of FMS Length Heated and with MLI on ID of FMS and PM Heated Shell	143	80	248	11	7	489
10	Transient Slew Cold Operational with 1/3 of FMS Length Heated and with MLI on ID of FMS and PM Heated Shell	159	82	150	62	7	460
11	SS Cold Ops γ=100°-Full FMS Heated With MLI on ID of FMS & Heated Shell Around PM	121	317	212	10	6	666
12	Transient Cold Ops γ=100° after 30° Roll in 10 minutes-Full FMS Heated With MLI on ID of FMS & Heated Shell Around PM	-	-	-	-	-	-
13	Transient Cold Ops γ=100° after 30° Roll in 10 minutes and hold for 12 hrs-Full FMS Heated With MLI on ID of FMS & Heated Shell Around PM	129	320	150	42	6	648
-	Updated analysis cases with 12 hr transient stability period before 30° Roll to allow system to reach flight steady state before maneuvers. 4-07-09 Updates (Cases Updated 11, Updated 12, Updated 13, New 13a).	126	315	150	40	6	637

Table 8.4.2-3. Telescope Temperature Predictions

Average Temperature Predict Summary, °C

Case		PM Avg Temps				FMS Avg Temps	Notes
		Isothermal	Axial Gradient	Radial Gradient	Diametrical Gradient		
1	SS Hot Operational	26.9	-0.15	2.08	0.74	24.84	Factory to Orbit Shift
2	SS Cold Operational	17.9	0.05	-2.69	1.12	20.00	Factory to Orbit Shift
4	SS Cold Operational with MLI on ID of FMS	11.1	-1.54	3.46	3.43	20.00	Factory to Orbit Shift
5	SS Cold Operational with Full of FMS Length Heated with MLI on ID of FMS and PM Heated Shell	17.3	-0.53	-2.98	0.81	20.00	Factory to Orbit Shift
7	SS Cold Operational with 2/3 of FMS Length Heated and with MLI on ID of FMS and PM Heated Shell	17.2	-0.60	-3.02	0.76	-1.83	Factory to Orbit Shift
9	SS Cold Operational with 1/3 of FMS Length Heated and with MLI on ID of FMS and PM Heated Shell	17.1	-0.67	-3.04	0.75	-19.05	Factory to Orbit Shift
11	SS Cold Ops γ=100°-Full FMS Heated With MLI on ID of FMS & Heated Shell Around PM	17.4	-0.55	-2.76	0.71	20.00	Factory to Orbit Shift
Updated 11	Steady state Cold Ops g=100°-Full FMS Heated With MLI on ID of FMS & Heated Shell Around PM	17.5	-0.53	-1.85	2.56	20.09	Factory to Orbit Shift

Average Temperature Stability Predict Summary over 24 hr Period, °C

3	Transient Cold Operational Slew	0.85	-0.03	0.02	0.54	0.42	On Orbit Shift
6	Transient Slew Cold Operational with Full of FMS Length Heated with MLI on ID of FMS and PM Heated Shell	0.13	-0.02	0.97	1.87	0.09	On Orbit Shift
8	Transient Slew Cold Operational with 2/3 of FMS Length Heated and with MLI on ID of FMS and PM Heated Shell	-0.03	0.00	0.98	1.98	-0.05	On Orbit Shift
10	Transient Slew Cold Operational with 1/3 of FMS Length Heated and with MLI on ID of FMS and PM Heated Shell	-0.26	0.02	0.95	2.18	-0.14	On Orbit Shift
12	Transient Cold Ops γ=100° after 30° Roll in 10 minutes-Full FMS Heated With MLI on ID of FMS & Heated Shell Around PM	-0.01	0.03	0.01	0.04	-0.01	On Orbit Shift
13	Transient Cold Ops γ=100° after 30° Roll in 10 minutes and hold for 12 hrs-Full FMS Heated With MLI on ID of FMS & Heated Shell Around PM	0.03	-0.02	0.81	1.87	0.05	On Orbit Shift
Updated 12	Transient Cold Ops γ=100° after 30° Roll in 10 minutes-Full FMS Heated With MLI on ID of FMS & Heated Shell Around PM	-0.0017	-0.00075	-0.00057	0.00045	-0.29	On Orbit Shift
Updated 13	Updated 13.Transient Cold Ops γ=100° after 30° Roll in 10 minutes and hold for 12 hrs-Full FMS Heated With MLI on ID of FMS & Heated Shell Around PM, WFE at 12 hrs after start of roll	-0.014	-0.017	-0.015	0.0087	-0.31	On Orbit Shift
New 13a	New 13a.Transient Cold Ops γ=100° after 30° Roll in 10 minutes and hold for 12 hrs-Full FMS Heated With MLI on ID of FMS & Heated Shell Around PM. Worst case 10 minutes after 12 hours of settling AFTER roll: Delta from Time=17.83 hrs to 18.0 hrs.	0.00027	-0.001	-0.0001	5E-05	-0.06	On Orbit Shift

Table 8.4.2-4. PM Surface WFE Predictions

Average RMS PM Thermal Distortion Estimates, nm

Case		PM Distortion	Notes
1	SS Hot Operational	5.4	Factory to Orbit Shift
2	SS Cold Operational	1.5	Factory to Orbit Shift, Full FMS Thermally Controlled
3	Transient Cold Operational Slew Stability over 24 hrs	1.0	On Orbit Shift
4	SS Cold Operational with MLI on ID of FMS	22.7	Factory to Orbit Shift, Full FMS Thermally Controlled
5	SS Cold Operational with Full of FMS Length Heated with MLI on ID of FMS and PM Heated Shell	7.0	Factory to Orbit Shift, Full FMS Thermally Controlled
6	Transient Slew Cold Operational with Full of FMS Length Heated with MLI on ID of FMS and PM Heated Shell	1.4	On Orbit Shift, Full FMS Thermally Controlled
7	SS Cold Operational with 2/3 of FMS Length Heated and with MLI on ID of FMS and PM Heated Shell	7.7	Factory to Orbit Shift
8	Transient Slew Cold Operational with 2/3 of FMS Length Heated and with MLI on ID of FMS and PM Heated Shell	1.3	On Orbit Shift
9	SS Cold Operational with 1/3 of FMS Length Heated and with MLI on ID of FMS and PM Heated Shell	8.6	Factory to Orbit Shift
10	Transient Slew Cold Operational with 1/3 of FMS Length Heated and with MLI on ID of FMS and PM Heated Shell	1.1	On Orbit Shift
11	SS Cold Ops γ=100°-Full FMS Heated With MLI on ID of FMS & Heated Shell Around PM	7.1	Factory to Orbit Shift
12	Transient Cold Ops γ=100° after 30° Roll in 10 minutes-Full FMS Heated With MLI on ID of FMS & Heated Shell Around PM	0.3	On Orbit Shift
13	Transient Cold Ops γ=100° after 30° Roll in 10 minutes and hold for 12 hrs-Full FMS Heated With MLI on ID of FMS & Heated Shell Around PM	1.3	On Orbit Shift
Updated 11	Steady state Cold Ops g=100°-Full FMS Heated With MLI on ID of FMS & Heated Shell Around PM	7.9	Factory to Orbit Shift
Updated 12	Transient Cold Ops γ=100° after 30° Roll in 10 minutes-Full FMS Heated With MLI on ID of FMS & Heated Shell Around PM	0.0092	On Orbit Shift
Updated 13	Updated 13.Transient Cold Ops γ=100° after 30° Roll in 10 minutes and hold for 12 hrs-Full FMS Heated With MLI on ID of FMS & Heated Shell Around PM, WFE at 12 hrs after start of roll	0.20	On Orbit Shift
New 13a	New 13a.Transient Cold Ops γ=100° after 30° Roll in 10 minutes and hold for 12 hrs-Full FMS Heated With MLI on ID of FMS & Heated Shell Around PM. Worst case 10 minutes after 12 hours of settling AFTER roll: Delta from Time=17.83 hrs to 18.0 hrs.	0.012	On Orbit Shift

Table 8.4.2-5. OTA Component 1σ Time Constants

Component	Time Constant, hrs
AMS	0.4
FMS	5.5
SM Shade	0.4
PM	0.3
FMS Front Plate	1.4
PM Shell, as applicable	0.5

Table 8.4.2-6. PM-SM Relative Motion Predictions

FMS Thermal Distortion Estimates, nm for translations, nanorad for rotations

Case		Translations (nm)				Rotations (nanorad)				Notes
		X	Y	Z	RMS	Θx	Θy	Θz	RMS	
1	SS Hot Operational	4.15E-04	-1.43E-02	-6.92E+01	40.0	7.59E-01	-5.44E-04	7.30E-03	0.44	Factory to Orbit Shift
2	SS Cold Operational	0.00E+00	0.00E+00	0.00E+00	0.0	0.00E+00	0.00E+00	0.00E+00	0.00	Factory to Orbit Shift, Full FMS Thermally Controlled
3	Transient Cold Operational Slew Stability over 24 hrs	1.00E-05	-4.60E-03	-9.07E+01	52.4	1.90E-01	-1.62E-04	1.24E-03	0.11	On Orbit Shift
4	SS Cold Operational with MLI on ID of FMS	0.00E+00	0.00E+00	0.00E+00	0.0	0.00E+00	0.00E+00	0.00E+00	0.00	Factory to Orbit Shift, Full FMS Thermally Controlled
5	SS Cold Operational with Full of FMS Length Heated with MLI on ID of FMS and PM Heated Shell	0.00E+00	0.00E+00	0.00E+00	0.0	0.00E+00	0.00E+00	0.00E+00	0.00	Factory to Orbit Shift, Full FMS Thermally Controlled
6	Transient Slew Cold Operational with Full of FMS Length Heated with MLI on ID of FMS and PM Heated Shell	1.25E-06	-1.07E-03	-2.18E+01	12.6	4.39E-02	-3.77E-05	2.79E-04	0.03	On Orbit Shift, Full FMS Thermally Controlled
7	SS Cold Operational with 2/3 of FMS Length Heated and with MLI on ID of FMS and PM Heated Shell	-8.04E-04	2.00E-01	3.74E+03	2158.1	-8.43E+00	7.08E-03	-5.71E-02	4.86	Factory to Orbit Shift
8	Transient Slew Cold Operational with 2/3 of FMS Length Heated and with MLI on ID of FMS and PM Heated Shell	-8.67E-06	-4.70E-04	-1.46E+01	8.5	1.52E-02	-1.55E-05	3.89E-05	0.01	On Orbit Shift
9	SS Cold Operational with 1/3 of FMS Length Heated and with MLI on ID of FMS and PM Heated Shell	-2.20E-03	2.60E-01	4.23E+03	2441.7	-1.15E+01	9.34E-03	-8.48E-02	6.63	Factory to Orbit Shift
10	Transient Slew Cold Operational with 1/3 of FMS Length Heated and with MLI on ID of FMS and PM Heated Shell	-1.43E-05	1.72E-04	-4.34E+00	2.5	-1.32E-02	7.53E-06	-1.72E-04	0.01	On Orbit Shift
11	SS Cold Ops γ=100°-Full FMS Heated With MLI on ID of FMS & Heated Shell Around PM	0.00E+00	0.00E+00	0.00E+00	0.0	0.00E+00	0.00E+00	0.00E+00	0.00	Factory to Orbit Shift
12	Transient Cold Ops γ=100° after 30° Roll in 10 minutes-Full FMS Heated With MLI on ID of FMS & Heated Shell Around PM	-7.36E-06	-7.46E-04	-1.97E+01	11.4	2.69E-02	-2.53E-05	1.20E-04	0.02	On Orbit Shift
13	Transient Cold Ops γ=100° after 30° Roll in 10 minutes and hold for 12 hrs-Full FMS Heated With MLI on ID of FMS & Heated Shell Around PM	-3.91E-06	-1.24E-03	-2.81E+01	16.2	4.83E-02	-4.29E-05	2.73E-04	0.03	On Orbit Shift
Updated 11	Steady state Cold Ops g=100°-Full FMS Heated With MLI on ID of FMS & Heated Shell Around PM	1.41E-06	-1.02E-03	-2.05E+01	11.8	4.17E-02	-3.57E-05	2.66E-04	0.02	Factory to Orbit Shift
Updated 12	Transient Cold Ops γ=100° after 30° Roll in 10 minutes-Full FMS Heated With MLI on ID of FMS & Heated Shell Around PM	-3.18E-05	-5.59E-05	-1.88E+01	10.8	-1.16E-02	1.37E-06	-2.72E-04	0.01	On Orbit Shift
Updated 13	Updated 13.Transient Cold Ops γ=100° after 30° Roll in 10 minutes and hold for 12 hrs-Full FMS Heated With MLI on ID of FMS & Heated Shell Around PM, WFE at 12 hrs after start of roll	-3.17E-05	2.49E-04	-1.23E+01	7.1	-2.39E-02	1.20E-05	-3.48E-04	0.01	On Orbit Shift
New 13a	New 13a.Transient Cold Ops γ=100° after 30° Roll in 10 minutes and hold for 12 hrs-Full FMS Heated With MLI on ID of FMS & Heated Shell Around PM. Worst case 10 minutes after 12 hours of settling AFTER roll: Delta from Time=17.83 hrs to 18.0 hrs.	-1.22E-05	-6.80E-04	-2.10E+01	12.1	2.21E-02	-2.25E-05	5.91E-05	0.01	On Orbit Shift

This page is intentionally left blank.

8.5 Pointing Control System (PCS)

Prepared by:

Paul Brugarolas, James Alexander, John Trauger, and Dwight Moody
(Jet Propulsion Laboratory)

Robert Egerman, Phillip Vallone, and Jason Elias
(ITT Space Systems LLC)

Reem Hejal, Vanessa Camelo, Allen Bronowicki, David O'Connor, Richard Patrick, Pawel Orzechowski, Connie Spitter, and Chuck Lillie
(Northrop Grumman Aerospace Systems)

This is a modified version of Section 8.5 that has been edited to remove proprietary and ITAR controlled information.

8.5 Pointing Control System (PCS)

8.5.1 Introduction

Coronagraphic observatories require a very high precision Pointing Control System (PCS) to achieve high contrast imaging of faint objects at extremely small angles from a star during science observations (Section 8.5.2), which typically require long exposures.

The philosophy behind this PCS design has been to propose the best pointing system for a mid-class space coronagraphic observatory with nearly available technology (TRL 6 or above). This led to a three-stage pointing control system; a fine guidance camera design within the coronagraphic instrument; and an extensive disturbance rejection strategy to minimize the environmental jitter. This work is partly based on the work that the authors performed for the Eclipse proposal [1, 2].

The three-stage pointing system starts with a standard 3-axis stabilized spacecraft bus and it is augmented with a hexapod telescope pointing system and a fine steering mirror. The addition of the hexapod enables pointing the telescope with a pointing stability ten times better than Hubble but with a spacecraft bus that is ten times less capable than Hubble. The addition of the fine steering mirror allows for additional pointing capability within the coronagraphic instrument (Section 8.5.3).

For fine guidance sensing we take advantage that coronagraphic observations have a bright star in the center of field of view. We have studied three different concepts for a fine guidance camera that guides from this bright star (Section 8.5.4).

The strategy towards disturbances is to minimize the jitter at the source. We have selected a quiet orbital environment (L2), designed a thermally controlled telescope and instrument, planned operational constraints during science observations (limitations on reaction wheel speeds, non operation of solar array drives and high gain antenna gimbals), and added reaction wheel isolators, solar array dampers and a vibration suppression capability within the hexapod. We have studied two possible options for the hexapod system (Section 8.5.5.3).

A detail simulation study was performed that included dynamic models of the structure, optics and models for the spacecraft ACS system, the hexapod pointing systems, the FSM and the fine guidance camera to demonstrate the feasibility of this design.

The Pointing Team brings an extensive experience base from three leaders in the Industry. JPL leverages experience from the Spitzer Space Telescope, Kepler and other missions, and from large investments in technology developments for programs such the Stellar Interferometry Mission and the Terrestrial Planet Finder. ITT is a leader in telescope manufacturing and design, and has two decades of investments on the development on pointing and vibration suppression mechanisms. Northrop Grumman brings as well an extensive experience on space observatories (Chandra, JWST, etc.) and many years in development of vibration isolators systems and pointing struts.

8.5.2 Pointing Requirements

Pointing errors adversely affect image contrast level in two main ways:

- Telescope pointing errors lead to contrast degradation due to wave-front errors associated with beam-walk over the primary and secondary mirrors; and
- Coronagraph occulting mask centering (on the star) errors produce contrast degradation due to light spillage outside the mask.

A detail modeling of the ACCESS coronagraph instrument and science observations (Section 8.8) has simulated the effect of the pointing errors and allocated the pointing stability requirements for the nominal science exposure duration of 1000 seconds.

These allocations define the fine pointing mode requirements for science observations. In particular, the telescope and coronagraph pointing requirements. The telescope pointing stability requirement of 1 mas for the tip/tilt of the line-of-sight (3σ, over 1000 s) drives the need to augment the spacecraft pointing capability with a hexapod pointing stage. The fine pointing requirements were derived for the most demanding science case, which corresponds to the smallest

Table 8.5.2-1. Pointing requirements (angle in the sky, 3σ)

Pointing Mode	Spacecraft Pointing (ACS)	Telescope Pointing (Hexapod)	Coronagraph Pointing (Fine Steering Mirror)
Normal (for SC ops and pointing acquisition)	Accuracy: 30 as		
	Stability/100 s: 1.5 as		
Fine (for science observations)	Accuracy: 30 as (p, y) 30 as (roll)	Accuracy: 1 mas (tip, tilt)	Accuracy: 0.1 mas (tip, tilt)
	Stability/1000 s: 100 mas (p, y), 5000 mas (roll)	Stability/1000 s: 1 mas (tip, tilt)	Stability/1000 s: 0.45 mas (tip, tilt)
		Jitter: 1 mas (<10 Hz) 0.1 mas (>10 Hz)	Jitter: 0.1 mas

occulting mask with sharp edges. The use of larger occulting masks with optically smoother edges can relax the pointing requirements offering graceful degradation and de-scope options.

The pointing requirements for nominal spacecraft operations and science acquisition are 3-axis pointing accuracy of 30 arcsec (3σ) and pointing stability over 100 seconds of 1.5 arcsec (3σ).

Table 8.5.2-1 shows the pointing requirements classified per pointing mode and control actuation stage used to achieve it.

8.5.3 Pointing Architecture

The architecture of the PCS is shown in Figure 8.5.3-1.

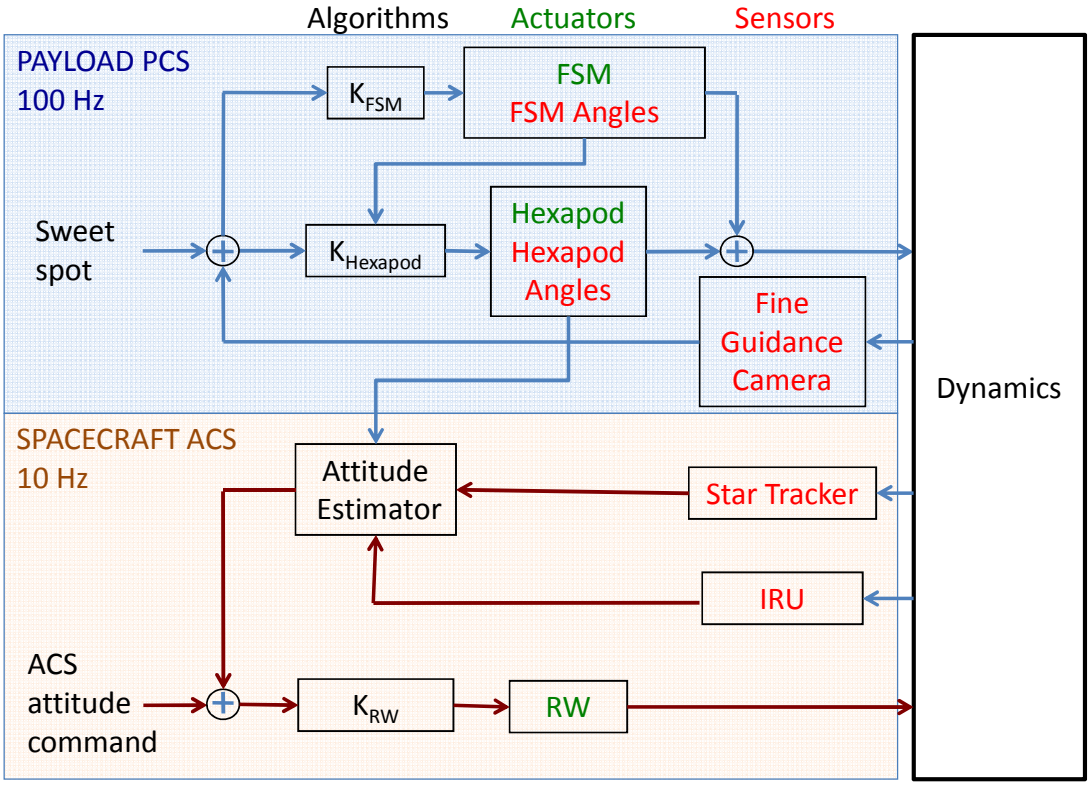

Figure 8.5.3-1. Pointing Control System Architecture

For control we propose a three-stage actuation system. The first stage is the SC ACS - reaction wheel system that stabilizes the SC to 100 mas in pitch and yaw and 5000 mas in roll. This pointing requirement on the spacecraft ACS is within the capabilities of midsize space observatories (Kepler). The second stage is a hexapod telescope pointing system that stabilizes the telescope line-of-sight to 1 mas in tip and tilt (corresponding to pitch and yaw axes of the SC). The hexapod in addition provides a vibration suppression capability. The third stage is the Fine Steering Mirror (FMS) within the coronagraphic instrument that centers the star in the occulting mask to 0.1 mas in tip and tilt.

For knowledge we proposed a fine guidance camera within the coronagraphic instrument that measures the tip and tilt errors. The information from the fine guidance camera is used by an advance control architecture, which commands the FSM and the hexapod. This architecture allows to offload the FSM to the hexapod smoothly and effectively. Basically the FSM loop has a high bandwidth loop that responds quickly to pointing errors, the hexapod has a mid bandwidth, which responds slower and offloads the FSM. In turn, the hexapod is offloaded to the spacecraft ACS by generating a highly accuracy offset angle derived from the hexapod pointing angles. Since the hexapod is tracking the guide star with a precision of 1 mas (1σ) means that a measurement of the hexapod pointing angles is the opposite of the spacecraft pointing error to the same accuracy level 1 mas (1σ). Another way to explain the control architecture is that the hexapod needs to correct for the spacecraft ACS error. Therefore the hexapod has a closed loop bandwidth of about 5 Hz which allows it to reject ACS errors with frequencies bellow 0.5 Hz. In addition the FSM has a closed loop bandwidth of 15 Hz, which allows it to correct for some residual errors at the hexapod stage. The performance has been evaluated in a detailed simulation environment.

The ACS attitude estimator using information from the IRU and the Star Trackers provides the knowledge to control the roll channel. Roll control errors will couple into LOS tip and tilt errors through misalignments and uncertainty on the roll axis. These errors, will manifest as line-of-sight tip and tilt errors with the frequency spectrum of the ACS pointing errors. These errors are within the bandwidths of the hexapod and FSM controllers and will be rejected along with the ACS pitch and yaw errors.

As discussed in (Section 8.8), the selection of high performance optical elements for the optics ahead of the FSM can relax the telescope pointing requirements. If the telescope pointing stability requirement is relaxed to 10 mas, this opens the opportunity to eliminate the hexapod stage by optimizing the spacecraft ACS design to achieve a pointing stability of 10 mas.

Other de-scope options are elimination of the fine alignment mechanism to center the PSF at the cross-hairs of four pixels of the fine guidance camera, and elimination of the Fine Steering Mirror.

8.5.4 Fine Guidance Camera Trade Study

We have studied three different concepts for coronagraphic fine guidance cameras. The first (Option 1, Spot) was to collect all the light reflected from a coronagraph occulter on to a focal plane, producing a Airy-type point spread function (PSF), allowing almost all of the star light from the central star to be used for centroiding. The second approach, referred to as punctured disk (Option 2, punctured disk) collects the light that bypasses a central obscuration, producing a PSF with a punctured central disk. The final approach (Option 3, Lyot) collects light after passing through the occulter at the Lyot stop.

The "centroiding" performance for each concept is evaluated, making use of both the shape of the star image on the tracking focal plane, and the amount of light that is available as a function of star magnitude for that concept. The term centroiding should not be taken to imply a center of brightness algorithm, but an estimation of image position. The amount of light available to the FGS from a star plays an important role in the overall pointing accuracy. It depends on the particular concept; the Option 2 FGS receives half the light of Option 1, and the Option 3 (Lyot option) FGS only about 1% to 2% of the light of Option 1.

The study included generation of representative images for each option by the science team, followed by an engineering evaluation of a centroiding or a photometric algorithm for each option. The options are described in more detail:

Option 1: Light reflected from the occulting mask is picked off and sent to the tracking focal plane. An advanced centroiding algorithm that incorporates a model of the Point Spread Function (PSF) is used for the position estimation process. This option requires making use of the fine alignment stage of the fine guidance selection mirror to center the PSF within 15% of the crosshairs of four adjacent pixels to make the position estimate more sensitive to small changes of the image location. An additional key requirement is that a reference centroid x-y point on the tracking detector needs to be determined that represents the optimal pointing for the coronagraph. Since this is not a direct measurement, simultaneous measurements of the coronagraph and FGS are needed as part of an alignment procedure. A representative image of the raw PSF is shown in Figure 8.5.4-1, and Figure 8.5.4-7 (illustrated using the Option 2 image) highlights the alignment issues.

Option 2: Light reflected from the circular occulting mask is picked off and sent to tracking focal plane. The central occulting mask makes the resulting PSF look like a punctured version of the Option 1 PSF. A representative image is shown in Figure 8.5.4-2. The image used for tracking has roughly 50% of the light acquired in Option 1. Additionally, as in Option 1, a separate alignment procedure is required. A photometric centroiding algorithm that evaluated the variation of intensity with pointing error was used for the analysis. While losing half of the light, this approach has the benefit of removing the high central region, reducing the dynamic range needed on the detector, and additionally providing a sharp transition area, (the dark central disk), which can be used to make more sensitive measurements. This case is analogous to the proposed PIAA coronagraph low-order-wavefront-sensing concept [3]. The overall performance of this approach appears (to be shown later, see Figure 8.5.4-6) slightly worse than in Option 1. However, this approach reduces the risk of the detector becoming saturated by images created by bright stars using the Option 1 approach, and should be considered in new trades.

Figure 8.5.4-3 shows a direct comparison (linear scale) between images from Option 1 (left) and Option 2 (right). Note the central cylindrical volume of right PSF (Option 2) has been eliminated with respect to the left PSF (Option 1).

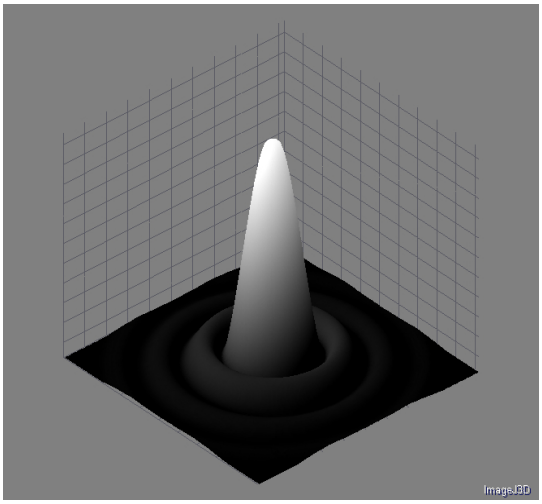

Figure 8.5.4-1. Option 1 3-D PSF

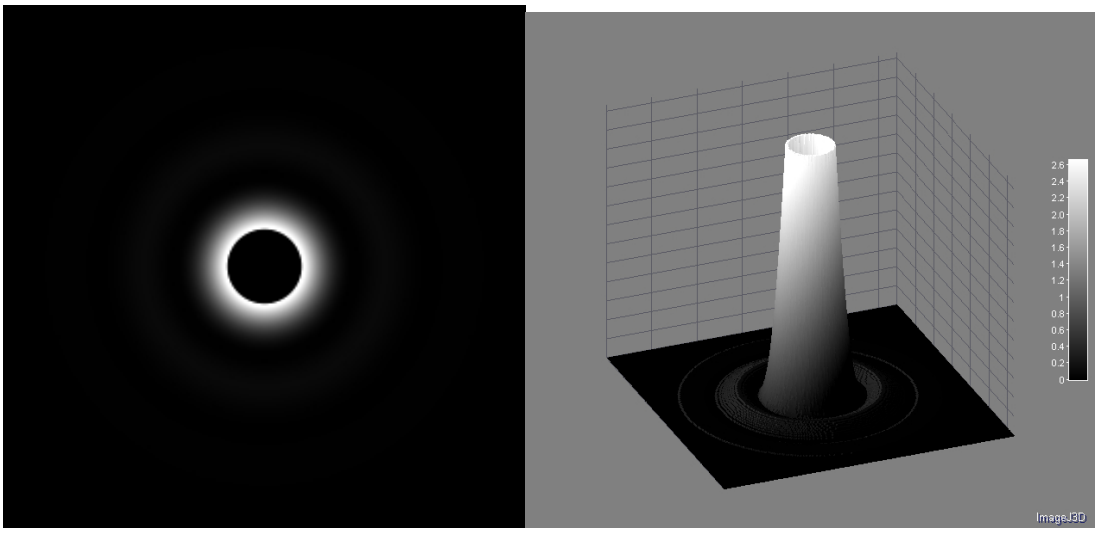

Figure 8.5.4-2. Option 2 2-D (*left*) and 3-D (*right*) PSF for the punctured disk

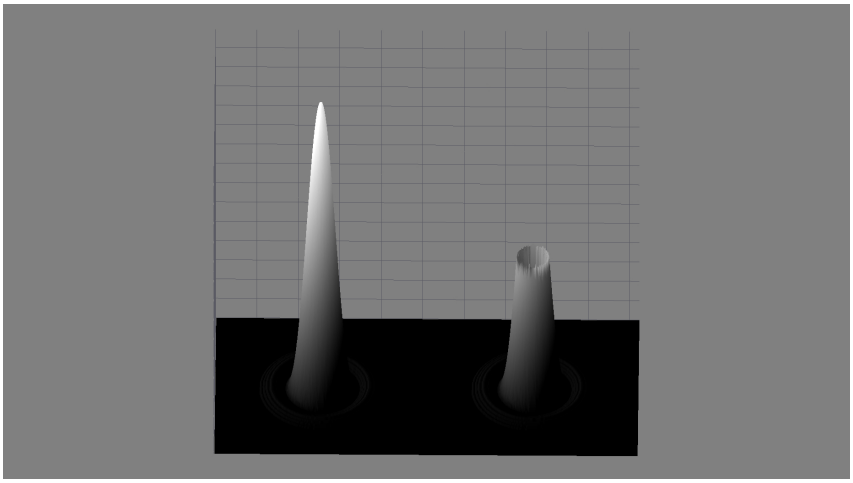

Figure 8.5.4-3. Option 1 and 2 3-D PSF

Option 3: Light reflected from the Lyot stop is picked off after the light has passed through a linear occulting mask. A representative image is shown in Figure 8.5.4-4. A photometric technique was used in this case to evaluate the pointing performance. Here the image used for tracking directly represents the light used by the coronagraph (both images discard the central portion of the star image), and the alignment becomes significantly easier. A downside is that some of light used by the coronagraph is required for the tracking measurement. Currently 10% of the coronagraph light, plus the longer wavelengths (to about 950 nm) is send to the tracking focal plane. The total light provided for tracking purposes is only about 1% to 1.5% of the light obtained by Option 1.

Figure 8.5.4-5 shows a set of images obtained by moving the PSF in 0.1 mas increments across the occulting mask. The images displayed are computed to be the difference between an offset pointing image and a zero offset pointing image (which was shown in Figure 8.5.4-4 left). Visual inspection of these images shows the sensitivity of this technique to measure pointing errors.

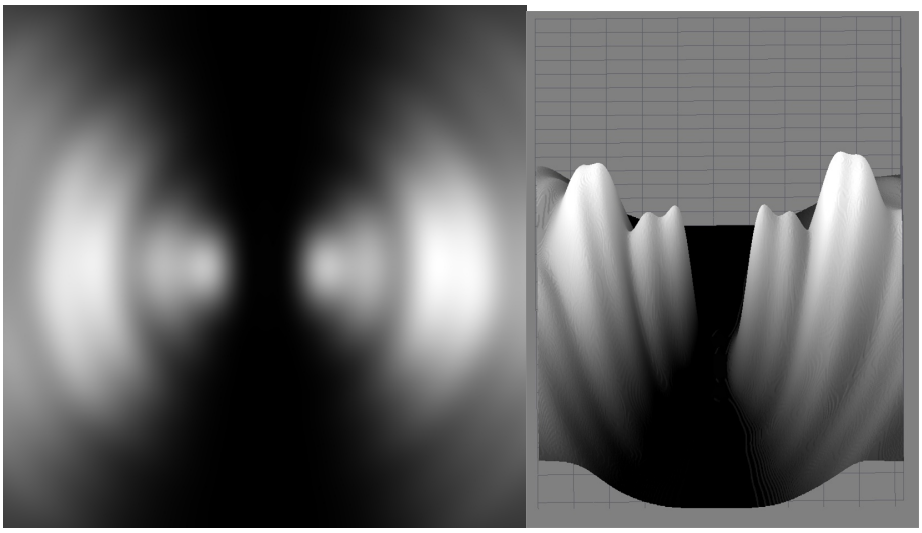

Figure 8.5.4-4. Option 3 2-D PSF (*left*) and 3-D PSF (*right*). The 3-D plot is on the same spatial scale, but the total signal is a factor of nearly 100 compared to Option 1.

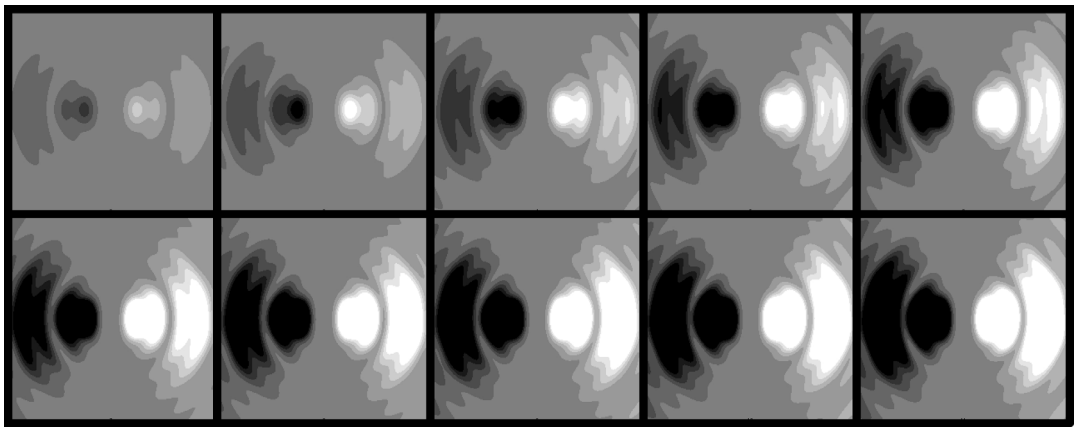

Figure 8.5.4-5. Option 3 Photometric incremental sensitivity to pointing errors; the image is simulated moving from left to right in 0.1 mas steps. The rapid change of relative signal intensity highlights the "shape" sensitivity of this approach to motion.

The results of this trade study are shown in Figure 8.5.4-6 and summarized in Table 8.5.4-1 for star magnitudes 3 and 7. The performance of course depends largely on the photons available for guiding, which is limited by the FGS design. All options were evaluated assuming a 0.01 second integration window to support a 100 Hz fine guidance camera measurement update. Option 1 has a very large number of photons available to it because of the large aperture of the telescope and the brightness of the star. Option 2 has about half the photons of Option 1. And because Option 3 has only about 1% of the photons of Option 1, Option 3 did not address the magnitude 7 star case because the photons available could not support a 100 Hz measurement rate.

The assumed signal (measured in electrons/per second from the detector) as a function of star magnitude (option 1, magnitude 7 used as a reference) is presented in Table 8.5.4-2. The amount of signal available for a magnitude 7 star for Option 1 is roughly 100,000e. The signal available for Options 2 and 3 uses the same optical and detector efficiency and the additional effect of the masking.

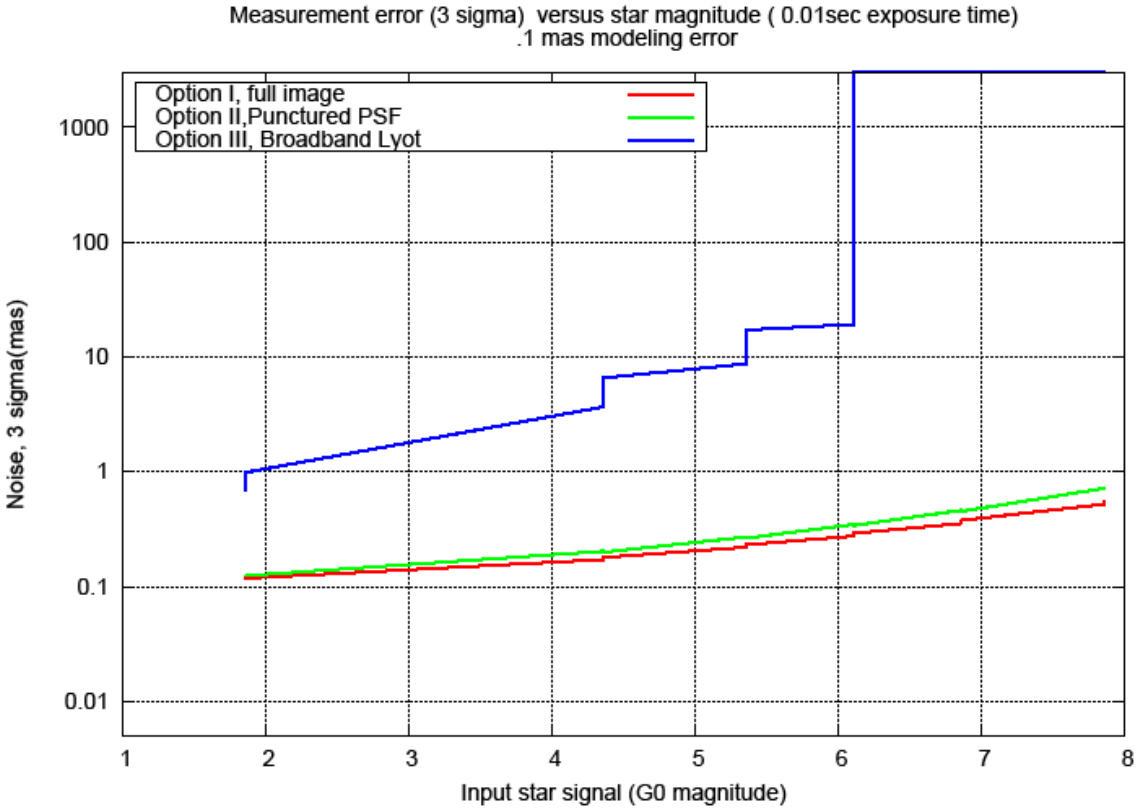

Figure 8.5.4-6. Centroiding performance for Options 1 to 3 for Fine Guidance Camera concepts versus star magnitude (G type stars)

Table 8.5.4-1. Pointing performance of Fine Guidance concepts (angle in the sky, mas, 3σ)

	Star Magnitude 7	Star Magnitude 3
Option 1: Centroiding on reflected image	0.3	0.18
Option 2: Photometric Technique punctured-PSD	0.3	0.18
Option 3: Photometric Technique at Lyot after linear occulting mask		2.1

Table 8.5.4-2. Signal levels for Fine Guidance concepts

Signal/ electrons per 10ms			
Magnitude (G0 star)	**Option 1 PSF**	**Option 2 Punctured PSF**	**Option 3 Lyot**
10 ms exposure			
0	63,348,416	31,674,208	633,484
3	3,997,015	1,998,507	39,970
5	633,484	316,742	6,335
7	100,400	50,200	1,004
9	15,912	7,956	159
11	2,522	1,261	25

Option 1 has been selected as the baseline because it is independent of the type of occulting mask used and provides the best overall performance. Option 2 and 3 will require specialized photometric algorithms for each type of mask.

Overall noise is illustrated in Figure 8.5.4-6. Modeling error accounts for roughly 0.1 mas error; it is possible that this could be improved by more detailed modeling. The bulk of the remaining error is noise and image jitter over the exposure period.

Spot Centering, Centroiding Approach

After the alignment of the coronagraph to the fine guidance system, a "nulling" point on the FGS focal point is determined by calibration, such as shown in Figure 8.5.4-7.

This alignment is implemented by a fine alignment mechanism that is part of the Fine Guidance Camera selection mirror (see Section 8.6 for additional information).

If the star image meets our modeling assumptions, and the star "centroid" can be driven to that nulling point shown in Figure 8.5.4-6, the contrast for the coronagraph will be maximized. For Options 1 and 2, the nulling point is determined by making coronagraph measurements on a bright star (to shorten the integration time), and determining physical point in the tracking focal plane, such as shown that maximizes the contrast. For the Lyot Option 3 case the alignment is significantly easier. For each case, image models are built, to describe the change of star signal (the photometric sensitivity) as the star moves from the nulling point.

In all the cases, our model evaluates the change in the star signal in the pixels, and uses the change to determine a correction factor. Because the alignment point is fixed, and the control system maintains tight pointing control, (better than a few milliarcseconds), the change in star signal as a function of displacement from the alignment reference point can be linearized, resulting in less than 5% error in the resulting correction term (displacement errors of 1 mas would result in less than 0.05 mas error). Most of the important signal for centroiding is in the 2×2 to 4×4 region around the alignment point with a pixel size of 70 mas. Figure 8.5.4-5 illustrates the change of image signal with displacement for the case of Option 3.

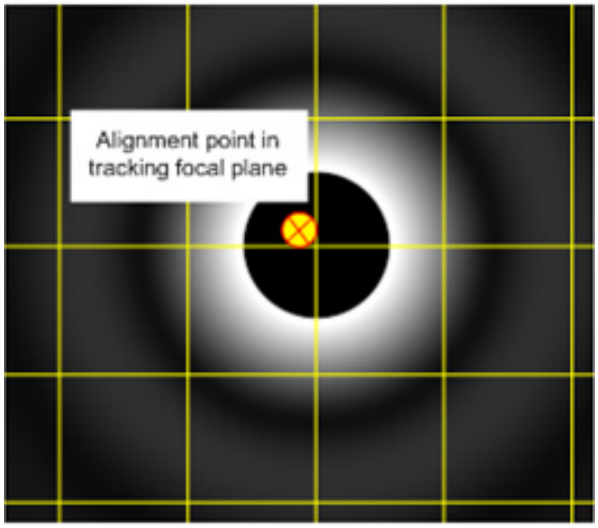

Figure 8.5.4-7. PSF is shown aligned to the cross-hairs of 4 FGS pixels. The "X" represents the point to which the center of the dark disk needs to be placed to optimize coronagraph performance. The thin yellow grid lines are the pixel boundary. As shown, the offset of the optimal pointing location from the cross-hairs of 4 FGS pixels is roughly 15% of a pixel, which is the desired alignment requirement.

Other Options and Notes

A variation of options 1 and 2, which could be used if only bright stars—those brighter than magnitude 9—were observed as science targets, would be to spread the image over a full 10×10 or larger pixel area, creating a smaller angular pixel size, and digitally rebinning the data to maintain a simple nulling algorithm. The alignment requirements relative to the pixel boundary could then be relaxed, since the pixel size could be <25 mas. This has the downside that the pixel read noise plays a much larger role. The number of pixel measurements would grow by factors of 25 to 100. A more complicated algorithm, which uses optimized weights for each of the pixels has been previously looked at, but requires significantly more calibration effort, and has more color dependence as the pixels get further from the center.

8.5.5 Integrated Pointing Design

8.5.5.1 Structural Design

The spacecraft (SC) structure provides mounting interfaces which meet field of view (FOV) requirements, and maintenance of critical alignments for the telescope (TS) and SC bus components of the ACCESS space segment with a configuration that fits within the launch vehicle static envelope.

The SC bus consists of a primary structure supporting the propulsion module, spacecraft equipment panels, payload panels, and solar array assemblies. The easy-to-build, test-proven, modular design maximizes equipment accessibility and integrates passive thermal control. The all Aluminum SC structure is efficient, lightweight, and has high-stiffness.

The structural dynamic characteristics of the SC are designed to meet the minimum frequency requirement specified by the launch vehicle supplier, to support the vibroacoustic responses of the mounted payload (PL) and SC bus equipment, and to minimize jitter response at the PL interface (I/F) during operation within acceptable limits.

The SC structure is designed to have sufficient strength to react loads derived by a Launch Vehicle (LV)-observatory coupled loads analyses and additional vibroacoustic loads with the applicable factors of safety.

Deployables solar array (SA) panels and associated tie-down and release devices provide the required SA stiffness for launch. The SC bus structure includes the Propulsion Module, the equipment panels, a two-wing solar array (SA) with tie-downs and release devices, and miscellaneous loose brackets.

The propulsion module encloses the propellant tank and uses a central cylinder to carry the primary structural loads. The central cylinder offers an efficient structural load path from the payload to the LV. The central cylinder and cone are based on the heritage EOS design, with a transition cone to the launch vehicle interface. Panels and fittings support the propellant tank inside the central cylinder/cone.

Similar to the GeoLITE heritage design, vertical and horizontal shear panels provide the interface between the equipment panels and the central cylinder.

The equipment panels are dedicated to providing support and thermal protection of the SC electronics equipment and spacecraft batteries. The equipment panels are aluminum honeycomb and contain embedded heatpipes, similar to GeoLITE, and are attached to the spacecraft structure by titanium flexures. This allows the use of lower-cost aluminum panels in place of composites without impacting spacecraft dimensional stability.

The mounting interface with the Payload Support Bi-pod Struts is at the intersection of the three vertical shear panels with the +Z platform. The interface fittings transfer load from the payload to the vertical shear panels, which provide a direct load path to the central cylinder.

The SA Mechanical Assembly is based on the GeoLITE design and consists of two wings with three panels each, which fold in a flat-pack configuration, with cable-activated latch/release locations per wing.

8.5.5.1.1 Structural Model

Analytical Finite Element Models (FEM) of the SC bus have been generated for the stowed and deployed configurations to verify design feasibility for launch and on-orbit performance (Figure 8.5.5-1). The stowed model was used to verify minimum frequency stiffness requirements and to provide initial sizing for structural mass estimates. The deployed model is derived from the stowed model and was integrated to the telescope (TS) model provided by ITT to perform on-orbit jitter and controls trades to verify design feasibility to satisfy on-orbit performance requirements.

The analytical model generated represents the current design consisting of the central cylinder spanning the SC height from the LV interface adapter to the PL platform. Shear panels radiating from the central cylinder to the equipment panels are included. Equipment panels are attached to shear panels and the upper and lower platforms. Equipment mass has been included based on current mass properties defined by various subsystems.

Two versions of the SC design have been modeled, a rectangular and a hexagonal bus. In both cases launch feasibility has been verified by initial sizing that satisfies the minimum lateral frequency requirement of the LV with the payload supported by the SC. The hexagonal bus offers a more efficient structure for the PL and has been adopted in the baseline design. The two bus models have been integrated to the telescope model provided by ITT.

A detailed model of the SC bus is included. The central cylinder is of composite construction, while the equipment panels are of Al Honeycomb construction. The TS is supported by the SC via six (6) struts in a kinematic arrangement. The struts have been angled and sized to obtain a fundamental lateral frequency of about 15 Hz when fixed at the strut end to SC. The struts are

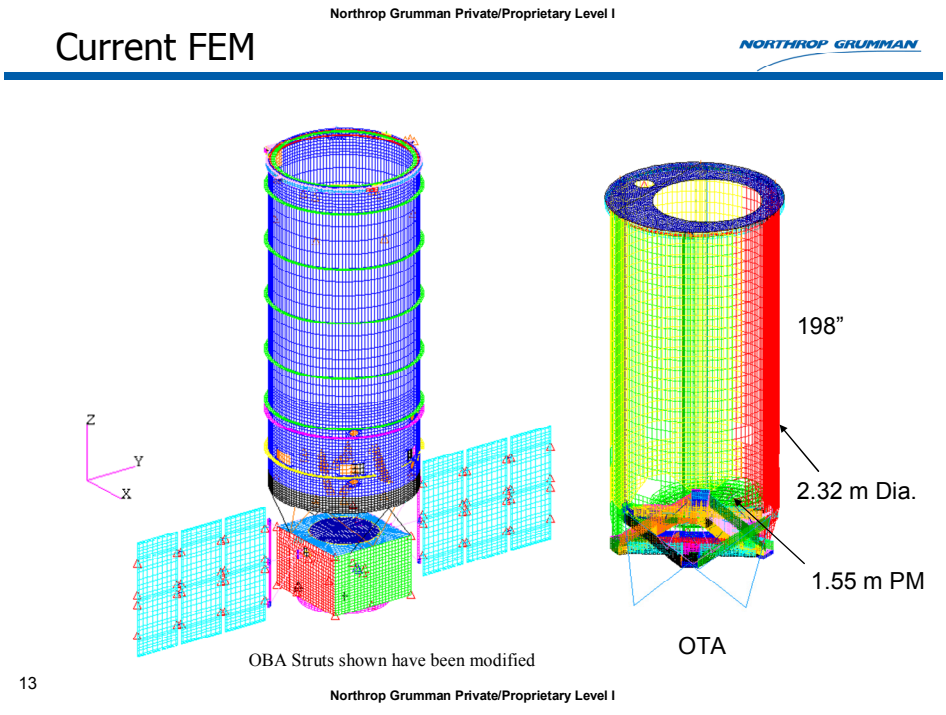

Figure 8.5.5-1. Finite Element Model.

intended to be supported directly by the primary structure for an efficient load path. This enables the observatory launch frequency to be above the minimum lateral frequency requirement of the LV. Two versions of the struts have been considered. The NG active/passive struts and the ITT AIM struts. The NG active/passive struts designated as the Active/Passive Spacecraft Isolator (APSI) are described below.

Each SA wing was modeled per current design to include three (3) panels that are stowed and locked via launch locks to the equipment panels. In its deployed configuration, each SA panel is attached to the adjacent panel via tape hinges with significant flight heritage. The three-panel solar array design has flight heritage in the GeoLite program. The solar arrays models are from the GeoLITE program and are at 0.3 Hz. A complete listing of deployed model frequencies is provided in Figure 8.5.5-2.

The integrated deployed FEM includes the SC, the TS, and the deployed SAs. SC Mass properties were based on current mass properties estimates with 43% contingency. The TS model was supplied by ITT and contains representations of Beam Walk (BW) LOS X and Y. The TS Mass properties are from ITT supplied FEM. The integrated model contains simplified models of the reaction wheels and their isolators as described below. The SC hexapod APSI isolator offers 6 degree of freedom isolation between 0.5 and 2 Hz. The current model is based on Control/Structure Interaction (CSI) testbed design of the long stroke isolators. The integrated model has been checked for grounding, particularly a LOS rigid body check has been performed and found acceptable.

A summary of the integrated deployed model development is shown in Figure 8.5.5-3. The integrated FEM is also shown. The integrated model was used to determine modes up to 300 Hz to account for high frequency wheel harmonics. The model is in English Units (mass is in lbf-sec^2/in), but metric versions have also been generated of the SC side. The integrated FEM as well as open and closed loop state space matrices have been provided to JPL for use in dynamics and controls trades.

Model mass properties and a summary of dynamic characteristics and SC isolation mode shapes are shown in Figures 8.5.5-2 and 8.5.5-4.

Summary of Model Free-Free Modes

NORTHROP GRUMMAN

- **SC Isolator**
  - **Y & X Rocking : 0.47 & 0.48 Hz**
  - **Rocking/ lateral: 1.60 & 1.62 Hz**
  - **Axial or Bounce mode : 1.69 Hz**
  - **Torsion or Twist: 1.8 Hz**
- **Reaction Wheel Isolator Modes**
  - **9 Hz Axial**
  - **7 Hz Rocking, 10 Hz Lateral**
  - **21 Hz about spin axis**
- **Observatory 1st Overall Flexible Mode ~ 25 Hz vs. 20 Hz (TBR Req't)**
- **SC 1st local mode > 35 Hz**
- **OTA ~ 16.4 Hz (w/ ITT struts)**
  - **22 Hz w/o struts**
- **OBA**
  - **OBA originally very low**
  - **Modified support struts led to ~ 12.5 Hz**
  - **To be revisited once hex bus design/ model is available**
- **Deployed Sunshade- not included in FEM: Will size above 0.2 Hz (TBR)**
- **Deployed SA ~ 0.3 Hz (GeoLITE SA model)**
- **Deployed HGA- Not included in FEM: Will size above 5 Hz (goal)**

No.	Frequency (Hz)	DESCRIPTION
1-6	0.00	rbm
7	0.30	SA Symmetric Out-of-Plane
8	0.34	SA Anti-ymmetric Out-of-Plane
9	0.47	PL iso Lateral (OTA moves along LOS Y direction)
10	0.48	PL iso Lateral (OTA moves along LOS X direction)
11	0.98	SA Symmetric In-Plane
12	1.02	SA Anti-symmetric In-Plane
13	1.36	SA Anti-symmetric Twist
14	1.36	SA Symmetric Twist
15	1.60	PL iso Rocking (OTA moves along LOS Y direction)
16	1.62	PL iso Rocking (OTA moves along LOS X direction)
17	1.69	PL iso Axial (OTA moves along LOS Z direction)
18	1.80	PL iso Torsional
19	1.95	SA 2nd Symmetric Out-of-Plane
20	1.99	SA 2nd Anti-symmetric Out-of-Plane
21	4.79	SA Wing Twist
22	4.79	SA Wing Twist
23	5.41	SA Higher Order Out-of-Plane
24	5.41	SA Higher Order Out-of-Plane
25 - 32	6.70 - 6.81	RWIA Rocking
33 - 36	9.09 - 9.16	RWIA Axial
37 - 40	9.73 - 10.24	SA Higher Order
41 - 48	10.51 - 10.58	RWIA Lateral/ Rocking
49 - 56	11.10 - 17.50	SA Higher Order
57 - 60	20.97 - 21.00	RWIA Torsion
61 - 62	24.21	SA Higher Order
63	25.00	OTA lateral
64 - 65	25.02 - 27.21	SA Higher Order
66	27.43	OTA Higher Order
67	27.79	OTA lateral
68 - 69	28.01 - 28.04	OTA Higher Order

10

Figure 8.5.5-2. FEM Free-Free Modes

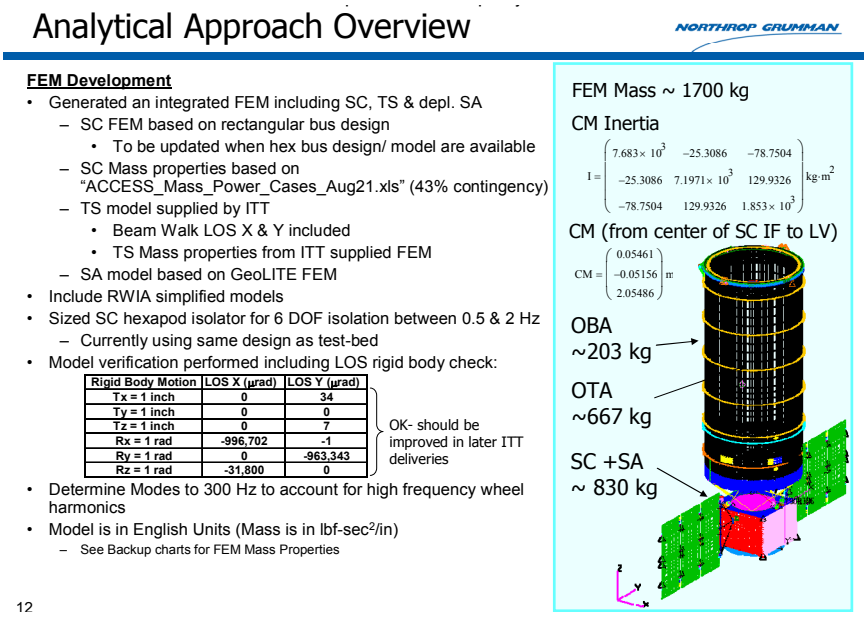

Figure 8.5.5-3. FEM development approach

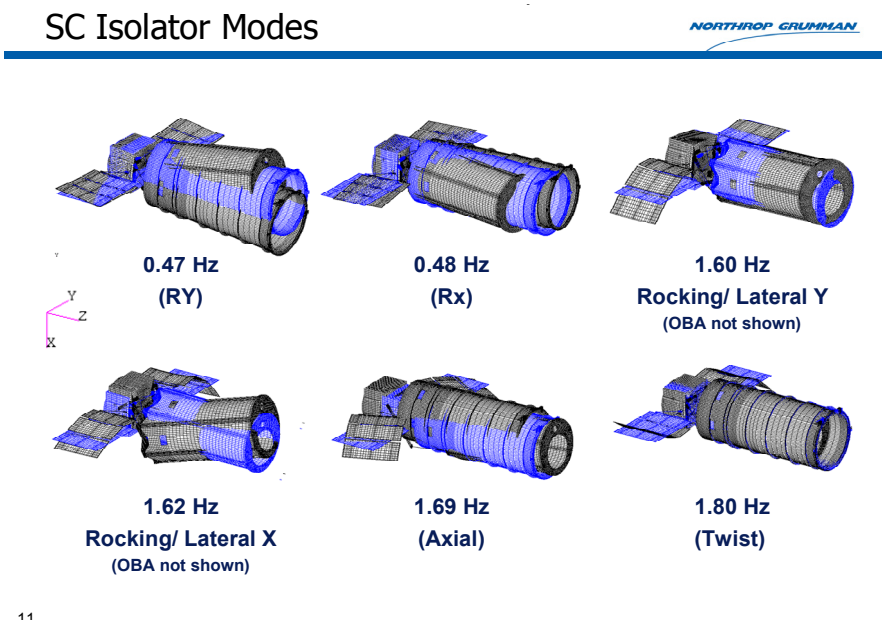

Figure 8.5.5-4. Illustration of APSI (Active Passive Spacecraft Isolator) Modes

8.5.5.1.2 Vibration Isolation

ACCESS has very stringent jitter and pointing requirements. Jitter above 10 Hz must be below 0.1 mas, while the pointing stability requirement is 1 mas.

Our approach to meeting the stringent on-orbit jitter budget is to utilize a dual stage isolation scheme between the main sources of jitter disturbances from the reaction wheels (RW) to the PL. Mounting the RWs on specially built passive isolators designed to attenuate wheel imbalances and disturbances in lateral, axial and bending degrees of freedom (DOF) provides the fist stage of isolation. An active/passive hexapod isolator assembly supporting the TS to the SC structure provides damped six degrees of freedom isolation above 2 Hz. Jitter response was evaluated using a

dynamic model of the on-orbit configuration with a TS model. Analyses showed that employing the dual stage isolation provides the attenuation necessary in a wide frequency range above 1 Hz. The dual stage isolation scheme also provides reduced risk of not meeting error and jitter budgets as it minimizes the sensitivity to modeling errors and modal interactions between the SC and the TS. NGAS has been successful in building passive isolators that are simple, compact and light and meet stringent on-orbit performance requirements. Flight-proven design heritage from previous NGAS programs will be applied in the design of both isolators. The Chandra wheel isolator and EOS SADA joint damper described herein are examples of successful passive isolators designed and flown by NGAS.

NGAS active isolation demonstrations have been implemented on the JPL MPI test bed and on SBL isolation and pointing demo. The long stroke isolator mentioned above has been incorporated in the NGAS CSI test bed where active/passive isolation has been demonstrated. LOS detection and optical performance demonstration are planned for the CSI test bed as part of the upcoming NGAS IRAD work for upgrade to TRL 6.

The current scheme to meet the fine pointing stability requirement of 0.1 mas is achieved in three stages. SC ACS provides the first stage of observatory pointing to 50 mas with the reaction wheels, using the Fine Steering Mirror (FSM) pitch/yaw angle measurements and roll knowledge from the Star Trackers. The second stage of pointing to 1 mas is furnished by the active stage of the TS to SC struts using pointing knowledge from the Fine Guidance Camera (FGC). The FSM then maintains fine pointing to accuracy of 0.1 mas, with the SC Isolator centering the FSM in an offload loop, and maintaining its travel at 1 mas.

The analytical approach followed to demonstrate feasibility of achieving ACCESS jitter and control requirements using the outlined isolation and control scheme is summarized in the Figure 8.5.5-5. Actuator commands for LOS X and Y are decoupled with four orders of magnitude separation as seen in the open loop transfer functions shown in Figure 8.5.5-5.

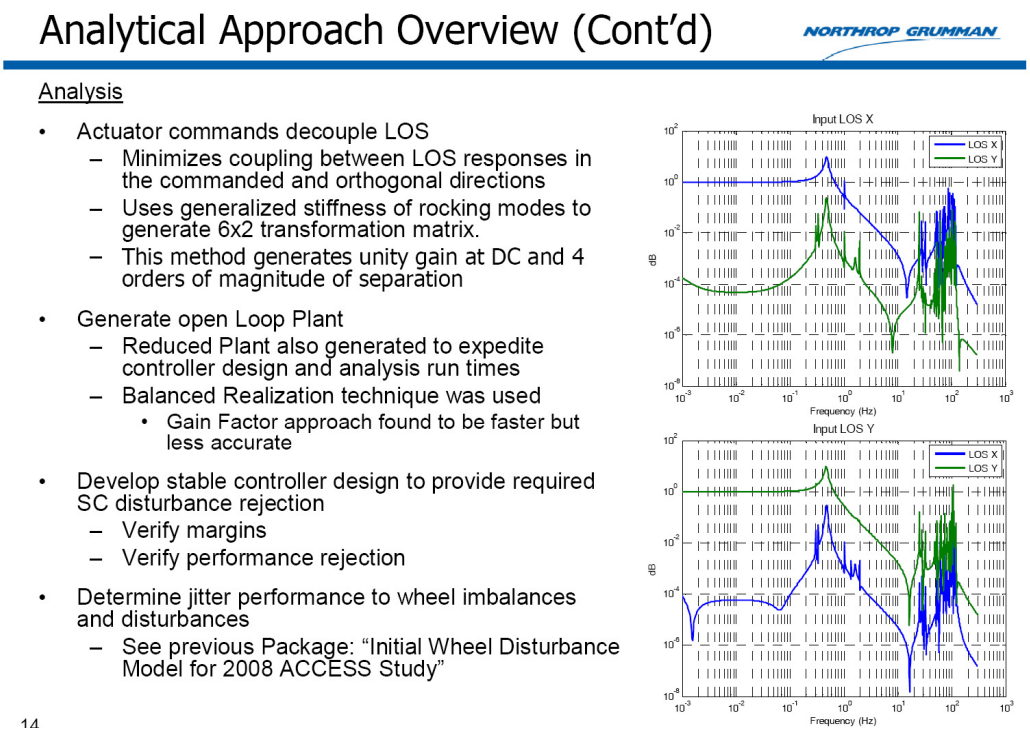

Figure 8.5.5-5. Analytical approach for the APSI Vibration Isolation Design and open loop transfer functions from Line-Of-Sight.

8.5.5.1.3 Reaction Wheel (RW) Isolator

The only significant source of jitter from the SC to the TS is due to the RW disturbances. These are due to RW static and dynamic imbalances and bearing noise disturbances which occur along five (5) degrees of freedom (DOF). Each RWA is mounted on an isolator of Chandra heritage (Figure 8.5.5-6). The RW Isolator Assembly (RWIA) provides the 1st stage of isolation of the wheels in all 5 degrees of freedom of wheel disturbances. Each RWIA consists of six machined Titanium springs fitted with Visco-Elastic material (VEM) to provide damping close to 5%. The RWIA springs have a load alleviation passive mechanism that provides damping and graceful load isolation for launch. This furnishes a soft ride for the RWs during launch which has proven to minimize vibrations into the RWs that tend to worsen RW disturbances.

The RWIA is designed to include two rocking modes around 6.7 Hz, followed by an axial mode around 9 Hz and the 2nd lateral/rocking modes around 11 Hz. The RWIA torsional mode is around 21 Hz. The RWIA has no modes of significance above 11 Hz and offers excellent isolation of wheel disturbances as demonstrated by transmissibility testing on the Chandra program. A simplified, test validated RWIA model has been included in the Access integrated model. The RWIA isolator model has been validated by comparing its predicted axial, lateral moment transmissibility to those measured on the Chandra program. Refer to the enclosed package for additional details on the RWIA.

Four wheels are included and have been oriented in the model per ACS requirements. The RW/RWIA assemblies are mounted via stiff RWA brackets to the central cylinder close to the shear panels interface.

In summary, the integrated ACCESS model was used to determine jitter performance due to wheel disturbances. Beam Walk (BW) LOS equations were represented in the TS model via MPC equations supplied by ITT based on their current optical design. A detailed RW disturbance model representing fundamental and higher wheel disturbance harmonics for all RW disturbances was used

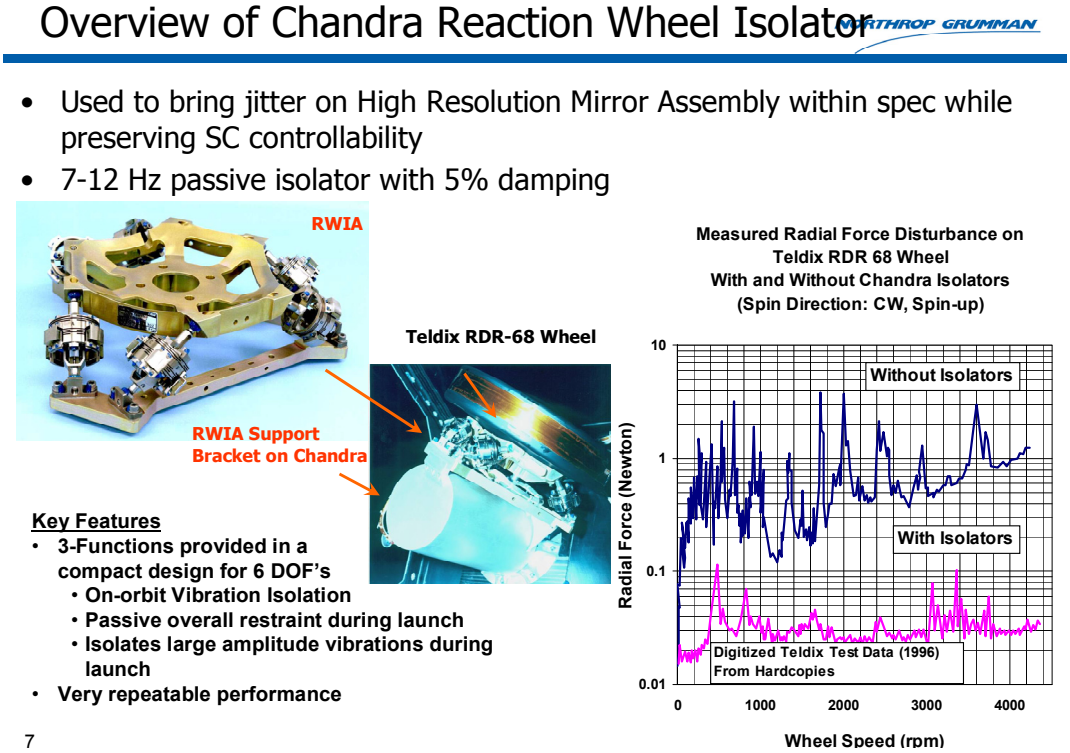

Figure 8.5.5-6. Reaction Wheel Isolator Heritage Chart

in the analysis. The RW disturbance model, which is based on Teldix RDR 68 measurements from the Chandra program, was used in the detailed jitter analysis. The disturbance model was provided to JPL and ITT as well. Refer to the enclosed package for RW disturbance model details.

The jitter analysis results shown demonstrate that the 0.1 mas maximum jitter requirement is achieved in a wide range of wheel rates below 6000 rpm. Jitter requirements would not be met if SC to TS isolator is not included. This is clearly demonstrated in Figures 8.5.5-7 and 8.5.5-8.

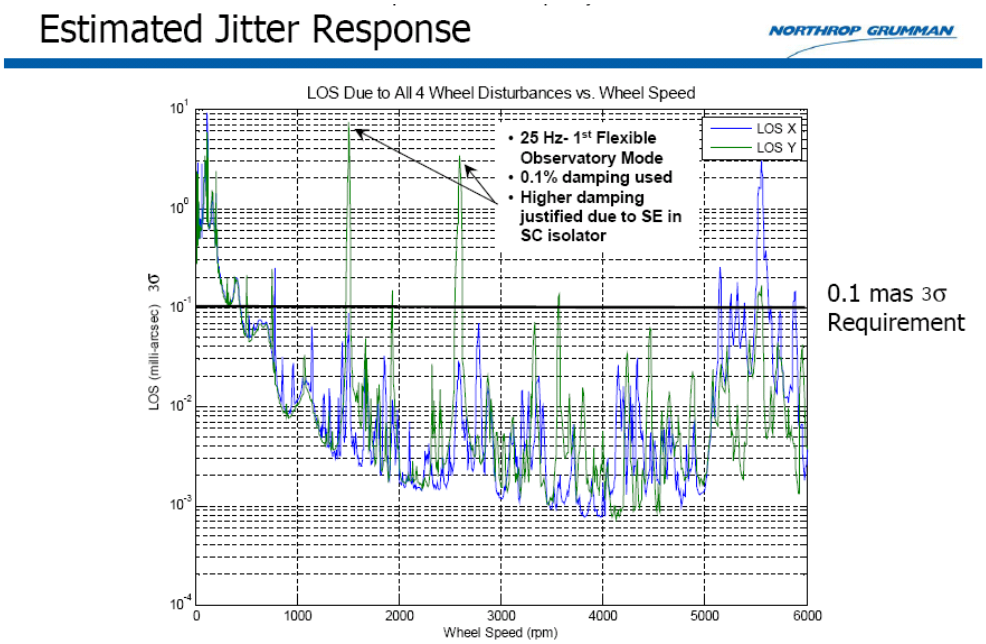

Figure 8.5.5-7. Line-of-Sight jitter versus Reaction Wheel speed

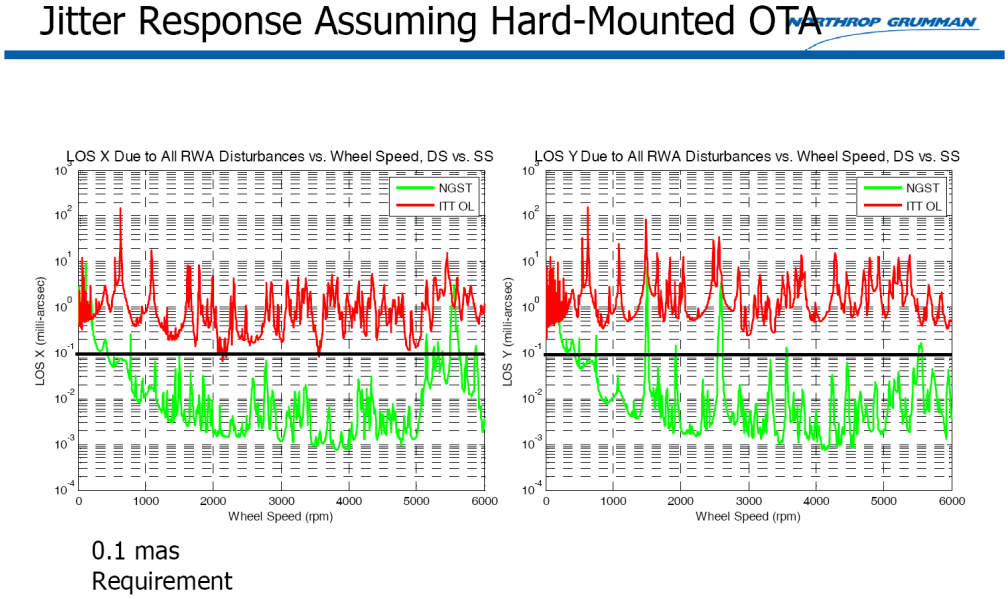

Figure 8.5.5-8. Line-of-Sight jitter versus Reaction Wheel speed plot showing comparison between NG passive isolator capability (*green*) in relation to rigid struts (*red*)

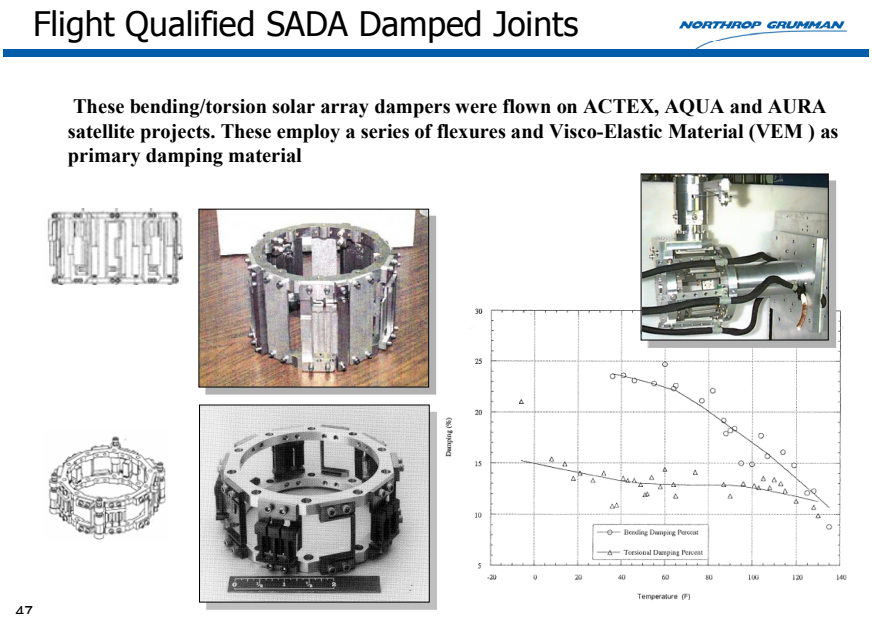

Figure 8.5.5-9. Solar Array Joint Dampers

8.5.5.1.4 Solar Array Joint Damper

An optional joint damper may be utilized to provide damping of low frequency Solar Array (SA) modes that may potentially couple with the controls bandwidth. The joint damper is of flight heritage in both EOS AQUA and AURA (Figure 8.5.5-9). It consists of a series of flexures and fitted with VEM for damping. The joint damper is attached to the SADA on one end and the SA yoke on the other end. Damping characteristics have been measured on for a wide range of temperatures and the choice of VEM will be selected based on ACCESS thermal environment.

8.5.5.2 Spacecraft Attitude Control System (ACS)

The ACCESS inertial referenced attitude control system (ACS) is shown in Figure 8.5.5-10. The Matlab/Simulink representation is shown in Figure 8.5.5-11.

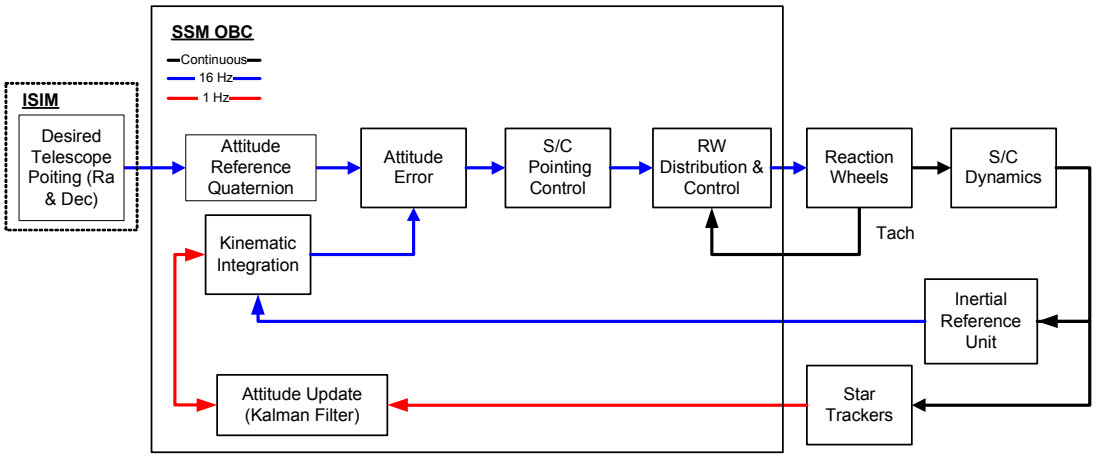

Figure 8.5.5-10. Integrated Pointing Control Architecture showing the ACCESS Observatory ACS

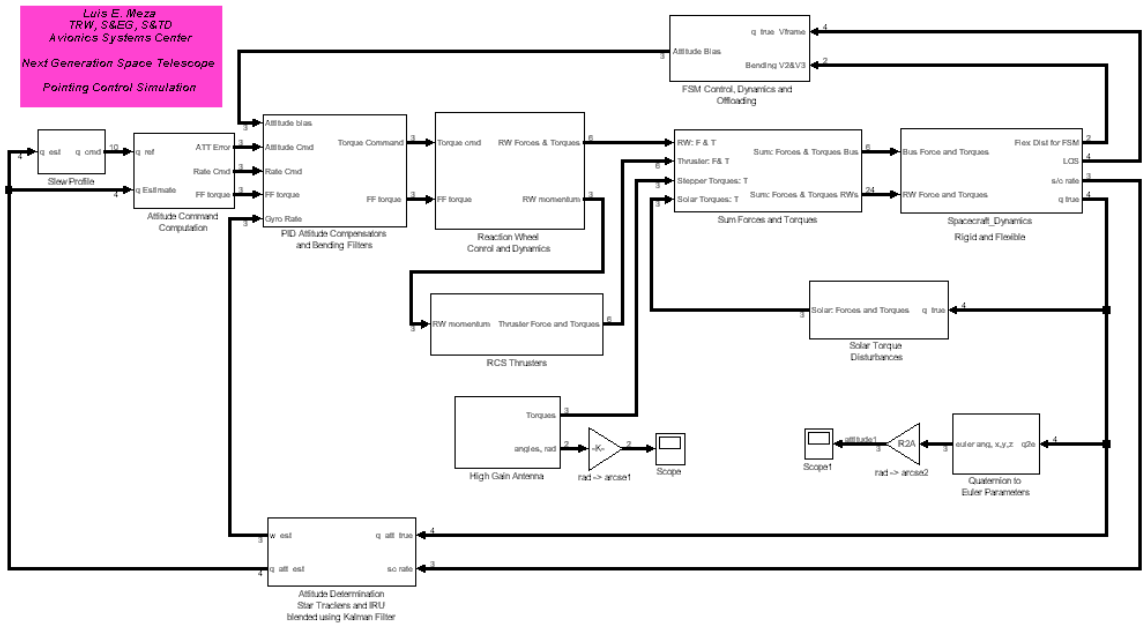

Figure 8.5.5-11. Matlab/Simulink respresentation of the ACCESS Pointing control system

8.5.5.2.1 Attitude Control System

The ACCESS ACS utilizes star trackers and IRUs for attitude determination, and reaction wheels for control. The ACS loop topology per axis consists of a Proportional + Integral + Derivate (PID) compensator, a second order bending filter to attenuate flexible modes, a momentum control loop for reaction wheel control, and an IRU (4 Hz bandwidth) for body rate information. The on-board attitude information is maintained and propagated as quaternions, by performing the kinematic integration using IRU data at every OBC minor cycle (0.064 sec). In addition, a Kalman filter is used at a slower rate (1.0 sec) to correct the IRU drift and the OBC attitude quaternion by using star tracker measurements referenced to a star catalog.

The ACCESS ACS uses a momentum exchange system which consists of a 4 reaction wheel cluster configured in a pyramid configuration to provide balanced momentum storage capability in each of the three spacecraft axes. The momentum control loop consists of a Proportional+Integral (PI) compensator, a first-order low-pass filter, a tachometer, and a tachometer-averaging filter for each wheel. The tachometer provides reaction wheel speed measurements at the quantization level of 19.5 rpm, based on its 48 pulses-per-revolution (ppr) performance and 0.064 sec readout rate. The reaction wheels can be set to a bias by using an additional bias control loop that regulates reaction wheel speed operation near a fixed speed in the null-space of the RWA cluster. This RW bias speed is chosen to minimize structural vibration excitation.

8.5.5.2.2 Time Domain Simulation

The ACS hardware models such as the reaction wheels, reaction wheel speed tachometer, reaction wheel disturbance models, and inertial reference units (IRUs) are all taken from JWST. ACS hardware parameters are shown in Table 8.5.5-1.

Table 8.5.5-1. Hardware parameters used for NGST Pointing Control Simulation

Hardware	Parameter	Value	Units
Reaction Wheels			
	Inertia	0.1295	Kg-m²
	Coulomb Friction	0.0050	N-m /rad
	Viscous Friction	2.1241e-005	N-m /(rad/sec)
	Static Imbalance	1.0787e-005	N /(rad/sec)
	Dynamic Imbalance	2.0107e-006	N-m /(rad/sec)
	Bearing Imperfection	2.0107e-006	N /(rad/sec)
	Command Quantization	0.0011	N-m
	Maximum Speed	6000	rpm
	Maximum Torque	0.12	N-m
Tachometer			
	Pulses per Revolution	48	-
	Sampling	0.064	sec
	Number of A/D Bits	16	-
IRU			
	Bandwidth	4	Hz
	Damping Factor	0.87	-
	Quantization	0.02	arc-second
	Angle Random Walk	0.009	arc-second /sec$^{(1/2)}$
	Rate random walk	3.17e-6	arc-second /sec$^{(3/2)}$
	Bias	0.001	arc-second/sec
	Number of A/D Bits	16	-
Star Tracker			
	Field of View	16° x 16°	Degrees
	Star Tracker Noise (1σ)	3.8	arc-second
Spacecraft	Inertia Tensor	[7.683E+03 -25.3086 -78.7504 -25.3086 7.1971E+03 129.9326 -78.7504 129.9326 1.853E+03]	Kg-m²

8.5.5.2.2.1 Pointing Control Hardware Models

The required pointing control hardware consists of sensors (star trackers, IRU's), and actuators (reaction wheels) whose input and output signals are converted and passed as counts. The sensor models are directly taken from ACCESS simulation and converted to a Matlab/Simulink equivalent. The star tracker model is ACCESS's model of the Galileo Avionica. The trackers bias and noise characteristics are modeled. In addition, the measurement residual between the measured and the estimated star locations are computed and sent to the Kalman Filter at a specified rate. The IRU is ACCESS's SSIRU model, with an integrated rate quantization of 0.02 arcsec/count. In addition, the IRU input rate is corrupted by three components: 1) a static bias term, 2) a rate random walk component, and 3) an angle random walk component. Continuous linear models represent the reaction wheels with coulomb and viscous friction in the feedback. The torque on the spacecraft is found by the appropriate transformations, which relate the torque on the spin axis and the disturbance torques due to dynamic imbalances in the transverse axes. Similarly, the reaction wheel disturbance forces due to static imbalances in the transverse axes, and bearing imperfections in the spin axis are transformed.

8.5.5.2.2.2 Pointing Control Software

The OBC software is digitally represented by using discrete transfer function blocks in Simulink to model the control loop topology, star tracker and Kalman filter which are written in C and embedded as CMEX S-Functions. The control loop gains are computed using linearized models in the frequency domain and are then used in the control laws in digital form. The multi-rate transitions are handled and regulated by Simulink by using equivalent sample and hold blocks to transition from the digital to the continuous and from the continuous to the digital domains.

8.5.5.2.2.3 Spacecraft Dynamics

The ACCESS spacecraft dynamics are modeled as a rigid body with flexible body modes superimposed. The rigid body spacecraft dynamics are represented by Euler's equations of motion $\underline{\dot{H}} + \underline{w} \times \underline{H} = \underline{T}$, where $\underline{H}$ is the spacecraft angular momentum vector, $\underline{w}$ is the angular rate vector, and $\underline{T}$ is the torque vector applied by the reaction wheels. The flexible dynamics are represented by a state-space model, which is constructed using the mass-normalized eigenvalues of the observatory finite element model (FEM) after performing a modal analysis. The flexible dynamics model is delivered to ACS from the dynamics group, with several available input-output nodes in the FEM such as the reaction wheel disturbance inputs and some desired outputs such as vibration at spacecraft c.g, and line of sight jitter. The resulting model is of the form $\dot{\underline{x}} = \underline{A}\underline{x} + \underline{B}\underline{U}$ with output equations $\underline{y} = \underline{C}\underline{x}$ for the desired output nodes, and $WFE = \| \underline{S}\underline{x} \|_2$ for the wavefront error, where $\underline{S}$ is the sensitivity matrix and $\| \|$ represent the Euclidean norm.

The rigid body spacecraft angular rate is then used in a continuous kinematic integration to obtain the true spacecraft attitude as a quaternion. The spacecraft rates used for input to the gyro for performing the on-board attitude propagation consists of the addition of the rigid and flexible body angular rates; the bus c.g. output nodes are chosen as the truth model corruption due to structural flexibility as the IRU model inputs. The onboard attitude propagation is performed at every OBC minor cycle of 64 msec.

8.5.5.3 Telescope Pointing System

Two telescope pointing systems have been studied: ITT Active Isolation Mount System and NGAS Active/Passive Spacecraft Isolator.

8.5.5.3.1 ITT Active Isolation Mount System (AIMS)

The Active Isolation Mount System (AIMS) was designed in the late 90s to serve two purposes: 1) to reduce transmission of bus-borne vibrations into the payload and provide damping to the payload modes, and 2) to enable fine 6-DOF (Degree Of Freedom) pointing control. The AIM system traditionally replaces the kinematic mount between the bus and payload. This implementation was used for the ACCESS study. AIMS hardware technology, including the associated AIMS Control Electronics has been flight qualified and has a NASA Technology Readiness Level (TRL) 6.

The dynamics lab located in Rochester NY, houses a fully functional 2.5meter-class dynamic testbed. This testbed is comprised of a flight-like telescope built with flight-traceable graphite-composites and it includes an aluminum bus simulator with in-class dynamics. The telescope mass is ~570 kg (1250 lbf) and the bus mass is ~1135 kg (2500 lbs). AIMS sits in between these two major subsystems and serves as the primary vibration attenuation stage between the bus and payload. A photo of the setup is shown in Figure 8.5.5-12.

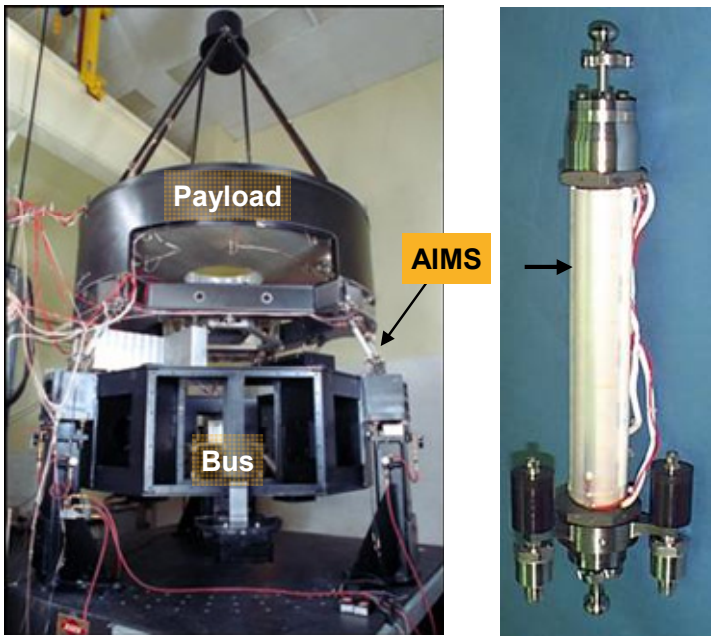

Figure 8.5.5-12. Dynamics Testbed and AIMS Photos

Figure 8.5.5-13. Gen-2 Active Isolation System

This bus-payload testbed has been highly characterized via detailed modal surveys of both the bus simulator and payload. There are 65 seismic accelerometers on the payload to measure the key performance parameters of LOS jitter and the primary mirror's wave-front error (WFE). The photo of the AIMS strut shown above is the *third generation* of active isolation struts. The first generation was built in the early 1990s. It was built very quickly in 10 months as a proof-of-concept for active vibration isolation. The performance was sufficient to show merit and the idea received further funding. A year later, the build of gen-2 active isolation began in collaboration with JPL and Draper Labs. This strut was significantly more refined and performed significantly better than the 1st generation. The JPL work was done under the direction of Dr. Robert Laskin. The testbed system that gen-2 was installed in is shown in Figure 8.5.5-13. (Note: this testbed has been reconfigured for other purposes)

The gen-2 strut had two significant issues:

1. Its ability to survive a launch was risky due to the use of a PZT stack. A stack has excellent load capabilities in compression, but very poor load carrying ability in tension. Displacement stops could have been implemented to reduce the risk, but they'd potentially introduce additional shock loads right when other dynamic loads are at their highest, keeping the solution at a high risk level. Preloading was considered, but this essentially doubles the compression load, reducing the robustness of the system. Launch locks could have been implemented as well, but they'd introduce another failure mode.
2. A PZT stack has significant hysteresis. This non-linearity can cause a transfer-function measurement of stability to appear acceptable at one input level, but change at another input level such that it was very difficult to accurately determine stability margins. A 6dB margin at one level can become only 3 dB at another input level.

However, even with these design shortcomings, the performance of this strut showed the merits of active vibration control. The AIMS was designed to address the gen-2 shortcomings (design is shown in Figure 8.5.5-12). The AIMS system has been developed and verified to a Technology Readiness Level of 6, including the hardware, control electronics, and software.

The measured open vs. closed loop performance of AIMS in the bus-payload testbed is shown in Figure 8.5.5-14. A 10× performance improvement is possible. Performance of AIMS in the bus-payload testbed is shown below as a 1 second snapshot of the line of sight vector on an X-Y plot. The specification (red circle in right figure insert) is 35 nano-rads (nrads) 1σ. Achieved performance is ~10 nrads 1σ. Measurement uncertainties of this test configuration are ~1 nrad, 1σ (>10 Hz), driven mostly by test environmental vibration.

Determination of pointing accuracy will have to be done in a vacuum chamber to eliminate air turbulence and reduce thermal disturbances from corrupting the data. ACCESS's 5 nrad 3σ pointing requirement will require such a test environment, and additionally this environment must be dynamically quiet. ITT has such a facility, an example of which is shown in Figure 8.5.5-15.

The success of AIMS resulted in other related dynamics developments, such as the "MagDamper." Using permanent magnets to create a static magnetic field, the MagDamper requires no power to achieve a purely viscous damping effect that is highly robust to environmental effects in an extremely reliable design. Figure 8.5.5-16 shows the MagDamper and its measured performance. ITT has flight heritage with visco-elastic material (VEM) treatments to increase damping on targeted structural modes. These technologies will be considered during future studies where the ACCESS PCS is fully optimized at the observatory level.

Other tools were developed, including "system identification" algorithms that can generate extremely accurate math models of a complex multi-input multi-output (MIMO) system, which can then be used to optimize a controller design. An example of one such MIMO model is shown below in Figure 8.5.5-17. Notice that the data set and model cover 4.5 decades of frequency and 120dB of dynamic range. No other known SysId technique can exceed this performance.

At this writing, the dynamics group at ITT Space Systems now totals 19 people, with several consultants regularly tasked. The experience level ranges from 1 year to over 35 years, with approximately 17 years as an average level of experience. Four members have PhDs, and several have mechanical/electrical cross degrees. All members have at least a Masters degree.

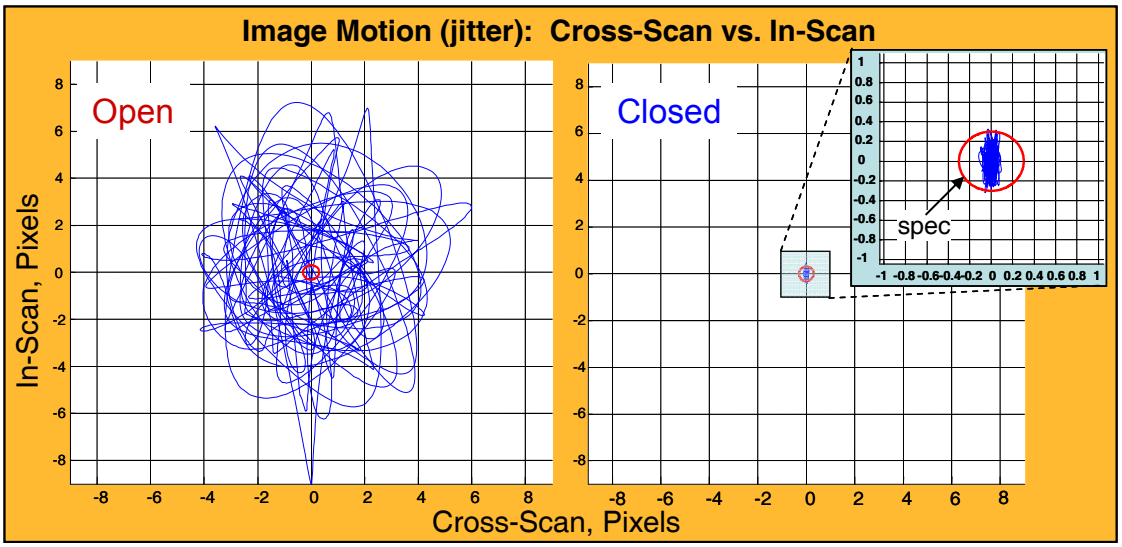

Figure 8.5.5-14. Measured AIMS Performance (spec = 35 nrads, 1σ)

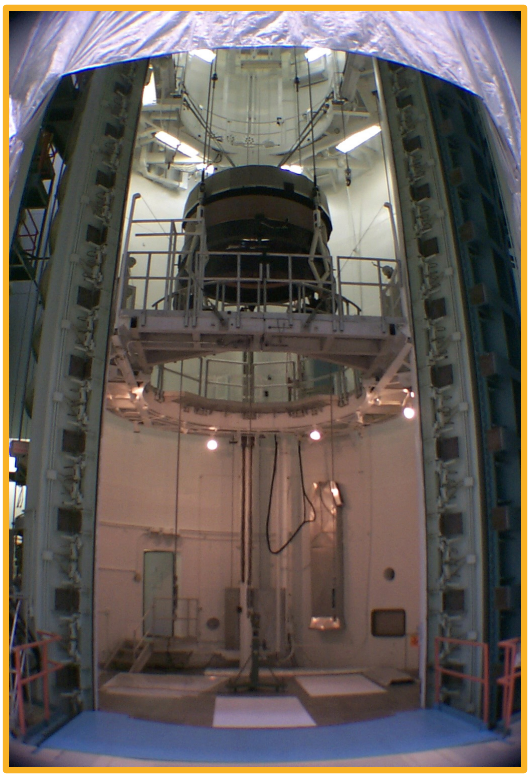

Figure 8.5.5-15. Example of ITT's Vibration Isolated Optical Vacuum Test Facilities

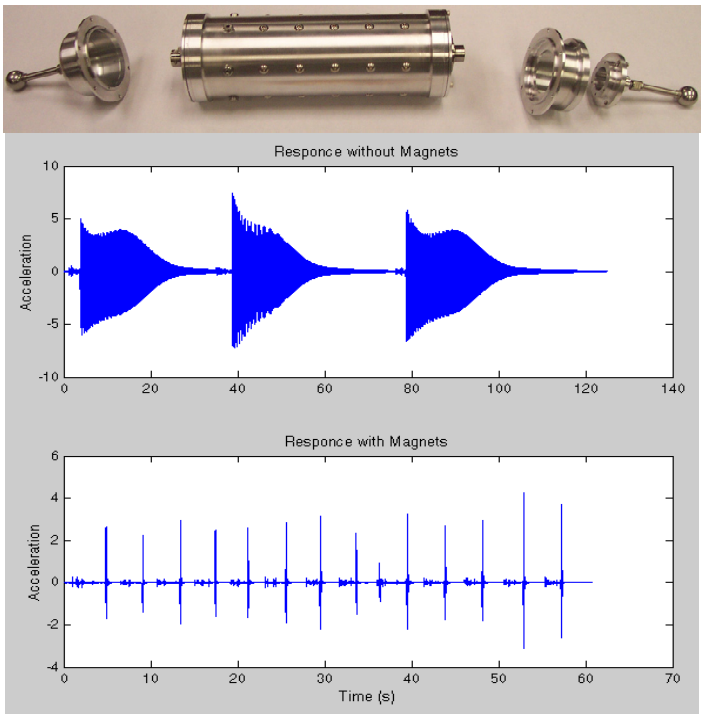

Tap Test: Top=3 hits w/ no damper, Bot.=14 hits w/ MagDamper (12% damping)

Figure 8.5.5.5-16. MagDamper with Measured Data

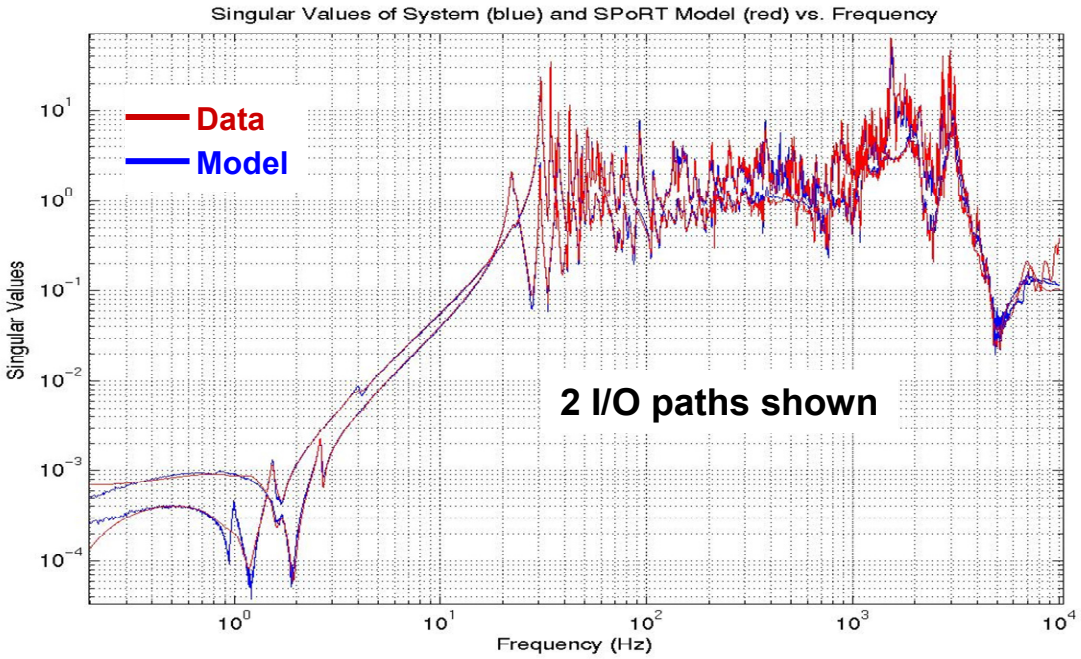

Figure 8.5.5-17. SysId Model vs. Test data (950th order model)

AIMS performance on the ACCESS Observatory

A controller was designed for the vibration control (VC) based around the 1st generation of ACCESS spacecraft (bus + payload) model. This model was not optimized and therefore the VC was not overly refined. A mesh wire-frame plot of the NASTRAN spacecraft model is shown in Figure 8.5.5-18.

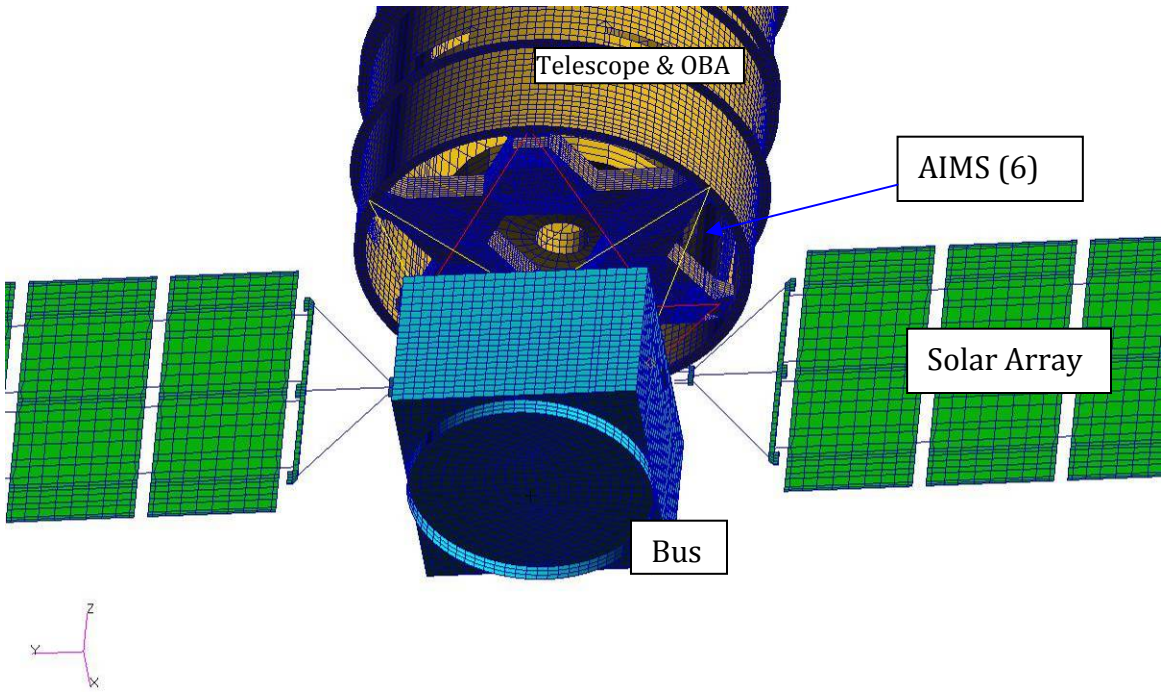

Figure 8.5.5-18. FEM Wire-frame Plot

Performance of the VC was verified and showed that the **0.5 nrads** of jitter, defined as LOS motion greater than 10 Hz, could be meet but only for a very small range of wheels speeds (RPMs) for the preliminary design shown in Figure 8.5.5-18. The degree of wheel speed restriction is not likely to be acceptable. Fortunately, just as this report was being written a new NASTRAN model of the telescope with updated representations and Outer Barrel Assembly (OBA) struts of the OTA Aft Metering structure, was integrated with a new NASTRAN model of the current baseline ACCESS bus design (which is hexagonal and considerably larger than the 1st bus design analyzed) and used to generate some additional results. It shows better open loop jitter performance than the previous system model, as seen in Figure 8.5.5-19. Part of this improved performance can be credited to the larger bus design enabling a more efficient interface between the OBA and the spacecraft in terms of strut mass and load path.

Unfortunately, this favorable pairing of bus + payload was not available for the subsequent analysis, but it is *important to keep in mind when reviewing the results that follow.*

The payload's response to wheel disturbances was modeled by bringing the NASTRAN model into Matlab in state-space form. Modal damping of 0.1% was assumed on all modes except the reaction wheels. This is the model that was used to analyze jitter from the wheels. Later, 5% modal damping was applied to all solar array modes below 2Hz; this model was used for the pointing control analysis (Note: results shown above are with lightly damped solar array modes). The AIMS vibration controller was then closed around the appropriate I/O of the plant state-space model. Open loop vs. Closed loop performance is shown of the same transfer function shown in Figure 8.5.5-19 (e.g., wheel to LOS) in Figure 8.5.5-20.

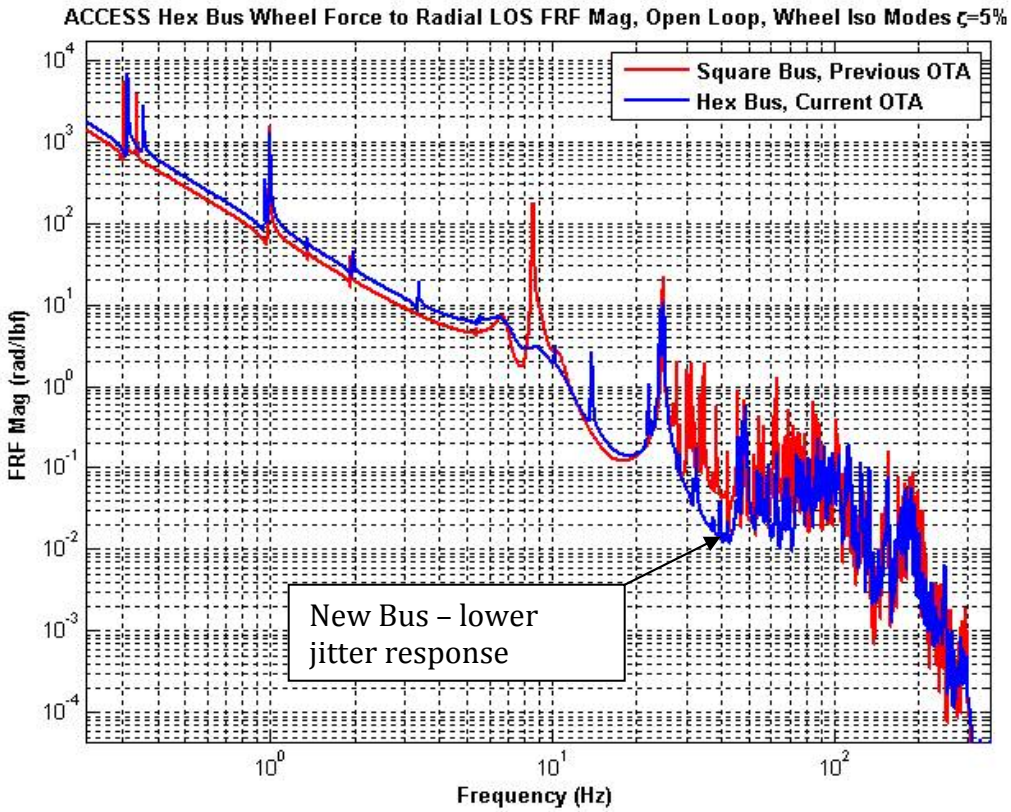

Figure 8.5.5-19. Frequency Response from Wheels to LOS, Old vs. New Bus

From the closed loop transfer function, it is clear that the 25Hz mode will be dominant in the jitter response. This frequency corresponds to a wheel speed of 1500 RPM. Subsequent efforts could optimize this mode for better controllability and/or localized control. Wheel disturbances were then analyzed over all wheels speeds and LOS results are shown in Figure 8.5.5-21.

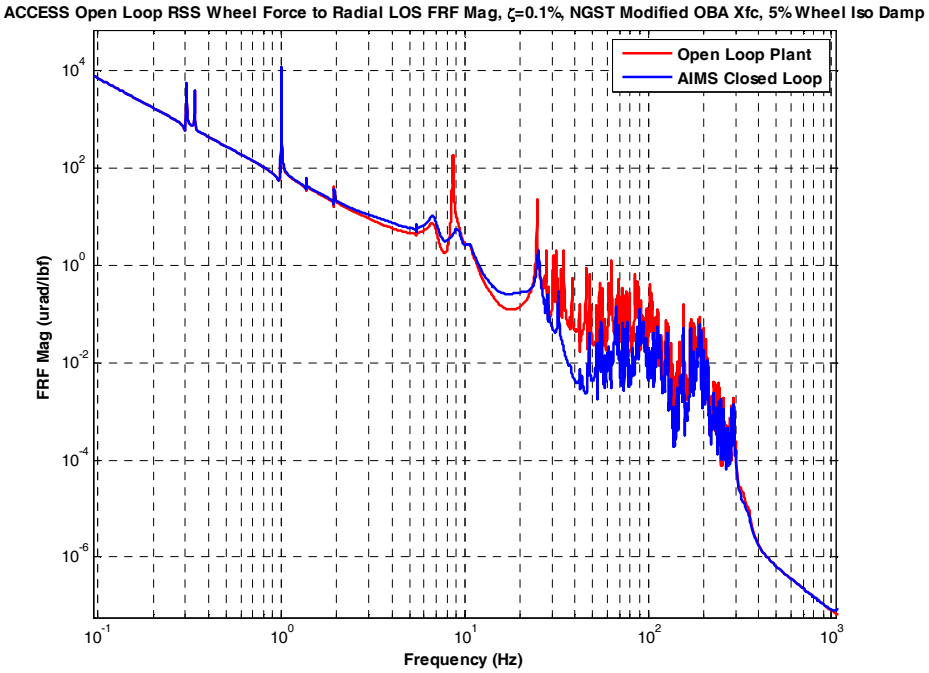

Figure 8.5.5-20. Frequency Response from Wheels to LOS, Open (red) vs. Closed Loop

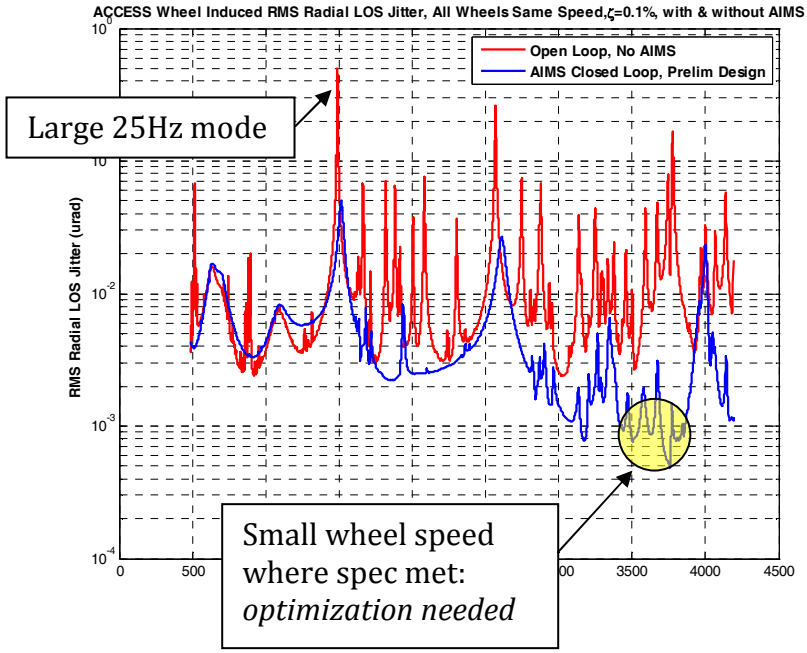

Figure 8.5.5-21. LOS vs. Wheel RPM, Open vs. Closed Loop

As seen in Figure 8.5.5-21, significant isolation doesn't start until approximately 30 Hz. A higher gain controller can be designed that will give better isolation, but for conservatism this lower gain controller was kept. That is, the peak loop gain of this controller is ~31 dB; for reference the loop gain used on the demo payload/bus system in the dynamics lab in Rochester NY is ~**55dB**. A **4X** performance increase over this baseline 31 dB spacecraft/controller design is achievable, and a 5X performance increase is not out of the question. The key will be to do the design as an integrated effort, with all components optimized to reduce jitter. It is likely that jitter will be one of the most difficult program-level specs to achieve.

An *estimated* jitter performance is depicted in Figure 8.5.5-22 into account 3 system design improvements:

1. Reduction of the wheel isolation frequency from 6 Hz to 3 Hz to yield approximately a 4× overall jitter reduction
2. Use of Proof-Mass Actuators (PMAs) to reduce key jitter producing components, like the SMA
3. Refinement of the AIMS controller in light of changes 1 and 2.

The green shaded box at the bottom of the graph in Figure 8.5.5-22 indicates at what reaction wheel frequencies the system meets the specification given the above assumptions. One can see that the allowable wheel speeds have increased significantly, but large keep out zones still exist. An integrated payload and control system design optimization performed at a future date should increase the allowable wheel speeds to greater than 90%.

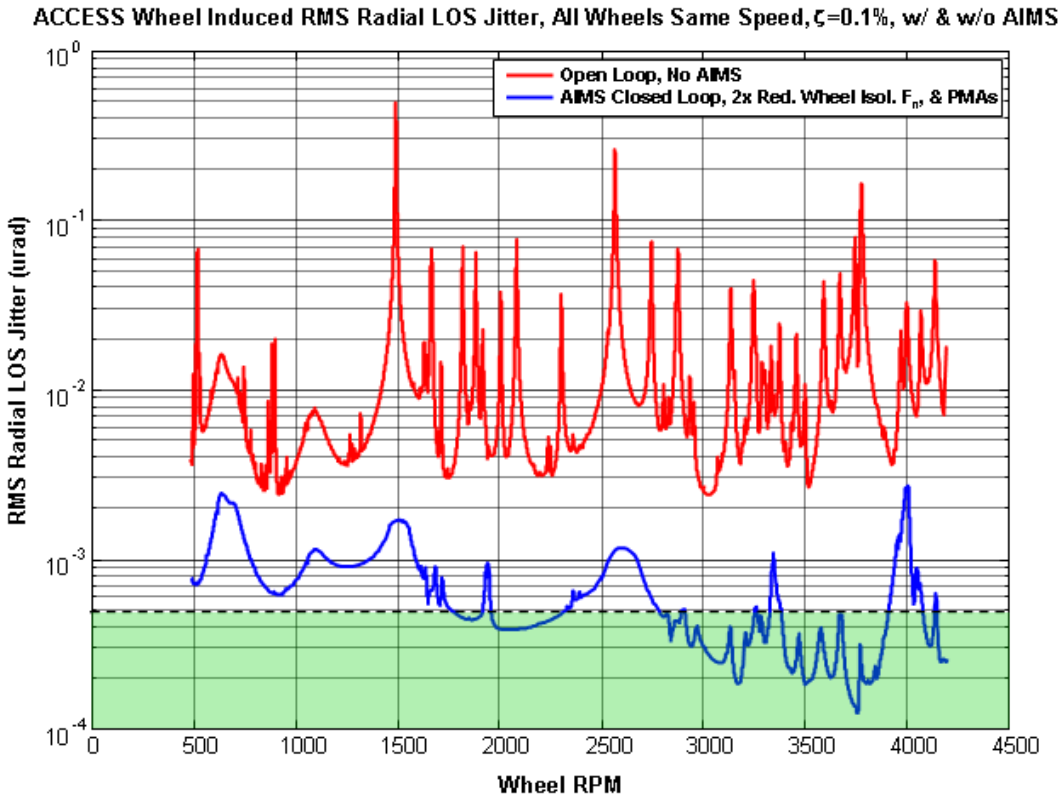

Figure 8.5.5-22. Wheel Jitter with Projected Improvements, *Excluding* System Optimization

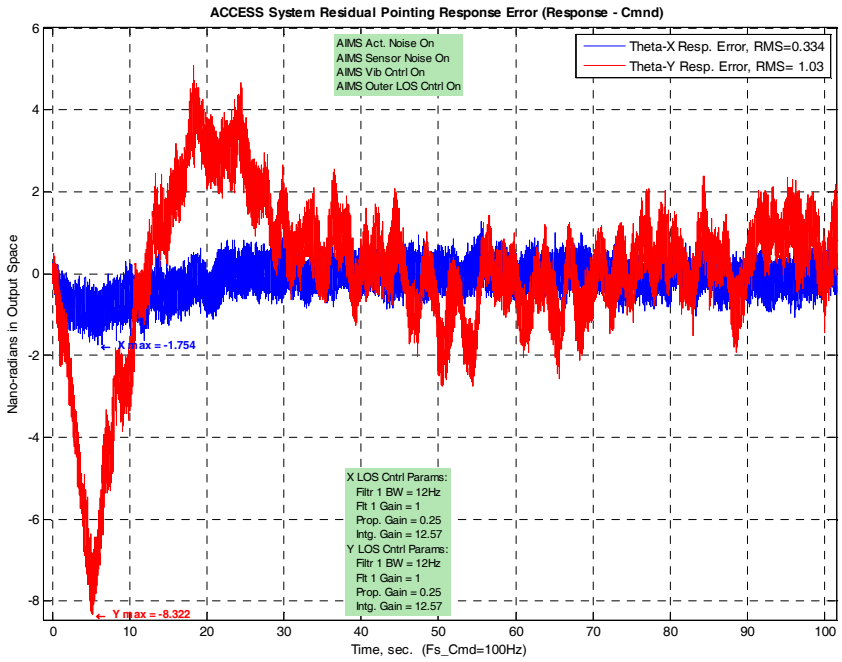

Figure 8.5.5-23. With minor design changes, the residual pointing error will meet the ACCESS 5 nano-rad requirement

ACCESS Pointing Control

Significant work was done on the ACCESS study to integrate the AIMS into the Pointing Control System (PCS) Architecture, The baseline controller with a peak loop gain of ~31dB was deemed usable as is for augmentation with pointing control The AIMS VC was augmented with the Pointing Command (PC) generation blocks provided by JPL. Numerous analyses were performed to understand the pointing errors, which culminated in the data shown in Figure 8.5.5-23.

Conclusions

Sufficient ACCESS specific analyses (which leverage techniques that have been correlated to a flight-like dynamics test bed) have been performed to demonstrate that a pointing control system that includes the AIMS and local damping treatments can be optimized to meet the ACCESS line-of-site and jitter requirements.

8.5.5.3.2 NG Active/Passive Spacecraft Isolator (APSI)

The 2nd hexapod option is Northrop Grumman's active/passive SC isolator (APSI). The APSI consists of a passive isolator stage consisting of six (6) springs arranged in a hexapod configuration to provide isolation in all 6 degrees of freedom. The 6 springs are attached to the TS struts at one end, and on the other to the SC upper platform/shear panel/central cylinder fittings. The passive isolation is achieved through stiffness of flexure spring and is easily tunable. The APSI struts have been sized in the integrated model to lead to isolation frequencies from 0.5 to 2 Hz. Damping is provided via VEM fitted around the spring. The passive isolator is a scaled version of the heritage Chandra wheel isolator described above. As such, the passive stage of APSI is considered to be of a high TRL maturity.

A long stroke version of the APSI has been demonstrated on the Control/Structure Interaction (CSI) testbed at NGAS (Figure 8.5.5-24). The APSI design is at least of TRL 5 maturity and a preliminary plan to bring its maturity to TRL 6 has been developed. A summary of long stroke isolator and plan to TRL 6 upgrade is shown.

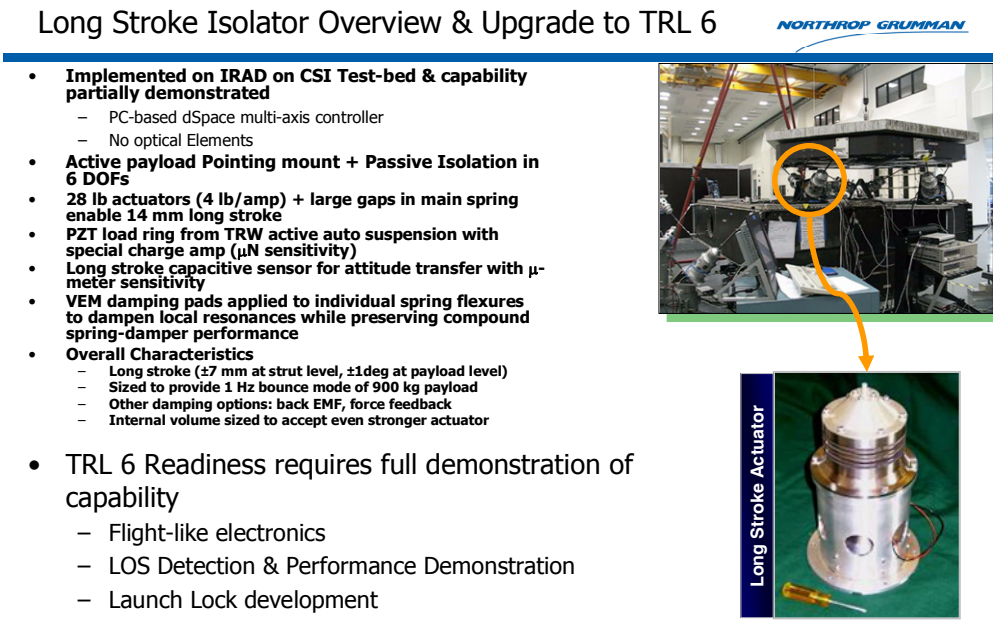

Figure 8.5.5-24. APSI Actuator overview

For launch, the struts will be locked to provide stiffness requirement for launch. Low shock, high-strength capability, commercial release devices will be used to provide the restraint needed for launch.

The passive struts are augmented with an active stage to provide the 50:1 attenuation of SC ACS pointing error required. A voice-coil is housed within each of the spring assemblies and is attached kinematically to the springs via upper and lower specially designed flexures. The voicecoils are commanded to adjust the struts based on FSM angles, providing a stable platform that minimizes FSM center movements to 1 mas.

Strut adjustment command is achieved using Independent Modal Space (IMS) Control to distribute commands to strut actuators using the fundamental isolation mode shapes. Because the fundamental isolator modes are easily measured, this scheme is very easy to implement and provides minimal risk. As such, this design is very advantageous as it is unnecessary to have knowledge of high frequency modes, and is insensitive to plant dynamics since the active part does not interact with higher TS modes. Actuator commands for LOS X and Y are decoupled with four orders of magnitude separation as seen in Figure 8.5.5-25.

The active isolator compensator offloads the FSM loop to maximize the range of travel for FSM. Controller synthesis is based on a high-fidelity continuous-time open loop FEM with 1330 modes. Continuous time controller employs a series of lead-lag compensators and a bending filter. The controller is a 2 × 2 transfer function with identical entries along the diagonal and zero entries elsewhere. With sampling time finalized the controller will be in discrete time domain with similar frequency characteristics including stability margins. The design is optimized for spacecraft induced disturbance rejection. Robustness metrics meet NGAS design-to goals of 10 dB gain margin and 30 deg phase margins. Margins were computed using unreduced plant with 2660 states. Similar margins are achieved for both control channels. Closed vs. open loop LOS transfer functions are shown below to exhibit significant attenuation below 1 Hz with active isolation.

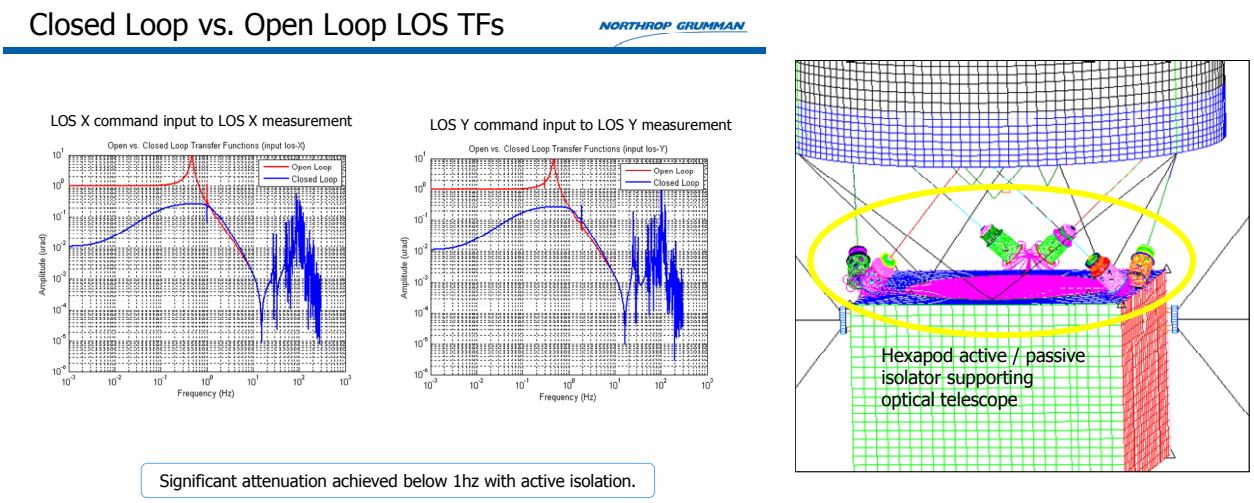

Figure 8.5.5-25. APSI Hexapod Pointing Closed Loop and Open Loop Transfer Functions (*left*), APSI FEM wire model (*right*)

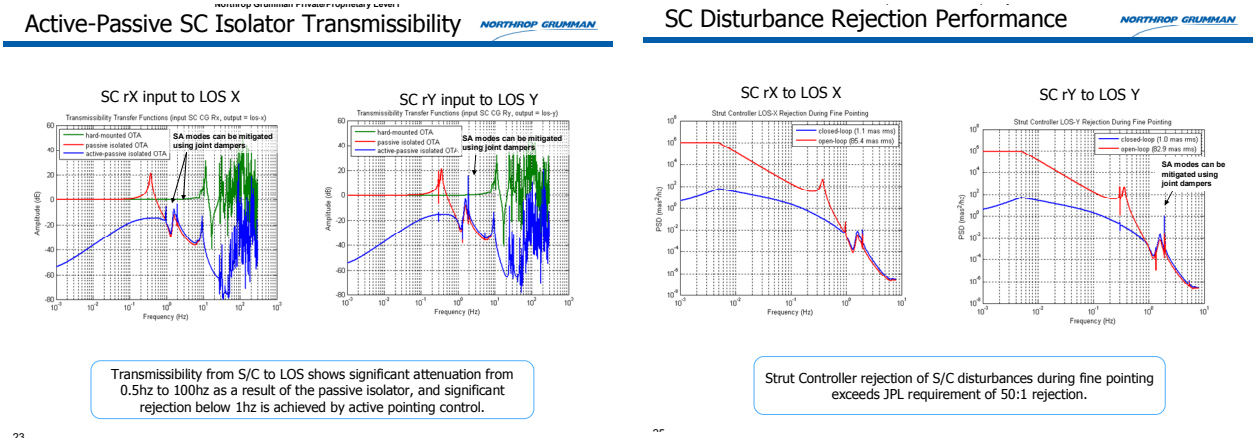

Figure 8.5.5-26. APSI Jitter Transmissibility (*left*) and APSI Disturbance Rejection Capability (*right*)

A detailed FEM of the CSI active/passive isolator has been included in the ACCESS integrated model to determine on-orbit performance. The model is test validated based on the CSI hardware measurements. An open loop model was generated for this purpose. Actuator commands decouple BW LOS and minimize coupling between LOS responses in the commanded and orthogonal directions. The generalized stiffness of the rocking modes was used to generate a 6×2 transformation matrix for strut control. The method generates unity gain at DC and 4 orders of magnitude of separation between LOS X and Y. A reduced open Loop Plant was then generated to expedite controller design and analysis run times. This was done using a Balanced Realization technique, truncating the least controllable/observable states. A stable controller design was achieved to provide the required SC disturbance rejection. The closed loop plant of the strut controller demonstrated gain controller margins and verified that strut controller rejection of SC disturbances exceeded the 50:1 rejection requirement, as is seen in Figure 8.5.5-26.

8.5.5.3.3 Telescope Pointing Trade Study

JPL performed an independent evaluation of both hexapod options. This evaluation consisted in assessing the closed loop performance for each hexapod. In this process, JPL tuned the controller designs for each option to optimize the performance. For this study, the ACS model described in Section 8.5.5.2.2 was used.

From the vibration isolation capability point of view, the APSI has better performance than AIMS. However, because of the availability of a dual stage Reaction Wheel Isolator that could reduce the jitter substantially, the pointing performance was seen as the key metric. Based on the improved pointing performance of AIMS, the AIMS was chosen to be the primary option and the APSI to be the secondary option. However, it is recommend to carry both options further since the pointing challenges could vary and both designs are very capable and have their own advantages.

8.5.5.3.4 Telescope Pointing Struts Trade Study Matrix

8.5.5.4 Coronagraph Pointing System

The coronagraph pointing system includes the fine guidance camera, the fine steering mirror (FSM) and the fine pointing algorithms that command all three stages of pointing control (ACS, hexapod, and FSM). The architecture of this design was described in Section 8.5.3. This coronagraph pointing system runs at 100 Hz. The fine guidance camera generates measurements of the line-of-sight tip and tilt errors with respect to the star. This measurement is used to control the FSM and the Hexapod. An advanced control law allows to offload the FSM to the hexapod smoothly and effectively [4]. Basically the FSM loop has a high bandwidth compensator that responds quickly to pointing errors, and the hexapod has a mid bandwidth compensator that responds slower and offloads the FSM.

In turn, the hexapod is offloaded to the spacecraft ACS by generating a highly accuracy offset angle derived from the hexapod pointing angles. Assuming the hexapod is tracking the guide star with a precision of 1 mas (1σ) means that the hexapod pointing angles are the opposite of the spacecraft pointing error to the tracking performance level 1 mas (1σ). A measurement of the hexapod pointing angles derived from measurements of the lengths of the hexapod struts is used to generate the offset pointing command for the ACS. The hexapod has a closed loop bandwidth of about 5 Hz which allows it to reject ACS errors with frequencies bellow 0.5 Hz. In addition the FSM has a closed loop bandwidth of 15 Hz, which allows it to correct for some residual errors at the hexapod stage. The performance is illustrated via closed loop simulation for tracking of a magnitude 7 star. Figure 8.5.5-27 shows the ACS pointing error. Figure 8.5.5-28 shows the hexapod struts angle in the sky commands. Note that they are the opposite of the pointing errors as expected in the tracking case. Figure 8.5.5-29 shows the telescope LOS pointing error, which is the residual error after the ACS and Hexapod control stages. Figure 8.5.5-30 shows the FSM angle in the sky commands. Here also they are the opposite of the telescope pointing errors as expected. Figure 8.5.5-31 the coronagraph pointing error. Figure 8.5.5-32 shows the fine guidance camera measurement of the coronagraph pointing error.

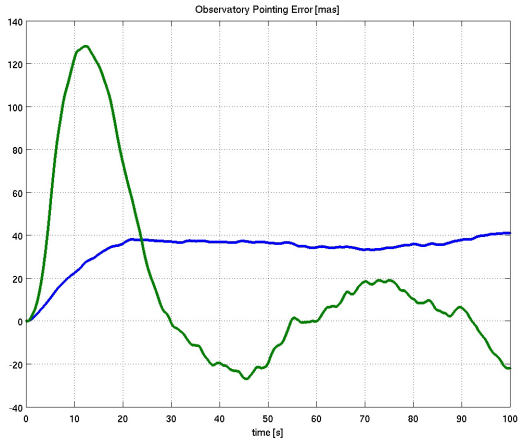

Figure 8.5.5-27. ACS Line-of-sight (LOS) Pointing Error

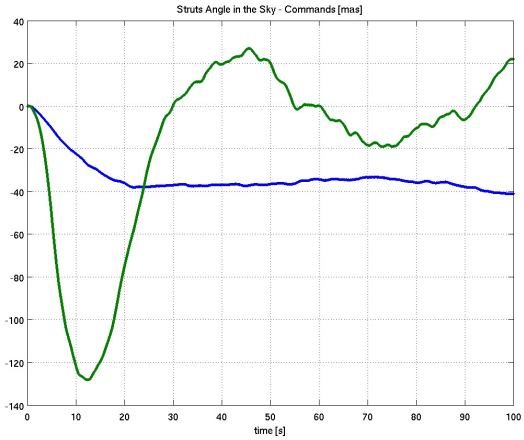

Figure 8.5.5-28. Telescope Pointing System (hexapod) LOS pointing commands.

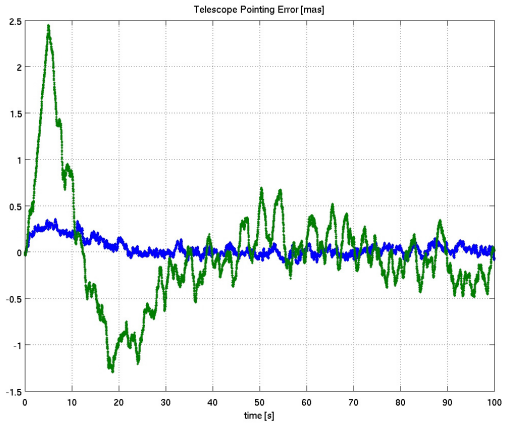

Figure 8.5.5-29. Telescope Pointing System (hexapod) LOS pointing errors.

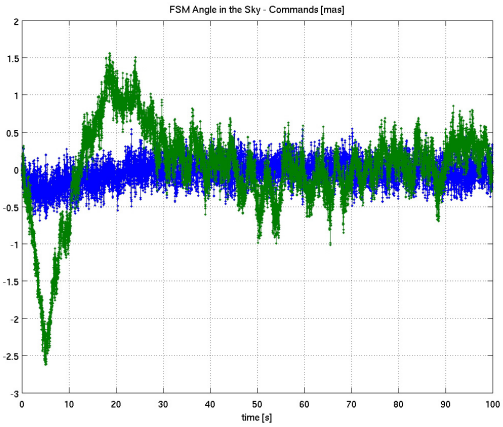

Figure 8.5.5-30. Coronagraph Pointing System (Fine Steering Mirror) LOS pointing commands.

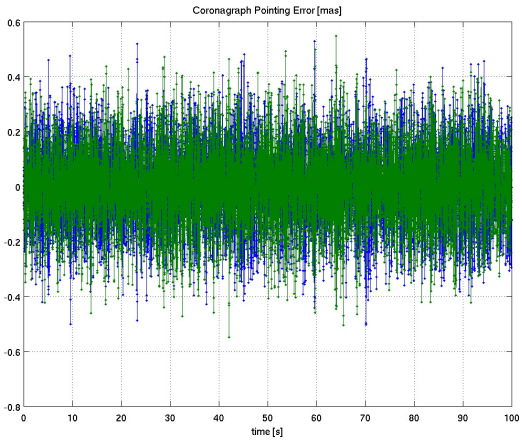

Figure 8.5.5-31. Coronagraph Pointing System (FSM) LOS pointing errors.

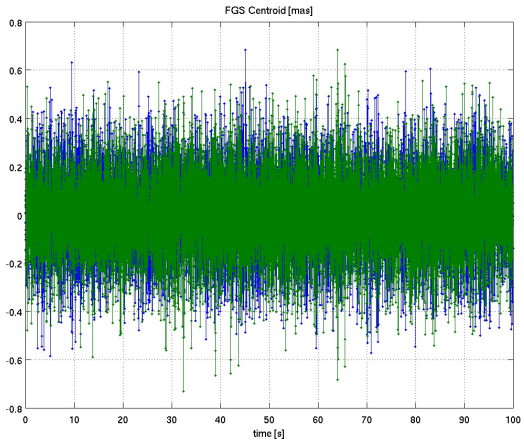

Figure 8.5.5-32. Fine Guidance Camera Centroid Measurements.

8.5.6 Operational Concepts

8.5.6.1 Pointing Acquisition

The ACCESS PCS employs three steps to achieve the high level of fine pointing performance required to center and maintain the target star on the occulting mask, which is similar to the approach proposed in [1]. This process is depicted in Figure 8.5.6-1. The observatory stability requirement (1.5 arcseconds over 100 seconds), ensures a stable enough environment for successful handoffs between these 3 steps.

The **first step** in fine pointing acquisition uses the SC ACS to point the telescope line-of-sight within 30 arcsec (3s) of the target star. The **second step** performs a step-and-stare mosaic search moving the observatory using the SC ACS (Eclipse 2006). The search region for the target star corresponds to uncertainty in the previous step, which corresponds to a 60 × 60 arcsec region. Since the FGC FOV is 35.8 × 35.8 arcsec, searching a 60 × 60 arcsec region requires a 2 × 2 mosaic allowing for a 5.8 arcsec of overlap. During the search, the hexapod and FSM are held at their reference known position with respect to the observatory. Once the star is found the SC ACS, hexapod and FSM control loops are controlled to their reference positions. In the **third step**, the FGC is transition to the 10 × 10 pixels tracking window mode and the software engages the high frequency hexapod and FSM control loops, and the generation of the offset pointing signal for the SC Attitude Estimator. This process is expected to take less than 5 minutes. A similar concept has been proposed for SIM-Planetquest [5].

8.5.6.2 Pointing Calibration

Calibration of alignments between the different pointing stages and the science instrument is necessary to achieve the desired performance. An Instrument Pointing Frame filter will be used to estimate the alignments at the beginning of the mission and mid-mission if necessary. Initially it will run during the In-orbit checkout phase [6]. Additionally a star centering calibration algorithm will be run to estimate the misalignment between the FGC predicted occultor center with respect to the actual center as seen in the science images. This filter will be run at the frequency needed to maintain the desired alignment within spec.

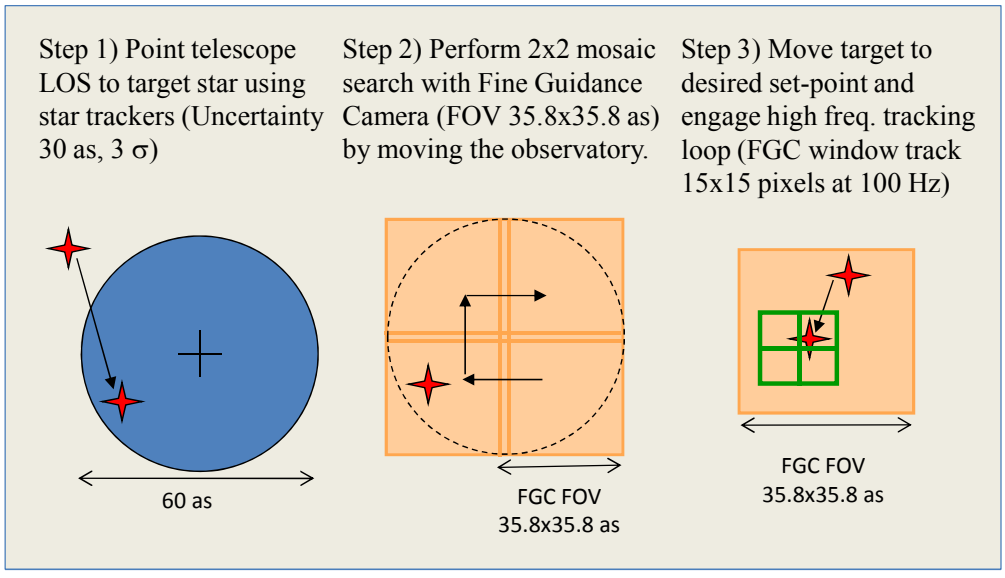

Figure 8.5.6-1. ACCESS pointing acquisition and stabilization strategy ensures placement of the star image on the occulting mask.

8.5.7 Discussion and Conclusion

The objective behind this Pointing Control System design has been to propose the best pointing system for a mid-class space coronagraphic observatory with nearly available technology (TRL 6 or above). This study began by setting up a set of pointing goals for the two key science driven pointing requirements: the telescope line-of-sight stability and the star centering on the occulting mask. These goals were set to enable science observations with high contrast at $2\lambda/D$ inner-working-angles. The pointing goals were set to 1 mas (3 sigma) for the telescope line-of-sight stability over 1000s and 0.1 mas (3 sigma) for the star centering on the occulting mask stability over 1000s.

These requirements in conjunction with the design principle to have healthy engineering margins led to include a three stage pointing actuation system; a fine guidance camera design within the coronagraphic instrument; and an extensive disturbance rejection strategy to minimize the environmental jitter.

The three-stage pointing actuation system starts with a standard 3-axis stabilized spacecraft bus and it is augmented with a hexapod telescope pointing system and a fine steering mirror. The addition of the hexapod enables pointing the telescope with a pointing stability ten times better than Hubble but with a spacecraft bus that is ten times less capable than Hubble. Hubble to date has achieved the finest pointing of all NASA space observatories. It has demonstrated a 10 mas (3 sigma) pointing capability. The pointing requirement set for the ACCESS ACS subsystem is 100 mas (3 sigma), which is consistent with mid-class space observatories (Kepler, Spitzer). The second stage is a Telescope Pointing System, the hexapod, allows to reach the 1 mas stability requirement. The third stage is the fine steering mirror, which allows for additional pointing capability within the coronagraphic instrument to center the star on the occulting mask to the 0.1 mas level. If the telescope pointing stability requirement were to be reduced to 10 mas (3 sigma) it could enable to simplify the design by eliminating the Telescope Pointing Control system but will require to optimize the ACS design to achieve Hubble class pointing performance.

For fine guidance sensing we take advantage that coronagraphic observations typically have a bright star in the center of their field of view. We have studied three different concepts for a fine guidance camera that guides from this bright star. This trade study indicated that a Fine Guidance Camera can achieve a pointing knowledge of 0.45 mas (3 sigma) at a sampling rate of 100 Hz for a star magnitude 7 or brighter. Therefore, the pointing requirement for the star centering was relaxed to this value.

The strategy towards disturbances has been to minimize the jitter at the source. We have selected a quiet orbital environment (L2), designed a thermally controlled telescope and instrument, planned operational constraints during science observations (limitations on reaction wheel speeds, non operation of solar array drives and high gain antenna gimbals), and added reaction wheel isolators, solar array dampers and a vibration suppression capability within the hexapod.

Two options for the Telescope Pointing System have been studied, the ITT AIMS system and NG APSI system.

A detail modeling and analysis effort has been performed to evaluate the feasibility and demonstrate the performance of this design. The modeling effort included dynamic models of the structure, optics and models for the spacecraft ACS system, the hexapod pointing systems, the FSM and the fine guidance camera/centroiding. The analysis effort included evaluation of the ACS pointing performance, a trade study between the two telescope pointing system that evaluated the jitter and pointing performance capabilities, and a coronagraph pointing system study that analyzed the multi-stage architecture. The telescope pointing system trade study led to the selection of the ITT AIMS system as the primary option for its improved pointing performance. However, NG APSI had better vibration isolation capabilities. The pointing performance was viewed as the key

metric since the vibration isolation requirement on the hexapod could be greatly relaxed by the addition of a dual stage reaction wheel isolator.

The results of this study indicate that additional performance could be gained by:

- Using dual stage reaction wheel isolators.
- Rigidly attaching solar array panels to the telescope body (like in the Spitzer Space Telescope and Kepler) to mitigate Solar Array flexibility interaction with control loops.
- Optimizing the structure to minimize control structure interactions and maximize controllability and vibration suppression.
- Adding magnetic dampers and/or proof mass actuators for local damping.

An important aspect of this mission is its "graceful degradation" to pointing errors. Because the pointing requirements are directly driven from the science instrument occulting mask inner-working-angle, and by this instrument carrying a filter wheel of candidate occulting masks with different inner-working-angles, this mission maintains a reduced science return capability under certain pointing system failures or degraded performance. For example, an 8^{th} order Lyot mask with a $4\lambda/D$ inner-working-angle [1] relaxes the pointing requirements by nearly two orders of magnitude providing robustness against failures or degraded performance on the telescope or coronagraph pointing elements.

In conclusion, we propose a robust high precision Pointing Control System for the ACCESS Mission concept. A design based on nearly available technologies (TRL >6) with limited complexity.

8.5.8 References for Section 8.5

[1] Brugarolas, P. B., Kia, T., Li, D., and Alexander, J. W. 2006. "Pointing control system for the Eclipse mission," in Space Telescopes and Instrumentation I: Optical, Infrared, and Millimeter. Edited by Mather, J. C., MacEwen, H. A., and de Graauw, M. *Proceedings of the SPIE* 6265: 62653R.

[2] Mayo, R. A., Spector, V. A., and Lillie, C. F. 2003. "Pointing and jitter control for the Eclipse mission," in Future EUV/UV and Visible Space Astrophysics Missions and Instrumentation. Edited by Blades, J. C., and Siegmund, O. *Proceedings of the SPIE* 4854: 544–553.

[3] Guyon, O., Matsuo, T., and Angel, R. 2009. "Coronagraphic Low Order Wavefront Sensor: Principle and Application to a Phase-Induced Amplitude Coronagraph," *The Astophysical Journal* 693(1): 75–84.

[4] Lurie, B. J., and Enright, P. J. 2000. *Classical Feedback Control with MATLAB*. Marcel Dekker, NY.

[5] Brugarolas, P. B., and Kang, B. H. 2006. "Instrument pointing control system for the Stellar Interferometry Mission: Planet Quest," in Advances in Stellar Interferometry. Edited by Monnier, J. D., Schiller, M., Danchi, W. C. *Proceedings of the SPIE* 6268: 626825.

[6] Bayard, D. S., Kang, B. H., Brugarolas, P. B., and Boussalis, D. 2004. "An integrated optimal estimation approach to Spitzer Space Telescope focal plane survey," in Optical, Infrared, and Millimeter Space Telescopes. Edited by Mather, J. C. *Proceedings of the SPIE* 5487: 146–157.

This page is intentionally left blank.

8.6 Coronagraph Optical Design

Prepared by:

Robert Gappinger and Olivia Dawson
(Jet Propulsion Laboratory)

8.6.1 Introduction

This study reviewed four potential coronagraphic types (Lyot, Vector Vortex, Shaped Pupil, and Pupil Mapping), each with a unique optical prescription and layout. All four layouts were modeled using the same telescope. Figure 8.6.1-1 shows the orientation of the coronagraph instrument layout behind the basic telescope configuration. One of our primary design criteria was to make the layouts as similar as possible in order to employ a level playing field for performance and cost comparison. The following sections provide descriptions and graphics for each layout.

The basic telescope design is a Gregorian telescope with a concave parabolic primary mirror, a convex elliptical secondary mirror and a concave parabolic tertiary mirror. The coronagraph instrument optics follow the tertiary mirror in all four layouts, as seen in Figure 8.6.1-1. Common to all layouts is a pair of deformable mirrors, including a fast steering mirror (FSM) mechanism. In addition, a fine guidance camera is used as feedback to the FSM. The coronagraph designs are optimized for shorter wavelengths and beamsplitters are employed to split the light into three wavebands (Figure 8.6.1-2).

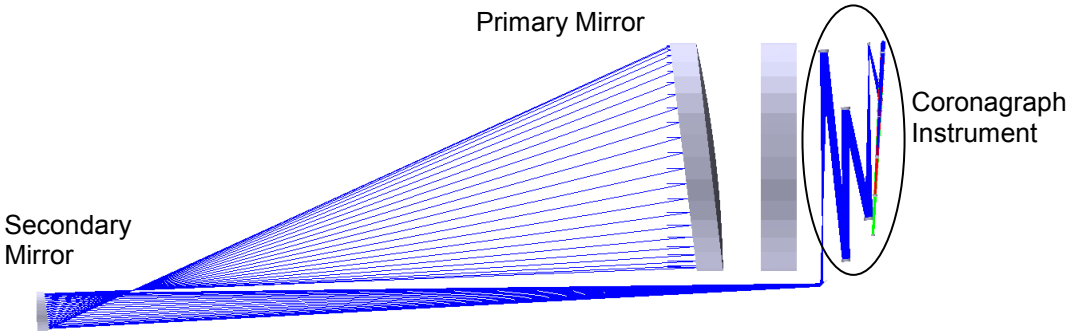

Figure 8.6.1-1. Gregorian telescope layout with coronagraph instrument behind

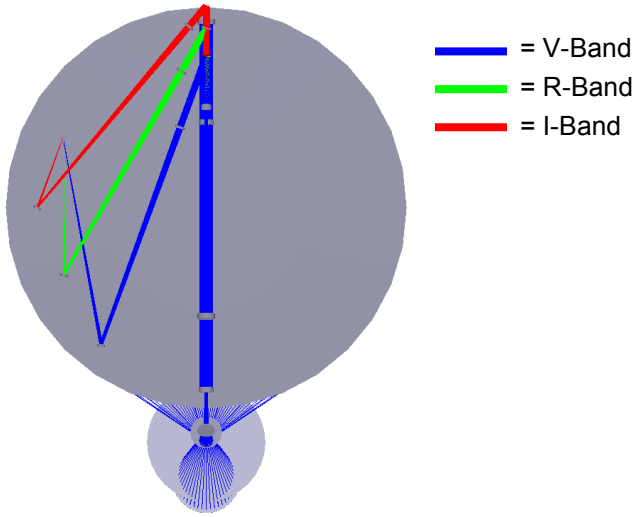

Figure 8.6.1-2. Rotated view to show possible paths for various wavebands

8.6.2 Lyot Layout

The band limited Lyot coronagraph uses a single occulting mask (OC-LY) and three Lyot masks (LM05-LY, LM10-LY, LM15-LY). All three wavebands are focused onto a single science camera focal plane. The final fold mirror in each waveband path can be used to shift the light onto a spectrometer, as shown in Figure 8.6.2-1.

8.6.3 Vector Vortex Layout

The Vector Vortex coronagraph uses a single occulting mask (OC-VV) and three Lyot masks (LM05-VV, LM10-VV, LM15-VV). All three wavebands are focused onto a single science camera focal plane. The final fold mirror in each waveband path can be used to shift the light onto a spectrometer, as shown in Figure 8.6.3-1.

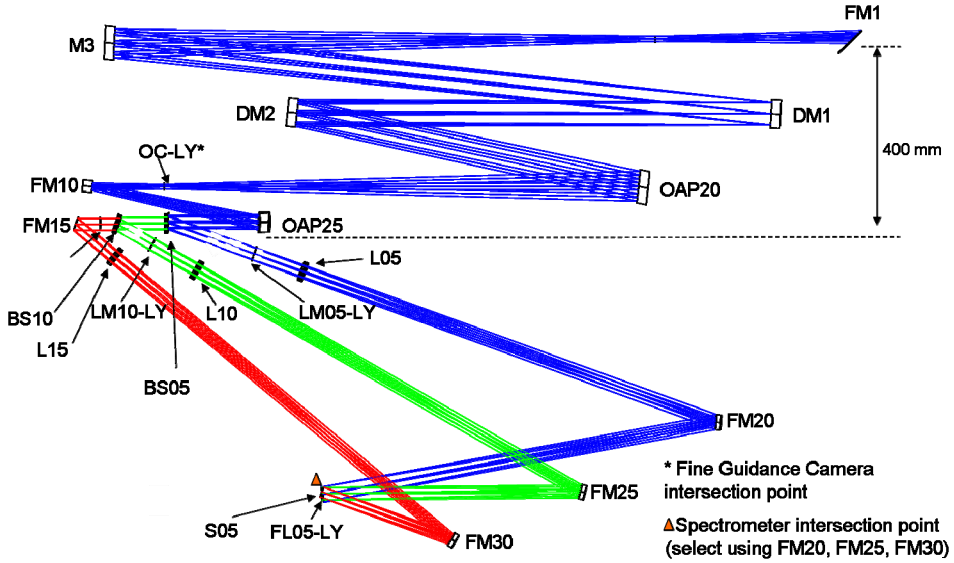

Figure 8.6.2-1. Band limited Lyot coronagraph instrument layout

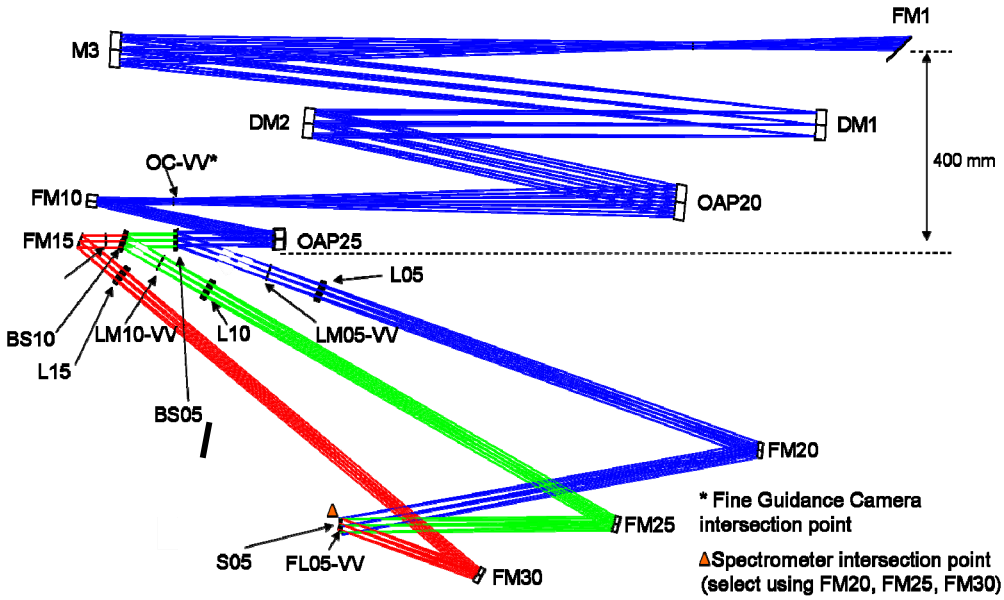

Figure 8.6.3-1. Vector Vortex coronagraph instrument layout

8.6.4 Shaped Pupil Layout

The Shaped Pupil coronagraph uses a single shaped pupil mask prior to a single occulting mask (OC-SP). All three wavebands are focused onto a single science camera focal plane. The final fold mirror in each waveband path can be used to shift the light onto a spectrometer, as shown in Figure 8.6.4-1.

8.6.5 Pupil Mapping Layout

The Pupil Mapping coronagraph uses a set of two PIAA mirrors (PIAA1, PIAA2), followed by an apodizing mask (APM) and an occulting mask (OC-PM). These are followed by two reverse PIAA optics (PIAA3, PIAA4) before the wavebands are split. All three wavebands are focused onto a single science camera focal plane. The final fold mirror in each waveband path can be used to shift the light onto a spectrometer, as shown in Figure 8.6.5-1.

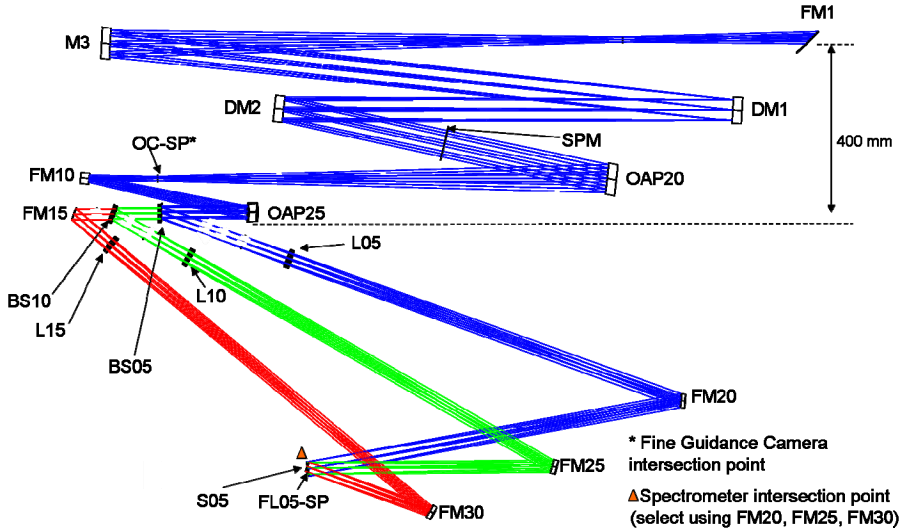

Figure 8.6.4-1. Shaped Pupil coronagraph instrument layout

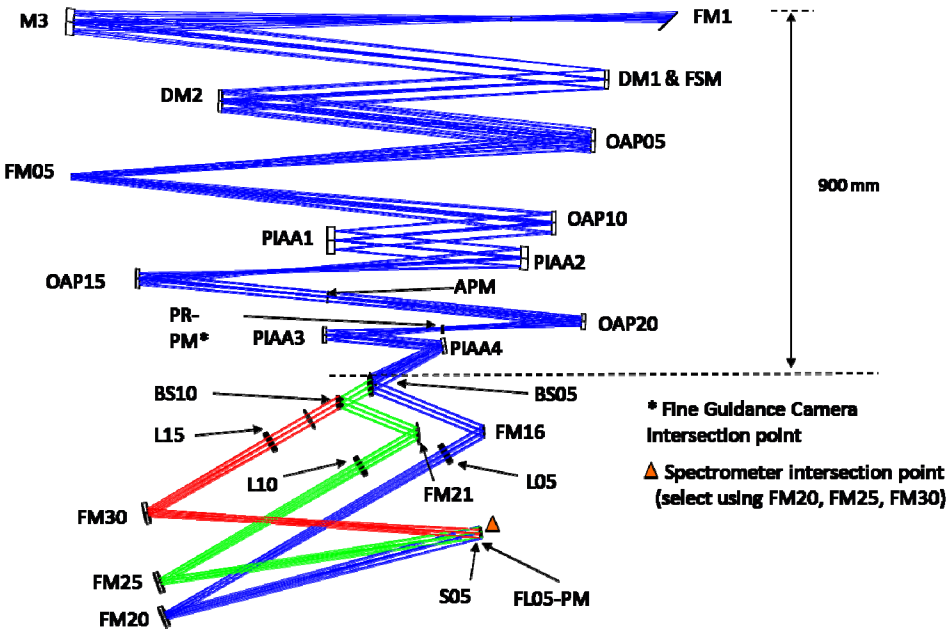

Figure 8.6.5-1. Pupil Mapping coronagraph instrument layout

8.6.6 Fine Guidance Camera Layout

The fast steering mirror (FSM) is controlled by detecting star motion on a fine guidance camera. Light from a partially reflecting surface in the coronagraph instrument beamtrain is focused by a lens onto the camera. For the Lyot, Vector Vortex, and Shaped Pupil versions, the partially reflecting surface is the occulting mask. In the case of the Pupil Mapping layout, the partial reflector is located near the focus preceding the PIAA mirrors, as shown in Figure 8.6.6-1.

8.6.7 Spectrograph

For more detailed spectral studies, a spectrograph has been designed for use with all four coronagraph layouts. The spectrograph is a simple Offner design using a concave spherical mirror to direct light to a convex spherical mirror with a diffraction grating. The diffracted light is then focused by the first concave spherical mirror onto a detector. The spectrograph as shown in Figure 8.6.7-1 has a resolution of 20.

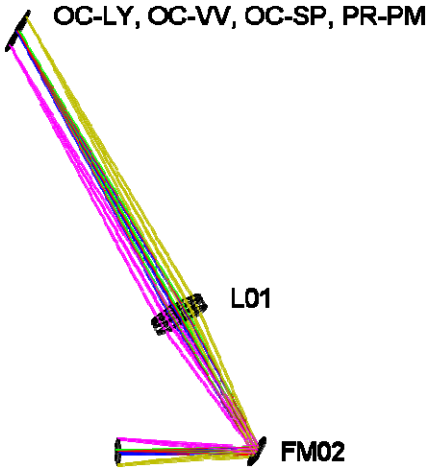

Figure 8.6.6-1. Fine guidance camera layout. Partial reflecting mirror locations can be found in preceding figures for each coronagraph layout.

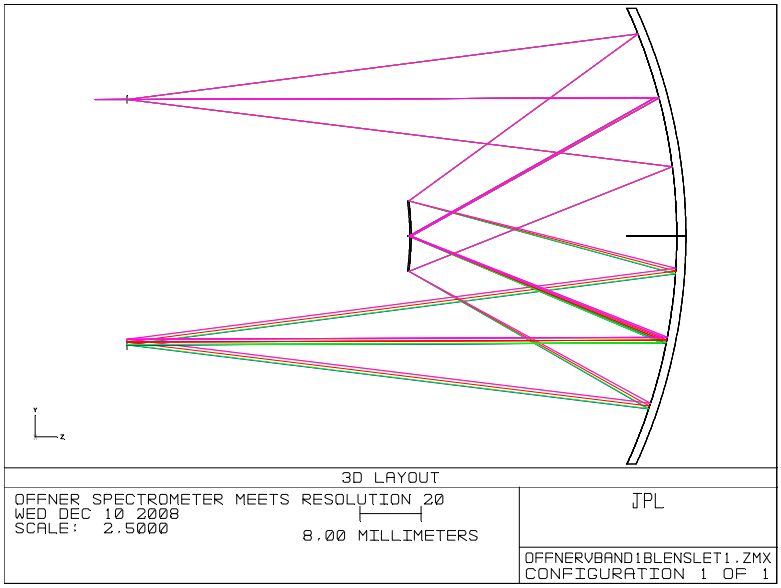

Figure 8.6.7-1. Offner design spectrograph

8.6.8 Layout Nomenclature

The following tables explain the labeling seen in the layout figures found in the preceding sections. Table 8.6.8-1 explains the basic labeling philosophy. Table 8.6.8-2 is a listing of all optical elements found in the layouts. Some components are identical across several or all layouts, while some components are unique to a given layout.

Table 8.6.8-1. Explanation of nomenclature

	Labeling scheme	Examples
1	Elements of the telescope follow the long established tradition of naming	M1, M2, M3
2	elements identical in more than one coronagraph option have the same name in each option	M1, FM15
3	elements unique to an option carry a suffix for that option	OC-LY, OC-SP, L20-LY
4	suffixes for the coronagraph options LY = lyot SP = shaped pupil VV = vector vortex PM = pupil mapping	
5	elements of a type are numbered consecutively as they appear in the beam train - some numbers are assigned by 5's so all elements do not have to be renumbered if another element is added in between existing elements	DM1, DM2 FM05, FM10, FM15 . . .
6	elements that are one of several of their type that can be inserted by moving a mechanism carry a subscript	$OC\text{-}LY_1$, $OC\text{-}LY_2$ . . .

Table 8.6.8-2. List of components in coronagraph optical layouts

Lyot	Vector Vortex	Shaped Pupil	Pupil Mapping	Label	Description	Mechanisms
x	x	x	x	M1	Primary mirror	
x	x	x	x	M2	Secondary mirror	
x	x	x	x	FM1	Fold mirror between M2 and M3	
x	x	x	x	M3	Tertiary mirror	
x	x	x	x	DM1	deformable mirror	Fast-steering mechanism
x	x	x	x	DM2	deformable mirror	
		x		SPM	shaped pupil masks (4)	linear positioner
			x	OAP05	off-axis paraboloid mirror	
			x	PR-PM	Partial reflecting mirror for fine guidance camera	
			x	FM05	fold mirror, science beam	
			x	OAP10	off-axis paraboloid mirror	
			x	PIAA1	first phase-induced amplitude apodization mirror	
			x	PIAA2	second phase-induced amplitude apodization mirror	
			x	OAP15	off-axis paraboloid mirror	
			x	APM	apodizer masks (4)	2-axis nanopositioner
x	x	x	x	OAP20	off-axis paraboloid mirror	
x				OC-LY	LY occulters (~10)	linear positioner
	x			OC-VV	VV occulters (~10)	linear positioner
		x		OC-SP	SP occulters (~10)	linear positioner
x	x	x	x	L01	lens for fine guidance cameras	
x	x	x	x	FM02	fold mirror for fine guidance cameras	2-position selector with 2-axis nanopositioning
			x	OC-PM	PM occulters (~10)	linear nanopositioner
x	x	x	x	FM10	fold mirror	
			x	PIAA3	first reverse phase-induced amplitude apodization mirror	
			x	PIAA4	second reverse phase-induced amplitude apodization mirror	
x	x	x		OAP25	off-axis paraboloid mirror	
x	x	x	x	BS05	V-band, beamsplitter	
x				LM05-LY	V-band, LY Lyot masks (4)	linear positioner
	x			LM05-VV	V-band, VV Lyot masks (4)	linear positioner
			x	FM16	V-band, fold mirror before lens	
x	x	x	x	L05	V-band, focusing lens onto science detector	
x	x	x	x	FM20	V-band, fold mirror onto science detector	3-position selector
x	x	x	x	BS10	R-band, beamsplitter	
x				LM10-LY	R-band, LY Lyot masks (4)	linear positioner
	x			LM10-VV	R-band, VV Lyot masks (4)	linear positioner
			x	FM21	R-band, fold mirror before lens	
x	x	x	x	L10	R-band, focusing lens onto science detector	
x	x	x	x	FM25	R-band, fold mirror onto science detector	3-position selector
x	x	x		FM15	fold mirror	
x				LM15-LY	I-band, LY Lyot masks (4)	linear positioner
	x			LM15-VV	I-band, VV Lyot masks (4)	linear positioner
x	x	x	x	L15	I-band, focusing lens onto science detector	
x	x	x	x	FM30	I-band, fold mirror onto science detector	3-position selector
x				FL05-LY	LY diagnostic lenses & filters (~4)	linear positioner
	x			FL05-VV	VV diagnostic lenses & filters (~4)	linear positioner
		x		FL05-SP	SP diagnostic lenses & filters (~4)	linear positioner
			x	FL05-PM	PM diagnostic lenses & filters (~4)	linear positioner
x	x	x	x	S05	shutter - science detector	shutter mechanism
x	x	x	x	SPEC	spectrograph	
27	27	25	34		Total optical elements in layout	

8.6.9 Beamwalk Sensitivities

This optical design was used to calculate beam spot movement at the Occulting Mask due to movement of other optical elements. Table 8.6.9-1 lists the resulting beamwalk sensitivity for potential tilts and translations of the mirrors preceding the Occulter in the Lyot Layout.

Table 8.6.9-1. Beam walk at Occulter due to tilt or translation of various optical components

Beam walk and exit pupil wavefront sensitivities for ACCESS telescope V-band.
For each case, the FSM/DM is tilted to recenter chief ray on occulter.

	Telescope Body Tilt about x 2 urad		PM tilt about x 1 urad		PM tilt about y 1 urad		PM shift along x 10 um		PM shift along y 10 um		PM shift along z 10 um		SM tilt about x 10 urad		SM tilt about y 10 urad		SM shift along x 10 um		SM shift along y 10 um		SM shift along z 10 um	
	x	y	x	y	x	y	x	y	x	y	x	y	x	y	x	y	x	y	x	y	x	y
FSM Tilt (urad)	-31.503	0.000	-31.678	0.000	0.000	-31.381	0.000	41.015	-39.759	0.000	9.557	0.000	-49.986	0.000	0.000	-49.498	0.000	-45.413	44.192	0.000	8.936	0.000
Beam Walk (mm)																						
Secondary Mirror	0.00000	0.00887	0.00000	0.00895	-0.00885	0.00000	0.01158	0.00000	0.00000	0.01127	0.00000	-0.00233	0.00000	0.00008	0.00010	0.00000	-0.01000	0.00000	0.00000	-0.00970	0.00000	0.00224
Fold 1	0.00000	-0.09509	0.00000	-0.09573	0.06534	0.00000	-0.08542	0.00000	0.00000	-0.12002	0.00000	0.02889	0.00000	-0.15237	0.10412	0.00000	0.09553	0.00000	0.00000	0.13464	0.00000	-0.02806
Tertiary Mirror	0.00000	-0.08818	0.00000	-0.08878	0.08758	0.00000	-0.11449	0.00000	0.00000	-0.11133	0.00000	0.02668	0.00000	-0.13704	0.13533	0.00000	0.12417	0.00000	0.00000	0.12101	0.00000	-0.02583
DM1 / FSM	0.00000	0.00000	0.00000	0.00000	0.00001	0.00000	-0.00001	0.00000	0.00000	-0.00001	0.00000	-0.00007	0.00000	0.00285	-0.00280	0.00000	-0.00257	0.00000	0.00000	-0.00257	0.00000	0.00013
DM2	0.00000	0.00000	0.00000	0.00008	0.00001	0.00000	-0.00001	0.00000	0.00000	0.00000	0.00000	-0.00007	0.00000	0.00285	-0.00278	0.00000	-0.00256	0.00000	0.00000	-0.00249	0.00000	0.00013
Occulter OAP	0.00000	0.00000	0.00000	0.00013	0.00001	0.00000	-0.00001	0.00000	0.00000	0.00001	0.00000	-0.00007	0.00000	0.00282	-0.00277	0.00000	-0.00255	0.00000	0.00000	-0.00241	0.00000	0.00012
Wavefront Error (Zernike Standard coefficients in rms waves at 550 nm)																						
Z 1 1	-0.000739		-0.000575		-0.000745		-0.000746		0.039171		0.165851		0.000621		-0.000745		-0.000746		-0.040711		-0.169768	
Z 2 4^(1/2) (p) * COS (A)	0.000000		0.000000		-0.004221		0.011113		0.000000		0.000000		0.000000		-0.006743		-0.011127		0.000000		0.000000	
Z 3 4^(1/2) (p) * SIN (A)	-0.002595		0.001740		-0.002596		-0.002596		0.007601		-0.007736		0.004294		-0.002596		-0.002596		-0.012807		0.002237	
Z 4 3^(1/2) (2p^2 - 1)	0.000004		0.000084		0.000001		0.000000		0.022939		0.095895		0.000764		0.000001		0.000000		-0.022966		-0.097294	
Z 5 6^(1/2) (p^2) * SIN (2A)	0.000000		0.000000		-0.006243		0.016439		0.000000		0.000000		0.000000		-0.010390		-0.016533		0.000000		0.000000	
Z 6 6^(1/2) (p^2) * COS (2A)	-0.000021		-0.006439		-0.000023		-0.000023		-0.016013		0.003792		-0.010661		-0.000023		-0.000023		0.016061		-0.005997	
Z 7 8^(1/2) (3p^3 - 2p) * SIN (A)	-0.000924		0.000603		-0.000924		-0.000924		0.002667		-0.002730		0.001502		-0.000924		-0.000924		-0.004520		0.000774	
Z 8 8^(1/2) (3p^3 - 2p) * COS (A)	0.000000		0.000000		-0.001486		0.003913		0.000000		0.000000		0.000000		-0.002374		-0.003918		0.000000		0.000000	
Z 9 8^(1/2) (p^3) * SIN (3A)	-0.000042		0.000021		-0.000042		-0.000042		0.000116		-0.000080		0.000058		-0.000042		-0.000042		-0.000201		-0.000009	
Z 10 8^(1/2) (p^3) * COS (3A)	0.000000		0.000000		-0.000062		0.000163		0.000000		0.000000		0.000000		-0.000098		-0.000163		0.000000		0.000000	
Z 11 5^(1/2) (6p^4 - 6p^2 + 1)	0.000333		0.000322		0.000333		0.000333		0.000250		0.000109		0.000314		0.000333		0.000333		0.000415		0.000557	
Z 12 10^(1/2) (4p^4 - 3p^2) * COS (2A)	-0.000006		0.000017		-0.000006		-0.000006		0.000051		-0.000027		0.000031		-0.000006		-0.000006		-0.000063		0.000014	
Z 13 10^(1/2) (4p^4 - 3p^2) * SIN (2A)	0.000000		0.000000		0.000023		-0.000060		0.000000		0.000000		0.000000		0.000036		0.000060		0.000000		0.000000	
Z 14 10^(1/2) (p^4) * COS (4A)	0.000000		0.000000		0.000000		0.000000		0.000001		-0.000001		0.000001		0.000000		0.000000		-0.000002		0.000000	
Z 15 10^(1/2) (p^4) * SIN (4A)	0.000000		0.000000		0.000001		-0.000002		0.000000		0.000000		0.000000		0.000001		0.000002		0.000000		0.000000	
Z 16 12^(1/2) (10p^5 - 12p^3 + 3p) * COS (A)	0.000000		0.000000		0.000003		-0.000009		0.000000		0.000000		0.000000		0.000005		0.000009		0.000000		0.000000	
Z 17 12^(1/2) (10p^5 - 12p^3 + 3p) * SIN (A)	-0.000003		-0.000007		-0.000003		-0.000003		-0.000011		0.000003		-0.000009		-0.000003		-0.000003		0.000004		-0.000009	
Z 18 12^(1/2) (5p^5 - 4p^3) * COS (3A)	0.000000		0.000000		0.000000		-0.000001		0.000000		0.000000		0.000000		0.000000		0.000001		0.000000		0.000000	
Z 19 12^(1/2) (5p^5 - 4p^3) * SIN (3A)	0.000000		0.000000		0.000000		0.000000		-0.000001		0.000000		0.000000		0.000000		0.000000		0.000001		0.000000	
Z 20 12^(1/2) (p^5) * COS (5A)	0.000000		0.000000		0.000000		0.000000		0.000000		0.000000		0.000000		0.000000		0.000000		0.000000		0.000000	
Z 21 12^(1/2) (p^5) * SIN (5A)	0.000000		0.000000		0.000000		0.000000		0.000000		0.000000		0.000000		0.000000		0.000000		0.000000		0.000000	
Z 22 7^(1/2) (20p^6 - 30p^4 + 12p^2 - 1)	-0.000001		-0.000001		-0.000001		-0.000001		-0.000001		0.000000		-0.000001		-0.000001		-0.000001		-0.000001		-0.000001	
Z 23 14^(1/2) (15p^6 - 20p^4 + 6p^2) * SIN (2A)	0.000000		0.000000		0.000000		0.000000		0.000000		0.000000		0.000000		0.000000		0.000000		0.000000		0.000000	
Z 24 14^(1/2) (15p^6 - 20p^4 + 6p^2) * COS (2A)	0.000000		0.000000		0.000000		0.000000		0.000000		0.000000		0.000000		0.000000		0.000000		0.000000		0.000000	
Z 25 14^(1/2) (6p^6 - 5p^4) * SIN (4A)	0.000000		0.000000		0.000000		0.000000		0.000000		0.000000		0.000000		0.000000		0.000000		0.000000		0.000000	
Z 26 14^(1/2) (6p^6 - 5p^4) * COS (4A)	0.000000		0.000000		0.000000		0.000000		0.000000		0.000000		0.000000		0.000000		0.000000		0.000000		0.000000	
Z 27 14^(1/2) (p^6) * SIN (6A)	0.000000		0.000000		0.000000		0.000000		0.000000		0.000000		0.000000		0.000000		0.000000		0.000000		0.000000	
Z 28 14^(1/2) (p^6) * COS (6A)	0.000000		0.000000		0.000000		0.000000		0.000000		0.000000		0.000000		0.000000		0.000000		0.000000		0.000000	
Z 29 16^(1/2) (35p^7 - 60p^5 + 30p^3 - 4p) * SIN (A)	0.000000		0.000000		0.000000		0.000000		0.000000		0.000000		0.000000		0.000000		0.000000		0.000000		0.000000	
Z 30 16^(1/2) (35p^7 - 60p^5 + 30p^3 - 4p) * COS (A)	0.000000		0.000000		0.000000		0.000000		0.000000		0.000000		0.000000		0.000000		0.000000		0.000000		0.000000	
Z 31 16^(1/2) (21p^7 - 30p^5 + 10p^3) * SIN (3A)	0.000000		0.000000		0.000000		0.000000		0.000000		0.000000		0.000000		0.000000		0.000000		0.000000		0.000000	
Z 32 16^(1/2) (21p^7 - 30p^5 + 10p^3) * COS (3A)	0.000000		0.000000		0.000000		0.000000		0.000000		0.000000		0.000000		0.000000		0.000000		0.000000		0.000000	
Z 33 16^(1/2) (7p^7 - 6p^5) * SIN (5A)	0.000000		0.000000		0.000000		0.000000		0.000000		0.000000		0.000000		0.000000		0.000000		0.000000		0.000000	
Z 34 16^(1/2) (7p^7 - 6p^5) * COS (5A)	0.000000		0.000000		0.000000		0.000000		0.000000		0.000000		0.000000		0.000000		0.000000		0.000000		0.000000	
Z 35 16^(1/2) (p^7) * SIN (7A)	0.000000		0.000000		0.000000		0.000000		0.000000		0.000000		0.000000		0.000000		0.000000		0.000000		0.000000	
Z 36 16^(1/2) (p^7) * COS (7A)	0.000000		0.000000		0.000000		0.000000		0.000000		0.000000		0.000000		0.000000		0.000000		0.000000		0.000000	
Z 37 9^(1/2) (70p^8 - 140p^6 + 90p^4 - 20p^2 + 1)	0.000000		0.000000		0.000000		0.000000		0.000000		0.000000		0.000000		0.000000		0.000000		0.000000		0.000000	

This page is intentionally left blank.

8.7 ACCESS Coronagraph Performance Comparisons

Prepared by:

John Trauger, Curt Henry, Dimitri Mawet, Gene Serabyn, Laurent Pueyo
(Jet Propulsion Laboratory)

Rus Belikov
(National Aeronautics and Space Administration /Ames)

Olivier Guyon
(University of Arizona)

ACCESS has selected four specific coronagraph architectures as representative of the major coronagraph types. The central issue in our comparisons is engineering readiness of the critical coronagraph technologies. We consider three levels of technology readiness. First, we use technology *already demonstrated* in the laboratory as a measure of coronagraph performance that is achievable with current technologies, and we define this as the "performance floor" for ACCESS. Thereby, these criteria for the minimum performance can be used to model and establish a "minimum science mission" for the ACCESS study.

Second, we consider advances in the coronagraph technology that are likely to be demonstrated in the coming year (by ~April 2010, before the anticipated announcement of opportunity to propose a NASA medium-class exoplanet mission), based on ongoing funded and scheduled technology developments with predictable near-term outcomes. Our main interest is in developments in the coming year that may provide a significant advance in the demonstrated state-of-the-art. We use these near-term performance predictions to model and compare the ACCESS science programs accessible to each of the coronagraph types.

Third, we discuss the potential for technology advancements that are not yet funded or scheduled, but which may provide significant advancements in the coming five years.

Assessment of Current Coronagraph Demonstrations and "Performance Floor" Criteria

Our first objective is to establish the performance level of a space coronagraph architecture that can be achieved with technologies already demonstrated in the laboratory, to thereby define a baseline performance floor for the ACCESS concept. It is not an assessment of advances expected from ongoing laboratory research during the coming year, or from new initiatives that are contemplated for future years, both of which will be discussed in the following sections of this Appendix 8.7. Here we collect the demonstrated laboratory results as of March 2009. We have plotted the contrast and spectral bandwidths already achieved in laboratory coronagraph demonstrations in Figure 8.7-1. These data are as follows:

a) Lyot coronagraph contrasts at 4 λ/D are taken from the TPF-C Milestone #1 Report [1] for monochromatic (785 nm) laser light, and from the TPF-C Milestone #2 Report [2] for 10% bandwidth (760–840 nm) filtered continuum light. In each case, the plotted number refers to worst of two contrast measurements: the average contrast in an "inner" region of the high contrast field (4–5 λ/D), and the average contrast in an "outer" region (4–10 λ/D). These measurements were all made with 4^{th}-order "linear sinc-squared" masks [3] on the HCIT.

   Lyot coronagraph contrasts at 3 λ/D were obtained in March 2009 with a hybrid (metal + dielectric) Lyot focal plane mask [4] on the HCIT. Again, the plotted data refer to the contrasts averaged over an "inner" region (3–4 λ/D) and an "outer" region (3–10 λ/D).

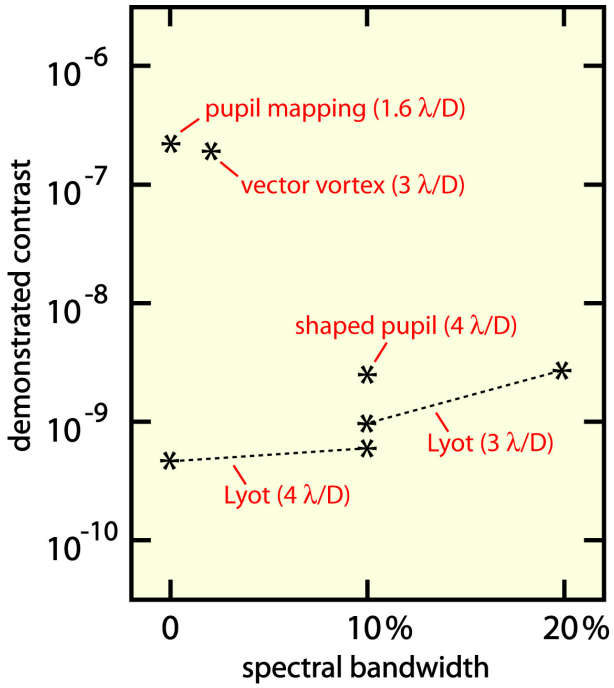

Figure 8.7-1. Coronagraph contrasts vs. spectral bandwidths that have been measured in the laboratory as of March 2009. Contrast is evaluated at the inner working angle for each coronagraph, as indicated.

Wavefront sensing and control for all Lyot contrast measurements were carried out over a half-dark-field with a single Xinetics 32 × 32-actuator deformable mirror and either speckle nulling or EFC using images in the coronagraph focal plane.

b) Vector vortex results were obtained in February 2009 on the HCIT, using the first example of a vector vortex phase mask manufactured with proprietary liquid crystal polymer technology from JDSU [5]. The half transmittance of the assembled vortex coronagraph was measured to be at a radial distance of 1.8 λ/D. Bandwidth in the experiment was 2% (784–800 nm), and IWA was chosen to be 3 λ/D. Wavefront sensing and control was carried out over a half-dark-field with a single Xinetics 32 × 32-actuator deformable mirror and EFC using images in the coronagraph focal plane.

c) The plotted pupil mapping result was obtained in the ambient air at the Subaru coronagraph laboratory [6]. The plotted value is the contrast averaged over a half-dark-field extending from 1.6 to 4.4 λ/D, obtained in monochromatic 633 nm laser light with a single Boston Micromachines 32 × 32 deformable mirror using a variation on the EFC algorithm. As of April 2009, experiments with the pupil mapping coronagraph have commenced on the HCIT, and new results are not yet available.

d) Shaped pupil results were obtained in experiments performed in 2007 on the HCIT [7]. Wavefront sensing and control was carried out over a half-dark-field with a single Xinetics 32 × 32-actuator deformable mirror using speckle nulling at the central wavelength of the 10% spectral band.

Based on this collection of laboratory results, we have selected the Lyot coronagraph as representative of the demonstrated state of the art, leading to the following "performance floor" criteria. Inner working angle = 3 λ/D. Spectral bandwidth = 20%, which for the purpose of mission simulations will be centered at 550 nm (V-band). Raw contrast of 2.5e-9 averaged over 3–4 λ/D and between the IWA and the outer working angle (OWA) = 20 λ/D as defined by the ACCESS wavefront control system. These parameters establish a common point of reference for our four

representative coronagraphs, anchoring the comparisons at a point in coronagraph performance trade space that corresponds to a well-defined minimum science mission for the ACCESS study. We recognize that each of the coronagraph types is capable, in principle, of exceeding these minimum requirements in one way or another. Enhancements in performance above and beyond these minimum criteria provide the basis for the definition of a "full science mission" specific to each coronagraph type. It is these distinguishing characteristics that provide the basis for a quantitative comparison of the viability and readiness among the coronagraph types.

Representative Coronagraph Configurations

In the following sections, we specify the representative coronagraph configurations used in our analysis. Having defined the "performance floor" for the ACCESS coronagraph, we now extend our considerations to specific versions of the four representative coronagraph types that use technologies that are already in development and can realistically be demonstrated in the laboratory in the coming year. We describe the coronagraph elements, unique to each coronagraph type, that are used to define the physical models for our comparisons.

Common Elements: the Coronagraph Front End and Back End

By design, many of the optical, structural, thermal, and mechanical elements are common to all coronagraphs. First we describe the elements of the ACCESS coronagraph instrument that are common to all four types. The instrument optical assembly is structurally attached to the bulkhead of the 1.5 meter unobscured Gregorian telescope. The optical telescope assembly (OTA) includes the telescope primary and secondary mirrors, a fold mirror, and a paraboloidal collimating mirror, thus a collimated beam is passed forward to the instrument. The instrument receives the collimated beam and relays an image of the primary mirror (the pupil of the system) to a deformable mirror mounted in a gimbaled tip/tilt fine steering mechanism. The optics to this point define the telescope line of sight (LOS), which is stabilized on the sky to 1 milliarcsecond (3σ) with an actively-damped attitude control system (ACS) described in Appendix 8.5. The beam passes to a second deformable mirror in a fixed mount, then to a paraboloidal mirror that brings the beam to a focus. The image of the target star is stabilized at this focal point to 0.45 milliarcseconds (3σ) with the pointing control system described in Appendix 8.5. Therefore, all coronagraph instruments share an observatory platform that provides (1) a stabilized telescope LOS, (2) an internal fine guiding sensor and tip/tilt mechanism that stabilizes the star image at the first instrument focus, and (3) a pair of high-technology-readiness precision deformable mirrors for wavefront sensing and control.

Optical elements specific to each coronagraph type follow this common "front end", and are described in the following sections.

Then there are "back end" elements, following the unique coronagraph optics, that are again common to all four coronagraphs. These elements use dichroic mirrors to split the light into three broad (VRI) spectral bands, then to project three spectrally filtered high-contrast coronagraph images simultaneously onto a common low-noise (3 electron/pixel read noise) CCD focal plane. An integral field spectrograph, with resolving power ($R = \lambda/\delta\lambda$) of 20, is coupled to the output beam. Finally, a realistic physical descriptions of these optical elements, consistent with commercial tolerances and available today, are embedded in a common optical diffraction propagation model written in IDL using the PROPER library of coronagraph elements.

The elements unique to each coronagraph type will be identified in the following sections of this Appendix. Each description includes (1) an explanation of the fundamental operating principles; (2) a specification of the coronagraph elements as entered into our computational models; (3) a summary of recent laboratory proof-of-concept experiments; and (4) a review of technology maturity, including the current state-of-the-art, expected improvements in the coming year based on

on-going funded activities, and prospects for future advancements requiring new funding in coming years.

The Observatory Platform

In addition to the demonstrated or projected coronagraph characteristics, the prediction of science mission performance requires an analysis of the observatory platform. The definition and analysis of the observatory optical design, pointing control, and thermal control systems has been a major part on the ACCESS study, as detailed in other Appendices in this report. Here we summarize a number of salient observatory characteristics that directly affect the engineering design of the coronagraphs.

More Common Elements: the End-to-End Computational Model

Each of these model coronagraphs are then presumed integrated into the same observatory platform, subject to the same telescope optical system, the same pointing and thermal control systems, and as much as possible the same end-to-end optical propagation methods. The nine elements of the analysis are as follows.

1. All modeling presumes the baseline ITT telescope, NGC spacecraft, ITT/AIMS stabilization of the telescope line-of-sight, fine pointing control with the Xinetics fine steering mirror internal to the coronagraph, precision wavefront control with a pair of Xinetics 48 × 48 actuator DMs, JPL/ITT observatory thermal control system, and the individual instrument raytrace layouts that have already been defined by the ACCESS engineering team;
2. End-to-end (i.e., including all optical elements from star to coronagraph focal plane) Fresnel propagation implemented in either Krist PROPER or Moody code (although a significant simplification is required in practice for propagation between the pupil mapping elements);
3. Standard surface figure errors assigned to each optical element, derived from surface PSD data for manufactured optical elements representative of the cost class for ACCESS;
4. DMs set for a full "two-sided" high-contrast dark field, derived using EFC nulling algorithm, using our standard model for Xinetics deformable mirror surface influence functions;
5. High contrast dark field extends from the inner working angle (IWA) of the coronagraph (i.e., the angular separation from the central star beyond which the transmitted energy of a planet equals or exceeds one half of the energy in the full planet PSF) to an outer working angle (OWA) determined by the number of DM actuators mapped across the pupil diameter. IWA and OWA are stated in units of λ_0/D on the sky, where λ_0 is the central wavelength of the spectral band (i.e., λ_0 = 550 nm for the 20% V-band [500–600 nm]) and D is the full diameter of the telescope primary mirror;
6. Monte Carlo simulations of pointing control dynamics, based on ACCESS analysis of telescope LOS pointing jitter (1 milliarcsec, 3σ) and knowledge-limited pointing correction accuracy with the fine steering mirror (0.45 milliarcsec, 3σ for a V = 7 star);
7. Simulation of the dominant thermal response (drift in primary mirror surface figure and mutual misalignment of the primary and secondary) to a 30° roll of the observatory about the line of sight to the star (with γ = 100°);
8. PSFs are the average of multiple (11 or more) independently-computed monochromatic PSFs distributed evenly over the $\delta\lambda/\lambda$ = 20% wavelength band (500–600 nm), using known wavelength-dependent effects of the coronagraph elements; and finally
9. Product is a coronagraph PSF, sampled at 5 pixels per λ_0/D on the sky.

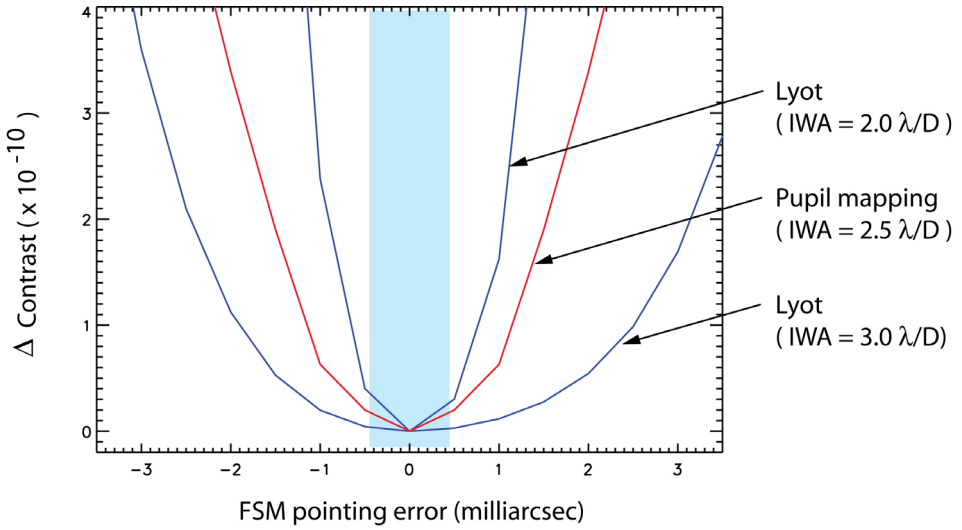

Figure 8.7-2. Delta contrast vs. fine steering mirror pointing errors. Contrast degradations for representative coronagraphs with inner working angles of 3.0, 2.5, and 2.0 λ_0/D (for λ_0 = 550 nm) are shown. Blue-shaded region indicates the estimated the ±0.45 milliarcsec 3σ pointing error limits estimated from the pointing control study. FSM pointing errors affect the contrast at the level of 3e-11 or less for a 2 λ/D IWA coronagraph.

8.7.1 Lyot Coronagraph

Among the leading architectures for the imaging and spectroscopy of nearby exoplanetary systems is the space coronagraph, which provides in principle very high (10 billion to one) suppression of diffracted and scattered starlight at very small separations (a few tenths of arcseconds) from the star. The band-limited Lyot coronagraph was introduced by Kuchner and Traub [8] and extended from 4th-order to 8th-order apodizations by Kuchner et al. [9]. These band-limited masks have been manufactured most recently as vacuum-deposited metal films [10]. The best high-contrast results to date have been obtained with a band-limited coronagraph in JPL's High Contrast Imaging Testbed (HCIT; [11]). The testbed has also been used to demonstrate long-term open-loop contrast stability of 10^{-11} over periods of five hours or more [12]. Recent work has shown that hybrid metal-dielectric masks, band-limited in both real and imaginary parts, can achieve high contrast over bandwidths of 20% or more. Analysis has shown that a trade can be made between useful throughput and inner working angle, and that IWAs as small as 2 λ/D are feasible.

8.7.1.1 Physical Principles of the Lyot Coronagraph

Lyot coronagraph focal-plane occulting masks have generally been described in terms of attenuation profiles free of any phase shift. However, phase shifts are expected and observed in physical occulting masks, with significant effect at billion-to-one coronagraph contrast levels in spectrally broad light, as required for the direct imaging and spectroscopy of nearby exoplanet systems. We describe the design and fabrication of hybrid focal-plane masks for Lyot coronagraphy, as proposed for ACCESS and as demonstrated over the past year at JPL's HCIT.

These masks, composed of thickness-profiled metallic and dielectric thin films superimposed on a glass substrate, are in principle band-limited in both the real and imaginary parts of the occulter characteristics. Together with a deformable mirror for control of wavefront phase, these masks offer Lyot coronagraph contrast performance better than 10^{-9} over spectral bandwidths of 20% or more with throughput efficiencies up to 67%.

The concept of a band-limited Lyot coronagraph provides the theoretical basis for mathematically perfect starlight suppression. However, these band-limited designs do not consider practical limitations encountered when manufacturing the masks. In practice, the optical characteristics of

physical materials and practical aspects of the fabrication processes impose limitations on contrast levels and spectral bandwidths that can be achieved in the real world. Dominant among these real-world effects are the phase shifts, required by the Kramers-Kronig relation, that necessarily accompany the prescribed band-limited attenuation profiles using physical materials. In general, such "parasitic" phase shifts violate the criteria for band-limited coronagraph masks, and further, these phase shifts may exhibit significant phase shift dispersion over spectral bandwidths ($\delta\lambda/\lambda$ = 10–30%) of interest for exoplanet astronomy. Additional phase-shift complications arise due to optical interference effects in the thin-film structures used for the masks.

Our procedure for design of hybrid mask includes the leverage of wavefront manipulation, a key element in the creation of the high-contrast dark field, as introduced by Malbet et al. [13] Without consideration of coronagraph design, Malbet et al. used a non-physical (pixillated) deformable mirror with actuator settings chosen to maximize contrast in a dark field, as computed by the Marquardt non-linear least squares algorithm. In 1997, Burrows introduced the speckle nulling algorithm in the context of the proposed CODEX coronagraphic instrument for HST, a speckle-by-speckle nulling approach based on manipulation of the DM and imaging in the coronagraph speckle field, that did not require knowledge of the specific coronagraph architecture or its detailed physical characteristics. This speckle nulling procedure was extensively used on the HCIT to demonstrate for the first time a monochromatic contrast of 5×10^{-10} in a laboratory setting [14, 12]. Borde and Traub [15] introduced a more efficient algorithm for sensing and control based on an idealized representation of the coronagraph and deformable mirror, minimizing energy in the entire coronagraph dark field in each iteration. Moody extended this approach to include the complex and wavelength-dependent characteristics of the physical coronagraph masks, to explore mask design options for broadband high-contrast coronagraphy. More recently, Giveon et al. [16] introduced a formal approach, known as EFC, to minimize the residual energy in the coronagraph field in a manner that easily accommodates multiple wavelengths and the physical characteristics of a given coronagraph architecture. Here, we use these wavefront control principles (i.e., without wavefront sensing) for guidance in the design of hybrid coronagraph masks for improved spectral bandwidth and throughput efficiency.

In the ideal case with perfect and oversized optics, and with the deformable mirror initially set to perfect flatness, the changes in the complex electric field at the coronagraph focal plane $V(x,y)$ are related to the complex attenuation of the coronagraph mask $A(x,y)$ by the following cascade of Fourier transforms:

$$V(x,y) = F\Big[\, F^{-1}\Big[\, F\big[P_0(u,v)\big]\cdot A(x,y)\,\Big]\cdot L(u,v)\,\Big],$$

where $P_0(u,v)$ defines the entrance pupil (taken to be circular and uniformly-illuminated) and $L(u,v)$ defines the Lyot mask (with an "eye-shaped" opening as illustrated in Figure 8.7.1-1).

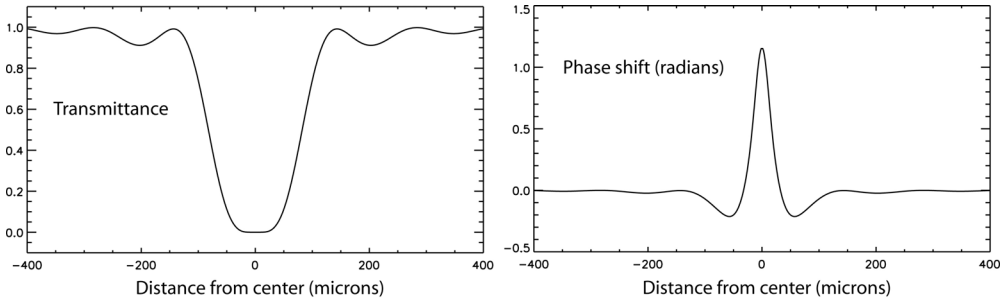

Figure 8.7.1-1. Computed transmittance and phase shift profiles for a 4th-order nickel-only mask with inner working angle of 4 λ/D, described above. The attenuation profile is scaled to reach 50% transmittance at 4 λ/D from center at the 800 nm central wavelength. The phase profile at the 800 nm center wavelength is shown here. Physical dimensions correspond to an f/25.8 beam at the 800 nm wavelength.

Iterative adjustments are made in the actuator positions, using steps small enough in each iteration that the linear approximation holds:

$$e^{-2\pi j\, s_i h_i(u,v)/\lambda} \approx 1 - 2\pi j s_i h_i(u,v)/\lambda .$$

Then the relation between these small DM actuator displacements $h_i(u,v)$ and the corresponding changes in the complex electric field at the coronagraph image plane can be expressed as the product $s_i \cdot H_i(x,y)$, where:

$$H_i(x,y) = F\Big[\, F^{-1}\Big[\, F\big[P_0(u,v)\cdot 2\pi j h_i(u,v)/\lambda\big]\cdot A(x,y)\Big]\cdot L(u,v)\Big].$$

We define $c(x,y)$ as the complex electric field in the coronagraph focal plane after the application of a set of DM displacements:

$$\sum_i s_i H_i(x,y) + V(x,y) = c(x,y).$$

and use SVD to estimate the set of actuator displacements s_i that minimize the sum of $\|c(x,y)\|^2$ overall pixels in the high-contrast fields in the coronagraph focal plane, while keeping DM actuator displacements within the linear approximation above using a merit function that penalizes excessive DM actuator displacements. After the first iteration, the DM will depart from perfect flatness. For the second and all subsequent iterations, this evolution of the wavefront must be accounted for by substituting $P_n(u,v)$ in place of $P_0(u,v)$ in the above expressions for $V(x,y)$ and $H_i(x,y)$:

$$P_n(u,v) = P_0(u,v)\cdot(e^{-2\pi j\, g_i/\lambda}), \text{ where } g_i = \sum_n s_i h_i$$

captures the cumulative effects of all n previous (small) actuator motions $s_i \cdot h_i$. This applies to a single wavelength of light. For a finite spectral bandwidth, we have

$$\sum_i s_i H_i(x,y,\lambda) + V(x,y,\lambda) = c(x,y,\lambda)$$

which now includes terms for a set of representative wavelengths λ across the spectral band, and the goal becomes the minimization of the sum of $\|c(x,y,\lambda)\|^2$ over the pixels in the high contrast field of interest and over all λ across the spectral band. SVD is used with this final equation to estimate the DM settings for optimal broadband contrast, as reported in the following paragraphs.

Metal-only Lyot Masks

We first consider a coronagraph mask composed of a thin metallic film on glass. We refer to the literature [17] for absorbing materials that closely approximate the criteria for zero wavelength dispersion in a deposited film: $n(\lambda) - 1 \propto \lambda$ and $k(\lambda) \propto \lambda$. Nickel is selected, as one of the common metals that offer a favorable relationship between the refractive indices and wavelength [18, 19], providing useful and nearly constant *OD*s across the visible spectrum. We have assumed a central wavelength of 800 nm for the target 10% bandwidth, but note that the central wavelength could have been chosen anywhere in the visible wavelength range.

The profile is based on a 4th-order sinc-squared profile. Its width is scaled to give an intensity transmittance of 50% at an angular separation of 4 λ/D from the central peak. Here λ is the central wavelength of the 10% band and D is the diameter of the circular pupil of the system. Because the sinc-squared profile specifies zero transmittance at the central peak, which is not physically possible, we clip the amplitude transmittance to a peak value of 10^{-4}, a level that corresponds to a maximum OD = 8. Further, we smooth the clipped OD profile by convolving with a gaussian function. The

width of the attenuation profile is adjusted again to provide 50% attenuation at a separation of 4 λ/D from the central "star."

$$OD(x) = -2\log_{10}\left[A(x)\right] \otimes \left(1/\sigma\sqrt{2\pi}\right) e^{-(1/2)(x/\sigma)^2}, \text{ where}$$

$$A_S(x) = 1 - \left(\frac{\sin(\pi x/w)}{(\pi x/w)}\right)^2, \; A(x) = \max(10^{-4}, A_S),$$

with $w = 142.0\,\mu m,\ \sigma = 9.0\,\mu m.$

The Lyot mask is set to ε = 0.36, giving a clear area = 55.1% of the pupil area. The predicted contrast is 1.3×10^{-10} in the inner 4–5 λ/D region, closest to the attenuated star, and 1.4×10^{-10} in the outer 4–10 λ/D field. The resulting transmittance phase-shift profiles for a thickness-profiled nickel film are shown in Figure 8.7.1-1.

The physical mask was fabricated by vacuum deposition. The OD profile indicated above was converted into a thickness profile by first computing the OD vs. thickness for a thin nickel film on fused silica, using the standard formulae for an absorbing thin film on a transparent substrate [20], then deconvolving the measured slit function with a kernel representing a slit of width 20 microns. The 20-micron slit, etched into a silicon wafer, was mounted on a translation stage driven in 1-micron steps by a computer-controlled stepper motor. A table of relative dwell times for deposition through the slit at each position across the substrate was generated using a measured relation between OD of the deposited metal film vs. the physical thickness indicated by a crystal monitor. Deposition was continued over multiple passes of the slit across a 3-millimeter pattern width, while monitoring the accumulated thickness measured by the crystal monitor. The deposition was terminated when the accumulated thickness at the peak of the profile indicated that the peak OD was within 2% of the target value. A comparison between the specified and measured transmittance profiles is shown in Figure 8.7.1-2.

The laboratory demonstration of high contrast with this mask was carried out in the HCIT as follows. A high-contrast field of view was defined with angular separations from the central bright star measured in units of the characteristic angle λ/D, where λ is the central wavelength of the spectral band and D is the pupil diameter for the optical system. An outer dark field includes separations that are both within a radius of 10 λ/D from the star and beyond a straight line that is 4 λ/D from the star at its closest point. This outer field represents a search area for a faint stellar companion. It can be seen in Figure 8.7.1-4. We also define an inner dark field, a square with dimensions equal to λ/D, entirely within the outer field and extending from 4 to 5 λ/D as a measure of the light scattered nearest the star. Our metric for scattered light is the average contrast within the boundaries of these dark fields in the coronagraph focal plane.

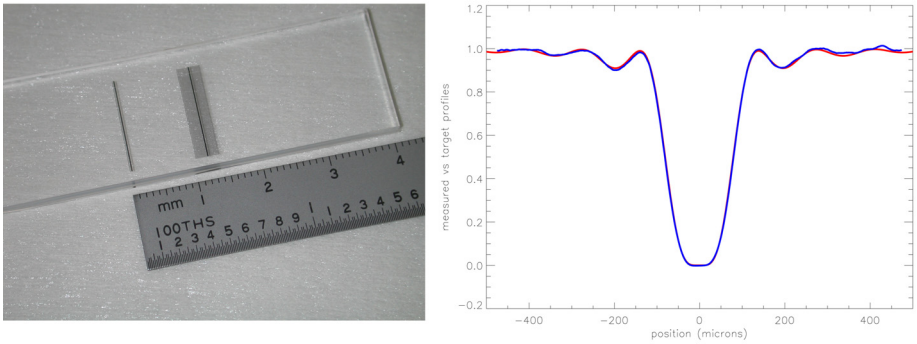

Figure 8.7.1-2. At left, the 4th order nickel mas on a fused silica substrate. At right, a comparison between the desired profile (*red*) and the measured profile (*blue*).

White light from a supercontinuum source in series with a filter wheel provided continuum white light filtered to five selectable spectral bands: a 760–840 nm band (10%) and five 2% bands spanning the 10% range (760–786, 786–792, 792–808, 808–824, and 824–840 nm). The DM was adjusted using a control algorithm that closely resembles the design procedure described above, but with the addition of a wavefront sensing (WFS) procedure, as follows. First, with the coronagraph elements removed from the beam, the DM setting was adjusted to present an approximately flat wavefront to the occulter focal plane using a focus-diversity Gerschberg-Saxton procedure. The coronagraph elements were then replaced in the beam, and the focal position of the occulter was adjusted for best contrast in the target area with the nominal flat-wavefront setting. The EFC procedure [16], placing small displacements on the DM in positive-negative pairs, then recording the resulting images of the coronagraph dark field, was carried out in each of three of the 2% spectral bands (760–786, 792–808, and 824–840 nm). The electric field was estimated from these focal plane images, then used to specify a new DM setting that would improve the contrast simultaneously all three wavelength bands, while restricting the strokes of the actuators. This procedure was repeated until the limiting contrast was obtained, typically in 10–20 iterations.

This experimental procedure is expected to find a DM setting similar to the setting predicted in the design procedure above since the procedures are closely related, with the following exceptions. The experimental procedure includes a wavefront sensing step that is unnecessary in the design algorithm, which benefits from perfect knowledge of the computed wavefront. Fresnel propagation is used, rather than the simple cascade of Fourier transforms described above, to account for experimental adjustments such as the focus offset of the occulter. P_n was not updated in each iteration as before, instead it was maintained at P_0, since the additional programming required to use P_n would not have resulted in significantly better contrast, given that the contrast floor was limited by experimental noise. In the future the WFC will include the updating of P_n.

The contrast obtained using this procedure was 6.4×10^{-10} for the inner 4–5 λ/D area and an average of 6.4×10^{-10} also for the outer 4–10 λ/D area in 10% bandwidth centered at 800 nm [21]. The contrast for each of the 2% bandwidths was better than 10^{-9} in both of these areas. The DM surface figures settings and resulting dark field are shown in Figures 8.7.1-3 and 8.7.1-4 respectively.

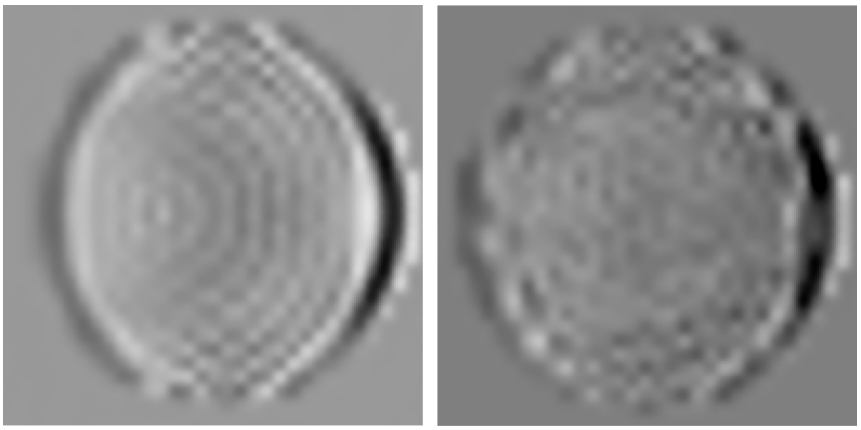

Figure 8.7.1-3. Wavefront solution for a nickel coronagraph mask and a single DM. The spectral bandwidth is 10% centered at 800 nm. At left is the predicted surface figure for the DM, displayed as grey scale stretched over a ± 30 nm range. At right is a voltage map representative of the surface figure applied to the DM to obtain the laboratory results shown below.

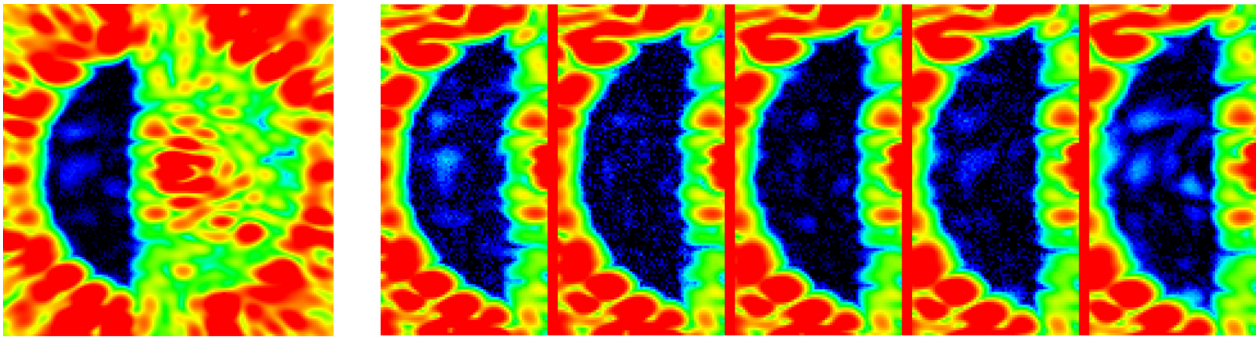

Figure 8.7.1-4. *Left:* Laboratory demonstration of Lyot coronagraph contrast averaging 6.4×10^{-10} across a 760–840 nm (10%) spectral bandwidth. The dark field extends from a vertical line offset 4 λ/D left of the occulted "star" to an outer radius at 10 λ/D centered on the "star." *Right:* Contrast images in five contiguous 2% passbands shows the evolution of the background field of speckles across the 10% bandwidth image at left.

Metal + Dielectric Masks Enable Smaller Inner Working Angles

In the previous case of a metal-only mask, our approach was to create a mask with an attenuation profile that matched a prescribed form, while accepting without change the resulting phase shifts. Here we shape the phase-shift profile with a non-absorbing dielectric layer. The metal and dielectric layers are superimposed on a glass substrate, either as a multilayer coating on one side of the substrate or as separate layers on opposite sides of a thin substrate. The thickness profiles of the films are chosen to produce the desired attenuation and phase-shift profiles, as predicted by standard formulae[11] for absorption and phase shift, including interference effects, in thin metal and dielectric films on a fused silica substrate.

We have carried out designs for 4th-order hybrid masks designed for four inner working angles: 4 λ/D, 3.5 λ/D, 3 λ/D, and 2.5 λ/D. We discuss the 3 λ/D design in greater detail, as representative of the 4th-order hybrid masks, while the characteristics of all four are summarized in Table 8.7.1-1.

Table 8.7.1-1. Summary of the IWAs, predicted contrast limits, and throughput efficiency for the coronagraph masks in the above sections.

Mask Configuration	Inner Working Angle	Spectral Bandwidth	Inner Contrast (x 10 -10)	Outer Contrast (x 10 -10)	ε	Lyot Throughput
nickel 4th-order	4 λ/D	10%	1.3 (4 - 5 λ/D)	1.4 (4 - 10 λ/D)	0.36	55%
hybrid 4th-order	4 λ/D	20%	2.1 (4 - 5 λ/D)	3.1 (4 - 10 λ/D)	0.26	67%
hybrid 4th-order	3.5 λ/D	20%	4.5 (3.5 - 4.5 λ/D)	4.5 (3.5 - 10 λ/D)	0.30	63%
hybrid 4th-order	3 λ/D	20%	4.9 (3 - 4 λ/D)	5.0 (3 - 10 λ/D)	0.35	57%
hybrid 4th-order	2.5 λ/D	20%	8.8 (2.5 - 3.5 λ/D)	8.2 (2.5 - 10 λ/D)	0.41	49%

Again, we select a central wavelength of 800 nm for the target 20% bandwidth, and note that the metal and dielectric materials would allow the central wavelength to be placed anywhere in the visible wavelength range. The attenuation profile is now acknowledged to be complex. The form for the real part of the amplitude profile is a sinc-squared profile, with the width parameter is adjusted to give 50% attenuation at the 3 λ/D inner working angle (IWA) from the central "star" at the central wavelength. Simultaneously, we specify the imaginary part of the attenuation profile as follows:

$$A_{REAL} = \max(10^{-4}, A_S), \text{ with } w = 133.2\,\mu m,$$

$$A_{IMAGINARY} = 0.49\left\{\frac{\sin(\pi x/w_1 + \pi)}{(\pi x/w_1 + \pi)}\right\} + 0.49\left\{\frac{\sin(\pi x/w_1 - \pi)}{(\pi x/w_1 - \pi)}\right\}, \text{ with } w_1 = w/2 = 66.6\,\mu m.$$

Next, this complex attenuation profile is decomposed in terms of amplitude and phase. The attenuation (amplitude) of the profile defines the *OD*(*x*) of the metallic layer:

$$OD_{metal}(x) = -2\log_{10}\left\|A_{REAL} - jA_{IMAGINARY}\right\| \otimes (1/\sigma\sqrt{2\pi})\, e^{-(1/2)(x/\sigma)^2},\ \sigma = 4.5\,\mu m.$$

The phase shift due to the profiled metal layer is computed using the bulk optical indices for nickel[8]. A phase shift profile is computed for the dielectric layer, using the bulk indices for a thin dielectric layer (such as MgF_2) on a fused silica substrate. Since we are free to choose any overall phase shift profile, we shape the dielectric layer to give real and imaginary parts of the complex mask that are each band-limited. The profile of the dielectric layer is adjusted to bring the overall phase shift (δ phase) to the following specification:

$$\delta\, phase_{metal+dielectric}(x) = phase\left(A_{REAL} - jA_{IMAGINARY}\right)$$

For an IWA of 3 λ/D, the Lyot mask is set to ε = 0.35, giving a Lyot clear area = 57% of the pupil area. The resulting transmittance and phase shift profiles are shown in Figure 8.7.1-5. The predicted contrast for a 20% bandwidth is 4.9×10^{-10} in the inner 3–4 λ/D region, closest to the attenuated star, and 5.0×10^{-10} averaged over the outer 3–10 λ/D field. The evolution of the contrast with wavelength over the 20% band is shown in Figure 8.7.1-6, along with the corresponding DM surface pattern.

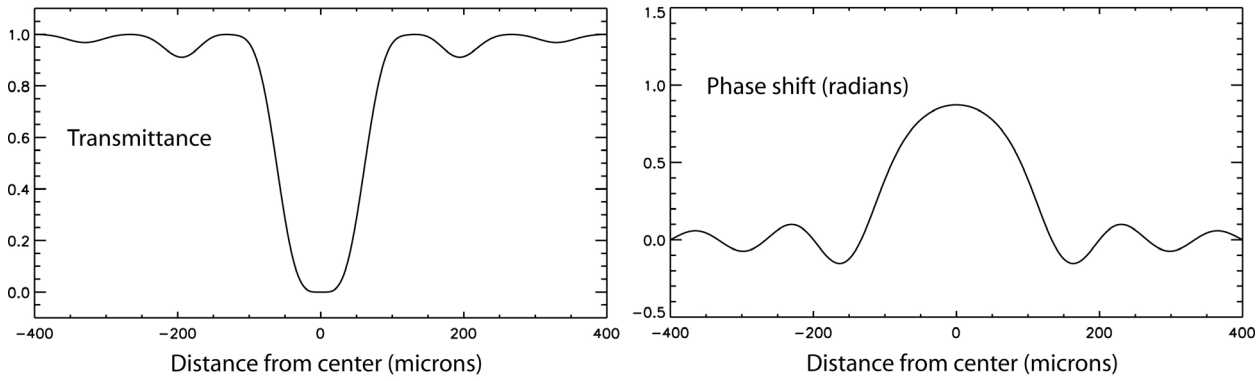

Figure 8.7.1-5. Attenuation and phase shift profiles for a 4th-order mask with inner working angle of 3 λ/D. The attenuation profile is scaled to reach 50% transmittance at 3 λ/D from center at the 800 nm central wavelength. The phase profile varies significantly with wavelength, the profile at the 800 nm center wavelength is shown here. Physical dimensions correspond to an f/25.8 beam at the 800 nm wavelength.

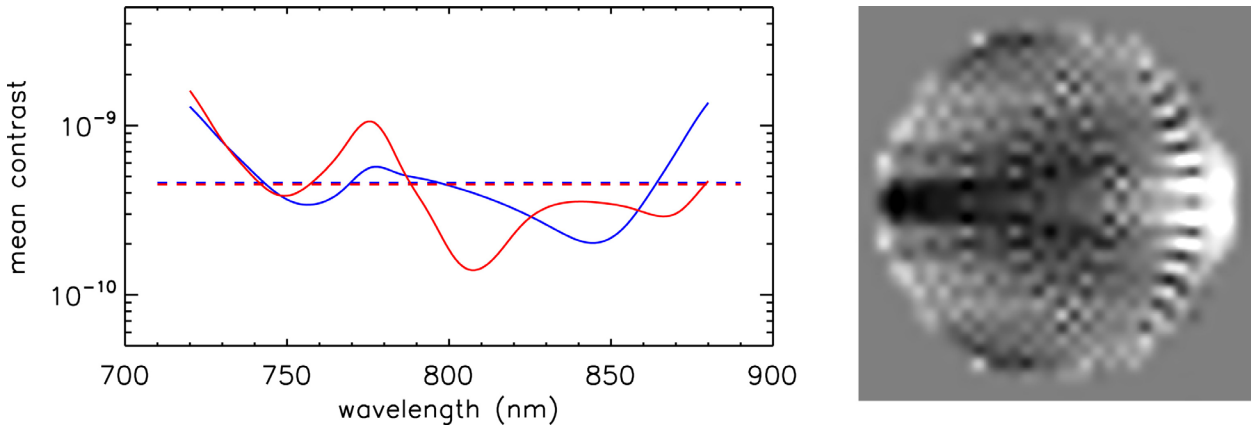

Figure 8.7.1-6. Wavefront solution for a coronagraph mask with an inner working angle of 3 λ/D, designed with an attenuating nickel film and a phase-correcting dielectric film on a fused silica substrate, and a single DM. The spectral bandwidth is 20% centered at 800 nm. At left, diagram traces the contrast vs. wavelength averaged over the outer 3–10 λ/D region (solid curve) and in inner 3–4 λ/D region (dashed curve); and horizontal fiducial lines mark the contrast integrated over the 20% bandwidth. At right is the surface figure of the DM, displayed as grey scale stretched over a ± 30 nm range.

Our study includes both the design of the (complex) attenuation profiles for the coronagraph and the optimal wavefront phase corrections that can be achieved with a single DM. Five examples are summarized in Table 8.7.1-1.

8.7.1.2 Specification of the Representative ACCESS Lyot Coronagraph

The specific optical configuration for the Lyot coronagraph modeling for ACCESS is shown in Figure 8.7.1-7.

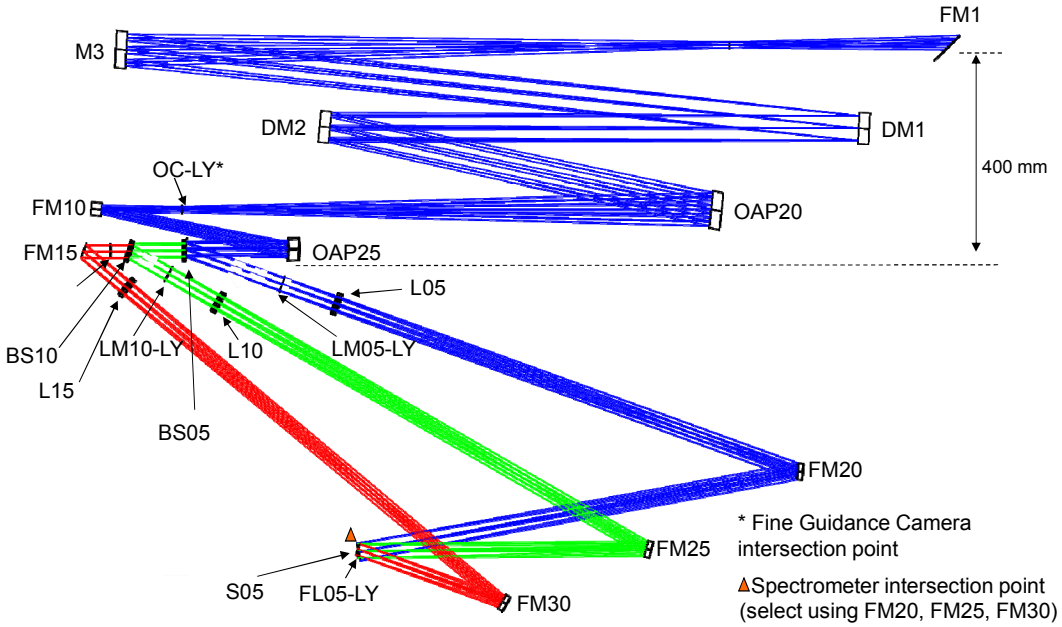

Figure 8.7.1-7. Optical layout for the Lyot coronagraph option for ACCESS

8.7.1.3 Summary of Recent Laboratory Experiments

We have shown, through computations and experiments, that profiled metal and dielectric masks provide new degrees of freedom in Lyot coronagraph mask design, leading to improvements in both spectral bandwidth and coronagraph throughput efficiency. As indicated in the introductory paragraphs in Section 8.7, and in Figure 8.7-1, recent experiments with a 4th-order nickel + dielectric mask yielded a contrast of 1.2×10^{-9} with an inner working angle of 3 λ/D and a 10% bandwidth, and a contrast of 2.7×10^{-9} for the same 3 λ/D inner working angle and 20%.

8.7.1.4 Technology Readiness and Future Prospects

The metal + dielectric masks, composed of vacuum deposited nickel and dielectric films on fused silica, can be expected to be as robust as standard interference filters in space applications. The masks demonstrated to date in the HCIT vacuum environment are themselves clearly at or above TRL 6. Scheduled research and development in the coming 12 months will include the design, fabrication, and testing of new masks with inner working angles of 2.5 and 2.0 λ/D. We rate the likelihood high that progress will be made this year in reducing the inner working angles and the demonstrated contrast floor.

8.7.2 Vector Vortex Coronagraph

Phase mask coronagraphs have been proposed in a number of forms, including the circular phase mask [22], the four quadrant phase-mask [23], and a family of vortex masks [24, 25, 26]. The basic advantages of phase mask coronagraphs are a small inner working angle and high throughput. These advantages were evident in a comparison of coronagraphs for exoplanet detection, in which Guyon et al. [27] identified the vortex phase-mask coronagraph as one of the two types closest to ideal in coronagraphic performance. Moreover, of all phase mask coronagraphs, only the vector vortex mask has so far proven able to meet the requirement of low sensitivity to low-order aberrations such as tip-tilt errors, and also shows good prospects for very high levels of achromatization. For these reasons, our work here focuses on the vector vortex phase mask coronagraph.

8.7.2.1 Physical Principles of the Vector Vortex Coronagraph

8.7.2.1.1 Introduction

The optical vortex coronagraph family is a promising, nearly ideal phase-mask solution, proposed almost concurrently by Mawet et al. [25, 26] and Foo et al. [24]. An optical vortex is a phase singularity in an optical field, a point of zero intensity, resulting from a phase screw dislocation of the form $e^{il\theta}$, with l being the so-called topological charge (number of 2π radians that the phase accumulates along a close path surrounding a phase singularity), and θ the azimuthal coordinate. This anomaly forces the intensity to vanish by total destructive interference, creating a dark core. This dark core propagates and is conserved along the optical axis. Whether a dark core is created in the pupil or focal plane of a telescope will determine the way it further evolves. In Mawet et al. [25, 26], we demonstrated that the creation of a vortex of any even topological charge l at the focal plane can lead to a perfect coronagraph in the ideal case (no further phase aberrations in the system). This result has been confirmed later by Guyon et al. [27] and Jenkins et al. [28]. Even if "optical vortex" rigorously refers to a property of an optical beam, for the sake of simplicity we will use this nomenclature in the following to refer either to the optical property or the optical element that induces it. There are two kinds of optical vortices (and thus of elements that induce them):

- Scalar optical vortex, based on the longitudinal phase delay (which applies to both polarizations identically), and implemented by a structural helical phase ramp [24]

- Vectorial optical vortex, based on the "geometrical" or Pancharatnam phase[1] [29], obtained by manipulating the transverse polarization state of the light with space-variant birefringent elements

8.7.2.1.2 Vectorial vs. Scalar Vortices

The manufacture of an optical vortex device requires generation of a highly accurate helical phase profile, $e^{il\theta}$. To build a scalar vortex in which the phase is generated by a longitudinal phase delay, the helical phase must be etched directly into a piece of glass. The total etched thickness t must be precise to a tiny fraction of λ/n, where λ is the wavelength of the incident light and n is the refractive index of the glass. In the most demanding application of Earth-like planet detection, the helical phase ramp profile would need to be accurate to the nanometer level, which is very challenging even for state-of-the-art etching techniques inherited from the micro-electronics industry (e-beam lithography and reactive ion etching). Moreover, the induced longitudinal phase profile $\Delta\phi = 2\pi/\lambda \times (n(\lambda) - 1) \times t$, is very chromatic, with a hyperbolic dependence on the wavelength of light and subject to the glass refractive index dispersion.

On the other hand, a vectorial vortex optical element possesses no structural phase ramp per se, as it consists simply of a halfwave plate (HWP) in which the optical axes rotate about the center (see Figure 8.7.2-1). In the following we will show that the rotationally symmetric spatial variation of the optical axes manipulates the transverse polarization state in such a way that a *virtual* phase ramp is generated.

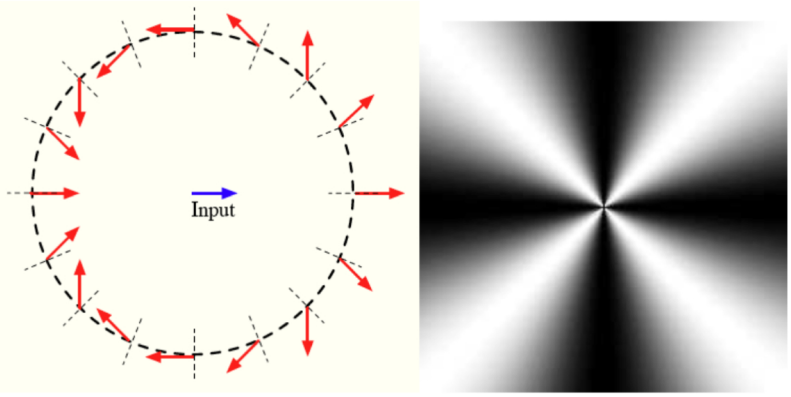

Figure 8.7.2-1. Particular example of an OVVC of topological charge lp = 2, illustrating the concepts needed to describe vectorial vortices. *Left*: the figure shows a HWP with an optical axis orientation ω that rotates about the center as ω = θ, where θ is the azimuthal coordinate (dashed lines perpendicular to the circumference). The textbook net effect of a HWP on a linear impinging polarization is to rotate it by −2 × α where α is the angle between the incoming polarization direction and the extraordinary (e) optical axis. Applying this property to the space-variant HWP, assuming an incoming horizontal linear polarization, we see that the latter is transformed by the vectorial vortex so that it spins around its center twice as fast as the azimuthal coordinate θ (arrows). In this case, the angle of local rotation of the polarization vector Φp corresponds to the "geometrical" or Pancharatnam phase: upon a complete rotation about the center, Φp has undergone a total 2 × 2π virtual phase ramp, which corresponds to the definition of an optical vortex of topological charge 2. *Right*: computation of the periodic modulation of the intensity transmitted by an OVVC between crossed polarizers.

[1] The Pancharatnam phase, or geometrical phase was discovered by Pancharatnam in 1955. Pancharatnam showed that a cyclic change in the state of polarization of light is accompanied by a phase shift determined by the geometry of the cycle as represented on the Poincare sphere. The Geometric phase can be defined as the argument of the inner product of the two Jones vectors describing the light beam whose state of polarization is made to change $\phi_p = arg\langle E(r,\theta), E(r,0)\rangle$. In scalar fields, topological charges are defined according to the number of 2π radians that the phase of the scalar wave accumulates along a closed path surrounding a phase singularity. The topological charge of the vectorial vortex is defined in the same manner, but uses the Pancharatnam phase instead of the scalar phase $l_p = \frac{1}{2\pi}\oint \nabla\phi_p ds$ where the integration path encircles the phase singularity.

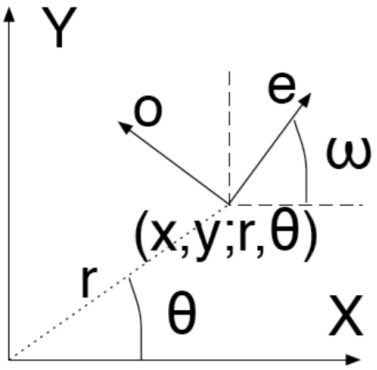

Figure 8.7.2-2. Space-variant birefringent medium vectorial analysis. **X** and **Y** are the unit vectors of the chosen cartesian basis. *o* and *e*, are the local *ordinary* and *extraordinary* optical axis unit vectors of the birefringent medium.

8.7.2.1.2.1 Spatial Variation of the Optical Axis Orientation

When the local birefringence characteristics of an optical component vary from point to point, it is said to be space variant. Space-variant birefringent optical elements (SVBOE) are extensively used as polarization control devices. The range of applications is manifold: polarimetry, laser-beam shaping, laser machining, tight focusing, particle acceleration, atom trapping, contrast enhancement microscopy, image encryption, etc. SVBOE can be represented by a function describing the spatial variation of the optical axis orientation (here extraordinary, *e*)

$$\mathbf{e}(r,\theta) = [\cos[\omega(r,\theta)]\mathbf{X} + \sin[\omega(r,\theta)]\mathbf{Y}]$$

where r, θ are the polar coordinates, while X and Y are the cartesian unit vectors. ω is the local direction of the optical axis frame with respect to X (Figure 8.7.2-2). Let us now consider the case of the helical geometrical phase SVBOE. For a helical phase, the optical axis frame orientation is given by $\omega(r,q) = (l_p/2)q$, where l_p is the "Pancharatnam topological charge." The optical axis frame function, therefore, becomes

$$\mathbf{e}(r,\theta) = [\cos[(l_p/2)\theta]\mathbf{X} + \sin[(l_p/2)\theta]\mathbf{Y}]$$

8.7.2.1.2.2 Optical Vectorial Vortex Coronagraph

A *vectorial vortex* is a SVBOE with rotational symmetry properties. In other words, it is a halfwave plate in which the optical axes rotate about the center. As such it can be represented by a space-variant Jones matrix [30]. Let us assume that *JHWP* is the Jones matrix for the equivalent spatially uniform halfwave plate, i.e.,

$$J_{HWP}(r,\theta) = \begin{bmatrix} \eta_o e^{-i\Delta\phi_{o-e}/2} & 0 \\ 0 & \eta_e e^{+i\Delta\phi_{o-e}/2} \end{bmatrix}$$

where $\Delta\Phi_{o-e}$ (for the sake of simplicity, $\Delta\Phi$ in the following) is the *ordinary–extraordinary* phase shift (also called the linear retardance), and where η_o and η_e are the local SVBOE amplitude transmission coefficient along the *ordinary* and *extraordinary* directions of polarization, respectively.[2] For a perfect HWP, we have $\Delta\Phi=\pi$, and $\eta_o = \eta_e = 1$. The resultant Jones matrix for a helical retarder is

[2] Assuming no diattenuation, these transmittances can still be different because of the different Fresnel reflection coefficients resulting from the existence of the two different refractive indices that give birth to the birefringence.

$$J_v(r,\theta) = R[\omega(r,\theta)]\, J_{HWP}(r,\theta) R[\omega(r,\theta)]^{-1}$$

where $R[\omega(r,\theta)]$ is the rotation matrix (which depends on (r,θ))

$$R[\omega(r,\theta)] = \begin{bmatrix} \cos\omega(r,\theta) & -\sin\omega(r,\theta) \\ \sin\omega(r,\theta) & \cos\omega(r,\theta) \end{bmatrix}$$

For phase errors only ($\eta_o = \eta_e = 1$), the final Jones Matrix is then

$$J_v(r,\theta) = \sin\frac{\Delta\phi}{2}\begin{bmatrix} \cos l_p\theta & \sin l_p\theta \\ \sin l_p\theta & -\cos l_p\theta \end{bmatrix} - i\cos\frac{\Delta\phi}{2}\begin{bmatrix} 1 & 0 \\ 0 & 1 \end{bmatrix}$$

or, assuming that $\Delta\Phi = \pi + \varepsilon$ with $\varepsilon \ll 1$,

$$J_v(r,\theta) = \begin{bmatrix} \cos l_p\theta & \sin l_p\theta \\ \sin l_p\theta & -\cos l_p\theta \end{bmatrix} + i\frac{\varepsilon}{2}\begin{bmatrix} 1 & 0 \\ 0 & 1 \end{bmatrix}$$

The rotating output field is represented by the first term (see Figure 8.7.2-2) while phase deviations show up in the second matrix (and are polarized in parallel to the input field). Although the analysis has so far been presented in the linear basis (see also [25, 26]), the beauty of the vectorial vortex theory reveals itself in the so-called helical basis, i.e., with right and left-handed circular polarization unit vectors

$$RC_{in} = \begin{bmatrix} 1 \\ 0 \end{bmatrix},\ LC_{in} = \begin{bmatrix} 0 \\ 1 \end{bmatrix}$$

In the helical basis, the vortex Jones matrix must be transformed via

$$J_v(r,\theta) = U J_v(r,\theta) U^{-1}$$

With the so-called helical-basis transformation matrix

$$U = \frac{1}{\sqrt{2}}\begin{bmatrix} 1 & i \\ 1 & -i \end{bmatrix}$$

The right substitution using the above set of equations finally yields the vectorial vortex Jones Matrix

$$J_v(r,\theta) = V\begin{bmatrix} 0 & e^{il_p\theta} \\ e^{-il_p\theta} & 0 \end{bmatrix} + L\begin{bmatrix} 1 & 0 \\ 0 & 1 \end{bmatrix}$$

where $V = \frac{1}{2}(\eta_o e^{-i\Delta\phi/2} - \eta_e e^{+i\Delta\phi/2})$ and $L = \frac{1}{2}(\eta_o e^{-i\Delta\phi/2} + \eta_e e^{+i\Delta\phi/2})$ are weighing coefficients depending on the local imperfections of the HWP, i.e., the retardance, and polarization component transmittances. In the perfect case where the transmittances are equal (and equal to 1, which means 100% throughput), i.e., $\eta_o = \eta_e = 1$, and the retardance $\Delta\Phi = \pi$, we obtain as respective outputs to the input vectors RC_{in}, LC_{in}

$$RC_{out} = \begin{bmatrix} 0 \\ e^{i(l_p\theta)} \end{bmatrix},\ LC_{out} = \begin{bmatrix} e^{-i(l_p\theta)} \\ 0 \end{bmatrix}.$$

Several results are thus evident in the helical basis. First, vectorial vortices present the same screw phase dislocation $e^{il_p\theta}$ as scalar vortices do. Second, the ideal output polarization states are simply the reverse of the input states. As a result, the helical states remain orthogonal and therefore decoupled. As natural unpolarized light can always be decomposed into two orthogonal and mutually incoherent polarization states, the vectorial vortex, even though based on polarization manipulation, thus actually works in natural unpolarized light. Third, in the non-ideal case, *Jv* is composed of two

terms. The first term is the pure vortex term of weight V, bearing the geometrical phase ramp structure $e^{ilp\theta}$. This phase modification is geometrical, i.e., induced only by the space variation of the optical axis orientation across the component. Therefore, it is *achromatic* by nature. Fourth, the second (error) term, with weighing coefficient L, carries no phase modification and is a leakage term. A very important property of vectorial vortices as opposed to scalar vortices is thus that the polarization of the chromatic leakage due to the local imperfections of the HWP is orthogonal to the pure achromatic vortex term. This important fundamental difference between the two approaches suggests that one might be able to reduce the effect of the manufacturing defects (retardance and transmittance mismatches) by appropriate polarization filtering: e.g., input left-circular polarization state yields a right-circularly polarized vortex output and a left-circularly polarized leakage. A right-circular analyzer at the output would thus only transmit the pure vortex term, while blocking the left-circularly polarized leakage.

8.7.2.1.3 Sensitivity to Low-order Aberrations—Off-axis Transmission and Inner Working Angle

The optical vortex coronagraph attenuation sensitivity to low-order aberrations like tip-tilt *tt* (pointing error) has been shown, numerically by Mawet et al. [25, 26] and Guyon et al. [27], and analytically by Jenkins [28] to be proportional to tt^l, where l is the topological charge. Leakage due to the finite size of stars can then be very easily estimated using a model of a uniform stellar disk which is a superposition of incoherent point sources. Assuming for instance an angular size of 0.01 λ/d where d is the telescope diameter, one get a leakage at e.g., 3 λ/d of 1e-7 for a topological charge l = 2, 1e-11 for l = 4, 1e-15 for l = 6, respectively.

The power law is only valid very close in, well inside the λ/d radius. The transmission of an off-axis companion is also affected by the vortex, but in a very minor way compared to amplitude coronagraphs (see Figure 8.7.2-3 for a topological charge 4 VVC).

8.7.2.1.4 Manufacturing the VVC

Several techniques exist to implement a VVC. One can think of using natural birefringent crystals, but this is obviously not convenient to generating the desired smooth birefringent space-variant distributions. The second possibility is to use artificial "form birefringence," i.e., a subwavelength grating structure [25, 26]. Several prototyping operations are underway using this technology.

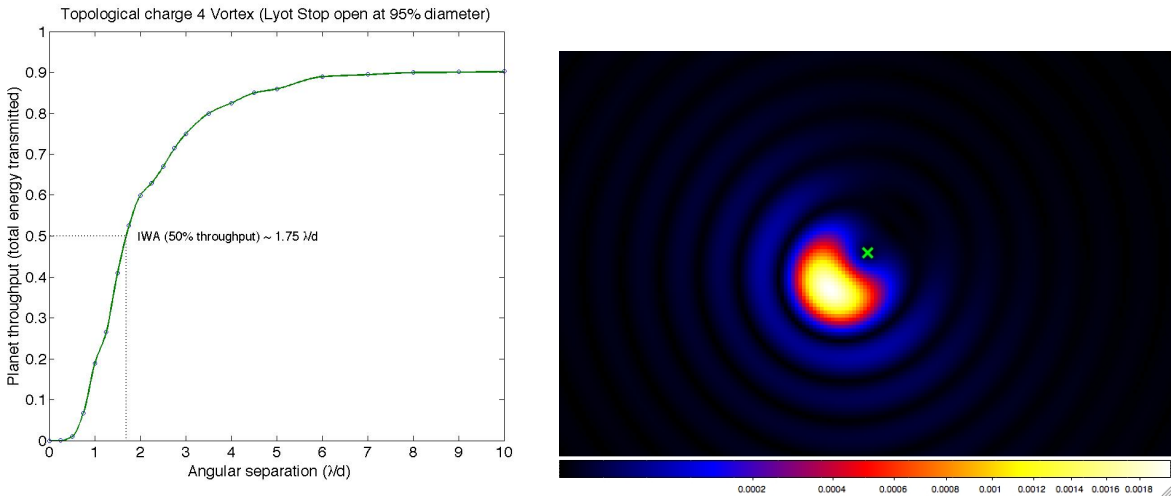

Figure 8.7.2-3. *Right*: off-axis transmission and IWA for a topological charge 4 VVC with 95% diameter Lyot stop. *Left*: off-axis PSF at the IWA of 1.75 λ/d.

However, the technique is very difficult at optical wavelengths because of the large aspect ratio needed in the grooves. Thus, this technology may be more suitable to longer wavelengths. Third, one can think of using photonic crystal structures, those structures analog to subwavelength gratings suffer from high chromaticity and flexibility issues in the design (topological charges greater than 2 are currently impossible to manufacture). Finally, a fourth approach is based on liquid crystal polymers (LCP) [30]. As this latter approach appears fairly promising [31], we focus on this approach in the following.

8.7.2.1.4.1 Liquid Crystal Polymer Technology

Liquid crystal polymers are materials that combine the birefringent properties of liquid crystals with the excellent mechanical properties of polymers. The orientation of a LCP is achieved through photo-alignment. Once aligned and cured, the polymer reaches a very stable solid state. A description of the specific proprietary process used by JDSU Uniphase (formerly Optical Coating Lab, Inc.) to make the LCP vortices follows. A photo-alignment layer (ROP108 from Rolic) is spin-coated onto the substrate, baked, and then the alignment is set through exposure to linear polarized UV (LPUV) light. The alignment layer is exposed through a narrow wedge shaped aperture located between the substrate and the polarizer. Both the polarizer and the substrate are continuously rotated during the exposure process in order to create a continuous variation in photo-alignment orientation as a function of azimuthal location on the substrate. The variation in fast axis orientation with azimuthal angle is determined by the relative rotation speeds. The LCP precursor (ROF5104 from Rolic) is then spin-coated and subsequently polymerized using a UV curing process. It naturally orients itself according to the photo-alignment layer. A post-bake stabilizes the films into a solid SVBOE (Figure 8.7.2-4).

The polarization properties of an initial prototype device were mapped on an Axoscan Mueller Matrix Spectro-Polarimeter available from Axometrics. The sample is placed on an x-y stage and mapped at a 0.5 × 0.5 mm xy-resolution over a 20 × 20 mm area. The beam size is about 2 mm, so the measurement at each point represents an average over the beam area. Summary maps of (a) linear retardance; (b) fast axis orientation are provided in Figure 8.7.2-5. The fast axis maps are given in degrees and with a range from −90 to 90 degrees. The orientation in all cases varies continuously. Those results showed excellent match to the specifications.

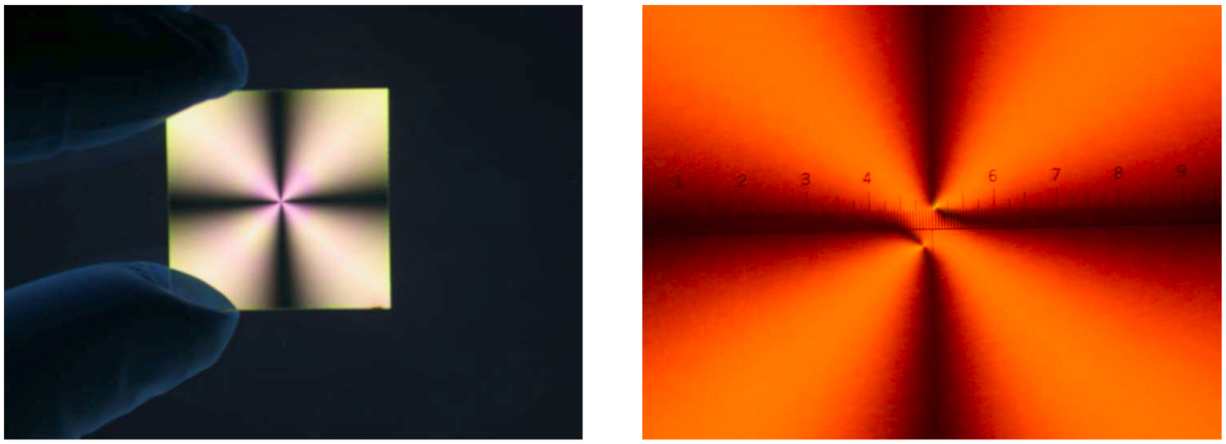

Figure 8.7.2-4. Pictures of the topological charge 2 LCP device of generation 0. *Left*: global picture taken between crossed polarizers (size = 2 inch square). *Right*: zoom under polarimetric microscope at 100× magnification, showing a superimposed graduated scale (1 unit = 100 microns).

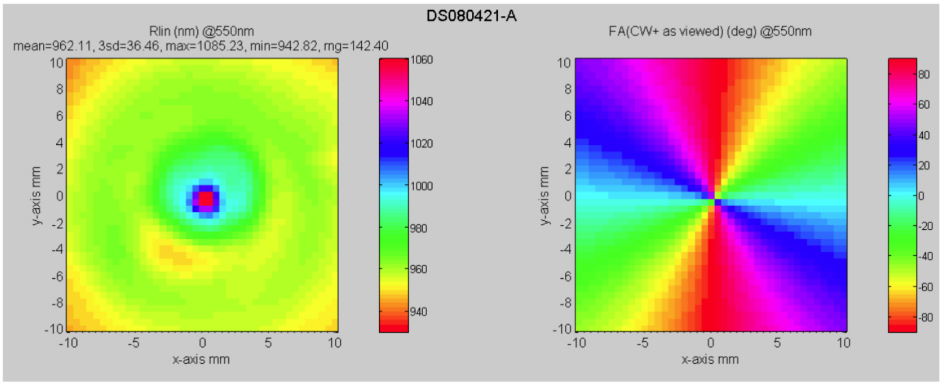

Figure 8.7.2-5. Axoscan sample characterization at λ = 550 nm. Left: linear retardance in nm. Right: fast axis orientation. Taking the LCP retardance dispersion behavior into account, the measured retardance value of 962 nm at λ =550 nm is found to be equivalent to the target retardance of 826.5 nm at λ =1650 nm (halfwave). The retardance map suggests a small relative rise in retardance at the center region.

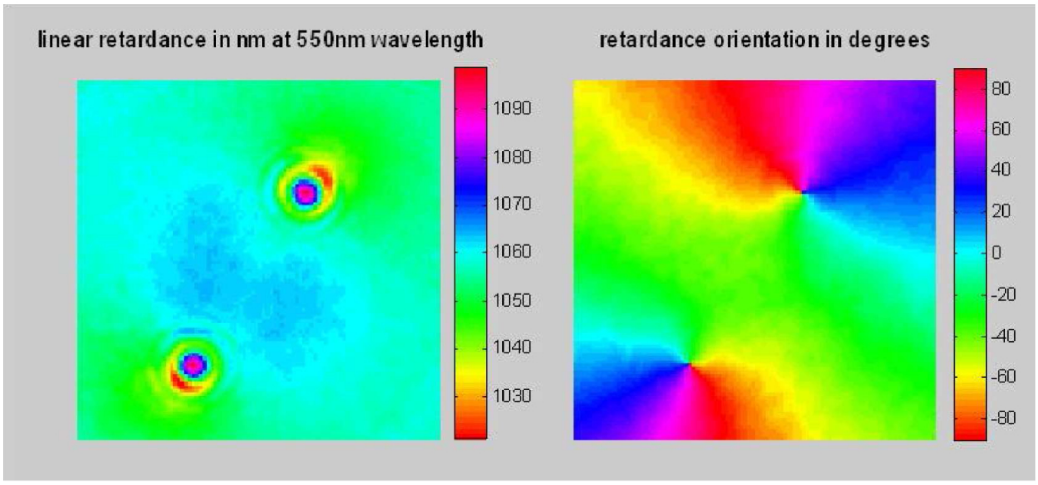

Figure 8.7.2-6. Magnified image of the linear retardance in nm (*left*) and retardance orientation (*right*) for the first prototype measured using a Mueller Matrix microscope. The field of view is 100 × 100 microns.

The first prototype samples were then measured on a Mueller Matrix microscope to determine the specific polarization properties of the sample close to the center of the vortex phase mask at ultra high resolution. The system used to make these measurements was a Mueller Matrix imaging polarimeter setup such that the microscope and camera field of view was approximately 100 microns. The instrument is located at the University of Arizona College of Optical Sciences polarization laboratory. The CCD detector active area was 100 × 100 pixels so the instantaneous field of view of each pixel was 1 micron. The measurement wavelength was 550 nm matching that of the Axoscan polarimeter. The measurement of the retardance and retardance orientation is given in Figure 8.7.2-6. The retardance measurement at 550 nm indicates the retardance is uniform except at two points symmetrically spaced about the center at radii of < 34 microns, where the orientation spatial variation is large. The value of the retardance is very close to that measured by the Axoscan at the center of the vortex retarder. The retardance orientation measurement indicates that the orientation is continuous at the 1-μm resolution. This point is of extreme importance and shows that the phase ramp induced by the VVC is continuous down to unprecedented smooth levels, compared to the scalar vortex.

8.7.2.1.4.2 Central Region of Disorientation

The MM measurements of the generation 0 prototype also showed that the orientation was discontinuous at the same 2 points close to the center (Figure 8.7.2-4 and Figure 8.7.2-6). The region between these two points defines a central zone which deviates from the overall large scale pattern (the "region of disorientation"). The distance between these points is approximately 68 μm. These two points are believed to originate from the manufacturing process. The cause of the microscopic polymeric chain confusion has been identified and is coming from misalignments in the manufacturing apparatus, which creates a gap between the narrow wedge photomask and the illuminated region of the LPP. Owing to Fresnel diffraction effects, the projection of the aperture vertex on the substrate is blurred by a significant factor.

Unfortunately, since most of the energy of the Airy diffraction pattern of the central point source effectively lands on the vortex center, this region of disorientation has to be as small as possible, and any remaining gap must be blocked by a well-dimensioned opaque mask. This requirement was the priority of the true generation-1 samples.

8.7.2.1.4.3 Generation 1 Prototypes—Reduction of the Size of the Region of Disorientation

Our manufacturer upgraded the photo-alignment apparatus, and managed to reduce the size of the central region of disorientation from 68 to 16 microns (4-fold improvement), for topological charge 2 samples (Figure 8.7.2-7, *left*). The remaining "confused hole" was covered with an opaque Al spot (Figure 8.7.2-7, *right*), well centered on the vortex.

Unfortunately, it appeared that the size of the region of disorientation scales with the topological charge. The topological charge 4 sample showed a 36 micron wide confusion zone (Figure 8.7.2-8). We covered it with a 40 micron Al spot.

8.7.2.1.4.4 Multi-layer Nature of a Sample

Any sample using the LCP technology is composed of several layers, as schematically shown in Figure 8.7.2-9. The LCP and LPP layer are deposited on a high optical quality, very-well polished (λ/20 PTV) glass substrate, 0.8 mm thick. The cover plate glass on which an opaque Aluminum mask of very high OD is applied is bonded to the LCP/LPP/substrate thanks to an optical adhesive.

The multi-layer structure of the LCP OVVC, with different material of different refractive indices, generate multiple low level ghosts (Figure 8.7.2-10). Those ghosts were affecting contrast and wavefront control in the first generation sample. By a careful optimization of the AR coating and material composing the layers (adhesive, substrate), ghosts can be significantly reduced down to acceptable levels (<1e-10).

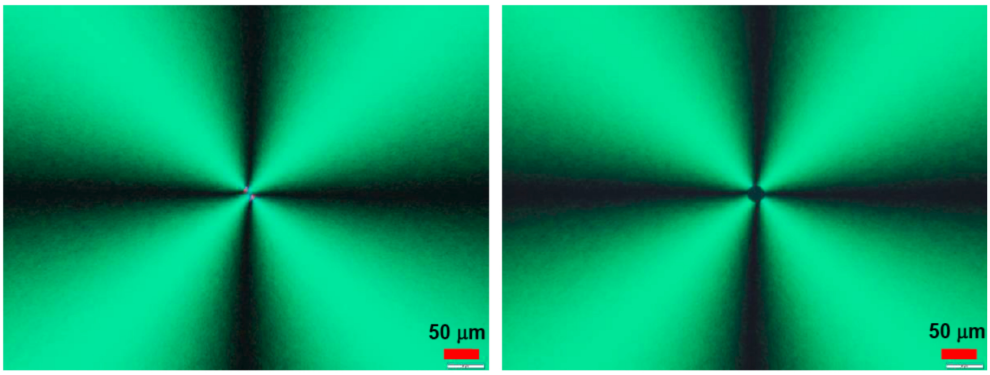

Figure 8.7.2-7. VVC topological charge 2 K-band sample between crossed polarizer before (*left*) and after (*right*) the lamination of the cover substrate on which the Al spot is coated (diameter of 25 microns). Note the good centering of the spot on the vortex center and the almost perfect symmetry of the pattern.

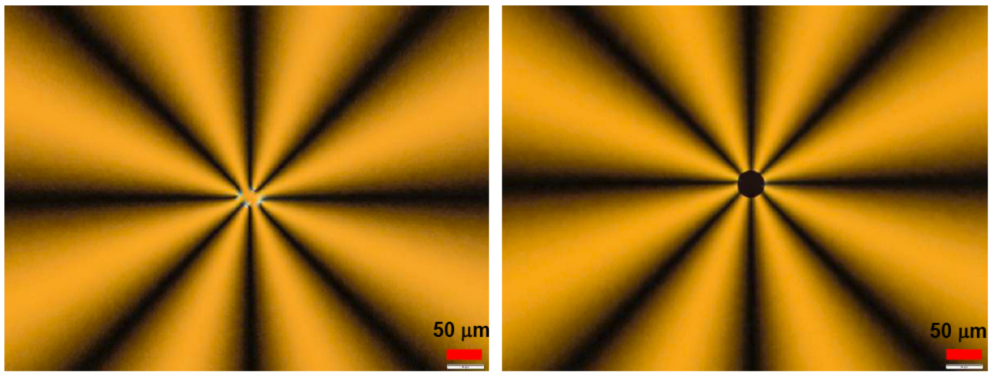

Figure 8.7.2-8. Topological charge 4 optical VVC sample between crossed polarizer before (*left*) and after (*right*) the lamination of the cover substrate on which the Al spot is coated (diameter of 40 microns). Note the good centering of the spot on the vortex center and the almost perfect symmetry of the pattern, which contains twice more azimuthal modulations than the topological charge 2 samples.

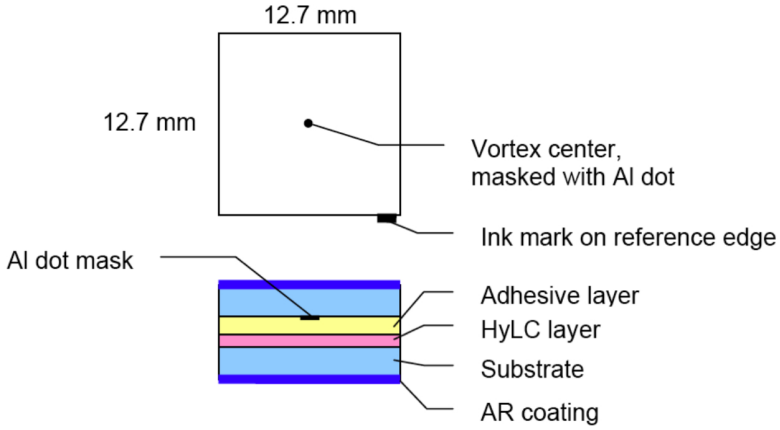

Figure 8.7.2-9. Structure scheme of the VVC samples (not to scale). The structure consists of the actual LCP (liquid crystal polymer) layer a few microns thick, a very thin LPP (precursor) layer about 40 nm thick, in sandwiched between two AR-coated infrasil substrates. An adhesive layer is used to laminate the top substrate on the LCP layer directly.

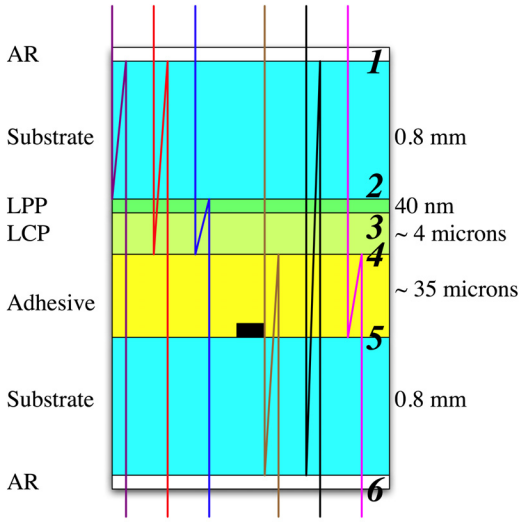

Figure 8.7.8-10. Multi-layer stack ghost analysis.

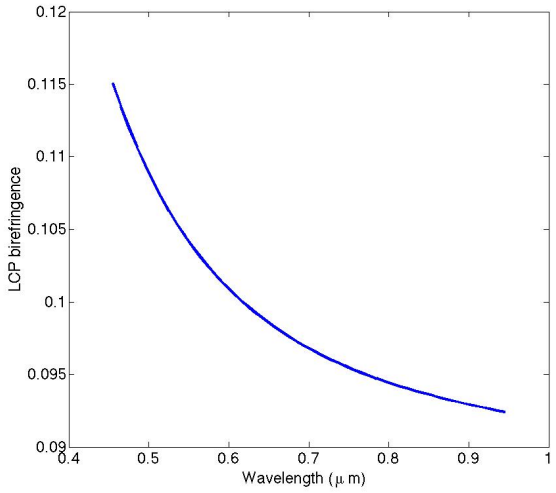

Figure 8.7.2-11. LCP theoretical birefringence (Sellmeier fit to experimental data).

8.7.2.1.4.5 Chromatic Leakage of the LCP

The dispersion of the extraordinary and extraordinary indices of the birefringent LCP has been measured and calibrated in the visible (see theoretical curve in Figure 8.7.2-11), allowing the precise calculation of the chromatic leakage term.

Retardance Error

The LCP retardance is chromatic and well characterized. Calculating the thickness t of the LCP to yield the necessary π radian retardance for a given wavelength λo from the birefringence $\Delta n(\lambda o)$ is trivial, $t = \lambda o / (2\,\Delta n(\lambda o))$. Then, the retardance dependence is $\Delta\Phi(\lambda) = 2\pi\,\Delta n\, t/\lambda$, which contains two chromatic factors. First, the LCP birefringence is dependent on wavelength (Figure 8.7.2-11). Second, the retardance depends hyperbolically on the wavelength λ. Those two factors lead to a non-zero chromatic leakage term in a single-layer LCP VVC, as discussed earlier, and as shown in the red curves of Figure 8.7.2-12.

However, a "superachromatic" design is possible for a VVC, again making use of the geometrical phase, but using a stack of several layers with offsets between their optical axes. This principle has been known for half a century [32] and is even commercially offered by waveplate vendors (e.g., Halle Gmbh). The basic three-layer design consists of three identical retarder layers (1, 2, 3) having nominal retardance values L1 = L2 = L3 = Lnom = π at some wavelength λ. The respective optical axes α1, α2, α3 of those layers are nominally defined as follows (relative to some arbitrary angle reference, see Figure 8.7.2-13): $\alpha 1 = +30^\circ$, $\alpha 2 = -(30^\circ+\delta)$, $\alpha 3 = +30^\circ$, where δ is a small modifier angle (i.e., on the order of 0 to a few degrees) that is adjusted produce the desired bandwidth (at the expense of retardance variation within the band). In practice, the six parameters at each spatial location (L1, L2, L3, α1, α2, α3) are subject to certain fabrication errors which result in some amount of deviation from the nominal design behavior. The retarder material has also a certain known dispersion of its birefringence with wavelength that has to be taken into account in the design of a VVC mask of a given desired bandwidth and rejection.

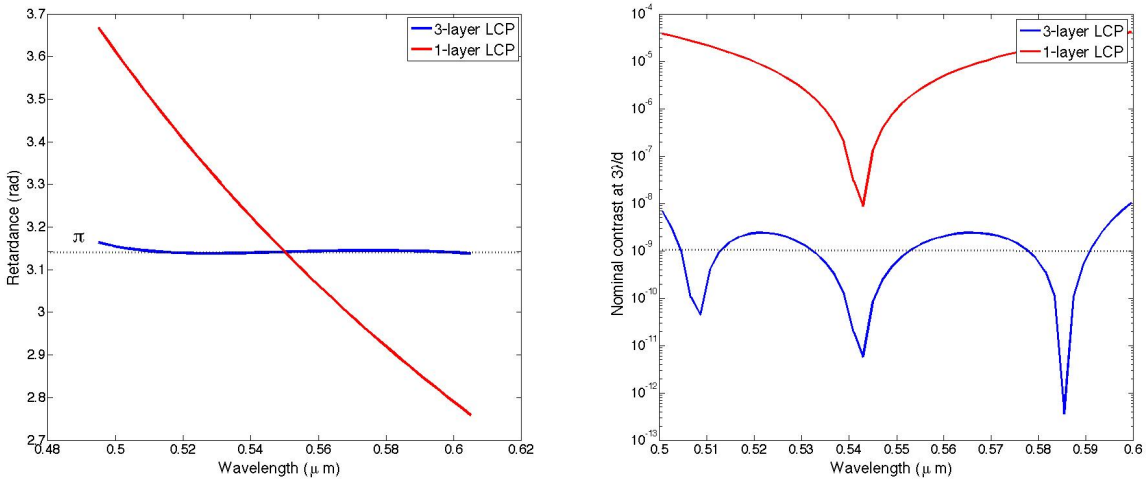

Figure 8.7.2-12. *Left*: retardance of a 1-layer LCP vs. 3-layer design LCP. The goal π retardance is represented by the constant dotted curve. Note the high chromaticity of the 1-layer design vs. the very high achromaticity of the 3-layer one. *Right*: left retardance curve transposed into contrast curve at 3 λ/d, via the nulling formula $(\Delta\Phi(\lambda) - \pi)^2/4$.

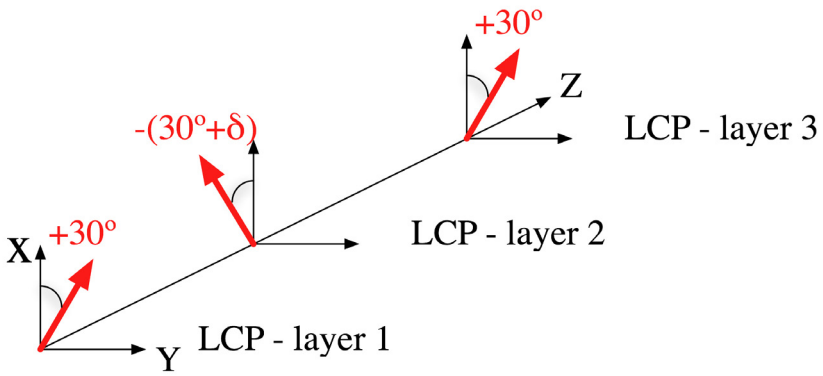

Figure 8.7.2-13. 3-layer superachromatic design. The red arrow shows the fast axis orientation in the X-Y plane.

Design 20—Influence of Manufacturing Errors

This design aims at a bandwidth of 20% with a contrast of 1e-9 at the inner working angle (IWA) of 2 λ/d. The modifier angle δ for this design is of 24 arcminutes (result of an optimization). Results in terms of retardance and contrast are shown in Figure 8.7.2-12 (left and right, blue curves). The dispersion of the LCP has been taken into account, but fabrication errors have not. To do that, we have performed a statistical analysis, assuming random thickness errors for each layer with a standard deviation of 0.5% on the thickness (this precision is currently achieved by the manufacturer), and a random error of 0.5 arcminutes on each layer offset angle of the optical axis. The results of the statistical analysis are shown in the histogram of Figure 8.7.2-14 (top), counting the number of samples yielding a given contrast. Aiming for 1e-9 with such errors, results in a probability of ~25% of obtaining a compliant sample.

Design 10—Influence of Manufacturing Errors

This design aims at optimizing contrast in a 10% bandwidth. The modifier angle δ for this design is of 8 arcminutes (result of an optimization). To assess feasibility, we have performed the same statistical analysis as for design 20, assuming the same random thickness errors for each layer with a standard deviation of 0.5% on the thickness, and a random error of 0.5 arcminutes on each layer

offset angle of the optical axis. The results of the statistical analysis are shown in the histogram of Figure 8.7.2-14 (bottom), counting the number of samples yielding a given contrast. Aiming for 1e-10 with such errors, results in a probability of ~12% of obtaining a compliant sample. Remarkably, the 1e-9 goal appears easy now, with a probability close to 50% of getting a contrast better than 1e-9.

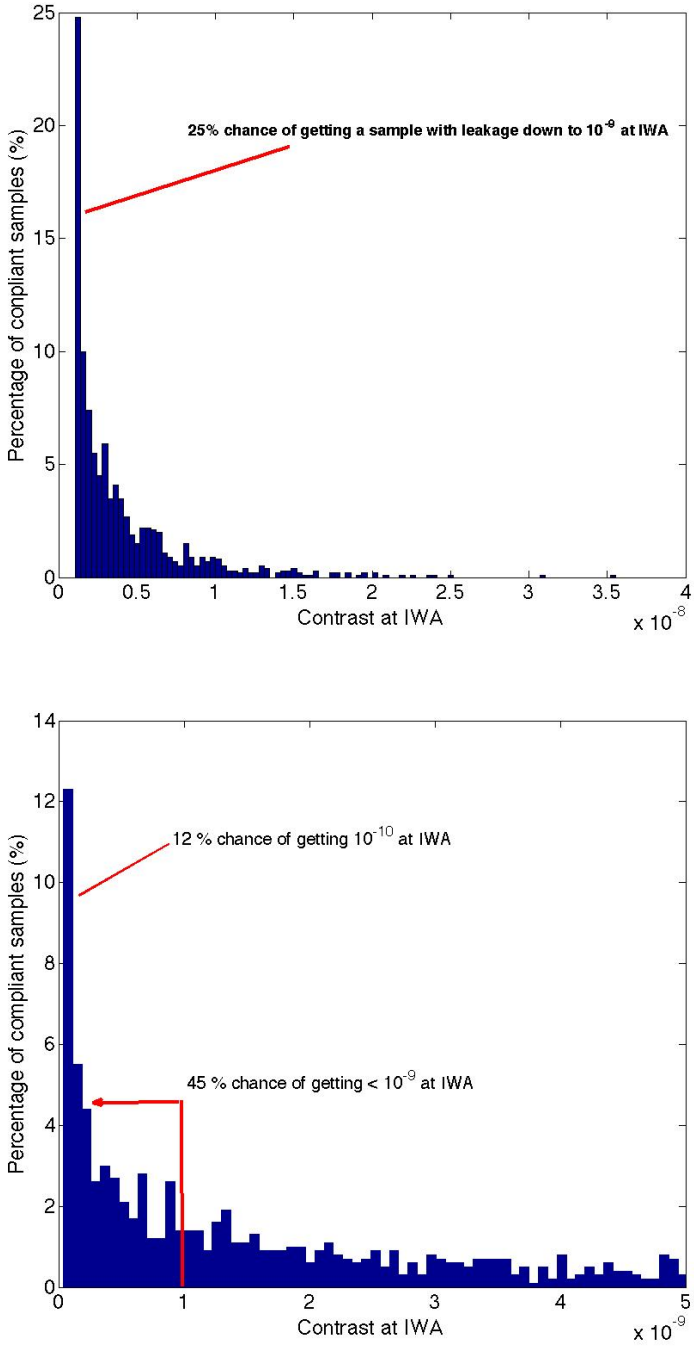

Figure 8.7.2-14. Statistical analysis of the influence of manufacturing error on the sample yield. *Top*: Design 20. *Bottom*: Design 10.

8.7.2.2 Specification of the Representative ACCESS Vector Vortex Coronagraph

ACCESS requirements are the most stringent ever imposed on a phase-mask coronagraph. To meet them, the three main VVC defects exposed earlier must be brought under control:

- The central region of disorientation must not be bigger than 10 microns (a factor of 4 improvement of what has already been realized for a 4th order mask).
- The chromatic leakage must be lower than 10^{-9} at 3 λ/d over a 20% bandwidth.
- Ghost reflections from the multi-layer nature of the VVC, must be lower than 10^{-9} at 3 λ/d.

8.7.2.2.1 VVC ACCESS Design

Details about the modeling are to be found in Appendix 8.8 (End-to-end Optical Propagation models). Here, we expose the VVC design that has been chosen for ACCESS. We have considered two optical cases, the first being with good 1.25 nm rms optics, and the second one considering extremely good optics 0.25 nm rms. Only the 1.25 nm rms optics case will be presented here, because it is the most realistic and because it already provides results compliant with the ACCESS requirements.

The VVC design is that of case 2, considered technically feasible this year

- Topological charge 4
- Central region of disorientation and opaque (OD > 6) Aluminum spot < 10 microns diameter
- 3-layer LCP design optimized for a 20% BW (D20) and/or 10% BW (D10)
- Ghost reflection brought under <1e-9 by a proper choice of substrate material and 0.05%-anti reflective coatings

Coronagraphic configuration

- Open Lyot stop at 90% diameter (throughput 81%)
- IWA defined at 2.0 λ/d (smaller, and therefore better than required)

VVC Model includes (see Appendix 8.8 for details)

- Chromatic effect of the central region of disorientation and opaque mask finite size
- Incoherent chromatic leakage, due to:
  - Retardance errors and chromaticity
  - Chromatic differential transmittances between local fast and slow axes.

Prescription (see Figure 8.7.2-15, and Appendix 8.8)

- PROPER ACCESS prescription with 0.25 nm rms and 1.25 nm rms optics
- Super-sampling of the vortex central zone by x 51
- Single polarization analysis (see Section 8.7.2.4)

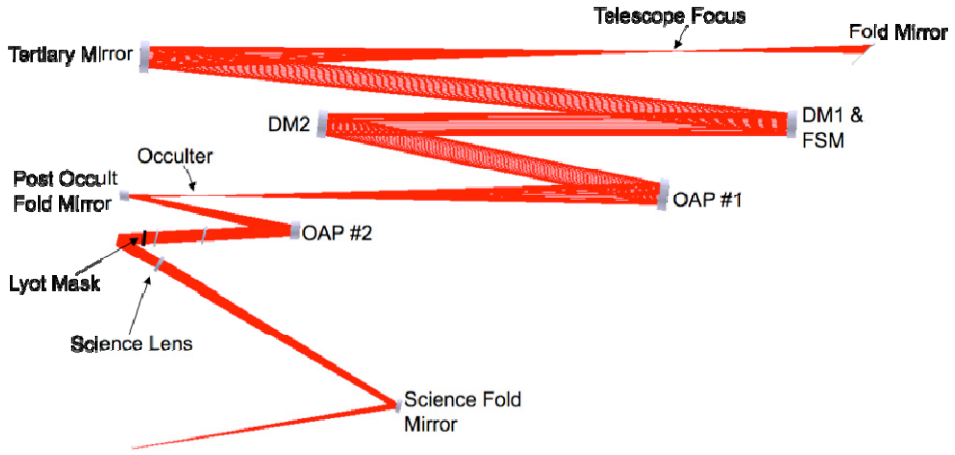

Figure 8.7.2-15. ACCESS optical prescription for the VVC, which is identical to the Lyot coronagraph.

Results

See Appendix 8.8 (End-to-end Optical Propagation models) and Appendix 8.9 (Science mission metrics).

8.7.2.2.2 VVC Sensitivity to Pointing Errors inside ACCESS

As mentioned in Section 8.7.2.1, the optical vortex coronagraph attenuation sensitivity to low-order aberrations like tip-tilt *tt* is proportional to tt^l, where l is the topological charge. Figure 8.7.2-16 shows the theoretical curve for a topological charge 4 vortex, while the blue one shows the numerical result obtained with the full access prescription and the realistic model of the VVC in a 20% BW. The result shows a negligible sensitivity to the ACCESS residual pointing error provided by the pointing control system (0.45 mas rms, 3s). Here we even conservatively assumed a PTV mispointing of 0.45 mas. The latter, overestimated on purpose, only contribute to the total contrast at 2.0 λ/d, by 3e-11, which is well below our contrast floor of 2.9e-9 at 2.0 λ/d. In conclusion, the pointing control system gives us plenty of margin.

8.7.2.3 Summary of Recent Laboratory Experiments on the HCIT

The High Contrast Imaging Testbed (HCIT), a laboratory facility at JPL, is the state-of-the- art coronagraphic bench (see Section 8.7.1). This facility highlights a vacuum chamber mounted on vibration isolation blocks, and a high-order 32 × 32 deformable mirror (DM) which is the key to the necessary wavefront active control. The HCIT light source is a supercontinuum laser, filtered by one of 6 passband filters; 5 filters have center wavelengths of 768, 784, 800, 816, and 832 nm and (nearly square) 16 nm bandpasses ($\Delta\lambda/\lambda$ = 2%). Inside the tank, the light from the source is passed through an unresolved pinhole.

When power is applied to the DM, the phase errors of the system are dominated (at the spatial frequencies of interest to us) by the surface of the DM, whose actuators have differing voltage-to-displacement relationships. After powering up the DM, the first activity is to flatten the system, using a modified Gerchberg-Saxton estimation procedure. The goal of this initialization step is to produce a front-end exit pupil with a uniform phase across the aperture, where front-end refers to the optics preceding the occulter. This technique typically leaves a 5 nm rms residual front-end

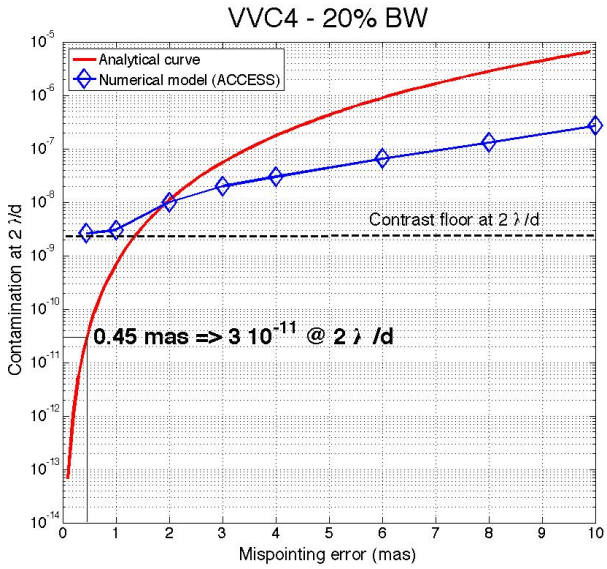

Figure 8.7.2-16. VVC theoretical sensitivity to pointing errors (red curve), and inside the ACCESS prescription with wavefront errors, and the realistic model of the VVC detailed here above (blue curve and diamond data points).

wavefront error. At periodic intervals during normal operation, the occulter is re-centered on the image of the source. Remotely controlled actuators translate the occulting mask to compensate for slow environmental drifts.

The photometric calibration is also periodically recalculated. The photometric calibration scheme used relates images taken with the occulter in-place to images taken with the occulter out-of-place, establishing a ratio between the light at the peak of the unocculted point-spread function (PSF) to the wings of the occulted PSF (well beyond the image region directly controllable to the Nyquist spatial frequency of the DM actuators). This ratio has been seen empirically to be quite stable (few % variations over months), and is used to photometrically calibrate every image taken during normal operation.

To create a so-called dark hole, i.e., a region of the image were the wavefront correction provided by the DM is applied, we used the electric field conjugation algorithm [33]. The name of the algorithm comes from the fact that the DMs actuators are set so as to superpose the negative of the electric field onto the image plane, conceptually making the image intensity zero. The algorithm is divided into two parts, estimation and correction. The complex electric field amplitude in the image plane is estimated, then the estimate is processed to determine a correction to be applied to the DM actuators. These two parts are functionally independent, and each could be used separately with other approaches. Each EFC iteration begins with a DM setting which is the result of the prior iterations correction result (or is the flat setting, to begin the first iteration).

8.7.2.3.1 Pupil Imaging

The HCIT is equipped with a pupil imaging mode, consisting of a very high quality re-imaging lens that can be inserted into the optical path. This mode allows checking the consistency of our model against the actual behavior of the VVC in the pupil plane. Indeed, the action of the VVC in the pupil is dramatic (Figure 8.7.2-17), as all the light originally inside the pupil theoretically emerges outside the pupil, as verified in practice (Figure 8.7.2-17, right).

8.7.2.3.2 Dark Hole Images and Contrast Results

We have performed a set of runs with the first topological charge 4 sample. Here are the detailed characteristics of this sample:

- Topological charge 4
- Single-layer design
- Central region of disorientation 36 microns in diameter
- Opaque Al spot 40 microns in diameter
- Central wavelength (π radian retardance) of 788.5 nm as measured by the Axoscan polarimeter

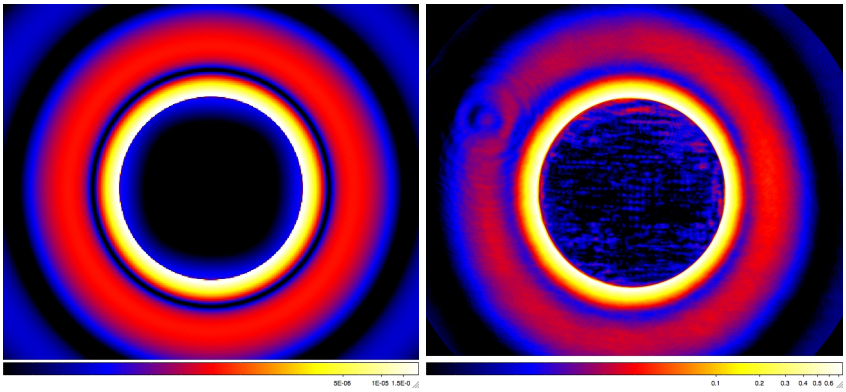

Figure 8.7.2-17. Pupil images from the model (*left*) and actual measurement on the HCIT using its pupil imaging mode (*right*). Note the very sharp edge defining the pupil contour. The scale is logarithmic.

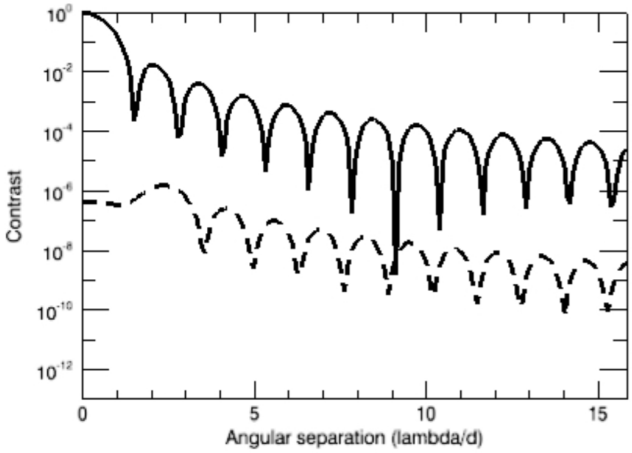

Figure 8.7.2-18. Expected results with a perfect wavefront, and our monochromatic, 40-micron Al-spot, first prototype of topological charge 4. The plain curve shows a radial cut in the PSF, while the dashed one shows the attenuated profile after coronagraphic action.

Expected Results with a Perfect Wavefront

We ran numerical simulation to assess the potential of this first sample, given the fact that a single-layer LCP was already known to be chromatic. We assumed a perfect wavefront at a single wavelength (788.5 nm) and the sources of defect mentioned here above. The results in terms of contrast were 1e-6 at 3 λ/d. The main source of monochromatic contrast degradation with a perfect wavefront is the size of the Al spot covering the central region of disorientation. The latter indeed creates diffraction effects, causing light to leak from the edges in the Lyot plane (see Figure 8.7.2-18).

Measured IWA on the HCIT

The effective inner working angle of the VVC was measured on the bench to be 1.8 λ/d, which corresponds to the theoretical value for a topological charge 4 vortex (Figure 8.7.2-3).

Measured Contrast Results on the HCIT

After trying different sources (LASER at 784 nm, then supercontinuum in 2% filters), different Lyot stop values (63%, 80%), and wavefront sensing schemes (unpolarized, polarized), we arrived at the following configuration, providing the best results for this first prototype:

- IWA set at 3 λ/d
- Lyot stop open at 80% diameter
- Sensing at 800 nm, and measuring in 5 2%-filters from 768 to 832 nm
- Circular polarizing beamsplitter in front of the camera, sensing and correcting in 1 polarization (see Section 8.7.2.4.1)

The result in terms of contrast at the inner working angle (3-4 λ/d, small box) and in the whole field is ~2e-7 at 768 nm (Figure 8.7.2-19 and Figure 8.7.2-20), which was a surprise for two reasons. First, the pump wavelength at which the probes are taken, and wavefront control is done, is at 800 nm (see the plain curve in Figure 8.7.2-20, showing a very obvious dip down to 5e-10 at that particular wavelength). Second, the sample central wavelength (where the retardance ought to be π according the Axoscan polarimetric measurement) should be 788.5 nm. We would have expected the chromatic leakage to be minimal at this wavelength. It is still unclear why contrast is best at the shortest wavelength.

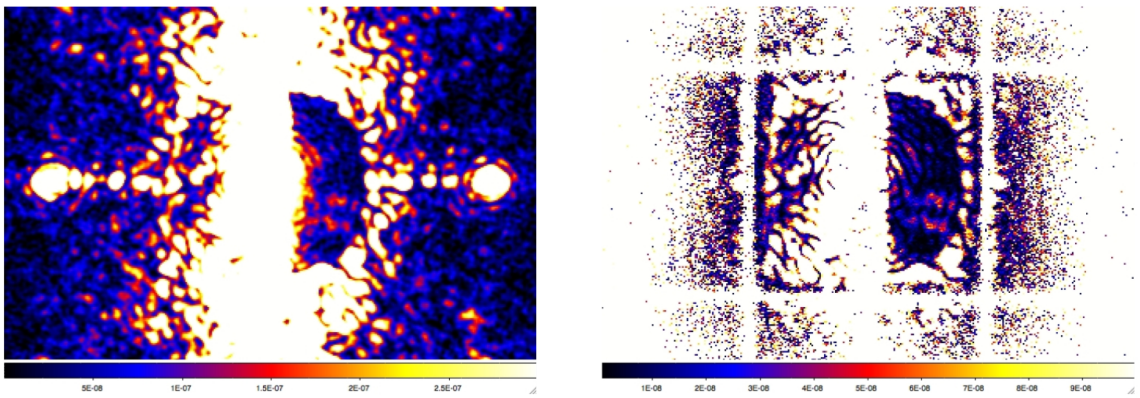

Figure 8.7.2-19. HCIT dark hole. *Left*: direct image (incoherent). *Right*: reconstructed image (coherent).

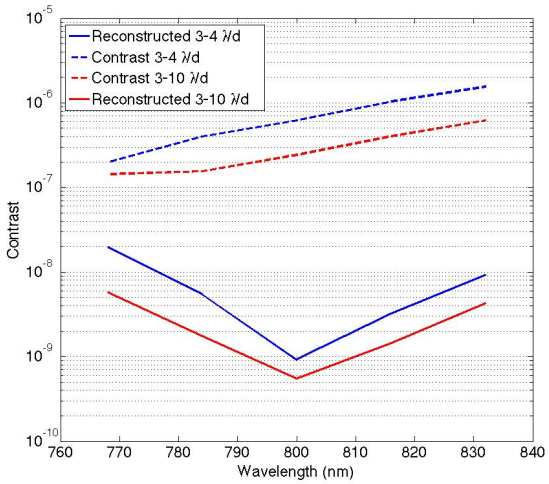

Figure 8.7.2-20. Contrast results obtained on the HCIT with the first topological charge 4 VVC. The blue curves show the contrast in the so-called small box (3-4 λ/d, 1 λ/d square). The red ones are integrated in the whole half dark hole (3–10 λ/d). The dotted curves show the chromatic dependence on the real measured contrast on wavelength. The plain curves show the computed contrast extracted from the reconstructed images (from the phase diversity applied to the DM).

The important conclusions of those preliminary tests were:

- The result with wavefront control is 10 times better than expected with a perfect wavefront.
- Splitting the polarizations and sensing in one polarization only at the end helps the wavefront control system, and appears mandatory to get to the highest contrast.
- The reconstructed image shows the same speckle morphology as the direct image, but at a level which is significantly lower (factor 10–100).
- The gap between the reconstructed and direct image is smaller at small wavelength.
- The chromaticity of the reconstructed image and direct image is different, with a very obvious dip and wings for the reconstructed image, and a smooth linear degradation with wavelength for the direct image.

The discrepancy between the reconstructed image and direct image behavior can be explained by considering mutual coherence of the VVC terms, and the fact that the reconstructed image is known to show the coherent content of the beam, while any discrepancy with respect to the reconstructed signal ought to be from incoherent sources. Here is a list of incoherent sources of light that can all be attributed to imperfections of our first prototype:

- Ghosts originating from the multi-layer structures
- Chromatic leakage, shown here above to be mutually incoherent with the pure vortex term

Our contrast results were affected by both sources, and both will have to be worked out for the next generation of masks. We proposed the solutions to this double issue, with the superachromatic design that will reduce the chromatic leakage down to acceptable levels, and with a careful index matching and AR-coating our the multi-layer stack.

8.7.2.4 Technology Readiness and Future Prospects

The current TRL of the Vector Vortex is TRL 5. This year will see a transition from TRL 5 to TRL6.

Future prospects are to be found in improvements of the following aspects:

- Exploration of higher topological charges (lp=6, lp=8)
- Reduction of the central region of disorientation down to a couple of microns and/or exploration of new hybrid phase/amplitude profiles
- Routine manufacturing of 3-layer achromatic designs, exploration of 3+ layer achromatic design feasibility and potential
- Structural optimization of the multi-layer stack, with new optical adhesive and substrate materials in order to reduce ghost reflection below 1e-10
- Dual-polarization optimization of the dark hole (see Polarization Management section on next page)
- Validation of the LCP material for space environments

8.7.2.4.1 Polarization Management

Because opposite circular polarization states pick up azimuthal phase ramps of opposite signs (see the VVC canonical formula), phase errors downstream of the vortex mask are not automatically corrected in both orthogonal polarizations everywhere in the field simultaneously (Figure 8.7.2-21). However, this issue can be sidestepped by splitting the two polarizations on the camera, and by integrating the electric field information of both polarizations into the wavefront sensing scheme (here the Electric Field Conjugation algorithm). Limitations will then arise from the level of amplitude errors (including phase-induced amplitude errors) generated downstream the vortex mask (including amplitude errors generate by the mask itself), and especially by the optics between the

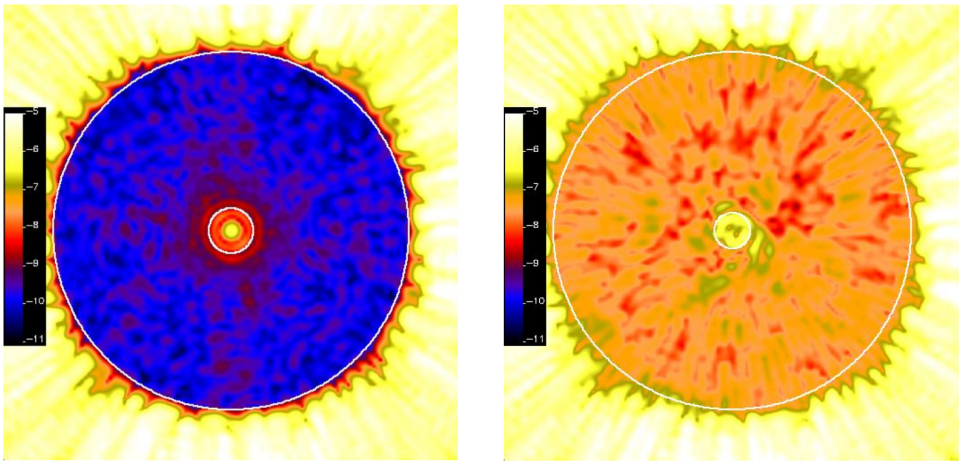

Figure 8.7.2-21. *Left*: dark hole for the left-handed circular polarization when the wavefront control system is asked to ignore the orthogonal right-handed state, the contrast level is of the order of 1e-10. *Right*: dark hole for the right-handed circular polarization state, keeping the same DM settings as for the left-handed circular polarization state. The contrast of the orthogonal state when it is not included in the wavefront sensing scheme is of the order of 1e-8.

vortex and the Lyot stop. If necessary, i.e. if the couple of incriminated optics cannot be manufactured with small enough aberrations, those errors can in turn be taken care of by one or more DMs downstream the coronagraph. This problem will be examined in greater details this year, but could be avoided by optimizing the prescription optical concept (see here below).

8.7.2.4.2 Optimizing the ACCESS Optical Concept for a VVC

To this point, we have tried to adapt the vector vortex coronagraph to the optical prescription of ACCESS. Apart from specific polarization management issues, its implementation is straightforward, and provides outstanding prospects, in terms of IWA, throughput and discovery space, as expected. Still, more could be gained by an optical design optimized for a VVC as the central coronagraph of ACCESS, which allows us to use the VVC polarization properties to our advantage. The unique polarization decoupling property offered by the VVC allows us to design a simple polarization filtering system that would solve the chromatic leakage issue, and would give us access to enormous bandwidth capabilities (in theory, 50% bandwidth could be achieved with on-the-shelf optical components). Coming back to the VVC fundamental Jones matrix

$$J_v(r,\theta) = V\begin{bmatrix} 0 & e^{il_p\theta} \\ e^{-il_p\theta} & 0 \end{bmatrix} + L\begin{bmatrix} 1 & 0 \\ 0 & 1 \end{bmatrix}$$

We note that the diagonals of the pure vortex and leakage term are crossed. In reality, this mathematical curiosity translates into an extremely interesting physical property: the leakage and pure vortex have orthogonal polarizations. An input left circular polarization yields a right-circularly polarized vortex and a left-circularly polarized leakage. An output right- circular analyzer would let the pure vortex out only, blocking the left-circularly polarized leakage (and the opposite would apply for the orthogonal input circular polarization). We can thus eliminate the chromatic leakage, by first splitting the input circular polarization states, and then refiltering the output polarization states. Thus, to first order, the filtered output of the vortex will always be pure, whatever the retardance precision is, and whatever the transmittance of the slow and fast axis are.

Note that any off-axis signal (point-source or extended source) will follow the polarization transformation of the pure vortex term and will not be attenuated by the filtering process.

In practice, the limitation will come from the extinction ratio (ER) of the circular polarizer/analyzer. The gain of the filtering process only depends on this ratio. Commercial circular polarizers (composed of a polarizer and a quarterwave plate), very easily provide an extinction ratio of 1e-4. This would imply the same gain in contrast over the leakage residual. Theoretical assessment of this potential is presented in Figure 8.7.2-22, showing better than
1e-10 contrast over 50% bandwidth.

Note that the loss of half the light is more than compensated for by the increased bandwidth. Of course, if desired, the orthogonal polarization state could by recovered at the cost of a duplicate optical train (Figure 8.7.2-23).

The gain of this optimized optical implementation would be three-fold [34, 35]:

- Each polarimetric channel could provide as much as 50% bandwidth, i.e., the whole visible spectrum, without requiring any other spectral channels, thus providing more instantaneous spectral information, lower spectral systematic errors, and enhanced observing efficiency.
- By simultaneously imaging two orthogonal polarization, we gain access to a speckle calibration technique (down to the non-common path errors between the two channels, if there is no internal modulation to the CPBS) that would not necessitate any roll of the spacecraft.

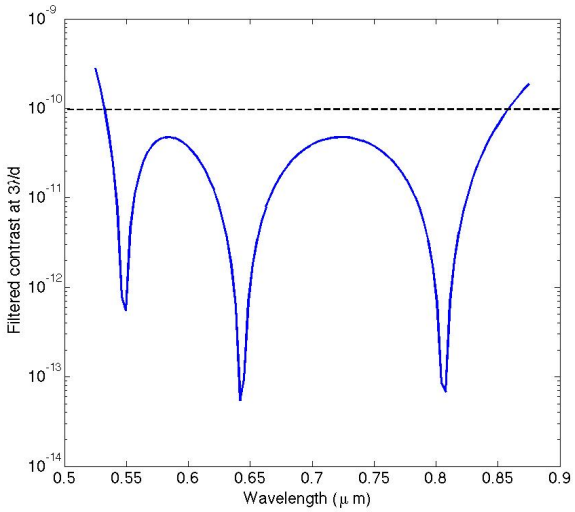

Figure 8.7.2-22. 1e-10 chromatic leakage of a dedicated 50% bandwidth 3-layer LCP design covering the whole visible spectrum, after polarization filtering with circular polarizer/analyzer with 1e-4 ER.

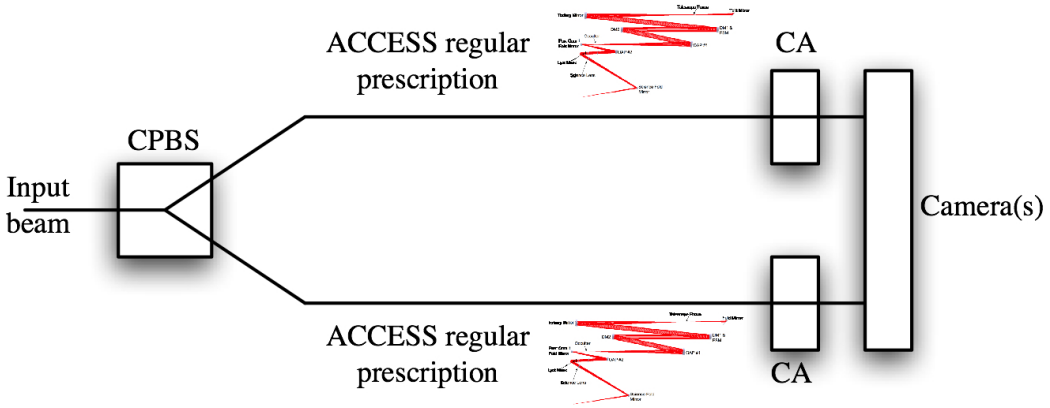

Figure 8.7.2-23. ACCESS prescription optimized to a vector vortex, which provides bandwidth and polarimetric capabilities. CPBS stands for circular polarizing beamsplitter. CA stands for circular analyzer.

- Adding spectroscopic capabilities to each channel would imply that the proposed system would be a spectro-polarimeter, one of the most complete characterizing instrument. Polarization is indeed known to be a substantial source of additional information for exoplanetary systems [36].

8.7.3 Pupil Mapping Coronagraph

8.7.3.1 Physical Principles of the Pupil Mapping Coronagraph

The principle of pupil apodization of a space telescope for high-contrast direct imaging of exoplanets appears in the literature even before the launch of the Hubble Space Telescope. Jacquinot and Roizen-Dossier [37] presented a comprehensive review of pupil apodization techniques for high contrast imaging. Bandermann et al. [38] proposed a space coronagraph for exoplanet imaging in the form of an unobscured off-axis gregorian telescope apodized with a Sonine

transmittance profile. This method for high-contrast imaging is nevertheless rendered impractical by an extremely low throughput, as for all transmissive ("classical") pupil apodization systems. A nearly lossless pupil apodization was proposed by Robb et al. [39], who described an exoplanet imaging telescope using a 5-lens system to map the uniformly illuminated telescope pupil into a Sonine or Gaussian intensity profile. The lens system alone was inadequate to bring the apodization to zero at the edges of the output pupil, therefore a transmission mask was introduced near the periphery of the final lens to complete the apodization.

The modern approach [40] uses a pair of aspheric mirrors to create an apodization specifically designed for high contrast exoplanet imaging at very small inner working angles. Guyon et al. [41] described an improved pupil mapping system that includes both forward and reverse mapping mirror pairs, plus an opaque focal plane occulting mask in the intervening space, known as the phase-induced amplitude apodization (PIAA) coronagraph. PIAA can in principle achieve high contrast and high throughput at inner working angles of 2 λ/D. Guyon et al. [41] and Belikov et al. [42] have shown that ancillary attenuating apodizations are required to improve bandwidth and contrast, leading to hybrid designs that achieve bandwidths of 20%. Studies have been made of the performance of the pupil-mapping coronagraph with one or two deformable mirrors [43]. The sensitivity of the pupil-mapped system to low-order wavefront aberrations has been analyzed by Belikov et al. [42]. The best reported laboratory performance with the first generation of PIAA mirrors is a contrast level of 2.2×10^{-7} averaged between 1.6 and 4.4 λ/D in monochromatic light [44].

8.7.3.2 Specification of the Representative ACCESS Pupil Mapping Coronagraph

The ACCESS pupil mapping design inserts a pair of deformable mirrors to the optical path upstream of the pupil mapping mirrors. The target apodization and specific shapes of the PIAA mirrors adopted for this study are as specified by Guyon [45] and manufactured by Tinsley under a contract from NASA/Ames. This is the "medium difficulty" Design 2, intended to be used with a post-PIAA apodizer that removes 15% of the light, mostly from the outer areas in the exit pupil. This PIAA design is scheduled for HCIT testbed evaluations in spring 2009, hence, this design provides the pathway for an improved experimental contrast demonstration in the coming year.

Our overall approach for ACCESS modeling is to first define optical elements with surface qualities that match, surface by surface, the corresponding elements in all four coronagraph types. Thus, with reference to the Figure 8.7.3-1, mirrors FM1, M3, DM1&FSM, DM2, and OAP05 are identical in every detail for all four coronagraphs. The pupil mapping design requires the addition of PIAA1, PIAA2, OAP15, OAP20, PIAA3, and PIAA4 to the path, elements that have no counterparts in the other coronagraphs. PIAA1, PIAA2, and PIAA4 are nominally flat mirrors, while PIAA3 incorporates an off-axis paraboloid into the figure to reduce the overall number of mirrors. Adopted surface figures errors for PIAA1 and PIAA2 are scaled from the as-measured (90 mm diameter) surface figure error maps, provided by Tinsley, to the 48 mm diameter of the ACCESS system. These maps were obtained with reference to the computer generated holograms (CGHs) used to guide the manufacture of the Design 2 system. Coronagraph contrast performance is considerably less sensitive to surface figure errors on the PIAA3 and PIAA4 mirrors, which appear in the optical path following the occulting mask, and are presumed to have the same surface error PSD as the OAPs.

The first of the PIAA mirrors, the "apodizing mirror," does the remapping from a uniformly illuminated pupil to a pattern of illumination concentrated towards the center in the form of the desired apodization. The second mirror, the "wavefront flattening" mirror, intercepts the beam at the point where the apodization is complete, and introduces the phase shifts needed to flatten the phase across the pupil. A transmissive post-PIAA apodizer is the next element in the pupil mapping performance. We illustrate the process with reference to Figure 8.7.3-2, taken from a design memo by R. Vanderbei [46]. At upper right, the target apodization for the apodizing mirror is plotted in blue.

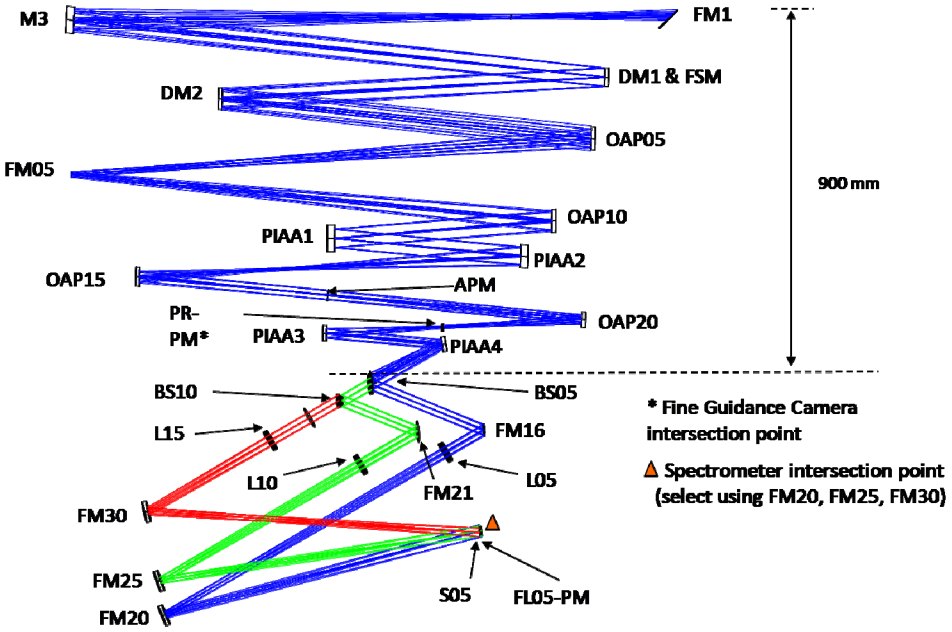

Figure 8.7.3-1. Schematics layout of the pupil mapping coronagraph.

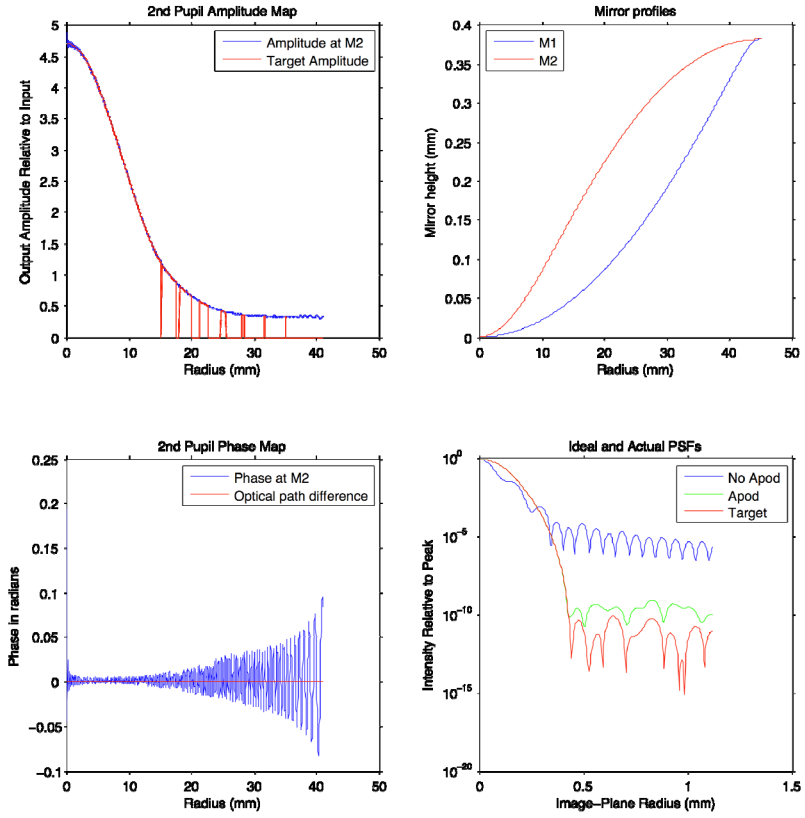

Figure 8.7.3-2. Design of the pupil mapping post-apodizer

The apodization is represented here by non-diffractive geometric mapping of rays, and is incomplete, reaching roughly 10% of the peak intensity at the edges of the pupil. A target apodization profile, designed to bring the apodization to zero intensity at the edges, is obtained by multiplying the blue curve by a grey-scale attenuating apodizer mask. At lower right are plots of the related pupil-mapping PSFs. The red "target" curve is the result of taking Fourier transform of the target apodization profile. It is this level of computational fidelity that we have used in the ACCESS modeling. For the actual optical system, it is necessary first to compute the diffractive propagation of light from the first to second mirror, corresponding to the blue "no apod" PSF curve at lower right, then a binary mask is designed (red pattern at upper left), resulting in the green "apod" PSF curve in the lower right plot.

The modeling of the wavefront propagation through the PIAA system is computationally intensive, a factor that has significantly limited the fidelity of the analysis possible within the scope of the ACCESS study, as compared to the other three coronagraph types. This has been discussed in greater detail in Appendix 8.9 in the context of modeling methods.

8.7.3.3 Summary of Recent Laboratory Experiments

The Ames-commissioned pupil-mapping system was integrated into the HCIT optical table in March 2009, and now scheduled for initial testing in a vacuum environment in the coming in May–July 2009. The first experiments will be carried out in monochromatic laser light. A pair of 32 mm diameter DMs are located in the optical path following the PIAA mirrors and the post-PIAA apodizing masks. Conventional EFC nulling will be applied to the DM pair. Inner working angle, determined by the design of the post-apodizer, will approach 2 λ/D. The outer working angle, imposed by the number of DM actuators across the pupil in the magnified post-PIAA optical path, will be approximately 3 λ/D.

The best contrast results to date were obtained in March 2009 at the laboratories of the Subaru Telescope. This result is plotted in Figure 8.7-1, along with other recent experimental contrast results. Further details can be found at http://caao.as.arizona.edu/PECO.

8.7.3.4 Technology Readiness and Future Prospects

We recommend investments in three areas critical to the pupil mapping approach.

First, an investment in fine-scale (~0.1 mm) ion beam figuring (IBF) of the pupil mapping mirrors, specifically to attack the severe curvature requirements for the outer few mm in radius of the M1 (apodizing) mirror. Improvement in aspheric figuring methods need to be improved over that which has been demonstrated to date, else pupil mapping performance will suffer from imperfect pupil apodization, leading to requirements for a more aggressive transmissive post-apodizer, reduced overall throughput and degraded inner working angles.

Second, we recommend investments to advance the computational techniques for pupil mapping. At this time, the single practical optical propagation algorithm with the fidelity required for end-to-end modeling of the pupil mapping coronagraph is the S-Huygens method [42], which is too slow for the many passes needed for setup of the wavefront control matrices and for optical tolerancing of the actively-corrected space coronagraph system. For example, the S-Huygens propagation from pupil mapping M1 to M2 involves the propagation of at least 400 azimuthal harmonics. The computation time for one end-to-end pass through the ACCESS optical system, which includes both a forward and reverse pair of pupil mapping mirrors, takes about 2.5 hours using an 8-processor, 64-bit, 3 GHz computer.

Third, a trade analysis of the optimal layout of pupil mapping and deformable mirrors. The ACCESS layout, for example, with DMs placed prior to the pupil mapping mirrors, provides a relatively large outer working angle, but also leads to a requirement for extremely high quality (~0.25 nm rms EUV lithography grade surfaces) in the optics between the pupil mapping mirrors and the occulting mask in order to achieve contrast better than 10^{-9} in a 20% bandwidth. These technology issues have generally been addressed by Belikov et al. [47].

8.7.4 Shaped Pupil Coronagraph

The Shaped Pupil Coronagraph (SPC) is a high-contrast imaging system pioneered at Princeton [48, 49] and originally designed for the TPF-C telescope. We summarize the work done to date on the SPC and evaluate its current and projected performance. What makes the SPC attractive is that it is very simple to make and set up, and it is inherently broadband. Owing to the simplicity of the SPC, it has quickly become a relatively mature technology with theoretical and experimental validations of its performance. Many shaped pupils have been designed to various specifications and tools are in place to quickly turn out more. Full vector-field simulations show that realistic shaped pupils can already achieve 10^{10} contrast in the absence of aberrations. A manufacturing process has been developed to make shaped pupils for as little as a few thousand dollars, at JPL and NIST. Shaped pupils have also been shown to be very insensitive to aberrations, and especially low order aberrations such as tilt and defocus. The SPC has undergone extensive studies in the lab, and in 2007 a suppression of 2.3×10^{-9} has been achieved in a 10% band of light (averaged across a region between 4 and 9 l/D), after EFC-based wavefront correction. The SPC lends itself well to many wavefront estimation and correction schemes. Simulations show that realistic shaped pupil manufacturing errors and realistic wavefront error can be corrected with a single DM at one wavelength, and 2 or 3 DMs in broadband. The main disadvantages of the SPC are throughput, PSF sharpness, and working angle, but the throughput disadvantage may be counterbalanced to an extent by the fact that SPC requires very few optical components and the fact that the light blocked by the mask may still be used for other things, e.g., to sense aberrations. A good journal overview article of shaped pupils is Kasdin et al. [50].

8.7.4.1 Physical Principles of the Shaped Pupil Coronagraph

Introduction

The SPC is a coronagraph that functions by apodizing the pupil in order to get a high-contrast PSF, and as such belongs to a large family of pupil-apodizing coronagraphs. The principle of apodizing the pupil in order to gain contrast was known for a long time (e.g., [51]). The essence of the technique is merely to replace the standard uniformly-illuminated pupil of the telescope by a different, apodized pupil, designed such that the resulting PSF of the telescope will be almost fully concentrated in a single spot and thus have a dark zone around it where planets can be found. As such, pupil-apodizing coronagraphs are probably the simplest way to achieve high contrast in an imaging system.

The uniqueness of the SPC is that the pupil apodization is binary and can therefore be made by cutting out or etching an appropriate shaped pupil mask in an opaque thin material. A wide variety of such binary apodizations can be found by nonlinear optimization techniques (e.g., [52–55]) to meet the original TPF-C specifications of 10^{10} contrast and 4 λ/D that are required to image Earth-like planets with a large (4–8 m) telescope. Unlike continuous apodizers such as those made by variably tinted glass, shaped pupil masks are intrinsically achromatic and free of phase error (at least to the extent they behave like binary masks), features that are very important for very high contrast in broadband. Furthermore, shaped pupil masks are relatively cheap and simple to manufacture.

A simplified schematic of a general telescope (not specifically ACCESS) with an SPC is shown in Figure 8.7.4-1. The system consists of the telescope, followed by the wavefront correction system and the SPC. The wavefront correction system can be designed to a large extent independently of the SPC. The SPC consists of the shaped pupil at a reimaged pupil plane, and the science camera with an optional star occulter if the camera itself is incapable of properly accepting light intensity with a 10^{10} dynamic range. The star occulter is a hard-edged mask designed to block the brightest portions of the PSF. If the star occulter cannot be placed very close to the chip, the science camera can be placed at a reimaged image plane downstream from the star occulter. Aside from imaging

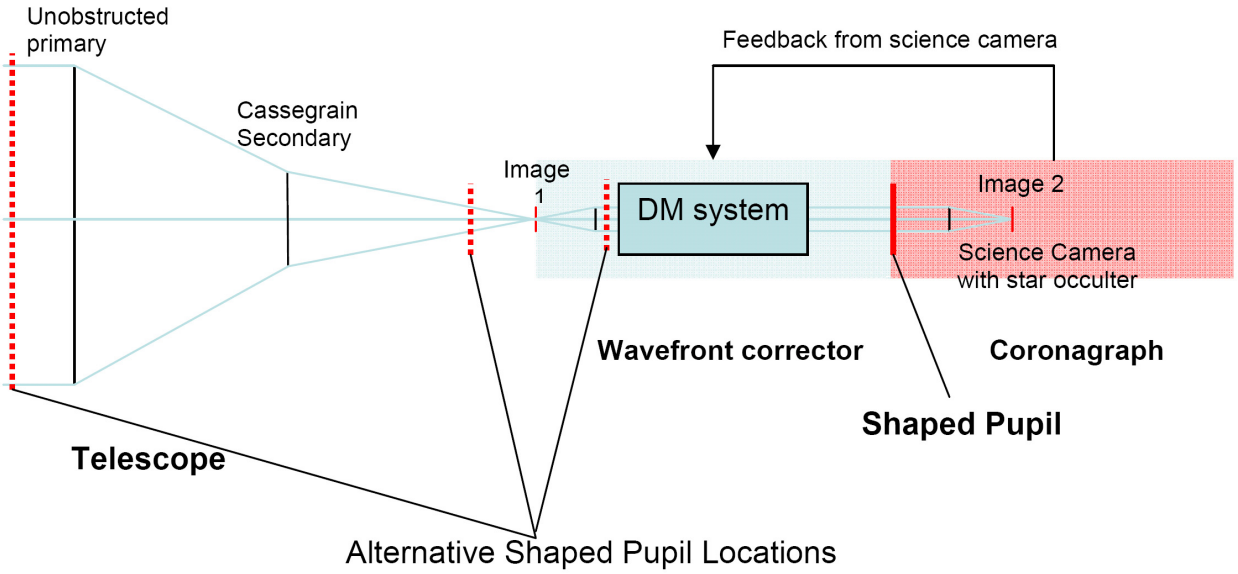

Figure 8.7.4-1. Simplified schematic diagram of the TPF telescope with a shaped pupil coronagraph. The shaped pupil can be placed in virtually any "pupil" plane.

planets, the science camera will also be used to estimate aberrations and feed this estimation data back to the wavefront correction system (additional cameras can also be used for this purpose).

Even though the typical position for the shaped pupil is as shown by the solid line in Figure 8.7.4-1, the shaped pupil can be located in many other planes, such as those indicated by the dotted lines. In fact, one attractive design is a single-mirror prime-focus telescope with a shaped pupil either in front of the primary or along the converging beam downstream. Such a prime-focus design is attractive not only because it is so simple, but also because it eliminates light losses and aberrations introduced by all optics except for the primary. (In fact, this design has no phase-induced amplitude or similar aberrations.) However, the prime-focus design may not be practical because it requires the ability to shape the primary to be free of aberrations and a few other technical challenges.

In any case, this flexibility of shaped pupil placement offers another advantage to shaped pupils, but unfortunately the exploration of this advantage was outside the scope of ACCESS. For purposes of ACCESS, the architecture adopted was similar for all the coronagraphs for reasons detailed in the body of the report and was not necessarily optimized for Shaped Pupils.

Shaped Pupil Design

The main design we decided to use for our ACCESS experiments is what we call the Ripple3, shown in Figure 8.7.4-2 along with its PSF. The design method was to start with sampled representations of 4 arbitrary openings in one quadrant of the mask and perform nonlinear optimization (using AMPL and the LOQO solver) to optimize throughput under the constraint that the contrast in the dark zone be less than 1×10^{-9}. (For more details, see [52–55].) The Ripple3 design has a theoretical contrast of about 3×10^{-10} (averaged from 4 to 10 λ/D), which is the contrast that would be observed in a perfect optical system with no wavefront control. The high contrast region has an inner working angle of 4 λ/D and two 90° openings as shown in Figure 8.7.4-2. The "ripple" style of shaped pupils is attractive because it lends itself easily to manufacturability as a free-standing mask (i.e., a cut-out from a substrate as opposed to an opaque mask deposited on a transparent substrate). This has the advantage that the light transmitted by the mask goes through free space and

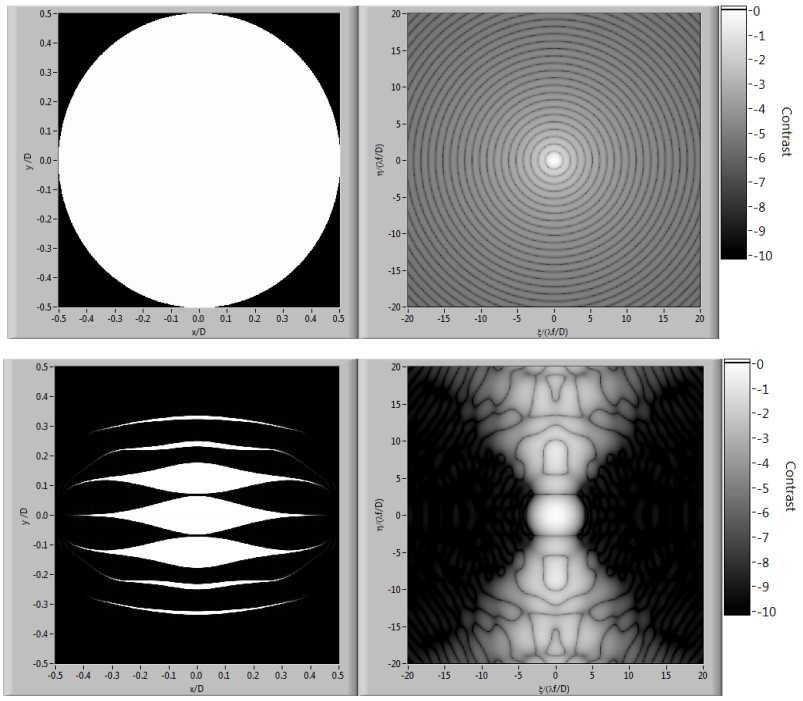

Figure 8.7.4-2. Two pupils (*left*) and their PSFs on a log scale (*right*). *Top*: Open circular aperture and its PSF, the Airy pattern. Note the absence of 10^{-10} contrast. *Bottom*: The "Ripple3" shaped pupil mask and its PSF, shown dark zones with high contrast.

Table 8.7.4-1. Comparison of three shaped pupils

Name	Contrast	IWA	Opening Angle	Total Throughput	Airy Throughput
Ripple3	3.00E-10	4 l/D	90 degrees × 2	17%	10%
Eclipse4	5.00E-08	4 l/D	90 degrees × 2	46%	33%
Ripple10	2.00E-08	3.2 l/D	45 degrees × 2	35%	25%

remains free of aberrations and ghosts. A disadvantage is that not the full 360-degree field of view is visible.

Even though for purposes of ACCESS, we have focused work on Ripple3, there are other designs that can be used. Out of many dozens of shaped pupils that have been created over the years, we would like to highlight three of them that we feel exemplify different trade-offs that are possible with the ripple-type shaped pupil design. The Ripple3 design has high intrinsic contrast but poor throughput and inner working angle. Eclipse 4 has high throughput but poor contrast and inner working angle. Ripple10 has good inner working angle but poor contrast and opening angle (see Table 8.7.4-1).

Simulations of Real Masks

In order for a real Ripple3 to retain a theoretical contrast of 10^{-9} or better (without wavefront control), it has to be manufactured precisely enough. According to simulations, shaped pupils turn out to be rather tolerant to random etching error (e.g., for a 30 mm-diameter Ripple3, a stray hole of up to 50 μm diameter is ok, as is random 0-mean error on the edges of up to several microns in variance; overetch or underetch of all the openings by as much as 200 nm is ok). All this is within the tolerances of the current manufacturing methods. However, the Ripple3 design calls for openings that can get extremely thin in places (see Figure 8.7.4-3. As was determined during one of

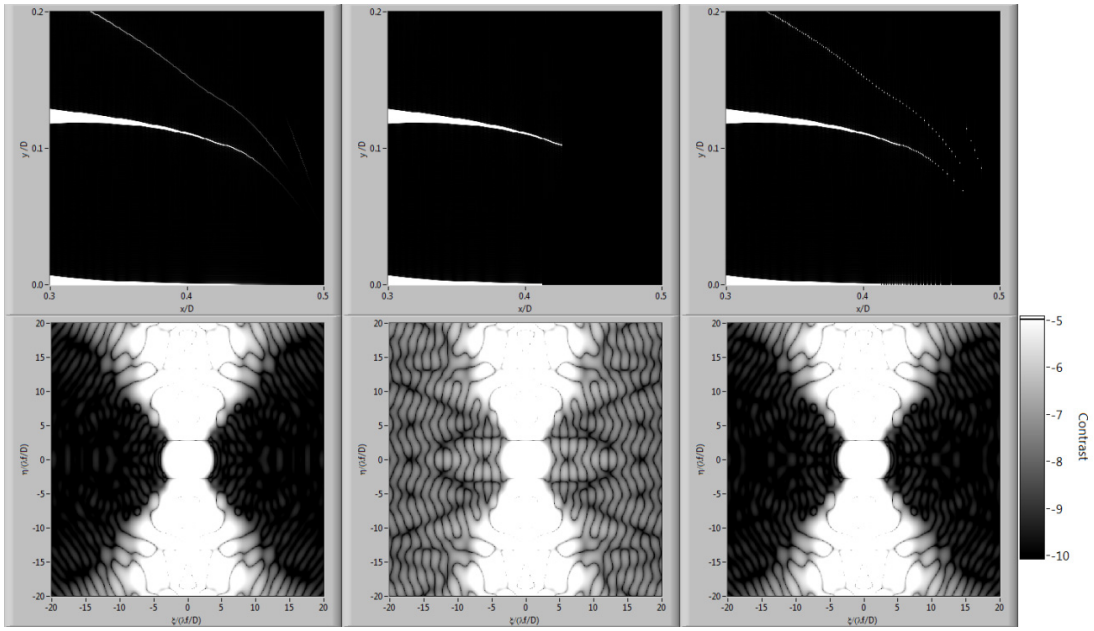

Figure 8.7.4-3. Different versions of Ripple3 masks (detail) and its PSF. *Left*: original version, with contrast 3e-9. *Middle*: Ripple3 with a trimming defect similar to the real one present on one of the early masks. Note the degradation of contrast, which is now ~1e-7. *Right*: Ripple3 employing the "dashing" trick that circumvents the manufacturing limitations and recovers the high contrast.

the early manufacturing runs [56], those portions of openings that have width less than about 10–15 μm do not get etched through completely (at least not for our 50 μm-thick mask). This causes what we call a "trimming" effect where the thin openings are cut off once they get to be thinner than 10–15 μm, as shown in Figure 8.7.4-3. This trimming can degrade the theoretical contrast to about 10^{-7}. Simulations show that a simple popular wavefront control algorithms called Speckle Nulling slows down considerably or even stops (depending on choice of algorithm parameters) once the speckle contrast reaches the level of this trimming error. Why this happens is not entirely understood, but may have to do with the fact that trimming tends to create a speckle field with very specific and fine structure—speckles with width on the order of 1 λ/D, the smallest possible for an aperture of size *D*.

The trimming problem was attacked on several fronts. The manufacturing process was improved, allowing for better control and smaller minimal width, and algorithms more efficient than Speckle Nulling were developed. However, the simplest solution is probably to merely design a shaped pupil that conforms to the minimal slit width constraint, if that is at all possible. It turns out that it is possible, by employing a trick. The problem of openings that are too thin has been encountered before in the context of the so-called barcode shaped pupils where all the openings are thin rectangles or slits. It is possible to replace the slits that are too thin by wider dashed slits that preserve the total area of the slit but are wide enough to manufacture. This "dashing" modification is very straightforward to implement on barcode masks and has worked very well for them. However, barcode masks that achieve 10^{-10} contrast are probably impractical to manufacture even when "dashed" in this fashion. Fortunately, as it turns out, the extension of dashing to easier shapes such as Ripple3 is possible, though not as trivial. After some trial and error, one of our dashing algorithms that we call Dash4 was found to perform particularly well. The results of its modification of Ripple3 are shown in Figure 8.7.4-3. In essence, Dash4 partitions the portions of all the Ripple3 openings that are too thin into a series of thin segments, and then replaces each of those thin segments by a dash (in this case, a circular-shaped dash) that has the same centroid and area as the

deleted segment. For our design of the 30 mm-diameter Ripple3, we set the minimal opening width at 12 μm, which was also the radius of the circular dashes. As can be seen from Figure 8.7.4-3, the Dash4 algorithm creates a manufacturable version of Ripple3 that maintains the contrast of the original Ripple3 mask but has no openings that are thinner than 12 μm.

Another real-world effect that is important to simulate is the 3D nature of the mask. The shaped pupils are designed assuming that the masks will be ideal and that the image plane is an exact Fourier Transform of the pupil plane. One important question is whether these assumptions are valid in practice. In what follows, we present the results of full vector simulations that show that in most cases of interest, these assumptions are indeed valid.

Ceperly et. al. [57] have performed finite-difference-time-domain simulations of the interactions between the vector electro-magnetic fields and the edges of a realistic mask (i.e., real material, non-0 thickness) and compared the results to the assumption of an ideal mask (i.e., ideal apodization, 0 thickness). The main results are summarized in Table 8.7.4-2. The left column specifies various cases that were simulated and the right column shows the magnitude of the difference between a real and an ideal mask (taking the worst case for the last 5 rows). By "vertical sidewalls," we mean the case where the edges of the mask have walls that form a 90 degree angle with respect to the substrate. By "20° undercut," we mean that this angle is 90°–20° (with the mask opening being narrower on the illuminated side of the mask). "Xmm opening" refers to the width of the mask opening in cross section. The value of the parameter on the right column (severity) corresponds to the width along the edge of the ideal mask that contains the same amount of energy as the perturbation due to the effect on the left column. The main conclusions of these simulations are that vertical sidewalls are to be avoided, and that small mask tilts, changes of polarization and wavelengths, and metal coatings are the least significant.

This data was used to study how vector interactions with the real mask affect the PSF of the real mask [58]. The main conclusions were that severities of less than l/4 do not degrade the 10^{10} contrast for mask sizes 10 cm and larger. Therefore, with a properly undercut mask, the mask can be assumed ideal and insensitive to polarization, wavelength changes, or coatings. For masks that are not undercut, the degradation depends on the mask type and size. In a 10 cm Ripple mask, contrast is degraded to 10^{9}, while for a 10 cm checkerboard mask, contrast is not degraded. All such effects will be insignificant compared to wavefront error. One important corollary to this work is that

Table 8.7.4-2. Extent of different effects on the fields around the edges

Mask Structure:	Severity:
Vertical sidewalls, Off-axis illumination, 10um Opening, 100um Thick	7 λ
Vertical sidewalls, Off-axis illumination, 10um Opening, 50um Thick	4 λ
Vertical sidewalls, On-axis illumination, 10um Opening, 100um Thick	3-4 λ
Vertical sidewalls, On-axis illumination, 10um Opening, 50um Thick	3 λ
Vertical sidewalls, On-axis illumination, 48um Opening, 50um Thick	3 λ
Vertical sidewalls, On-axis illumination, 48um Opening, 50um Thick	2-3 λ
20° undercut sidewalls, On-axis illumination, 48um Opening, 50um Thick	λ / 4
Physical effects on 50um thick Si masks with 48um openings at 630nm:	Worst case:
Undercut angle	3 λ
Small mask tilt	λ / 2 per degree tilt
Polarization	λ / 4
Wavelength (630nm to 785nm)	λ / 4
200nm Cr top-coat	λ / 100

manufacturing error or imprecision of the edges as large as l/4 is insignificant (at least to the extent that manufacturing errors along the edges are similar to effective errors due to vector effects). Such an error is well within modern manufacturing tolerances. The results presented in this section indicate that real masks can be manufactured today which, in the absence of wavefront aberrations, will achieve the 10^{10} contrast required by TPF (except for the trimming limitation discussed later, which can be overcome by specialized mask designs).

Manufacture

The Ripple3 mask (along with Ripple10 and Eclipse4) was manufactured by the Microdevice Laboratory (MDL) at JPL. The mask was made by Deep Reactive Ion Etching (DRIE) of a Silicon-On-Insulator (SOI) wafer and is shown in Figure 8.7.4-4.

The wafer was 400 microns thick, but in the vicinity of the boundaries of the openings, it was thinned down to 50 microns. The process is described in more detail in Balasubramanian 2006. For the latest run, an SOI wafer was used, enabling good control of the 50 micron thickness of the mask. All parts of the mask were etched correctly without any trimming defects, including the dashes. There was, however, an unanticipated systematic overetch by about 0.5 microns of all the openings. According to simulations, such a defect will degrade the theoretical contrast to 4×10^{-9} but is in principle correctable by wavefront control. According to the FDTD simulations described above, we expect 3D vector effects to appear at roughly 10^{-9} contrast level for our particular mask type and size. It is not clear whether these effects are correctable or not by wavefront control. If they turn out not to be correctable, one good solution would be to taper sidewalls as indicated on the right of Figure 8.7.4-4. For a taper angle as small as 10^{o}, the effects of vector sidewall interactions will be below 10^{-10} contrast as shown in Table 8.7.4-2. Another solution is to enlarge the mask. Enlarging it by a factor of 3 (i.e., 90 mm diameter) should reduce vector sidewall interaction effects to 10^{-10} level as well.

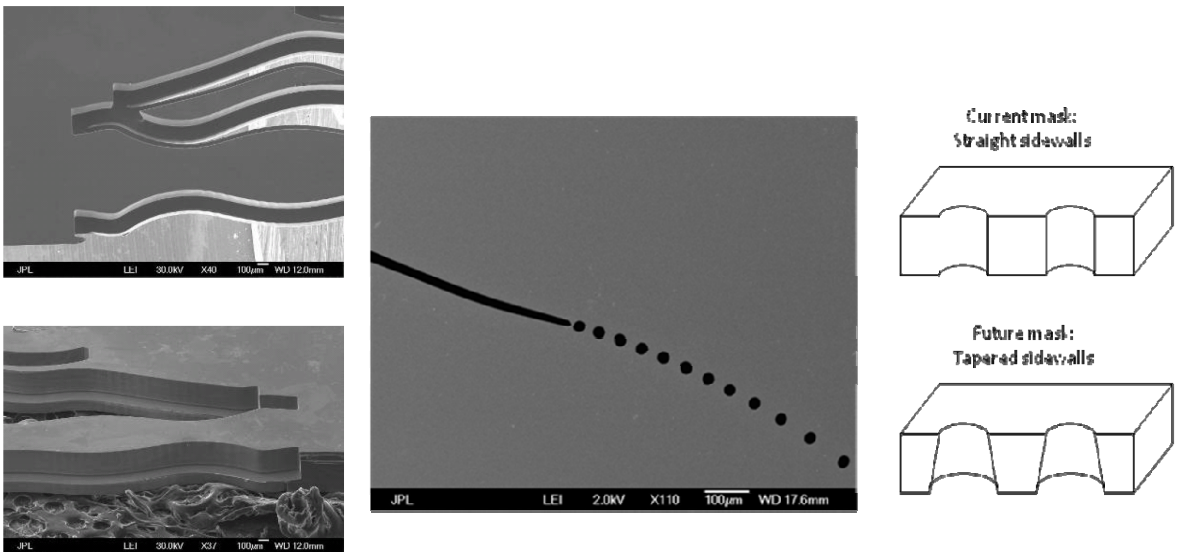

Figure 8.7.4-4. SEM images of a shaped pupil mask (*left*) and detail (*center*) showing dashes from the top. On the right is a 3D cross-section of the sidewalls on the dashes. Light enters from the top. Vertical sidewalls lead to undesired interactions with the electrical field that degrade contrast.

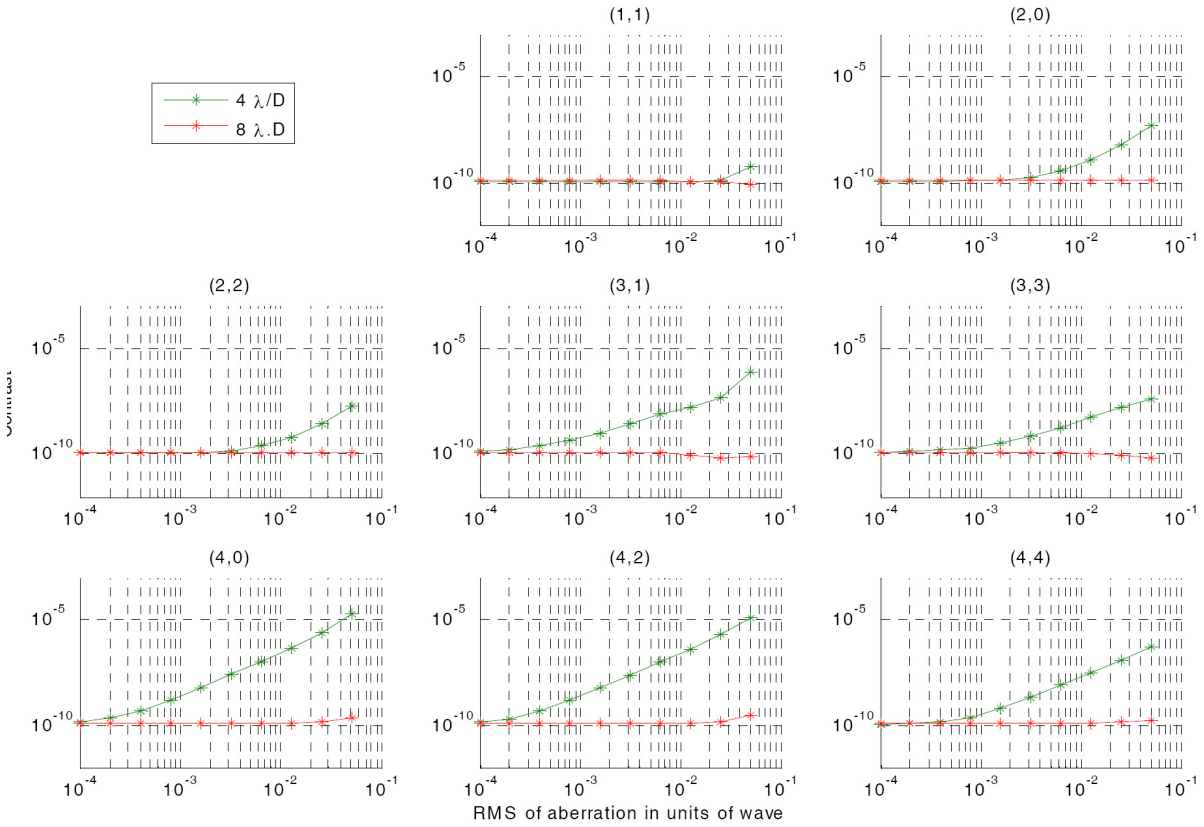

Figure 8.7.4-5. Sensitivity to different Zernike aberrations for a concentric ring shaped pupil mask as a function of RMS of aberrations, at inner working angles of 4 and 8 l/D. The title of each graph is the Zernike radial and azimuthal index.

Sensitivity to Wavefront Aberrations

In order to assess the sensitivity of shaped pupils to wavefront aberrations, we simulated different Zernike aberrations at the pupil plane and studied their effects at the image plane [59]. Some of these results are summarized in Figure 8.7.4-5. For these simulations, we assumed a circular concentric ring shaped pupil. Each subplot corresponds to a different Zernike (starting from tilt, defocus, etc.), and shows the contrast in the image plane at a particular working angle (4 or 8 l/D) as a function of RMS of aberration. Just as with many other coronagraphs, the sensitivity is more pronounced at lower inner working angles and higher Zernike orders. The main conclusion of this work, however, is that the SPC is intrinsically relatively insensitive to aberrations (especially to pointing error or other forms of tilt, defocus, and astigmatism). The wavefront flatness requirement depends on the aberration, but assuming typical power spectral density fall-off such as $1/f^3$, the total flatness requirement needs to be on the order of l/10,000.

Wavefront Sensing and Control with Shaped Pupils

The ability to sense and correct for aberrations all the way to 10^{10} contrast in a SPC system that has real masks like those already manufactured today has already been shown theoretically in monochromatic light. Figure 8.7.4-6 shows a simulation of the EFC wavefront control algorithm [60], in a system having phase and amplitude errors as well as the observed manufacturing errors (trimming) on the mask.

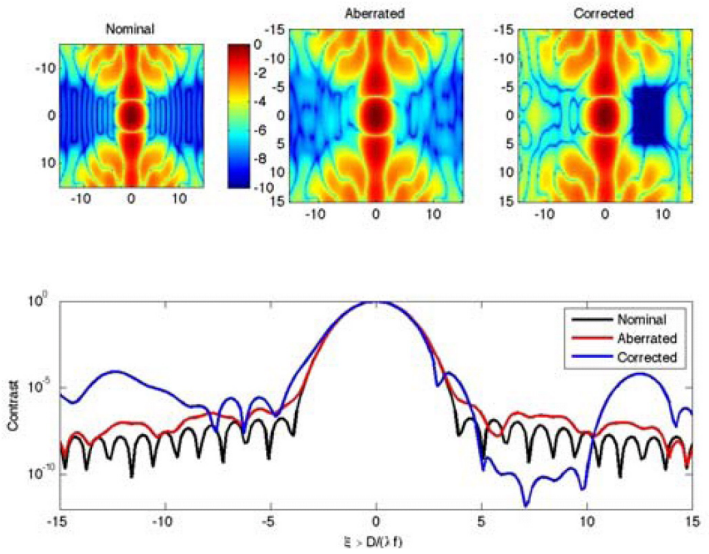

Figure 8.7.4-6. Demonstration of Peak-a-boo sensing and correction with a realistic shaped pupil having manufacturing defects (trimming), in monochromatic light.

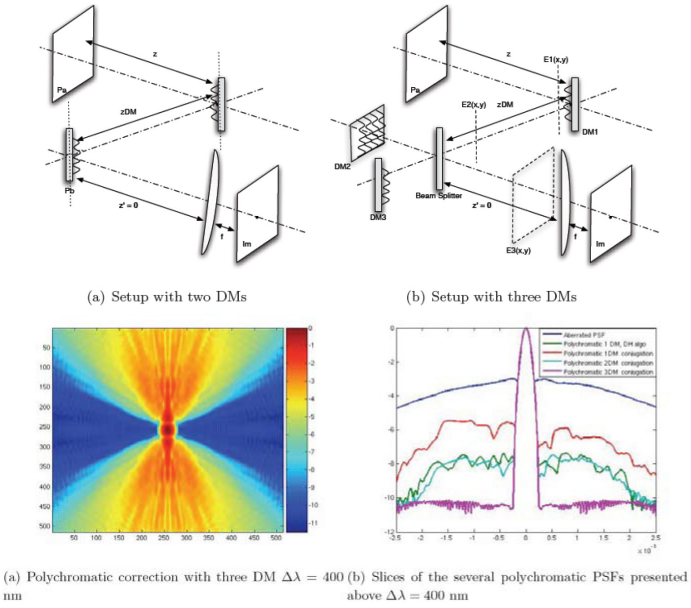

Figure 8.7.4-7. Top: Multi-DM configurations that allow corrections for realistic wavelength-dependent errors. Bottom: Even a severe case where wavelength-dependent aberrations limit the contrast to 103 can be fully corrected by a system of 3 DMs. In this simulation, perfect estimation of the aberrations is assumed.

Such corrections work well for monochromatic light, or even in polychromatic light assuming no wavelength dependence of aberrations. However, in reality, both phase and amplitude error will have a non-negligible dependency on wavelength, due to a variety of mechanisms [61], severely limiting the bandwidth across which aberrations can be fully corrected. Nonetheless, in such cases, the required 10^{10} contrast can still be achieved with the SPC if one uses more than 1 DM for correction. Figure 8.7.4-7 shows some possible configurations of 2 and 3 DMs designed to correct for wavelength-dependent errors along with a simulation of correcting for such errors with a 3-DM correction system. Furthermore, the present study showed that the ACCESS wavefront control architecture is adequate to provide broadband control down to 10^{-9} contrast for shaped pupils.

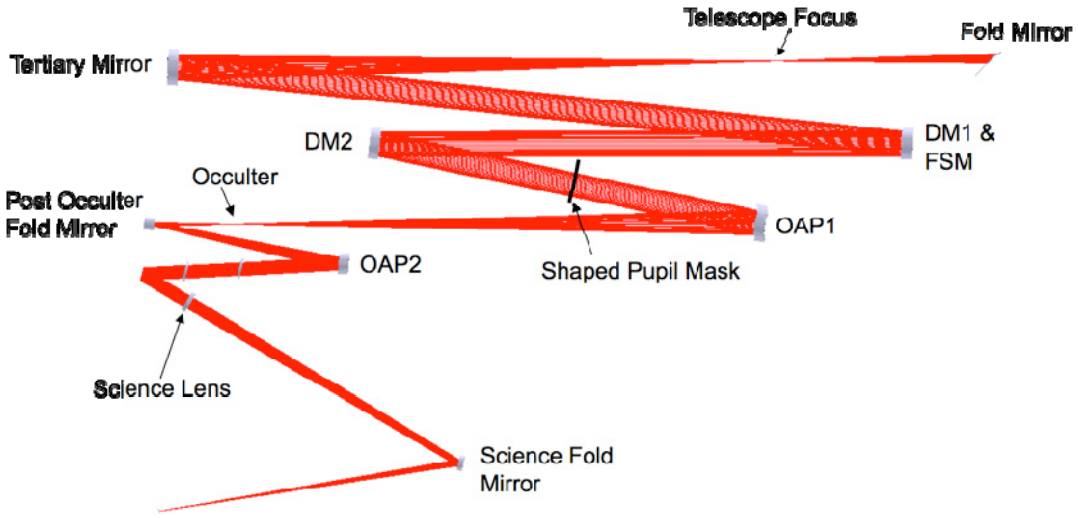

Figure 8.7.4-8. Diagram of the ACCESS instrument with the Shaped Pupil Coronagraph

8.7.4.2 Specification of the Representative ACCESS Shaped Pupil Coronagraph

For purposes of ACCESS, we wanted to do as little modification as possible to the existing baseline architecture, which was developed with the BLC coronagraph in mind. The flexibility of placing the shaped pupil made this easy. First, we decided to put the SP occulter in the same place as the BLC occulter. (Even though the occulter for shaped pupils is not required in principle, it helps in practice as mentioned above; and it is simply a hard-edged stop that has been trivial to manufacture by using exactly the same technique as for shaped pupils.) Since the shaped pupil has to be upstream of the occulter, and since it does not have to be in a reimaged pupil plane, a convenient location for it was chosen between DM2 and OAP1, as shown in Figure 8.7.4-8.

We settled on the Ripple3 shaped pupil for ACCESS, because of its good intrinsic contrast. A quick simulation confirmed that Ripple3 at the location between DM2 and OAP1 still delivers better than 10^{-9} contrast for the case of no aberrations.

8.7.4.3 Summary of Recent Laboratory Experiments

There has been significant experimental work with shaped pupils, with the initial tests being performed at the Princeton testbed and final vacuum testing at the High Contrast Imaging Testbed (HCIT) at the Jet Propulsion Laboratory (JPL). The results below were obtained with the Ripple3 mask at HCIT and were originally published in Belikov et al [62]. HCIT is a state-of-the art facility for testing high contrast coronagraph designs and wavefront control systems. It consists of a vacuum chamber, a vibration isolated optical bench, a flexible optical configuration that accepts at least the BLC and SPC coronagraphs, a 32 × 32-acturator Xinetics deformable mirror, a supercontinuum source that can be filtered either with a broadband 10% bandpass filter (760 nm–840 nm) or one of 5 spectrally adjacent narrowband 2% filters within that 10% band, and finally a computer interface that can control everything remotely.

The optical layout is shown in Figure 8.7.4-9 and is very simple if the main functional components in the layout are highlighted. OAP1collimates the beam and the DM is placed at the first pupil plane. This pupil plane is then reimaged to a second pupil plane where the shaped pupil is located. OAP4 brings the beam to first focus, where the so-called "bowtie" mask, or occulter, is placed that blocks the bright parts of the PSF. This image plane is the reimaged to a second image plane where the CCD camera is placed. (The purpose of the bowtie mask is to prevent blooming and related artifacts on the CCD, but it is not necessary in principle.)

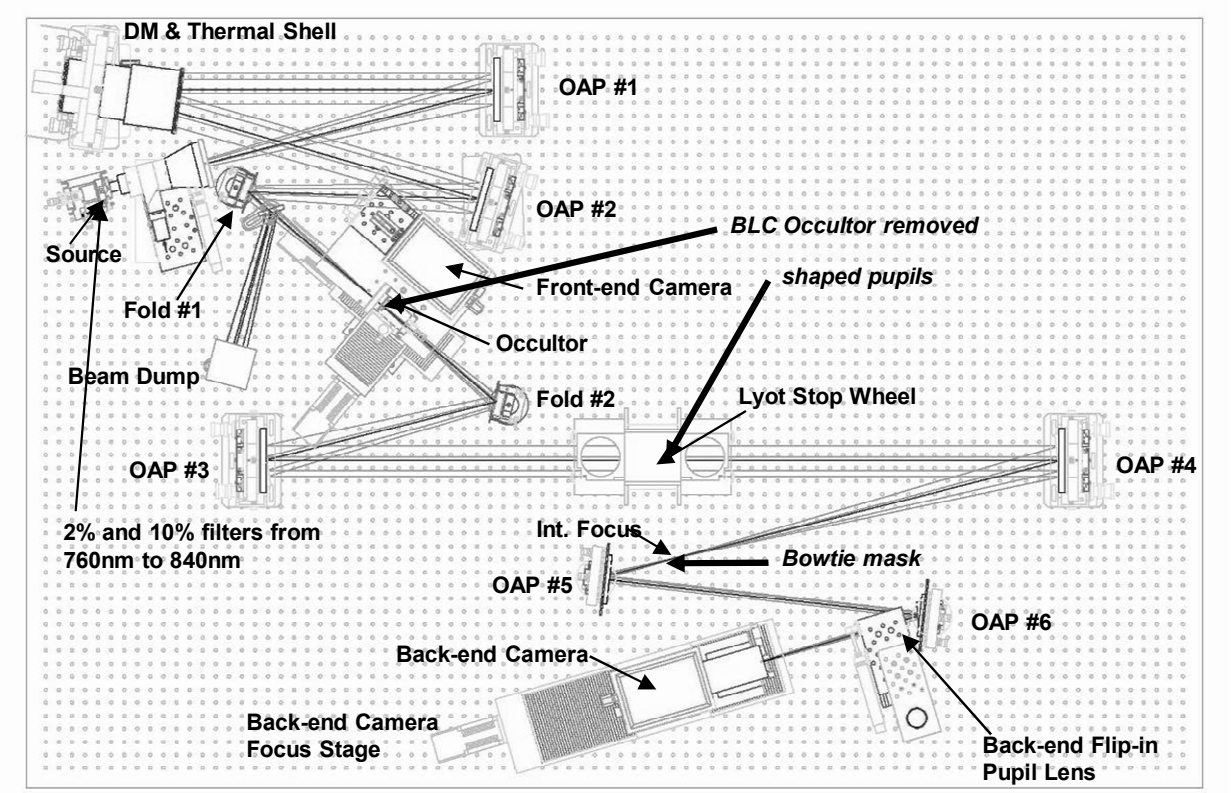

Figure 8.7.4-9. Optical layout of the HCIT in the Shaped Pupil Coronagraph configuration. Bold arrows indicate the changes required to convert the testbed from the default BLC configuration to the SPC configuration.

It should be noted that the shaped pupil is tilted by about 4 degrees with respect to the optical axis in order to avoid back-reflections. Such a tilt means that the incident field now sees tilted sidewalls instead of vertical ones. Assuming geometrical optics, this tilt will slightly reduce the effective area of each mask opening. This reduction will create an error in the image plane on the order of 10^{-9} contrast, but will luckily actually cancel some of the error due to the 0.5 enlargement of the openings mentioned above that was caused by an overetch. However, geometrical optics is probably not a good approximation in this case and these effects may be dominated by the increased vector interactions with the tilted sidewall. A tapered sidewall mask will eliminate this issue.

We performed several runs of the EFC wavefront control algorithm within a span of about 1 week. The difference between different runs was some change with the goal of improving the asymptotic contrast: e.g., a better model, slightly different calibration, parameter set, or customization of the algorithm. Our strategy for each run was to run EFC in its monochromatic form to completion using the 2% light centered at 800 nm, and when good results were obtained, hold the DM setting and measure the contrast for all the other 2% bands and the 10% one.

Narrowband (2% at 800 nm) Results

Figure 8.7.4-10 shows the results of one of our runs in 2% light around 800 nm. The contrast we achieved was 1.16×10^{-9}, averaged across the dark zone—a trapezoid between 4 and 10 λ/D.

The next step is to identify the current limiting factor and to eliminate it, and go even deeper. At this point, it is not entirely clear what the limiting factor is, but educated conjectures can be made. For example, simulations suggest that almost all known errors, tolerances, and approximations in manufacturing, optical layout, and model are either irrelevant or should be correctable by wavefront

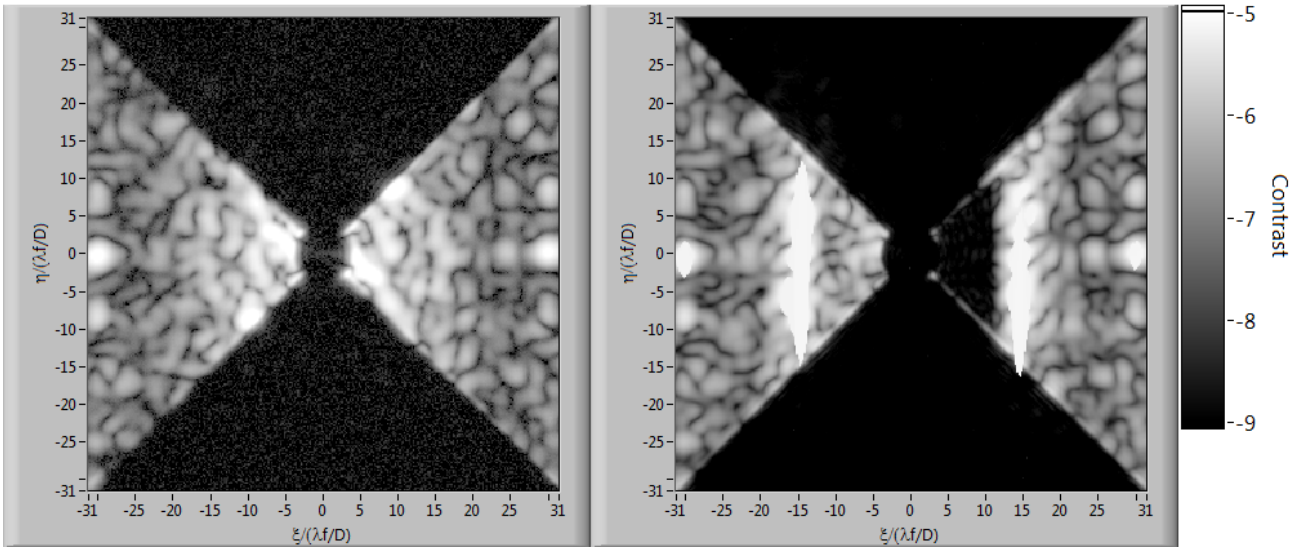

Figure 8.7.4-10. Before wavefront correction (*left*) and after wavefront correction (*right*) images in 2% bandpass light centered around 800 nm. The hour-glass black shape is the bowtie that blocks the bright portions of the PSF. Regions to the right and the left are the dark zones of the PSF but contain a lot of speckle due to aberrations. These speckles are suppressed by wavefront control in a trapezoidal region between 4 and 10 λ/D to a level of 1.16e-9 contrast.

control (such as the 0.5° overetch, for example). One of the remaining possibilities, however, is noise on the DM actuator positions. Another one is the vector sidewall interactions, especially since they are exacerbated by the 4° tilt. The effects of these are indeed predicted to occur at about 10^{-9} contrast level, and are difficult to model, particularly because they may require a departure from the scalar field assumption in EFC which is probably impractical. Another clue to the limiting factor is that the shape of the residual speckle pattern looks rather regular, with small, 1 λ/D-sized speckles, rather than the more random pattern typical of an uncorrected speckle field. This pattern is reminiscent of the speckles one gets due to trimming (though at a much lower contrast), and is what one would expect from an error on the outer edges of the pupil plane, i.e., the portion of the pupil plane responsible for fast, 1 λ/D-sized variations in the image plane. Now, for the Ripple3 mask, the vector sidewall interactions (especially those exacerbated by tilt) are more significant for smaller openings such as dashes, which occur on the outer portions of the pupil plane. It is therefore, at present, our working hypothesis that the limiting factor is either DM actuator noise and/or vector sidewall interactions —either intrinsic, or exacerbated by tilt. Vertical sidewalls can be eliminated by making a tapered mask as described in Section 3.

Multi-Wavelength and Broadband (10% @ 800) results

After obtaining our best result in 2% light, we held the DM setting and switched to the other 2% wavelengths as well as the full 10% band. The results are shown in Figure 8.7.4-11. Most notably, the contrast in 10% light is 2.4×10^{-9}. This was at the time was the world record of contrast in 10% light for inner working angles as small as 4 λ/D.

There are two observations we would like to make about these results. The first observation is that the contrast is not the same in all the wavelengths but rather obeys more or less a quadratic curve with the minimum at the central (800 nm) wavelength. This, of course, is consistent with the contrast in the 10% band being worse than in the central 2% one. Clearly there is some first-order chromaticity somewhere in the system, i.e., one that induces a quadratic contrast dependency on wavelength. For purposes of being concise, for the rest of this section we will use the term

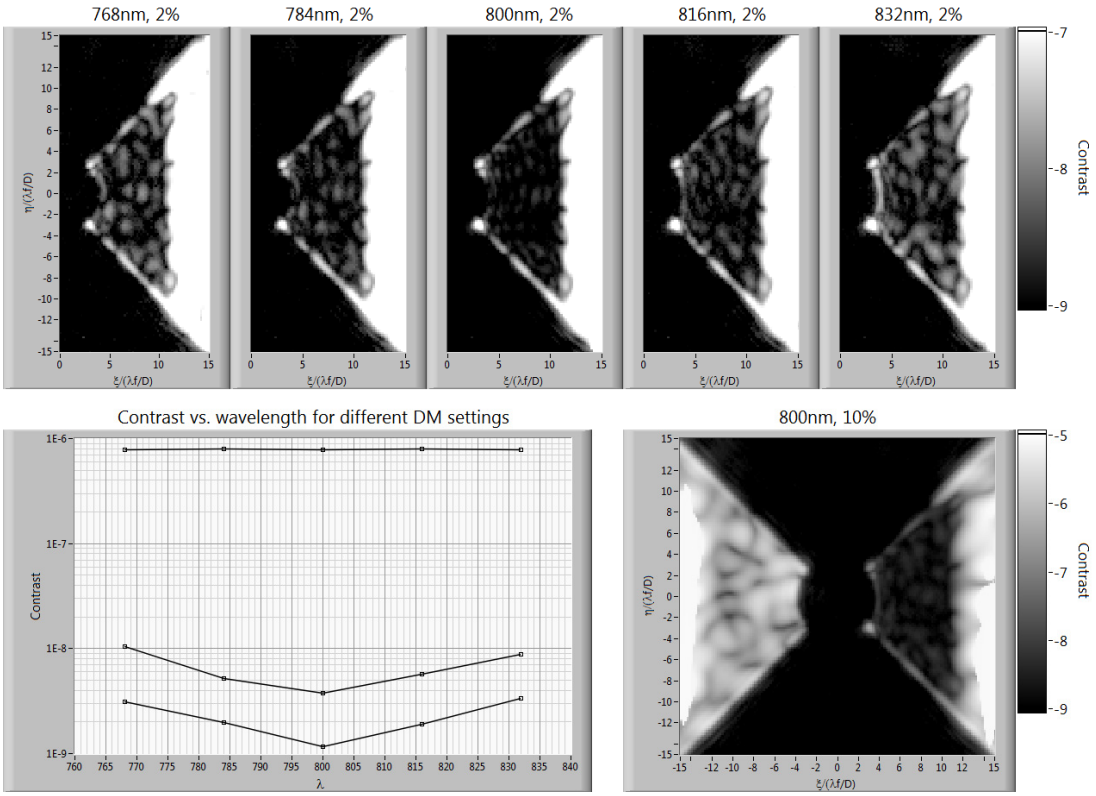

Figure 8.7.4-11. *Top:* Post-correction images in different wavelength bands. *Left:* Plots of contrast vs. wavelength for different DM settings (bottom plot corresponds to the top images). *Right:* Post-correction image in the full 10% band, showing a record 2.4e-9 contrast in the dark zone between 4 and 10 λ/D.

"chromaticity" to refer to the contrast variation with wavelength in the dark zone. We can write the dark zone contrast as

$$C(\lambda,\alpha) \approx C(\lambda_0,\alpha) + \left(\frac{\Delta\lambda}{\lambda_2}\right)^2 \left[C_{sys} + C_{dm}(\alpha)\right]$$

where $C(\lambda)$ is the contrast at wavelength λ and DM setting (i.e., actuator matrix) α; λ_0 = 800 nm and $\Delta\lambda = \lambda - \lambda_0$; $C_{dm}(\alpha)$ represents all the terms of the chromaticity that depend on the DM setting, so that $C_{dm}(0) = 0$, and C_{sys} represents all the remaining terms that do not depend on the DM setting and hence must be due to some intrinsic system chromaticity (such as due to a coronagraph in case the coronagraph is chromatic). Let the three DM settings corresponding to the three curves in Figure 8.7.4-11 be α_1, α_2, and α_3, in order of worst to best. Clearly the chromaticity term

$$\left(\frac{\Delta\lambda}{\lambda}\right)^2 \left[C_{sys} + C_{dm}(\alpha)\right]$$

is not important until we dip below 10^{-8} contrast, at least for $\alpha = \alpha_2, \alpha_3$. Thus, everything on the testbed, including the shaped pupil, is pretty achromatic down to that level.

The second observation is about the relative sizes of C_{sys} and C_{dm}. Note that according to Figure 8.7.4-11,

$$\frac{C_{sys}+C_{dm}(\alpha_2)}{C_{sys}+C_{dm}(\alpha_3)} \sim 2$$

therefore, it cannot be the case that $C_{sys} \gg C_{dm}(\alpha)$ for both $\alpha = \alpha_2$ and $\alpha = \alpha_3$. This in turn implies that the DM is capable of inducing a chromaticity in the DZ at least comparable to any intrinsic chromaticity of the system. Furthermore, if we assume that C_{sys}, $C_{dm}(\alpha_2)$, $C_{dm}(\alpha_3)$ are all positive (if they are not, it means that by doing our best at 800 nm, we are actually doing even better at another wavelength without even looking at it), then it must be the case that $C_{sys} < C_{dm}(\alpha_2)$, and possibly much less. Therefore, the curvature of the plots in Figure 8.7.4-11 is very likely dominated by some random chromaticity induced by the DM and not any intrinsic chromaticity in the system. In particular, this implies that the intrinsic shaped pupil chromaticity at 10%, if any, is below about 10^{-9} contrast (possibly much below), as expected. Of course, this simple argument does not rule out the possibility that the chromaticity is caused, for example, by some way in which the DM modifies or amplifies some small intrinsic system chromaticity, in which case the real limiting factor for broadband light may still be external to the DM. Neither does the fact that the DM can vary the chromaticity beyond the intrinsic system chromaticity necessarily imply that the DM can eliminate it altogether. However, it does suggest that there is some DM setting that can at least improve the chromaticity currently observed, and therefore we have not yet reached the limit in 10% contrast with the existing hardware. We can find this DM setting by using a better (multi-spectral) wavefront control algorithm.

Amplitude Error Correction using Two Sequential DMs

The results presented above were obtained with a single DM. Because a single DM can only modulate phase, and in practice we have both phase and amplitude errors, a single DM does not have enough degrees of freedom to correct both phase and amplitude errors independently in the entire dark zone. That is why the dark zones above are limited to a half-plane. Recently the Princeton Laboratory presented an experimental proof of a two sequential DM system that corrects both amplitude and phase errors on both sides of the PSF. The second DM is necessary for the correction of amplitude errors, which is illustrated on Figure 8.7.4-12 by the presence of a symmetric high-contrast dark field in the image plane.

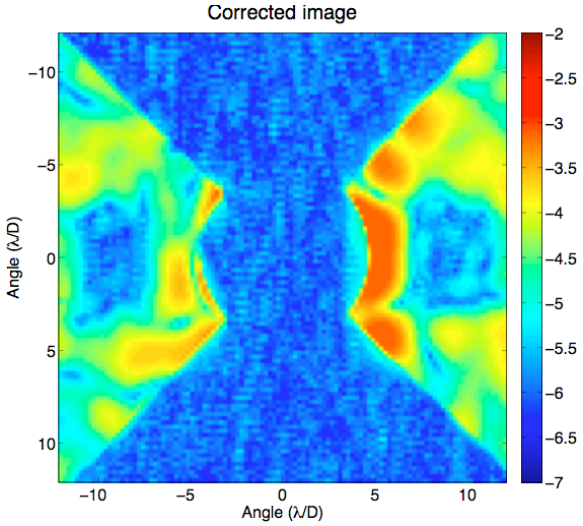

Figure 8.7.4-12. Symmetric Dark Hole obtained using two sequential DM

8.7.4.4 Technology Readiness and Future Prospects

As we have shown above, shaped pupils are a very simple and mature technology. Shaped pupils are easy and cheap to design and make, and ~10^{-9} contrasts have been demonstrated with shaped pupils in broadband light, which is close to world record performance, and this was done with total HCIT time of several weeks. This performance is arguably sufficient to be able to detect Earth-like planets on a large (4 m or larger) telescope with differencing techniques. Virtually all the relevant aspects of shaped pupil physics have been modeled and are understood.

The only drawback to shaped pupils is performance, and in particular the inner working angle. No pure shaped pupil has been found yet that provides 10^{-9} contrast at 3 λ/D in a reasonably open dark zone. However, it is possible, by a clever use of special DMs, to enhance the performance of shaped pupils.

A Hybrid Approach—Performance Enhancement through Soft Remapping using DMs

In the ACCESS setting, the sequential pair of DMs can be thought of as an actively adjustable pupil mapper. When used with shaped pupils, the DMs behave like a hybrid pupil mapping system, and this approach can be used to improve the performance (both throughput and inner working angle) of the shaped pupil coronagraph as well as compensate for wavefront errors. The design problem reduces to solving a single partial differential equation (PDE) for each mirror surface. This PDE, known as the Monge-Ampere equation, was first discovered in problems of minimum energy optimal transport under constraints and has been extensively explored by mathematicians for solutions to various problems (cf., [63, 64]). In fact, it has been recently revisited in the context of pupil mapping under arbitrary geometries [65]. Unfortunately, developing algorithms for such arbitrary geometries is formidable and remains a work in progress that we hope to address soon. However, for the case of circular symmetries it can be shown that two DMs can be shaped such that they can carry some of the starlight suppression burden, allowing a less aggressive shaped pupil apodizer to be chosen. This means a system with higher throughput and a smaller inner working angle, as shown on Figure 8.7.4-13. The corresponding mirror shapes and resulting PSF at various wavelengths across the visible are shown in Figure 8.7.4-14.

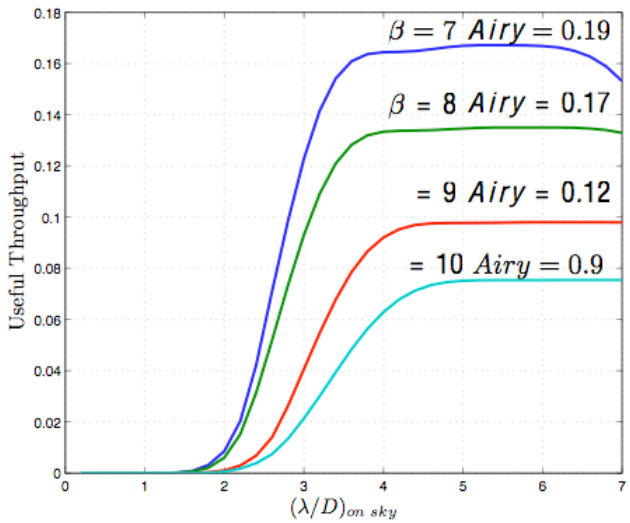

Figure 8.7.4-13. Useful thoughput for several circularly-symmetric apodizer + 2 DM designs.

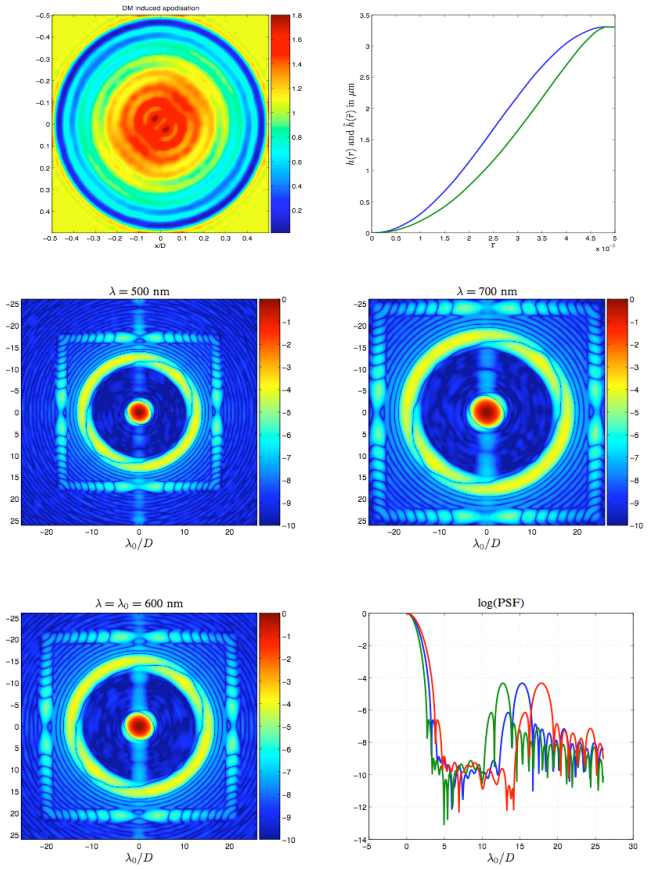

Figure 8.7.4-14. *Top Panel:* Mirror shapes associated with the beta = 7 design. The size of the DMs is 1 cm; *Bottom Panels:* PSFs across the visible for this design

Both theoretical aspects, generalization to arbitrary geometries for better performances using shaped pupils, and experimental validation of these techniques are now being investigated at Princeton and JPL. We expect a conclusive outcome to the theoretical study, namely an optimal design that leads to the best useful throughput curve given the current state of the art DM technology, by the end of 2009. This solution would only rely on existing hardware and thus, if experimentally validated, would present the same level of technology readiness for the shaped pupil as for band-limited Lyot coronagraphs.

8.7.5 Coronagraph Comparison Matrix

The following sections describe the four coronagraph options in detail. This section describes how the different options are evaluated in this study.

The four coronagraph types are evaluated against each other using two sets of criteria. The first of the criteria listed in Table 8.7.5-1 define a performance floor that corresponds to TRL 6 coronagraph performance that has been demonstrated in JPL's High Contrast Imaging Testbed (HCIT), a space-like environment for technology validation. These are minimum performance requirements for the ACCESS mission and help define the minimum science mission.

Table 8.7.5-1. Performance floor criteria

Performance Floor	Notes
>9 known RV planets can be observed	
>50 other stars that can be searched in 3 years	
Contrast floor of 10^{-9} or better	For planet searches
Spectral bandwidth of >/= 10%	For planet characterization
Spectral resolution of >/= 20	For planet characterization
Inner working angle </= 3 λ/D (half field)	For planet searches
Requires only a single spacecraft	Affordability
Fits allocated volume for instrument (<1.0 m height)	Affordability (do not outgrow LV fairing)
Cost <$100M	Affordability

The second set of criteria listed in Table 8.7.5-2 provides discriminators among the coronagaph types. Here, we rank the four types according to performance metrics that may be achieved and demonstrated in the HCIT test environment in the coming 12 months. Each criterion receives a relative weight and a score listed in Table 8.7.5-3.

Weights were formulated by averaging votes from science team advocates for each of the options with a vote for the engineering team. Each option got one vote in an attempt to minimize bias in the outcome. An arbitrary number of points (300) were chosen for distribution amongst the criteria. The group chose to distribute these points relatively equally amongst the three categories of discriminators: Performance (78 points), Cost (108), Risk or Engineering Difficulty (114). Performance would have been weighted more heavily had it not been already represented by the performance floor criteria. Each option receives a score *relative to the other options* that is multiplied by the weight for that criterion to arrive at a weighted score. These weighted scores are then summed to arrive at a total. Totals are compared. A greater total indicates a more favorable option. The absolute score is irrelevant—there is no minimum score that qualifies an option as good enough or as unsatisfactory. What matters is how one option's score relates to the others. The scores were debated by the group and occasionally adjusted to more accurately capture what the group valued most. Note that some criteria were anticipated to be discriminators at the beginning of the study but were subsequently shown to be equal across the options. These are shaded light blue in the matrix.

The outcome is that a Lyot design would be optimum for this mission *given what is known and demonstrated today*. The vector vortex, owing to its simplicity, may advance significantly this year with process refinements. The shaped pupil did not score quite as well; it has demonstrated high contrast in the HCIT should not be ruled out as a viable candidate. The promise of greater performance of the pupil mapping option does not yet compensate for its additional cost, complexity, and current uncertainty and would not be recommended if project start were imminent. The Lyot option continues to be attractive because it is the most mature in terms of its demonstrated capability and in the validation of the analytical model of its performance. It has demonstrated performance that defines the minimum science mission for ACCESS. The vector vortex is attractive because it is easy to combine with the Lyot and offers the promise of somewhat greater performance. The shaped pupil could gain on the others if a design that works at 3 λ/D and covers the 20% bandwidth can be demonstrated. While the pupil mapping option trails, additional development of this technology over the next 2–4 years could improve its appeal, but only if it proves it can offer a significant performance improvement over the other options. It must be better, not just as good, because it is more complex and expensive.

Table 8.7.5-2. Discriminator criteria

Discriminators (300 points to distribute)	Notes
Performance	
# of known RV planets beyond minimum	Not a large discriminator
# of stars that can be searched outside of 3 λ/D	Jupiter analogs
# of stars that can be searched inside 3 λ/D	Expands the search space
Contrast floor below 10^{-9}	System robustness
Signal-to-Noise w. Zodi background of 10^{-9}	System robustness
Spectral bandwidth greater than 10%	All assumed at least 20%
Outer working angle	Set by deformable mirror
Earth twin within 3.5 parsecs, 1 zodi	None can do
Cost (70% probability)	
Instrument cost below must-have limit	Affordability
Accommodation cost (spacecraft & telescope deltas)	Level playing field implies common SC and telescope designs
Risk, Engineering Difficulty	
Optical tolerances & alignment sensitivity	System robustness
Technology readiness of the three least mature elements	Mission readiness
# of optical elements before occulting mask	Most demanding optical requirements
# of optical elements overall	Complexity
# of mechanisms	Complexity
Mass	Ease of accommodation, cost
Volume margin (stack height)	Ease of accommodation, cost
Maturity of techniques to model performance	Verification risk
Ease of I&T	Cost risk
Pointing requirements	Level playing field implies common SC and telescope designs
Temperature control requirements	Level playing field implies common SC and telescope designs
# of detectors	Similar for all
Susceptibility to ionizing radiation effects	Similar for all
Power (average)	Similar for all
# of electrical interfaces to telescope or S/C	Similar for all
Ease of calibration (pre- and post-launch)	Similar for all

Table 8.7.5-3. Comparative evaluation of the four coronagraph types using performance floor and discriminator criteria

	Weight Consensus	Lyot			Vector Vortex			Shaped Pupil			Pupil Mapping (PIAA)		
		Value	Relative Score 1 to 10	Weighted Score	Value	Relative Score 1 to 10	Weighted Score	Value	Relative Score 1 to 10	Weighted Score	Value	Relative Score 1 to 10	Weighted Score
Performance Floor													
> 9 known RV planets can be observed	Yes/No		Yes			Yes			Yes			Yes	
> 50 other stars that can be searched in 3 years	Yes/No		Yes			Yes			Yes			Yes	
Contrast floor of at least 10-9	Yes/No		Yes			Yes			Yes			Yes	
Spectral bandwidth of >/= 10%	Yes/No		Yes			Yes			Yes			Yes	
Spectral resolution of >/= 20	Yes/No		Yes			Yes			Yes			Yes	
Inner working angle </= 3λ/D (half field)	Yes/No		Yes			Yes			Yes			Yes	
Requires only a single spacecraft	Yes/No		Yes			Yes			Yes			Yes	
Fits allocated volume for instrument (<1.0 m height)	Yes/No		Yes			Yes			Yes			Yes	
Cost < $100M	Yes/No		Yes			Yes			Yes			Yes	
Discriminators (300 points to distribute)	**300**												
Performance	78												
# of known RV planets beyond minimum	8.2	#	5	41	#	5	41	#	5	41	#	5	41
# of stars that can be searched outside of 3λ/D	23.2	175	8	185.6	189	9	208.8	#	5	116	212	10	232
# of stars that can be searched inside 3λ/D	10			0			0			0			0
Contrast floor below 10-9	6.2	1x10-10		0	2x10-10		0	#		0	8x10-10		0
Spectral bandwidth greater than 10%	9	20%	5	45	20%	5	45	20%	5	45	20%	5	45
Signal-to-Noise w. Zodi background of 10-9	7.6	#		0	#		0	#		0	#		0
Outer working angle	9		5	45		5	45		5	45		5	45
Earth twin within 3.5 parsecs, 1 zodi	5	2-3	5	25	2-3	5	25	2-3	5	25	2-3	5	25
Cost (70% probability)	108	FY08 $M			FY08 $M			FY08 $M			FY08 $M		
Instrument cost below must-have limit	55	$70M	5	275	$70M	5	275	$69M	5	275	$83M	3	165
Accommodation cost (spacecraft & telescope deltas)	53	FY08 $M	5	265	FY08 $M	5	265	FY08 $M	5	265	FY08 $M	5	265
Risk, Engineering Difficulty	114												
Optical tolerances & alignment sensitivity	12		5	60		5	60		5	60		4	48
Technology readiness of the three least mature elements	14		5	70		4	56		5	70		3	42
# of optical elements before occulting mask	7.4	7	10	74	7	10	74	8	9	66.6	14	3	22.2
# of optical elements overall	6.8	25	5	34	25	5	34	23	6	40.8	29	4	27.2
# of mechanisms	5.6	12	5	28	12	5	28	10	7	39.2	10	7	39.2
Mass	4.8	147 kg	5	24	147 kg	5	24	142 kg	6	28.8	196 kg	1	4.8
Volume margin (stack height)	5.6	0.4 m	5	28	0.4 m	5	28	0.4 m	5	28	0.95	3	16.8
Maturity of techniques to model performance	4	n/a	5	20	n/a	4	16	n/a	5	20	n/a	2	8
Ease of I&T	7.8	n/a	5	39	n/a	5	39	n/a	5	39	n/a	3	23.4
Pointing requirements	13.8		5	69		5	69		5	69		5	69
Temperature control requirements	10.6		5	53		5	53		5	53		5	53
# of detectors	4	5	5	20	5	5	20	5	5	20	5	5	20
Susceptibility to ionizing radiation effects	3.8	n/a	5	19	n/a	5	19	n/a	5	19	n/a	5	19
Power (average)	3.8	42 W	5	19	42 W	5	19	42 W	5	19	42 W	5	19
# of electrical interfaces to telescope or S/C	3.2	#	5	16	#	5	16	#	5	16	#	5	16
Ease of calibration (pre- and post-launch)	6.6	n/a	5	33	n/a	5	33	n/a	5	33	n/a	5	33
Total				**1488**			**1493**			**1433**			**1279**

8.7.6 References for Section 8.7

[1] Trauger, Kern, and Kuhnert. 2007. TPFC-Milestone #1 Report.

[2] Kern, Kuhnert, and Trauger. 2008. TPF-C Milestone #2 Report.

[3] Kuchner and Traub. 2007. "A Coronagraph with a Band-limited Mask for Finding Terrestrial Planets," *The Astrophysical Journal* 570(2): 900–908.

[4] Moody, et al. 2009. "Design and Demonstration of Hybrid Lyot Coronagraph Masks for High-Contrast Imaging of Exoplanet Systems from Space," American Astronomical Society, AAS Meeting #213, #451.08, *Bulletin of the American Astronomical Society* 41: 345

[5] Mawet, D., Serabyn, E., Liewer, K., Hanot, C., McEldowney, S., Shemo, D., and O' Brien, N. 2009. *Optics Express* 17: 1902.

[6] Guyon, et al. 2009. Subaru's PIAA website. http://www.naoj.org/PIAA/.

[7] Belikov, et al. 2007. "Demonstration of high contrast in 10% broadband light with the shaped pupil coronagraph," *Proc SPIE* 6693.

[8] Kuchner, M., and Traub, W. 2002. "A coronagraph with a band-limited mask for finding terrestrial planets," *Astrophys. J.* 570: 900.

[9] Kuchner, M., Crepp, J., and Ge, J. 2005. "Eighth-order image masks for terrestrial planet finding," *Astrophys. J.* 628: 466.

[10] Moody, Gordon, and Trauger 2008. "Design and demonstration of hybrid Lyot coronagraph masks for improved spectral bandwidth and throughput," *Proc. SPIE* 7010: 70103P.

[11] Trauger et al. 2007. "Laboratory demonstrations of high-contrast imaging for space coronagraphy," *Proc. SPIE* 6693: 66930X.

[12] Trauger, J., and Traub, W. 2007. "A laboratory demonstration of the capability to image an Earth-like extrasolar planet," *Nature* 446: 771.

[13] Malbet, F., Yu, J., and Shao, M. 1995. "High dynamic range imaging using a deformable mirror for space coronagraphy," *P.A.S.P.* 107: 386.

[14] Trauger, J., Give'on, A., Gordon., B., Kern, B., Kuhnert, A., Moody, D., Niessner, A., Shi, F., Wilson, D., and Burrows, C. 2007. "Laboratory demonstrations of high-contrast imaging for space coronagraphy," *Proc. SPIE* 6693: 66930X.

[15] Borde, P., and Traub, W. 2006. "High-contrast imaging from space: Speckle nulling in a low aberration regime," *Astrophys. J.* 638: 488.

[16] Giveon, A., Kern, B., Shaklan, S., Moody, D., and Pueyo, L. 2007. "Broadband wavefront correction algorithm for high-contrast imaging systems," *Proc. SPIE* 6691: 66910A.

[17] Palik, E. 1998. *Handbook of Optical Contants of Solids*, Academic Press, New York.

[18] Balasubramanian, K., Wilson, D., Kern, B., and Sidick, E. 2007. "Thickness-dependent optical properties of metals and alloys applicable to TPF coronagraph image masks," *Proc. SPIE* 6693: 66930Z.

[19] Balasubramanian, K. 2008. "Band-limited image plane masks for TPF coronagraph: materials and designs for broadband performance," *Appl. Opt.* 47: 116.

[20] Heavens, O. S. 1991. *Optical Properties of Thin Solid Films*, Dover Publications, New York.

[21] Kern, B., et al. 2008. "TPF-C Milestone #2 Report."

[22] Roddier, F., and Roddier, C. 1997. *PASP* 109: 815.

[23] Rouan, D., Riaud, P., Boccaletti, A., Clenet, Y., and Labeyrie, A. 2000. *PASP* 112: 1479.

[24] Foo, G., Palacios, D. M., and Swartzlander, Jr., G. A. 2005. *Opt. Lett.* 30: 3308.

[25] Mawet, D., Riaud, P., Absil, O., and Surdej, J. 2005. *ApJ* 633: 1191.

[26] Mawet, D., Riaud, P., Baudrand, J., and Surdej, J. 2005. *Appl. Opt.* 44: 7313.

[27] Guyon, O., Pluzhnik, E. A., Kuchner, M. J., Collins, B., and Ridgway, S. T. 2006. *ApJS* 167: 81.

[28] Jenkins, C. 2008. *MNRAS* 384: 515.

[29] Berry, M. 1987. *J. Mod. Opt.* 34: 1401.

[30] McEldowney, S. C., Shemo, D. M., Chipman, R. A., and Smith, P. K. 2008. *Opt. Lett.* 33: 134.

[31] Mawet, D., Serabyn, E., Liewer, K., Hanot, C., McEldowney, S., Shemo, D., and O' Brien, N. 2009. *Optics Express* 17: 1902.

[32] Pancharatnam, S. 1955. *Proc. Indian Acad. Sci. A* 44: 247.

[33] Give'on, A., Kern, B., Shaklan, S., Moody, D. C., and Pueyo, L. 2007. *Proc. SPIE* 6691: 66910A.

[34] Mawet, D. 2007. *Proceedings of the conference In the Spirit of Bernard Lyot: The Direct Detection of Planets and Circumstellar Disks in the 21st Century*. June 4–8, 2007. University of California, Berkeley, CA, USA. Edited by Paul Kalas.

[35] Schneider, J., Boccaletti, A., Aylward, A., Baudoz, P., Beuzit, J. -L., Brown, R., Cho, J., Dohlen, K., Ferrari, M., Galicher, R., Grasset, O., Grenfell, L., Griessmeier, J. -M., Guyon, O., Hough, J., Kasper, M., Keller, Ch., Longmore, A., Lopez, B., Martin, E., Mawet, D., Menard, F., Merin, B., Palle, E., Perrin, G., Pinfield, D., Sein, E., Shore, P., Sotin, Ch., Sozzetti, A., Stam, D., Surdej, J., Tamburini, F., Tinetti, G., Udry, S., Verinaud, C., and Walker, D. 2008. Update of a White Paper submitted to the ESA ExoPlanet Roadmap Advisory Team, eprint arXiv:0811.2496.

[36] Stam, D. 2008. *A&A* 482: 989.

[37] Jacquinot, P., and Roizen-Dossier, B. 1964. "Apodization." *Progress in Optics* 3: 29.

[38] Bandermann, L., and Pohle, R. 1979. NASA report NAS2-10030; and

Bandermann, L., Pohle, R., Murphy, J., Vorreiter, J., and Black, D. 1981. "Satellites for the detection of nonsolar planets," *AIAA J. Spacecraft* 18: 164

[39] Robb, P., Bandermann, L., and Haisch, B. 1998. "Telescope design for direct imaging of extrasolar planets." *Proc. SPIE* 3356: 588.

[40] Guyon, O. 2003. "Phase-induced amplitude apodization of telescope pupils for extrasolar terrestrial planet imaging." *A&A* 391: 379.

[41] Guyon, O., Pluzhnik, E., Galicher, R., Martinache, F., Ridgway, S., and Woodruff, R. 2005. "Exoplanet imaging with a phase-induced amplitude apodization coronagraph I. Principle." *Ap.J.* 22: 744.

[42] Belikov, et al. 2006. "Diffraction-based Sensitivity Analysis of Apodized Pupil-Mapping Systems," *ApJ Vol* 652(1): 833–844.

[43] Shaklan, et al. 2007, "Broadband wavefront control in a pupil mapping coronagraph," Techniques and Instrumentation for Detection of Exoplanets III. Edited by Coulter, Daniel R. *Proceedings of the SPIE* 6693: 66930R–66930R-11.

[44] Guyon, O. 2009. "Imaging and Characterizing the Habitable Zones of nearby Planetary Systems with the Pupil mapping Exoplanet Coronagraphic Observer (PECO)," American Astronomical Society, AAS Meeting #213, #234.08; *Bulletin of the American Astronomical Society* 41: 507.

[45] Guyon, O. 2008. "Design of the second generation PIAA system." Subaru Observatory document.

[46] Vanderbei, R. 2008, "Linear stability of ring systems around oblate central masses," *Advances in Space Research* 42(8): 1370–1377.

[47] Belikov, et al. 2009, "Demonstration of the PIAA coronagraph for exoplanet imaging at NASA Ames," AAS Meeting #213, 41: 345.

[48] Spergel, D. N. 2001. "A New Pupil for Detecting Extrasolar Planets," *astro-ph*/0101142.

[49] Kasdin, N. J., Vanderbei, R. J., Spergel, D. N., and Littman, M. G. 2003. "Extrasolar Planet Finding via Optimal Apodized and Shaped Pupil Coronagraphs," *Astrophysical Journal* 582: 1147–1161.

[50] Kasdin, N. J., Vanderbei, R. J., and Belikov, R. 2007. "Shaped Pupil Coronagraphy," *Comptes Rendus Physique* 8(3-4): 312–322.

[51] Slepian, D. 1965. "Analytic solution of two apodization problems," *Journal of the Optical Society of America* 55(9).

[52] Vanderbei, R. J., Spergel, D. N., and Kasdin, N. J. 2003. "Circularly symmetric apodization via starshaped masks," *Astrophysical Journal* 599: 686–694.

[53] Vanderbei, R. J., Spergel, D. N., and Kasdin, N. J. 2003. "Spiderweb masks for high contrast imaging," *Astrophysical Journal* 590: 593–603.

[54] Vanderbei, R. J., Kasdin, N. J., and Spergel, D. N. 2004. "Checkerboard-Mask Coronagraphs for High-Contrast Imaging," *Astrophysical Journal* 615.

[55] Vanderbei, R. J., Kasdin, N. J., and Spergel, D. N. 2004. "Rectangular-mask coronagraphs for high-contrast imaging," *Astrophysical Journal* 615.

[56] Balasubramanian, K., et al. 2006. "Fabrication and Characteristics of Free Standing Shaped Pupil Masks for TPF-Coronagraph," *Proc. of SPIE* 6265.

[57] Ceperley, D., Neuteuther, A., Miller, M., Lieber, M., and Kasdin, N. J. 2006. "Stray-light sources from pupil mask edges and mitigation techniques for the TPF Coronagraph," *Proc. SPIE* 6271: 62711F.

[58] Lieber, M., Neureuther, A. R., Ceperley, D., Kasdin, J., Hoppe, D., and Eisenman, A. 2005. "Evaluating the end-to end performance of TPF-C with vector propagation models: Part I. Pupil mask effects," *Proc. of SPIE* 5905: 173–184.

[59] Belikov, R., Kasdin, N.J., and Vanderbei R.J. 2006. "Diffraction-based Sensitivity Analysis of Apodized Pupil-Mapping Systems," *ApJ Vol* 652(1): 833–844.

[60] Give'on, A., Belikov, R., Shaklan, S., and Kasdin, J. 2007. "Closed loop, DM diversity-based, wavefront correction algorithm for high contrast imaging systems," *Optics Express* 15(19): 12338–12343.

[61] Shaklan, S. B., Green, J. J., and Palacios, D. M. 2006. "The terrestrial planet finder coronagraph optical surface requirements," *Proc. of SPIE* 6265.

[62] Belikov, R., Give'on, A., Kern, B., Cady, E., Carr, M., Shaklan, S., Balasubramanian, K., White, V., Echternach, P., Dickie, M., Trauger, J., Kuhnert, A., and Kasdin, N. J. 2007. "Demonstration of high contrast in 10% broadband light with the shaped pupil coronagraph," *Proc SPIE* 6693.

[63] Monge, G. 1781. "Sur la theorie des deblais et des remblais," *M`em. de lacad. de Paris.*

[64] Caffarelli, L. A., and Milman, M. 1999. "Monge Ampere Equation: Applications to Geometry and Optimization," *Amer. Math. Soc.*

[65] Glimm, T., and Oliker, V. 2002. "Optical design of two-reectorsystems, the Monge-Kantorovich mass transfer problem and Fermats principle."

This page is intentionally left blank.

8.8 End-to-End Modeling of ACCESS

Prepared by:

John Krist, Dwight Moody, and Dimitri Mawet
(Jet Propulsion Laboratory)

End-to-end modeling of a coronagraph involves computing the propagation of a wavefront through a realistic optical system, sensing the wavefront at the image plane, deriving settings for the deformable mirrors to create a dark field around the star in the image, and then computing the final image using those settings. During this process, the performance of a given optical configuration can be evaluated in terms of sensitivity to and ability to control wavefront errors over a given bandpass. From this, requirements can be set on critical optical surfaces and telescope pointing.

8.8.1 Simulation Environment

Wavefront Propagation Software

The accurate modeling of how the wavefront changes as it passes through the ACCESS optical system requires algorithms that compute the effects of diffraction and scattering at each surface. Fraunhofer (far-field) diffraction, which can simply be computed by the Fourier transform of the wavefront, may be used when propagating directly from a pupil plane (e.g., the primary mirror) to an image plane and vice-versa. However, it does not account for the effects of intermediate optics that are important to high contrast coronagraphic imaging.

As the wavefront propagates, phase errors gradually transform into amplitude errors and vice-versa (the *Talbot effect*; see [1]). A surface height deviation in an optic, perhaps caused by imperfect polishing, will alter the wavefront's phase. If that optic is located somewhere other than a pupil or image plane, the phase error will turn into a combination of phase and amplitude errors by the time the wavefront reaches the detector. Scattered light in the image plane behaves differently with wavelength depending on whether it was created by a phase or amplitude error, and the two types of errors are corrected differently. The correction of amplitude errors in the image plane actually makes use of the Talbot effect by altering the wavefront's phase with a deformable mirror located at an intermediate plane [2]. Thus, it is critical to use more complex algorithms that can handle optics at intermediate (near-field) planes when modeling high contrast systems. For most systems, Angular Spectrum and Fresnel propagation algorithms suffice.

For this study we have applied two different optical modeling packages that utilize the same near-field and far-field propagation algorithms and produce similar results. The first is proprietary code written by Dwight Moody at JPL. It has been used extensively for simulating coronagraphs in the High Contrast Imaging Testbed (HCIT) at JPL and has been verified against actual HCIT results. It was used for simulating the bandlimited occulter Lyot coronagraphs in this study. The other package is the PROPER optical propagation library for IDL [3]. PROPER is free and publicly available from www.openchannelsoftware.com. PROPER has routines that compute both near and far-field diffraction using automatically-chosen algorithms. It can create amplitude and phase errors on each optic specified by Zernike polynomials, power spectra, or user-provided maps. It also includes a model of a Xinetics deformable mirror with measured actuator influence functions. PROPER was used to simulate the optical vortex and PIAA coronagraphs in this study. The Moody software has similar routines.

Both packages compute the wavefront through an unfolded system (i.e., no tilted optics), so for the ACCESS simulations the components were extracted from the Zemax optical prescription and placed along a single axis. Mirrors were converted to equivalent thin lenses. The same unfolded

layout was used for the bandlimited and optical vortex coronagraphs. The PIAA system, which has a number of additional components, shared only the first few optics and required a largely different layout. Only the V-band channel was modeled.

Propagation within the bandlimited Lyot, optical vortex, and shaped pupil coronagraphs can be modeled using standard algorithms, though the representation of the vortex mask is complicated. PIAA, however, requires custom algorithms to propagate between the remapping optics, as detailed later.

Wavefront Representation and Sampling

The wavefront in the simulations is represented by a 2048 × 2048 double-precision complex-valued array. This size is sufficient to accommodate the highest spatial frequency surface errors of concern and can be efficiently processed on the available computers. All of the simulations produce sampling in the image plane that is better than the Nyquist criterion (0.5 λ/D per pixel). This is accomplished by defining the entrance pupil diameter to be less than half the wavefront array diameter. In the case of the optical vortex, the image sampling is even finer (0.1 λ/D per pixel).

Occulter Definition

Each coronagraphic system has an image plane occulter. The hybrid bandlimited Lyot coronagraph occulter has a greyscale amplitude transmission profile as well as a phase-modulating coating that provides a 4th order aberration tolerance. The occulter profile is defined to have 50% intensity transmission at a radius of 2 or 3 λ/D radians (D is the telescope diameter) at the central wavelength (550 nm). The PIAA occulter is a hard-edge spot located at the focus of the PIAA mirrors. It produces a 50% transmission at a radius of 2.5 λ/D. The optical vortex has a phase mask of charge=4 (4th order aberration tolerance) with a small hard-edge spot at the center with a radius of 0.25 λ/D.

Dark Hole Size

The inner radius of the dark hole is set by the size of the occulter. We chose an inner working radius of 2–3λ/D radians at the central wavelength (550 nm), depending on the coronagraph. However, the effective IWA is not fully a function of the coronagraph, as wavefront control at the lower spatial frequencies corresponding to these radii is critical to achieving the required contrast. The outer radius is limited by the number of DM actuators that span the pupil diameter. If a DM has N actuators across the pupil, the maximum region that it can correct is $N\lambda/D$ radians in diameter. In practice, deep contrast fields can only be achieved using even smaller outer limits. In this study we use DMs having 48 actuators across the pupil diameter and limit the outer radius of the dark hole to be equal to 20 λ/D at the shortest wavelength.

Optical Fabrication Errors

A two-dimensional map of surface errors was generated for each optic in the system. The spatial frequency distribution of the errors was defined by power spectral density (PSD) curves derived from actual high-quality optics. The primary mirror was set to have an RMS surface error of 7.5 nm. The other optics were set to have 1.25 nm RMS surface errors. Such high-quality surfaces, even on off-axis aspherical mirrors, are well within the capability of commercial fabricators (e.g., Tinsley, ASML, etc.). During our modeling it became apparent that certain components (flat mirrors near focus and the mirrors between the PIAA optics and occulter) required even lower errors in order to achieve the necessary 10^{-9} contrast performance. At these critical locations phase errors can create large amplitude errors that are impossible to fully correct in broadband light. Measured surface error maps of PIAA optics created by Tinsley were used for the two forward PIAA mirrors.

Coating errors that cause non-uniform reflection can also reduce the contrast performance. Because of its size, the primary mirror represents the most difficult optic to coat uniformly. We

generated a synthetic reflectivity error map for the primary based on a reflectance PSD derived from test samples that were distributed within a large-optic coating chamber at ITT. We assumed that the uniformity on the smaller ACCESS optics was not important and thus did not include reflectivity maps for them.

Simulation of the PIAA system requires that the wavefront be distorted by the forward PIAA and undistorted by the reverse PIAA. This is implemented via interpolation. During PIAA remapping, the wavefront errors are spatially compressed near the beam axis. In order to prevent aliasing from high spatial frequency aberrations during the forward and inverse remapping steps, the surface and primary reflectivity maps were filtered to a maximum spatial frequency of 45 cycles across the beam diameter (85 cycles for the optics between the forward PIAA and occulter). Thus, at the final focus the uncorrected scattered light caused by these errors can be seen extending out to 45 λ/D radians. This is sufficient to encompass high spatial frequency errors that through folding and other effects scatter light into the 20 λ/D radius dark hole region.

8.8.2 Wavefront Control

The simulation software is used to generate images at the final focus of the system. The wavefront can be derived from such images either by: (1) introducing a variety of known wavefront disturbances (e.g., altering the DM surface with specific patterns), measuring the image plane intensities, and solving for the common wavefront; or (2) directly using the complex electric field computed by the propagation software. Option (1) represents what would be used for a real system in which only wavefront intensity can be measured by the detector. Our experience shows that both methods produce the same results in simulation, while (2) is faster.

Using either method, the wavefront in our simulations is "sensed" within the image region in which we wish to create a dark hole at 5 or 6 monochromatic wavelengths sampling the bandpass. This allows a polychromatic solution to be derived, whereas sensing at just one wavelength would produce a less optimal broadband result.

The DM settings that create the dark hole are derived using the Electric Field Conjugation (Energy Minimization) method. This technique makes the approximation that the wavefront responds linearly to changes induced by the DMs. The effect of each DM actuator on the image plane electric field is computed at each sensing wavelength by pistoning the actuator by a small amount (0.1–1 nm) and propagating the effect through the model system. The electric field at the image plane is stored in a DM response matrix. This represents the most time-consuming portion of the simulation process as there are about 3600 active actuators total on both DMs. For some systems we can take advantage of symmetry and compute the responses for a fraction of the actuators.

The wavefronts at the sensing wavelengths and the DM response matrix form a linear system that can be solved in a least-squares sense. Because the system is not truly linear, this process must be iterated. Regularization is used to limit the actuator strokes to the linear regime, with the optimal regularization value achieved through trial-and-error.

Once a suitable dark hole has been generated, other aberrations can be introduced to determine the sensitivity of the system to the effects of pointing errors and thermally-induced wavefront changes.

8.8.3 Modeling the Bandlimited Lyot Coronagraph

The Lyot coronagraph used in the ACCESS study has a bandlimited mask that varies both the phase and amplitude in the image plane. The wavefront is propagated to the intermediate image plane and multiplied by the complex-valued occulter pattern. The beam is then propagated to a pupil image where the Lyot stop is applied. The stop is a simple aperture smaller than the pupil diameter and matched to the modified pupil pattern created by the occulter. The simplicity of the Lyot coronagraph allows it to be easily and accurately modeled using common propagation algorithms.

Caveats

Propagation through the Lyot coronagraph utilizes standard techniques like those used in PROPER. Models of bandlimited Lyot coronagraphs have been compared to results from HCIT at contrast levels equal to those required for ACCESS. The simulated and observed results match very well, and the models have been used to guide experiments. The major expected source of inaccuracies in the modeling results is that the occulter phase and amplitude transmissions in the models are wavelength independent (e.g., the same phase shift in radians is applied at each wavelength). A real occulter would have some wavelength-dependent dispersion that would reduce the performance over a broad bandpass. This can be minimized with a judicious choice of dielectric coatings. Predicted dispersions based on multilayer coating calculations will be applied in future modeling efforts.

Results

The hybrid bandlimited occulter Lyot coronagraph, as modeled, easily meets the contrast requirement for a system having non-primary-mirror optical surface errors of <1.25 nm RMS. It appears to allow for the correction larger wavefront errors over a broad bandpass than is possible with PIAA. This is may be due to the particular structure of the actuator response function as seen in the final image plane along with the ability to use actuators located behind the Lyot stop.

Future Modeling Studies

The wavelength-dependent amplitude and phase terms of the occulter will need to be included in future models. These must be computed from the known properties of the metal and dielectric coatings used in the occulters. These deviations from the ideal wavelength-independent model used in this study may result in lower contrast dark holes or, in order to maintain the current contrast levels, reduced bandwidth. Manufacturing errors (e.g., deviations from the desired amplitude profile) should also be included (these have in previous studies for HCIT experiments).

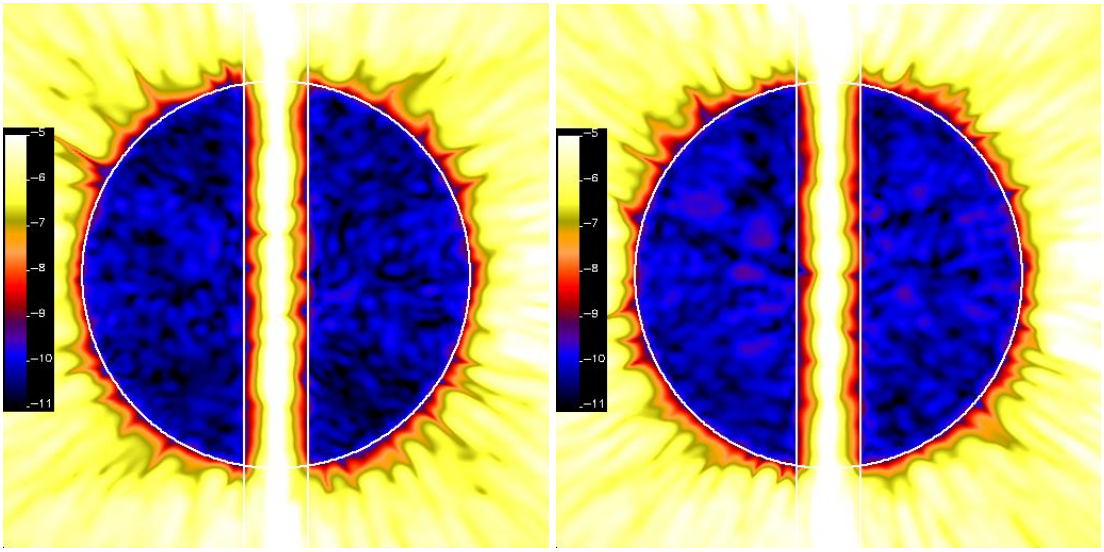

Figure 8.8.3-1. Contrast maps for a hybrid occulter Lyot coronagraph over λ=500–600 nm after wavefront correction. A linear occulter was used. The color scale indicates $\log_{10}$(contrast). The outer radius of 20 λ/D @ λ=500 nm and inner radius of 3 λ/D @ λ=550 nm are outlined. The left map shows the results for a system with 0.25 nm RMS surface error non-primary optics, and the right shows the contrast with 1.25 nm RMS non-primary optics. The primary has 8 nm RMS surface errors.

8.8.4 Modeling the Optical Vortex Coronagraph

The OVVC effectively produces a phase ramp through fractional manipulation of the polarization of the incoming wavefront. Rather than duplicating the physics involved in this process, it is easier to simulate its result, the phase screw, when modeling wavefront propagation through the system. Even so, the fact that there is a numerical singularity at the center of the screw causing rapid phase changes that cannot be exactly represented on the computational grid means that additional steps must be taken to produce a sufficiently accurate simulation.

The image of the PSF in the plane of the vortex mask must be highly oversampled to match the fine sampling required to adequately represent the phase screw. This is accomplished by using a small pupil diameter relative to the size of the computational wavefront array. In the ACCESS OVVC simulations, the pupil diameter is 204.8 pixels while the grid diameter is 2048 pixels, producing a PSF that is sampled by 0.1 λ/D (5 times better than the Nyquist criterion).

In the representation of the phase screw, the central 127 by 127 pixel region, including the occulting spot, is generated on a grid subsampled by a factor of 51 in each direction (6477 pixels on a side) and then rebinned to the wavefront sampling. The outer regions of the mask are directly computed. At the subsequent Lyot plane, the reimaged pupil is masked by a circular stop with a 90% clear diameter.

Both the OVVC and Lyot coronagraphs can be modeled using PROPER and its default propagation algorithms. Both can utilize the same optical prescription and surfaces.

As discussed in the OVVC description earlier in this document, the design results in a "leakage" of unsuppressed PSF light that is incoherent with the residual field. To approximate this term, a PSF is generated by propagation through the system without the image plane mask. This PSF is then normalized by a fractional leakage factor and added in intensity to the coronagraphic field.

Caveats

The OVVC is a relatively new concept and to date only one such mask has been tested in the HCIT. Thus, only a limited amount of model verification has been done, none at the contrast levels required for ACCESS. The models agree with analytical calculations, and expectations are that the models produced using the phase screw described above are accurate to better than 10^{-9} contrast.

Results

The OVVC was simulated using PROPER for both 10% (525–575 nm) and 20% (500–600 nm) bandpasses. The inner working angle was $2\lambda/D$ at λ=550 nm. The occulting spot was 0.25 λ/D in radius. Using EFC, dark hole fields were generated for each case. The 20% bandpass simulation has a mean contrast value of 1.9×10^{-10} over the entire hole and 2.9×10^{-9} at r = 2-3 λ/D. With a 10% bandpass, the mean contrast is 5.0×10^{-11} and 1.3×10^{-9} at 2-3 λ/D. In both cases the results represent fields observed at one polarization.

The models show that the OVVC, as simulated, can achieve the required dark field over a 10% bandpass and also at 20%, though the region near the IWA is slightly higher than desired.

Future Modeling Studies

More accurate representation of the wavelength-dependent terms is needed to provide a better estimate of the broadband performance of the OVVC. Polarization effects also need to be examined in greater detail. Specifically, simulations are needed to determine if it is possible to create a sufficiently deep dark hole in both polarizations using one pair of DMs (rather than having two separate polarization channels, each with its own DM pair, which would increase cost and complexity).

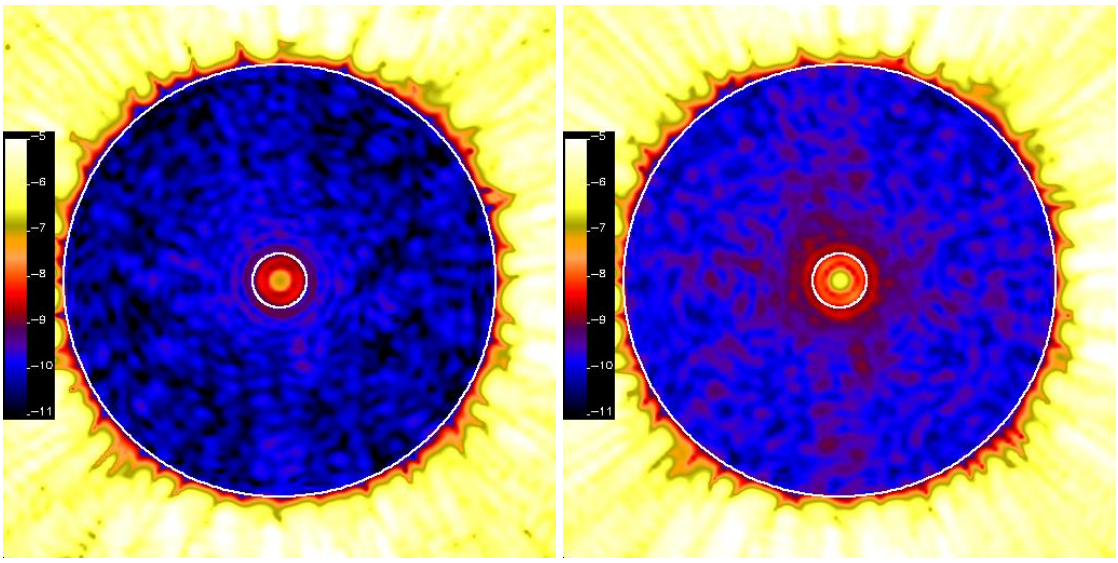

Figure 8.8.4-1. Contrast maps for OVVC after wavefront correction. The color scale indicates $\log_{10}$(contrast). The outer radius of 20 λ/D @ λ=500 nm and inner radius of 2 λ/D @ λ=550 nm are outlined. The left map shows the results for a system operating at λ=525–575 nm (10% bandpass) and on the right is λ=500–600 nm (20% bandpass).

8.8.5 Modeling the Shaped Pupil

The shaped pupil is implemented with a mask located in a collimated beam within the coronagraphic system. We have chosen the "Ripple 3" design that in an aberration-free system can provide a region of $<10^{-9}$ contrast. This particular mask has an inner working angle of 4 λ/D and a dark field opening angle of 90°, providing a 180° field of view.

The complex openings in the mask are defined by points through which a spline curve is fit. The mask must be created with subpixel precision with antialiased edges. Adequate sampling must be used to ensure that the narrow openings are sufficiently defined to create the required contrast levels. After the beam has passed through the mask, it is focused onto an occulter that blocks the core and extended bright regions of the PSF.

Standard propagation methods are used. The shaped pupil has been tested to contrasts approaching 10^{-9} in the HCIT. The results generally agree with the models, but more extensive comparisons are needed.

Caveats

The implementation of the shaped pupil is rather straightforward. Mask defects have not been taken into account. Also, at contrast levels of $<10^{-9}$, field interaction with the metal masks must be taken into account using more complex modeling techniques.

Future Modeling Studies

Further work is needed to verify the models with HCIT results over broad bandpasses at contrast levels of $<10^{-9}$. The ability of a wavefront control system to correct chromatic errors in a shaped pupil coronagraph has not been sufficiently explored.

A modification to the shaped pupil system has been proposed that would use the DMs to create a pseudo-PIAA system that would allow a shaped pupil provide a smaller IWA with greater throughput than would be possible with a shaped pupil alone.

8.8.6 Modeling PIAA

Simulating propagation between the two PIAA mirrors presents a considerable challenge. To produce strong beam apodization, the surface curvature rapidly changes near the outer edge of the first PIAA mirror, introducing a large wavefront variation that cannot be adequately sampled using conventional Fourier-based algorithms without impractically large arrays. Three alternative algorithms have been devised:

1. S-Huygens: Vanderbei [4] derived a method to accurately compute propagation within the PIAA system called S-Huygens. It is the only method presented here that includes the effects of diffraction. Belikov et al. [5] described the application of S-Huygens for propagating wavefronts that can be decomposed into radially-weighted azimuthal harmonics. We have developed code that can propagate an arbitrary wavefront through PIAA with this method. However, the number of harmonics needed to sufficiently describe the wavefront for the ACCESS study is about 450 (to adequately sample a feature at the edge of the pupil that has a diameter ~$1/50^{th}$ of the pupil). A multithreaded version of the code running on an 8 processor system takes one hour to propagate a monochromatic wavefront between the optics in both the forward and reverse PIAA systems (propagation from/to the PIAA systems is done using conventional propagation algorithms). This makes S-Huygens impractical for routine computations, as thousands of separate wavefront propagations are needed to compute the DM response matrix.
2. Geometric remapping with propagation of harmonics: This method approximates the propagation of a harmonic wavefront error (i.e., a ripple in amplitude or phase) between the two PIAA mirrors. By separately propagating different harmonics and then adding the results, the propagation of a more complex wavefront aberration can be simulated with Talbot effects included. This technique, however, completely ignores diffraction by assuming that its effects are sufficiently suppressed using a post-PIAA apodizer. Propagation of an arbitrary wavefront is a three-stage process. First, the wavefront is decomposed into its component harmonics by computing its Fourier transform. Second, the complex-valued, two-dimensional representation of the wavefront error described by that particular harmonic is then geometrically distorted to represent remapping by the PIAA optics and an apodization function applied to represent the combined PIAA and post-apodizer system. Finally, the distorted wavefront is multiplied by two phase terms, one that propagates the wavefront over some distance while the other, which is dependent on the spatial frequency of the aberration, replicates the Talbot effect. This method is somewhat faster than S-Huygens. The greatest drawback is that it propagates only pure harmonic signals that are assumed to have infinite extent. A decomposition of a pupil-bounded wavefront into harmonics will result in "impure," finite-extent harmonics that contaminate the propagator and create artifacts. Unless this problem is solved, perhaps by deconvolution of the aberration frequency spectrum, we cannot use this method except when manually specifying individual spatial frequency aberrations. This method is also too slow to be practical for this study.
3. Geometric remapping only: This is the simplest method. The wavefront is distorted and then multiplied by the PIAA and post-apodizer apodization functions. This completely ignores both diffraction and Talbot effects. It is very quick, however, and captures some of the important effects caused by remapping.

Due to time constraints the third method is used for propagation between the two PIAA mirrors in both the forward and reverse PIAAs. The wavefront up to the first PIAA mirror (PIAA M1) is computed using the default PROPER routines. The measured surface error map of the Tinsley M1 optic is applied. The wavefront is then remapped via cubic convolution interpolation. Care must be taken to ensure that pixels at the edge of the pupil-bounded wavefront are interpolated accurately.

The error map for the M2 Tinsley mirror is then applied. The wavefront is then multiplied by a function representing the apodization provided by the first PIAA optic as seen at the second optic. The wavefront is then propagated to a mirror (apodizer OAP) that then creates an image of the 2nd PIAA mirror on the post-apodizer, where another apodization function is applied. There is then a propagation to another mirror (occulter OAP) that focuses the beam onto the occulter, which is represented by a solid disk. After that the beam is propagated to a mirror that then feeds the reverse PIAA system. In the reverse system the wavefront is again interpolated to undistort the wavefront and the apodization provided by the forward PIAA optics (but not the post-apodizer) is divided out. From there on the beam is propagated through other optics to the final image plane.

Caveats

A number of approximations must be made when modeling PIAA with an arbitrary input wavefront, especially with time constraints of this study. With the geometric remapping method, diffraction at the edge of the 1st PIAA optic is not accounted for. This likely results in an underestimation of the amount of unsuppressed PSF signal that leaks into the dark hole, a problem that is probably highly chromatic and difficult to remove using the DMs. In the models surface errors on the PIAA optic do not alter the apodization function, as they would in reality (including creating chromatic amplitude errors). The conversion of phase-to-amplitude errors and vice-versa by the Talbot effect are not handled. All of these will limit the accuracy of the broadband response of the system. Comparisons with more sophisticated methods (namely S-Huygens) have not yet been made for complex wavefronts.

None of the propagation methods have been verified against results obtained with actual PIAA optics at contrast levels approaching the ACCESS requirements. There are plans to do so in the HCIT within the next year.

Results

To the level of accuracy provided by the geometric remapping method, the PIAA system as implemented in the ACCESS study can achieve a mean dark hole contrast of 8.3×10^{-10} in a 20% bandpass (though some speckles as bright as 5×10^{-9} in contrast occur). This level can only be achieved with certain critical optics having extremely low surface errors (<0.25 nm RMS). Specifically, these are the two fold mirrors prior to the occulter that are located near a focus and the two OAPs between the forward PIAA optics and occulter. The contrast requirement is not reached if any of these four optics has surface errors of >0.5 nm RMS, while the other non-primary-mirror optics in the system can have 1.25 nm RMS surface errors.

The residual high level speckles are highly chromatic and are brightest at the shortest wavelength. It has been demonstrated that optics near focus must be very smooth or else the phase errors they introduce will turn into chromatic amplitude errors that cannot be fully corrected [2]. The aberrations on the post-PIAA OAPs appear to the DMs and the detector (both located outside of the distorted PIAA image space) as highly magnified towards the center of the pupil and compressed near the edge. High spatial frequency aberrations on the OAPs appear as a combination of much lower frequency ones that the DMs can correct and higher frequency errors that it cannot. These residual aberrations, through frequency folding, may create highly chromatic scattered light inside the dark hole that cannot be corrected by the DMs. The effects of such errors will require further study.

It appears that it is more difficult to achieve a broadband dark hole with a PIAA system than with a bandlimited Lyot coronagraph given the same optical surface error levels. PIAA does not appear to have the same leverage to correct chromatic aberrations as the Lyot coronagraph has with its particular actuator response functions and actuators masked by the Lyot stop.

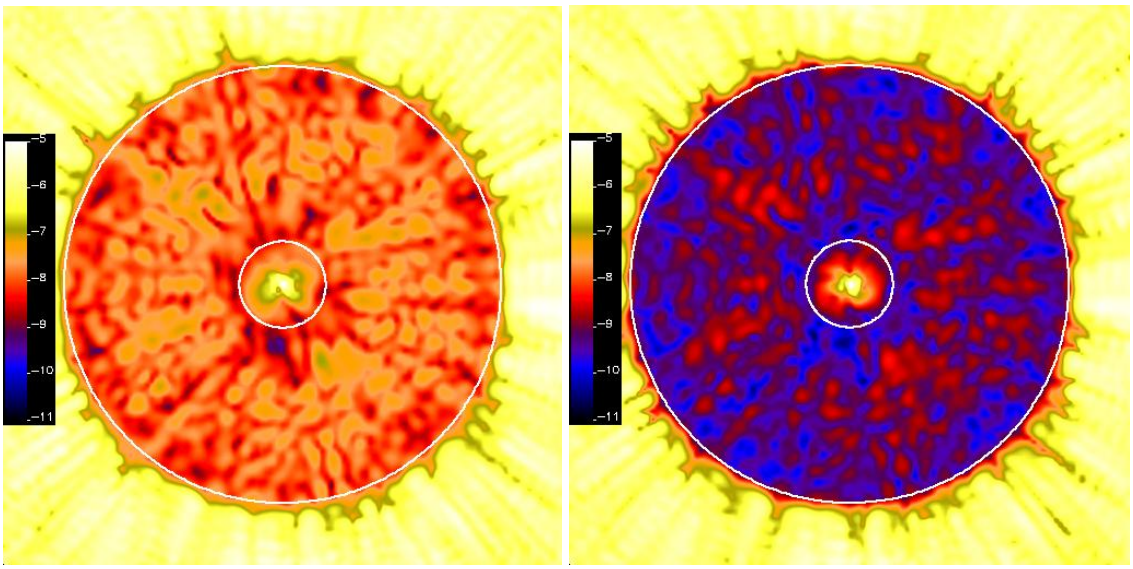

Figure 8.8.6-1. Contrast maps for a simulated PIAA system over λ=500–600 nm after wavefront correction. The color scale is given in $\log_{10}$(contrast). The outer radius of 20 λ/D @ λ=500 nm and inner radius of 3 λ/D @ λ=550 nm are outlined. In both cases the primary mirror had 8 nm RMS surface error. The left map shows the contrast limit when all of the non-primary optics have 1.25 nm RMS surface errors (mean contrast = 1.8×10^{-8}), and on the right when the surface errors on just the post-PIAA OAPs and near-focus flats are reduced to 0.25 nm RMS (mean contrast = 8.3×10^{-10}).

Future Modeling Studies

PIAA requires a significant advancement in modeling techniques in order to reach the same levels of simulation accuracies as are possible for the other coronagraphs. While S-Huygen can provide the accuracy, it is too slow to be useful for end-to-end modeling (it is useful for limited comparisons with other techniques, though). Comparisons of the other methods (remapping, remapping with harmonics) to S-Huygens and to testbed results are needed. Hopefully, some new method will be devised that provides the accuracy of S-Huygens but with considerably improved speed.

The apparent difficulty that PIAA has dealing with chromatic errors introduced by near-focus or post-PIAA optics needs further analysis. The surface requirements suggested by this study are at the extreme limits of current technology, and attempts to get contrast down to the 10^{-10} level required for an exo-Earth mission (rather than an exo-Jupiter mission like ACCESS) appear unlikely. This sensitivity of PIAA in the models needs to be verified against testbed results with a similar configuration (DMs prior to the PIAA optics, inverse PIAA optics included).

8.8.7 References for Section 8.8

[1] Goodman, J. 1996. *Introduction to Fourier Optics. Edition 2.* McGraw-Hill Companies, Inc.

[2] Shaklan and Green. 2006. *Applied Optics* 45: 5143.

[3] Krist. 2007. *Proc. SPIE* 6675: 66750P.

[4] Vanderbei. 2006. *Ap.J.* 636: 528.

[5] Belikov, et al. 2006. *Ap.J.* 652: 833.

This page is intentionally left blank.

8.9 Science Mission Metrics

Prepared by:

Karl Stapelfeldt, John Krist, Dwight Moody, and Dimitri Mawet
(Jet Propulsion Laboratory)

8.9.1 Objective

To quantify the search space for high contrast exoplanet detections available to the different coronagraph options for the ACCESS mission. Here we define a simple, transparent algorithm to provide a metric for comparisons among the ACCESS coronagraph types, and to give a rough measure of the science reach for the ACCESS mission. Ultimately, the optimal science strategy for the mission will employ targeting algorithms that balance search completeness and detailed studies of individual exoplanet systems, by adjusting priorities and allocating observing time in response to events and discoveries in real time during the mission [1].

8.9.2 Performance Assumptions

- 1.5 meter unobscured telescope aperture
- Pair of 48 × 48 element deformable mirrors with EFC wavefront control over bandpass from 0.5–0.6 μm. Outer working angle of 1.8 arcsec.
- read noise 3 electrons per pixel
- dark current 0.001 electrons per sec per pixel
- CCD detector gain 1 electron per DN
- Maximum individual exposure time = 3600 sec for CR split

PSFs for the on-axis occulted star and off-axis planet were provided by the Lyot, PIAA, and vortex mask teams—along with the amplitude transmission map of the specific occulting spot for each.

Planet brightness is calculated at mean illumination phase (90 degree phase angle): Relative to the star, Δmag = 22.5 for Jupiter, 22.9 for Saturn, 24.8 for Uranus, and 26.2 for a super Earth (all as seen at 5 AU asterocentric distance; scaled by $1/r^2$ when planets placed at different distances).

Zodiacal light background of V = 22.7 mag per square arcsec adopted.

Exozodi background surface brightness at the 1 zodi level is included, radial scaled by $1/r^2$.

Background count rate from scattering and diffraction is the azimuthal average of the full 2-D speckle pattern at radius where planet is being sought. Occulted PSF, scaled by stellar V magnitude, is used to define the stray light background.

Planet and sky background counts attenuated by local transmission of the occulting spot.

Inner working angle cutoffs of 0.23, 0.19, and 0.15 arcsec (corresponding to 3.0, 2.5, and 2.0 λ/D at 0.55 μm wavelength).

Input star catalog to the calculation: Digital version of the Hipparcos catalog, sorted by increasing order of stellar distance. From the distance to each star in the catalog, calculate the angular scale of the planet orbit to establish the local stray light background and occulting mask throughput. The apparent separation is considered for two cases 71% and 97% of the physical separation (corresponding to 45° and 15° of orbital longitude from maximum elongation). In this approach, the single-epoch obscurational completeness will be >50% and >16% respectively for exoplanetary systems confined to a plane that appears edge-on. The completeness metric will always be greater than these minimum values for systems that are more face-on and for exoplanetary systems with multiple giant planets. The completeness metric approaches unity for the prescribed six observing epochs spread over the mission lifetime.

Photometry is measured using a square box aperture 2 λ/D in size for the PIAA and Vortex cases. For the Lyot case, the PSF becomes elongated and a rectangular aperture 3 λ/D by 2 λ/D in

size is used. Furthermore, the photometry aperture near the inner working angle is "adaptive", such that no light is included from any part of the planet PSF that extends inside the specified inner working angle. This choice reduces throughput at the inner working angle, but excludes substantial stray light present inside the IWA and is thus beneficial in the Lyot case. The full size aperture (i.e., not adaptive) was used for the PIAA performance in the 3 λ/D case and for the Vortex performance in the 3 λ/D and 2.5 λ/D cases, since those coronagraph types were designed for 2.5 λ/D and 2.0 λ/D inner working angles respectively.

8.9.3 Definition of Terms Used in the Calculation

Desired Signal to Noise = S2N
Planet Count Rate = PCR
Diffraction+Scattering Count Rate = DCR
(Sky) Background Count Rate = BCR
Dark Rate per Pixel = DRKCR
Read Noise per Pixel = RNPP
Exposure Time = etime

$$signal = PCR \times etime$$

$$noise = \sqrt{\left(PCR + DCR + DRKCR + BCR\right) * etime + RNPP * RNPP}$$

$$S2N^2 = \frac{(PCR \times etime)^2}{\left(PCR + DCR + DRKCR + BCR\right) * etime + RNPP * RNPP}$$

$$PCR^2 etime^2 - S2N^2\left(PCR + DCR + DRKCR + BCR\right) etime - S2N^2 RNPP^2 = 0$$

Solve the above quadratic equation for etime; determine how many maximum-length exposures this requires; scale up the read noise accordingly, and solve for the corrected etime.

8.9.4 Results

Our primary metric for comparing the science achieved by the various coronagraph designs is the number of stars that can be surveyed for giant planets in a 5-year mission in which 50% of the observing time is allocated to planet searches. We assume that each target will be observed at 6 different epochs as a way of increasing the completeness of the planet search. The exposure time is chosen to yield, at each epoch, a detection of the fiducial planet at S/N = 10. The time needed to observe each target is subtracted from a pool of 12,264 hours (2.5 years of observing time, 70% observing efficiency), until the allocated pool of time is used up. The results for the number of systems searched vs. coronagraph type is:

Table 8.9.4-1. Number of nearby stars that can be surveyed for 5.2 AU Jupiters, IWA 3 λ/D

Coronagraph Type	Planet 45° from max elong	Planet 15° from max elong
Lyot	117	175
PIAA	166	278
Vortex	135	204

Table 8.9.4-2. Number of nearby stars that can be surveyed for 5.2 AU Jupiters, IWA 2.5 λ/D

Coronagraph Type	Planet 45° from max elong	Planet 15° from max elong
Lyot	153	218
PIAA	178	267
Vortex	154	228

Table 8.9.4-3. Number of nearby stars that can be surveyed for 5.2 AU Jupiters, IWA 2.0 λ/D

Coronagraph Type	Planet 45° from max elong	Planet 15° from max elong
Lyot	170	230
Vortex	164	241

Note: Accurate PIAA wavefront control solution not available for this IWA

Table 8.9.4-4. Sample output for Lyot coronagraph, 2.5 λ/D IWA case, 5.2 AU Jupiters 45° from max elongation, 1 zody background. In the rightmost 3 columns, "E" represents photoelectrons counted.

#	Star Name	V	D(pc)	Type	Exp (sec)	Estar	Eplan	Ezodi
1	69673	-0.1	11.3	K2IIIp	1.41E+02	7.53E+11	443.	2.178E+02
2	91262	0.0	7.8	A0Vvar	1.54E+02	7.64E+11	462.	1.526E+02
3	24608	0.1	12.9	M1: com	1.64E+02	7.81E+11	418.	2.312E+02
4	37279	0.4	3.5	F5IV-V	2.15E+02	7.59E+11	462.	8.931E+01
5	97649	0.8	5.1	A7IV-V	3.00E+02	7.61E+11	462.	1.398E+02
6	37826	1.2	10.3	K0IIIva	4.47E+02	7.85E+11	481.	3.317E+02
7	113368	1.2	7.7	A3V	4.50E+02	7.84E+11	474.	2.501E+02
8	36850	1.6	15.8	A2Vm	8.55E+02	1.02E+12	391.	3.164E+02
10	57632	2.1	11.1	A3Vvar	1.15E+03	8.21E+11	495.	5.554E+02
11	86032	2.1	14.3	A5III	1.22E+03	9.20E+11	417.	4.158E+02
12	32349	-1.4	2.6	A0m...	1.50E+03	2.88E+13	17703.	9.303E+02
13	105199	2.5	15.0	A7IV-V	1.91E+03	1.02E+12	414.	4.847E+02
14	67927	2.7	11.3	G0IV	1.99E+03	8.62E+11	507.	7.618E+02
15	61941	2.7	11.8	F0V+...	2.13E+03	8.74E+11	494.	7.461E+02
17	81693	2.8	10.8	F9IV	2.30E+03	8.84E+11	533.	9.061E+02
19	77952	2.8	12.3	F2III	2.36E+03	8.89E+11	503.	8.241E+02
20	2021	2.8	7.5	G2IV	2.38E+03	9.07E+11	544.	8.869E+02
21	107556	2.8	11.8	A5mF2 (	2.40E+03	8.87E+11	502.	8.162E+02
24	22449	3.2	8.0	F6V	3.54E+03	9.58E+11	584.	1.294E+03
25	46853	3.2	13.5	F6IV	3.61E+03	9.96E+11	496.	9.608E+02
26	44127	3.1	4.6	A7IV	3.63E+03	1.05E+12	476.	8.784E+02
27	116727	3.2	13.8	K1IV	3.79E+03	1.01E+12	502.	1.010E+03
32	86974	3.4	8.4	G5IV	4.59E+03	1.01E+12	618.	1.661E+03
34	8102	3.5	3.6	G8V	4.99E+03	1.03E+12	621.	1.638E+03
35	102422	3.4	14.3	K0IV	5.03E+03	1.11E+12	504.	1.128E+03
36	3821	3.5	6.0	G0V SB	5.05E+03	1.07E+12	618.	1.656E+03
37	17378	3.5	9.0	K0IV	5.14E+03	1.03E+12	635.	1.870E+03
38	95501	3.4	15.4	F0IV	5.14E+03	1.19E+12	481.	1.014E+03
40	89937	3.5	8.1	F7Vvar	5.40E+03	1.05E+12	640.	1.916E+03
41	57757	3.6	10.9	F8V	5.58E+03	1.05E+12	631.	1.941E+03
42	27072	3.6	9.0	F7V	5.59E+03	1.05E+12	648.	2.018E+03
43	99240	3.5	6.1	G5IV-Vv	5.67E+03	1.10E+12	636.	1.855E+03
45	16537	3.7	3.2	K2V	6.48E+03	1.08E+12	665.	2.132E+03
47	98036	3.7	13.7	G8IVvar	6.79E+03	1.14E+12	567.	1.645E+03
48	109176	3.8	11.8	F5V	6.91E+03	1.10E+12	645.	2.207E+03
52	78072	3.8	11.1	F6V	9.43E+03	1.39E+12	839.	3.203E+03
53	28103	3.7	15.0	F1V	9.47E+03	1.59E+12	642.	1.730E+03
55	14879	3.8	14.1	F8V	9.84E+03	1.52E+12	689.	2.054E+03
58	88601	4.0	5.1	K0V SB	1.26E+04	1.57E+12	960.	4.150E+03
59	14632	4.1	10.5	G0V	1.33E+04	1.63E+12	1000.	4.727E+03
62	12777	4.1	11.2	F7V	1.40E+04	1.64E+12	990.	4.659E+03
64	70497	4.0	14.6	F7V	1.43E+04	1.77E+12	803.	2.918E+03
65	7513	4.1	13.5	F8V	1.46E+04	1.71E+12	854.	3.355E+03
68	59199	4.0	14.8	F0IV/V	1.52E+04	1.91E+12	773.	2.635E+03
69	116771	4.1	13.8	F7V	1.54E+04	1.75E+12	873.	3.535E+03
73	105858	4.2	9.2	F6V	1.68E+04	1.78E+12	1103.	5.844E+03
75	64394	4.2	9.2	G0V	1.74E+04	1.81E+12	1118.	6.024E+03
77	1599	4.2	8.6	F9V	1.75E+04	1.82E+12	1120.	6.018E+03
78	61317	4.2	8.4	G0V	1.79E+04	1.84E+12	1131.	6.142E+03
79	102485	4.1	14.7	F5V	1.80E+04	2.05E+12	828.	3.081E+03
80	16852	4.3	13.7	F9V	1.98E+04	1.95E+12	971.	4.476E+03
81	15510	4.3	6.1	G8V	2.00E+04	2.02E+12	1166.	6.403E+03
84	64241	4.3	14.3	F5V	2.22E+04	2.13E+12	964.	4.376E+03
85	84405	4.3	6.0	K2:III:	2.24E+04	2.13E+12	1227.	7.170E+03
86	27913	4.4	8.7	G0V	2.27E+04	2.04E+12	1257.	7.780E+03
87	77257	4.4	11.8	G0Vvar	2.31E+04	2.02E+12	1185.	6.952E+03
88	19849	4.4	5.0	K1V	2.42E+04	2.09E+12	1278.	7.932E+03
91	12843	4.5	14.0	F5/F6V	2.82E+04	2.35E+12	1067.	5.460E+03
95	71284	4.5	15.5	F3Vwvar	3.11E+04	2.59E+12	1048.	5.207E+03
98	72659	4.5	6.7	G8V + K	3.19E+04	2.49E+12	1445.	1.038E+04
99	67275	4.5	15.6	F7V	3.27E+04	2.65E+12	1071.	5.465E+03

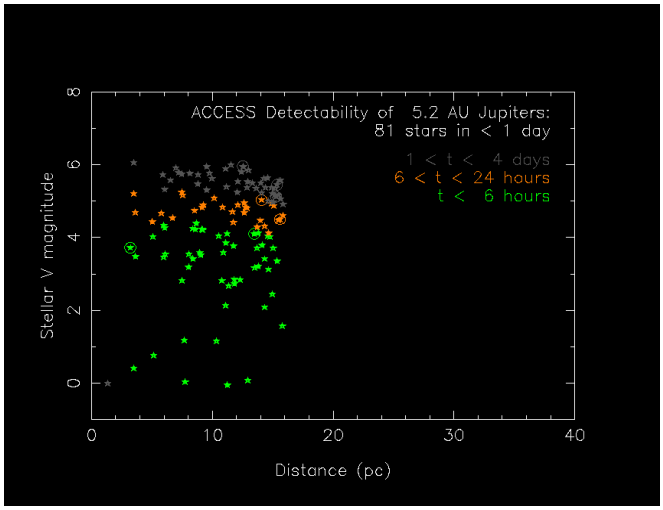

Figure 8.9.4-1. Lyot coronagraph performance, IWA 3 λ/D, planets 45° from max elongation

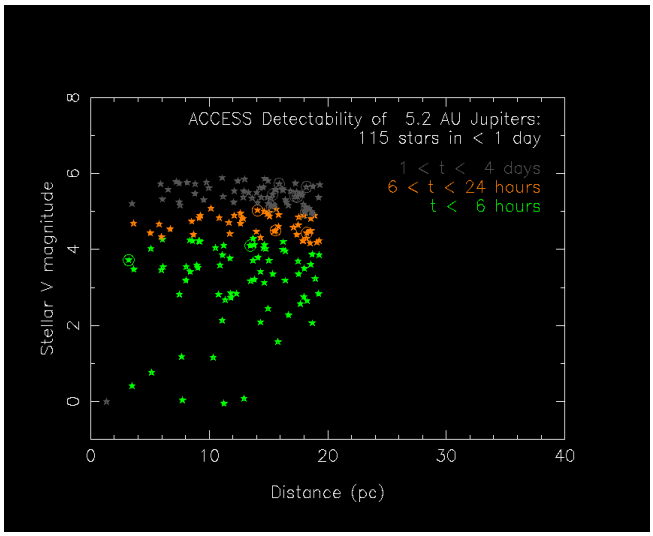

Figure 8.9.4-2. Lyot coronagraph performance, IWA 2.5 λ/D, planets 45° from max elongation

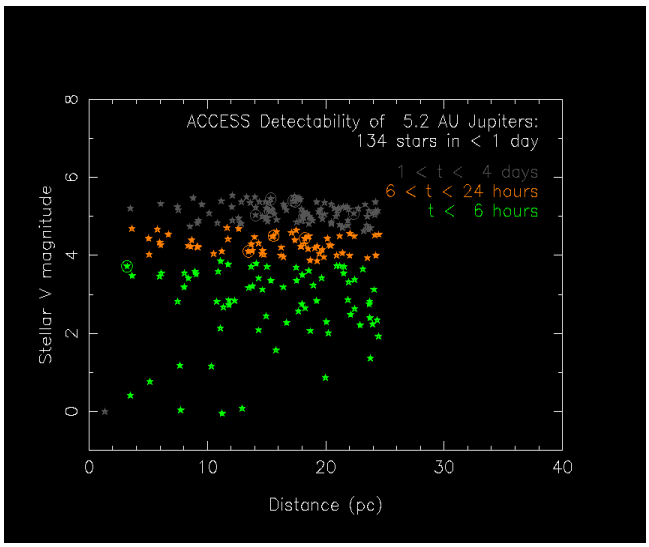

Figure 8.9.4-3. Lyot coronagraph performance, IWA 2 λ/D, planets 45° from max elongation

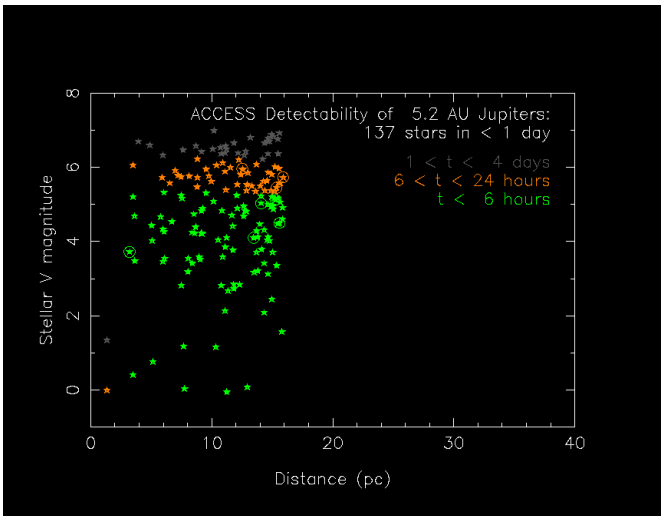

Figure 8.9.4-4. PIAA coronagraph performance, IWA 3 λ/D, planets 45° from max elongation

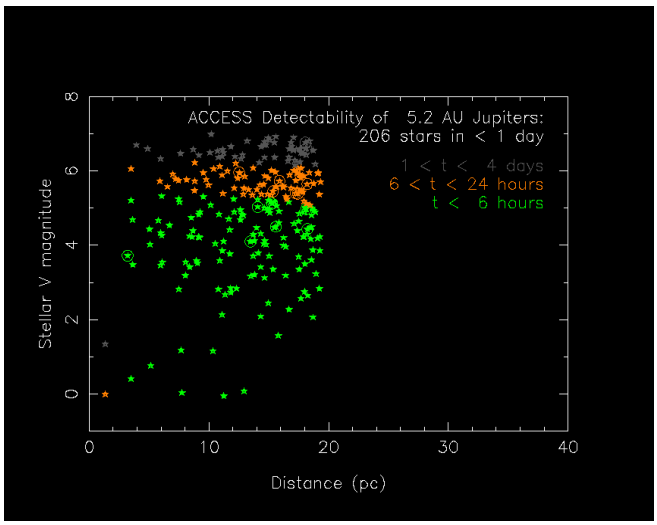

Figure 8.9.4-5. PIAA coronagraph performance, IWA 2.5 λ/D, planets 45° from max elongation

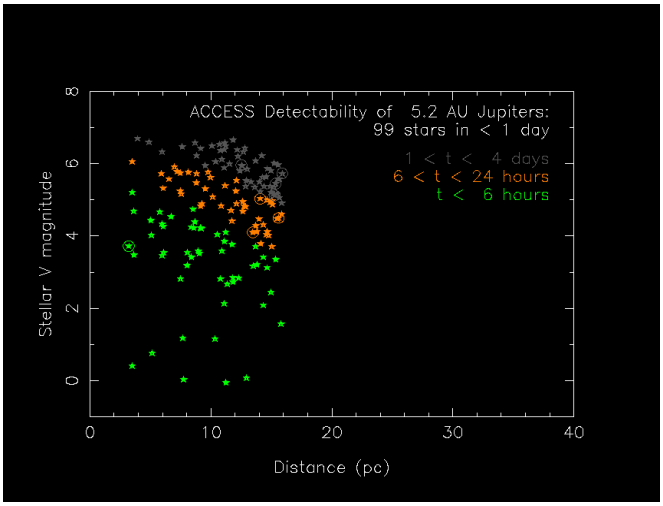

Figure 8.9.4-6. Vortex coronagraph performance, IWA 3 λ/D, planets 45° from max elongation

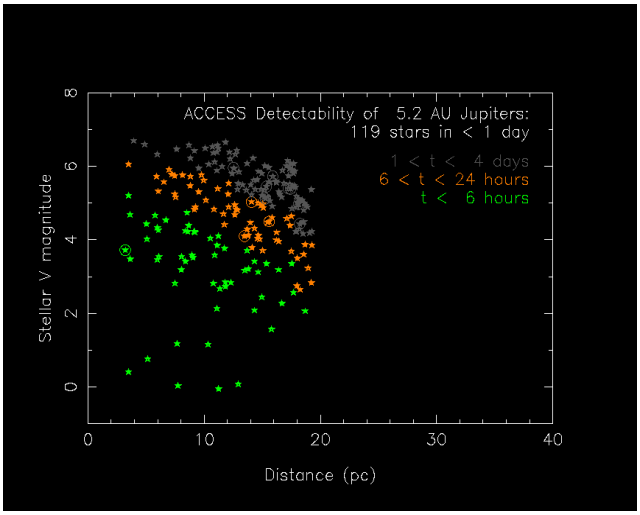

Figure 8.9.4-7. Vortex coronagraph performance, IWA 2.5 λ/D, planets 45° from max elongation

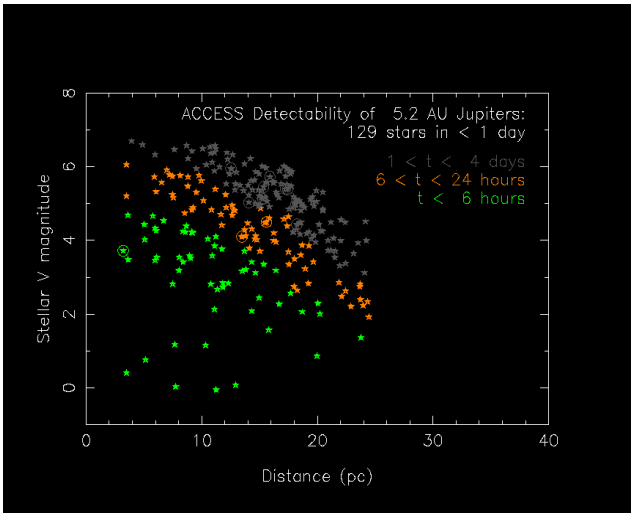

Figure 8.9.4-8. Vortex coronagraph performance, IWA 2 λ/D, planets 45° from max elongation

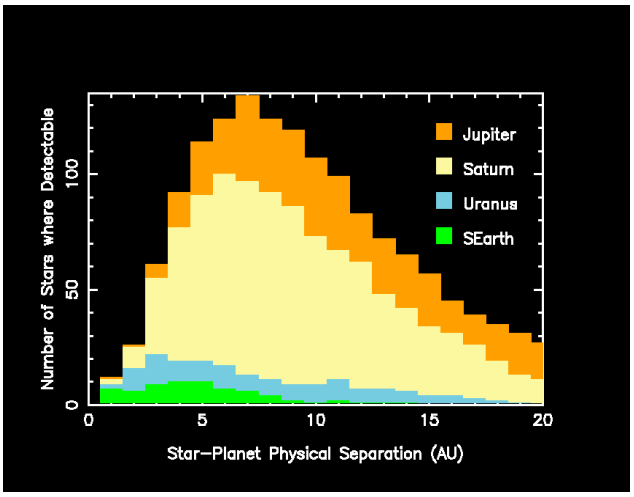

Figure 8.9.4-9. Number of planets detectable at S/N=10 with the ACCESS Lyot coronagraph, in integration times of 1 day or less, IWA of 2.5 λ/D.

8.9.5 Nearby Science Targets for the Access Probe-Scale Coronagraph Mission

8.9.5.1 Planets Identified by Radial Velocity Surveys

More than 300 planets have been discovered by radial velocity surveys as of early 2009 (see http://exoplanet.eu). Since intensive searches only began in the mid-1990s, the range of orbital periods probed to date is ~15 years. Most of the detected planets are found around stars similar to the Sun, and more often around stars with higher metallicity. Most appear to have masses comparable to that of Jupiter, although a few planets with masses at or below that of Neptune are now being found. The RV studies establish a planet's orbital period, orbital eccentricity, periastron epoch, and major axis orientation with respect to the sky plane, The orbit inclination and major axis position angle are not provided, and must be constrained by astrometric data (although the inclination can be determined in the fortunate circumstance of a transiting system).

The known RV planets present a particularly important target set for a probe-scale coronagraph mission. As detailed below, nearby RV planets provide targets whose brightness, contrast to their central star, and angular separation are within ACCESS' imaging capabilities. Imaging detections at two or more epochs will yield the two missing orbital elements; once the inclination has been measured, the planetary mass can also be established. This then allows the atmospheric properties measured from the planetary photons (brightness/albedo; broadband colors; presence and strength of major absorption spectral absorption features; brightness variation with orbital phase) to be related to the mass of the planet. Will all Jupiter-mass planets possess the same reservoir of internal heat, and thus have comparable effective temperatures and atmosphere properties? Or will Jupiter-mass planets be found with Uranus-like atmospheres, and vice-versa? ACCESS will provide the data to answer this question.

The available orbital elements allow a lower limit to the maximum elongation, and the epoch at which this takes place, to be calculated for each known RV planet. At the time of maximum elongation, the planet's radial acceleration is near its maximum value; at conjunction the radial acceleration is near its minimum value. The nominal maximum elongation angle of a planet will simply be (a/d) arcseconds, where a is the orbital semi-major axis and d is the distance in parsecs. A significant orbital eccentricity can increase the elongation angle to as much as a(1+e)/d arcseconds, if the major axis lies in the sky plane. However, in the case where the orbital major axis is aligned along the line of sight, the maximum elongation will actually decrease with increasing eccentricity. Fully considering the orbit alignment effects, we have calculated the 2 dimensional position of each nearby RV planet over the 10-year period 2013–2022 (the period during which an ACCESS-like mission could be brought to flight). Figure 8.9.5-1 shows example results. In these plots, the position of the planet is broken down along two orthogonal coordinate axes. The X-axis shows the offset between the star and planet in the sky plane, as established by the orbit semi-major axis, eccentricity, and argument of periapse Ω. The Y-axis shows the offset between star and planet i*n the orthogonal orbit plane*. Depending on the orbital inclination, all of this Y-axis offset could be seen (face-on orbit case) or none of it could be seen (edge-on orbit case). In reality, some fraction of the predicted Y-axis offset will be visible for the most likely intermediate orbit inclination. Furthermore, it should be noted that the position angle of the orbit major axis on the sky is not known a-priori, and thus the orientation on the sky of the X-axis elongation we plot is not known in advance. From these orbit plots, maximum elongation angles and they epochs when they occur have been extracted and are given in Table 8.9.5-1. *Thanks to the RV data, we already know exactly when nearby giant planets will appear at maximum elongation and how large that elongation angle will be.*

In addition to the above clear-cut targets, there are two additional groups of nearby stars that the radial velocity data point to for studies with ACCESS. First, there are the 25 additional stars within 20 pc of the Sun that have RV planets on orbits too close to the star to resolve with ACCESS. The known inner planets demonstrate that these 25 stars have a planetary system which may include

more distant, outer planets that ACCESS may be able to discover. We postulate that outer planets are more likely to be found in these systems than around stars lacking any inner planetary system. In addition, there are 13+ stars within 20 pc where the RV data shows long-term accelerations indicative of a long-period outer planet where a closed orbit solution cannot yet be derived (G. Marcy, personal communication). *Thus at least 35 additional stars within 20 pc have an enhanced probability of possessing a 5–15 AU outer planet detectable with a probe-class coronagraph mission such as ACCESS.*

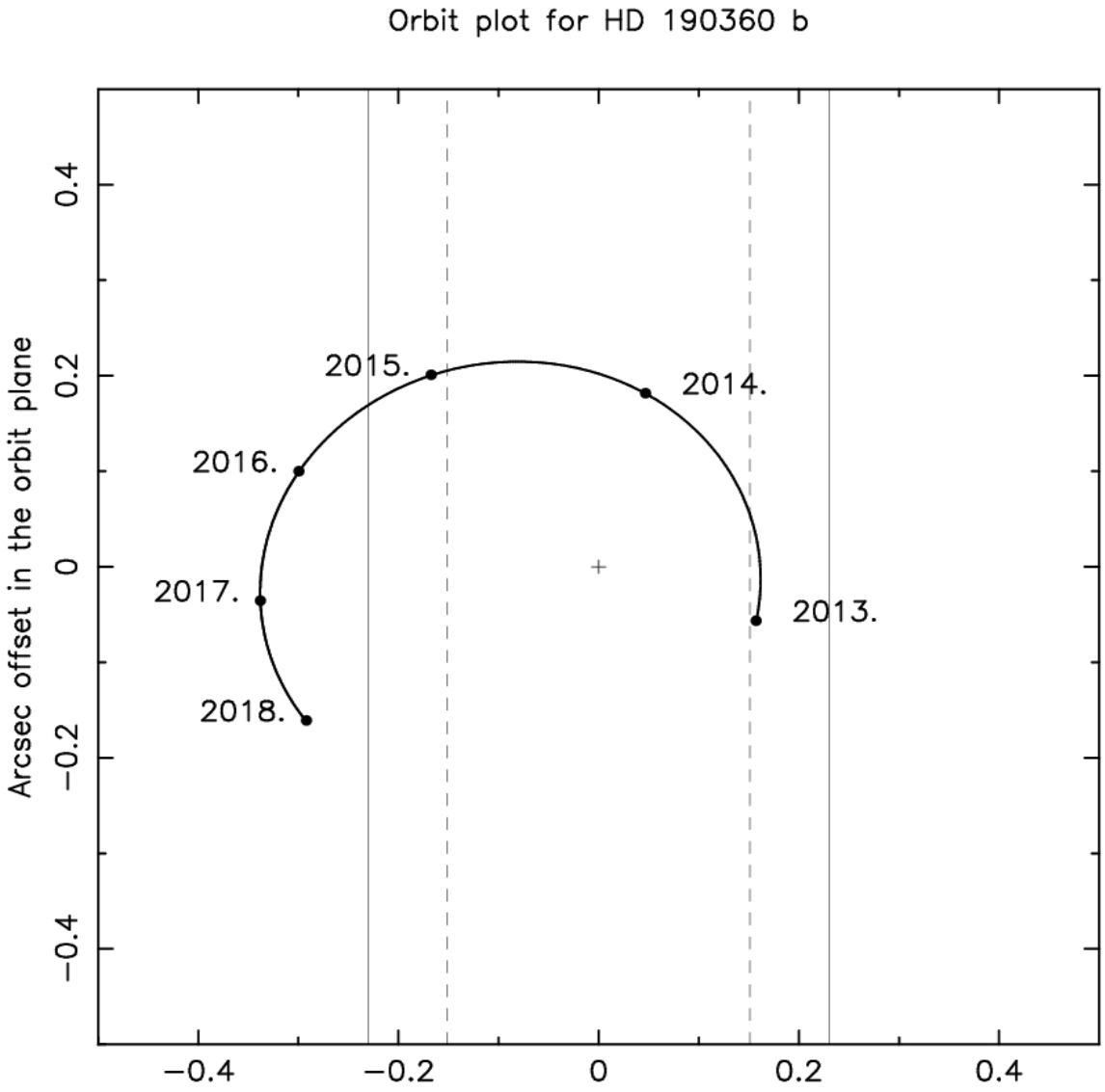

Figure 8.9.5-1. Example plot of the elongation of RV exoplanet HD 190360 b, as described in the above text. The solid and dashed vertical lines show the 3 λ/D and 2 λ/D inner working angle sizes for λ = 0.55 μm.

Table 8.9.5-1. Observability of nearby radial velocity planets with ACCESS. Shown are the 10 objects known (as of early 2009) with maximum elongations @ 0.23° (= 3 λ/D @ 0.55 μm = 2 λ/D @ 0.8 μm). Brightness estimates assume planet radius and albedo equal to that of Jupiter. Eight of these objects should be readily detected, but the two M-star planets will be very faint and difficult to study.

Planet / Stellar type	Max Elong Dates	Angular Sep (")	Linear Separation (AU)	Delta Mag	Apparent V mag
Eps Eri b	Dec 2013	1.31	4.3	22.1	25.8
K2	Mar 2017	0.70	2.3	20.7	24.4
always visible	Mar 2021	1.31	4.3	22.1	25.8
GJ 832 b M1.5	Sep 2014	0.74	3.6	21.7	30.4
	Dec 2017	0.42	2.1	20.5	29.2
55 Cnc d	Dec 2017	0.43	5.3	22.5	28.5
G8					
HD 160691 c	Aug 2015	0.36	5.6	22.7	27.9
G3	Jun 2022	0.36	5.6	22.7	27.9
HD 217107 c	Aug 2021	0.31	6.1	22.8	29.0
G8					
HD 190360 b	Dec 2016	0.34	5.4	22.6	28.3
G7	Nov 2024	0.34	5.4	22.6	28.3
47 Uma c	Oct 2014	0.27	3.8	21.8	26.9
G1	Dec 2017	0.26	3.7	21.8	26.9
	Nov 2021	0.27	3.8	21.8	26.9
HD 39091 b	Dec 2016	0.28	5.1	22.5	28.2
G0	Oct 2022	0.28	5.1	22.5	28.2
GJ 849 b	Jun 2015	0.25	2.2	20.6	31.0
M2.5	Dec 2017	0.28	2.5	20.9	31.3
	Aug 2020	0.25	2.2	20.6	31.0
HD 154345 b	Jun 2015	0.24	4.3	22.1	28.8
G8	Aug 2024	0.24	4.3	22.1	28.8

8.9.5.2 Imaging Searches for Previously Unknown Planets

Radial velocity surveys are incomplete for orbital periods >10 years, for early F and hotter stars lacking strong metallic lines in their spectra, for stars with high chromospheric activity, and for planets in nearly face-on orbits. Multi-epoch imaging with ACCESS has the potential to discover planets in the size range from Jupiters down to super-Earths around a large sample of nearby stars. To quantify ACCESS' capabilities to survey nearby stars for planets in reflected light, PSF simulations for the different coronagraph types were used to estimate integration times for detection of fiducial planets around the actual nearby stars listed in the Hipparcos catalog. The results show that ACCESS can detect Jupiter analogs over the 5–15 AU range around more than 100 nearby stars; Saturn analogs around nearly as many; Uranus/Neptune analogs around ~30 stars; and super-Earths in perhaps 10 systems (assuming low levels of exozodiacal dust). See Figure 8.9.4-9.

Young/massive planets can appear bright in their own thermal emission, and thus be detectable at large orbital separations where reflected light signatures would be too feeble. The recent discovery of young planets in the 30–110 AU range around HR 8799 and Fomalhaut [2, 3] provides a vivid demonstration of this potential. Within 20 pc of the Sun, there are 18 stars known with ages < 1 Gyr that will be prime targets for imaging warm young planets. At z band (0.9 μm), thermal emission models [4] indicate that the 10^{-9} contrast capability of ACCESS would allow detections of objects with 15, 8, 4, and 2 Jupiter masses around Sun-like stars with ages of 5, 1, 0.3, and 0.1 Gyrs

respectively – comparable to the sensitivity expected to be achieved at H band by the next generation of adaptive optics systems such as VLT/Sphere and the Gemini Planet Imager. ACCESS observations would extend their spectral characterization to $\lambda < 1$ μm, providing a strong check on the atmospheric and evolutionary models for these objects.

8.9.5.3 Detectability of Exozodiacal Dust

High levels of exozodiacal dust will be a major impediment to direct imaging of extrasolar terrestrial planets, no matter what telescope architecture is eventually employed. These dust clouds reflect starlight and emit in the thermal infrared, adding photon noise and scene confusion to exoplanet signals. If typical exozodiacal dust levels proved to be ~>10 times our solar system's, it would force the TPF mission design to high spatial resolutions that could only be accomplished with a very large telescope/coronagraph or a formation-flying interferometer. It is therefore crucial to assess the dust levels around nearby stars. Spitzer 70-micron observations have identified exo-Kuiper disks brighter than 100 zodis in spatially unresolved photometry; Herschel may improve on this sensitivity by a factor of 2. However, these observations detect cold dust far from the HZ. The Keck and LBT interferometers will use 10-micron nulling observations to probe HZ dust. However, initial Keck observations have shown that the combination of atmospheric and instrumental phase stability limits the null depth to sensitivities of roughly a hundred zodis. Additional ways to attack the problem are needed. Detailed coronagraphic imaging simulations show that ACCESS will be sensitive to dust levels of 1 zodi equivalent at 1 AU distances for 15 nearby stars. A much larger sample of 75 stars (V × 5) can be probed for 1 zodi dust levels at 3 AU separations, where transport models can be used to relate dust levels at 3 AU to those at 1 AU. 0.1 zodi sensitivity can be achieved at 3 AU in 13 systems. Reflected light observations with ACCESS will thus be an outstanding tool for assessing the dust content in the HZs of nearby stars, establishing the exozodiacal background levels that are a key factor in TPF design trades.

8.9.5.4 Structure of Exozodiacal and Exo-Kuiper Debris Disks

ACCESS will make the most sensitive imaging survey to date of tenuous debris disks, the signposts of planetary systems. These are clouds of small dust grains created by the mutual collisions of asteroids and comets, as well as by comet sublimation. Without continual replenishment by such events the dust would be cleared away within a small fraction of a star's lifetime by stellar radiation, stellar wind pressure, or self-radiation. The interplanetary dust cloud in our own solar system, which can be seen as the zodiacal light, is a debris disk created primarily by the collisions of asteroids. Spitzer observations have identified 40 stars within 25 pc that possess debris disk analogs to our Kuiper Belt, at the levels of a few hundred zodis. Some of these dust clouds have been spatially resolved and show warps, asymmetries, or narrow rings that are strongly suggestive of planetary perturbations. The Earth has resonantly trapped dust within a ring along its orbit, with a trailing wake of enhanced particle density [5]; the Fomalhaut debris disk has a significant eccentricity that requires dynamical forcing by a planet of at least Neptune mass [6]. The Fomalhaut planet was recently directly imaged at the located predicted from its perturbations to the disk structure [3, 7]. As a canvas on which planets can impress dynamical signatures, dust disk structures will enable indirect detections of planets too faint or dust-shrouded to be seen otherwise.

8.9.6 References for Section 8.9

[1] Brown, R.A. 2009. "Science-Operational Metrics and Issues for the 'Are We Alone?' Movement," arXiv:0903.5139.

[2] Marois, et al. 2008. "Direct Imaging of Multiple Planets Orbiting the Star HR 799," *Science* 322: 1348.

[3] Kalas, et al. 2008. "Optical Images of an Exosolar Planet 25 Light-Years from Earth," *Science* 322: 1345.

[4] Burrows, Sudarsky, and Lunine. 2003. "Beyond the T Dwarfs: Theoretical Spectra,Colors, and Detectability of the Coolest Brown Dwarfs," *Ap.J.* 596: 587.

[5] Dermott, et al. 1998. "A circumsolar ring of asteroidal dust in resonant lock with the Earth," *Nature* 369: 719.

[6] Kalas, et al. 2005. "A planetary system as the origin of structure in Fomalhaut's dust belt," *Nature* 435: 1067.

[7] Quillen, A. 2006. "Predictions for a planet just inside Fomalhaut's eccentric ring," *M.N.R.A.S.* 372: L14.

This page is intentionally left blank.